Daniel dos Santos Covita

High Precision Spectroscopy of the $3p-1s$ X-Ray Transition in Muonic Hydrogen

University of Coimbra
2008

Daniel dos Santos Covita

High Precision Spectroscopy of the $3p-1s$ X-Ray Transition in Muonic Hydrogen

Dissertation submitted to
Faculty of Science and Technology of the University of Coimbra
for the degree of *PhilosophiæDoctor* in Technological Physics

under the supervision of
Dr. Leopold M. Simons and Dr. Joaquim M.F. dos Santos

in collaboration with
PAUL SCHERRER INSTITUT
PSI
Switzerland

University of Coimbra
2008

to the memory of my granny Delfina,
– forever living in my heart

“*Deus quer, o homem sonha, a obra nasce.*
Deus quis que a terra fosse toda uma,
Que o mar unisse, já não separasse.
Sagrou-te, e foste desvendando a espuma,...”
FERNANDO PESSOA in *Mensagem* (1934)

“By fooling around with frogs’ legs and wires, physycists saw that Nature behaves in a certain pattern, and that Her behavior can be described by a set of equations. The equations, once written down, sing out a song, waiting patiently for someone with ears to hear.”
A. ZEE in *Fearful Symmetry* (1999)

"We are like dwarfs sitting on the shoulders of giants. We see more, and things that are more distant, than they did, not because our sight is superior or because we are taller than they, but because they raise us up, and by their great stature add to ours."
JOHN OF SALISBURY in *Metalogicon* (1159)

"If I have seen a little further it is by standing on the shoulders of Giants."
ISAAC NEWTON in a letter to his rival Robert Hooke (1676)

"Science is a community effort"

Acknowledgments

Science is indeed a community effort with many souls struggling to understand nature's design. This work is a tiny contribution on this long race of knowledge with many contributions which should not be forgotten. Hence, I would like to show my gratitude to those who made this investigation possible:

– Dr. Joaquim Santos, who has looked for the opportunity that I became a member of the πH collaboration and helped me on the transition from "Gas detectors" to "Exotic atoms". Thank you for helping during the reviewing of the thesis. Thank you so much for all the support since even before my graduation and for always having believed in my capabilities.

– Dr. Leopold Simons, who has welcomed me inside the collaboration and has given his best to taught me what experimental physics is about. Thank you for the guidance and the patience during the long and detailed explanations about the physical and experimental aspects of the experiment. Thank you for all the efforts to provide working software routines which have helped me and all the collaboration in the data analysis. Thank you for the reviewed literature which has clarified many misunderstood aspects. Thank you for all the enthusiasm and devotion put along the years on the development of the means to drive the investigations of the πH collaboration to successful results. Thank you for the crucial remarks about the present manuscript which resulted in larger improvements. I can proudly say that Dr. Leopold Simons was my supervisor and a true [doctor] father.

– Dr. Detlev Gotta, who has also taught me so much about experimental physics. Thank you for being always available, kind and generous to share your time in discussions which helped me to overcome many of the difficulties. Thank you for the valuable contribution by helping with the writing of the publications and by reviewing the thesis. Thank you also for all the dedication put in the development of the high resolution spectrometer which has made possible the investigations done by the πH collaboration in exotic atoms.

– Dr. Franz Kottmann, who has given me continuous support at Paul Scherrer Institut, particularly after Dr. Leopold Simons retired. Thank you for the valuable advice in uncountable discussions about the subject of my thesis. Thank you for the gentleness always demonstrated in the explanations. Thank you also for helping during the reviewing of the present manuscript.

– Dr. Albert Hirtl, Dr. Martino Trassineli, Thomas Strauch and Sophie Schlesser, my PhD colleagues with whom I had the privilege to work with during several beam times. Special thanks to Albert for the important maintenance work with the cryogenic target and more particularly for the close collaboration in the ECRIT data analysis. Special thanks to Martino for the explanations about the crystal spectrometer during my first run time and further discussions about Bragg crystal spectrometry. Special thanks to Thomas for some important remarks about the CSDCLUSTER and for providing the data related with the stability of the spectrometer during the μH run. Special thanks to Sophie, for their ideas about the geometry of the spectrometer and for helping in the miscut measurement. Above all, thank you for the friendship.

– Dr. Eric-Olivier Le Bigot, for helping in the interpretation of the results of the ECRIT data analysis and for the warm and valuable discussions about the ECRIT measurement. Thanks for the important help in writing the miscut publication.

– Dr. Johann Zmeskal, Dr. Tomoichi Ishiwatari, Alexander Gruber and Philipp Schmid who together with the collaboration of Dr. Albert Hirtl, were responsible for the development and maintenance of the cryogenic target during the beam time.

– Dr. Paul Indelicato, for sharing his theoretical calculations on QED and his important contribution in the development of the ECRIT. Thank you also for some valuable explanations during my first run time.

– Dr. Hubert Gorke, for his crucial help in mounting and operating the pnCCD detector system which was partially developed by himself.

– Dr. Nick Nelms, who together with his co-workers at the Leicester University had developed the CCD detector used during all the investigations of the πH collaboration. Thanks also for the availability for technical support and advice every time it was needed.

– Dr. Valerie Markushin, whose efforts have led to the development of the ESCM. Thank you for the theoretical advise and support and to have helped to write the initial proposal of the πH collaboration. Thank you for having adapted the MINUIT fit routine, which has extensively been used during my analysis.

– Dr. Thomas Jensen, for his major contributions in the development of the ESCM and for the scientific advise in the physics of the cascade deexcitation in exotic hydrogen. His PhD thesis has strongly supported the writing of chapter 3.

– Dr. Vladimir Popov and Dr. Vladimir Pomerantsev for their efforts to bring the ESCM calculations on new theoretical grounds and for their gentle sharing of newest results.

– Dr. Murat Ay, who had first the idea of a possibility of the characterization of the asymmetric cut angle in a bent crystal at the commercial X-ray Spectrometer available at PSI. Thank you for the support during the miscut measurements.

– Dr. Aldo Antognini for having revealed me the "world" of *gnuplot* and *Xfig* which I used to produce my plots and sketches. Thank you for the warm discussions in trying to find the physics behind the formulations. Thank you for kindly sharing the office with me in the last 6 months.

– Dr. Michael Nekipelov for helping to deal with Linux during the run time.

– Alfred Wasser and Lukas Stingelin for the precious technical development and support of the electronics needed for the microwave generator used in the ECRIT setup.

– Bruno Leoni, who has worked together with Dr. Leopold Simons and has given technical support in the construction and development of the cyclotron trap, the ECRIT source and many other crucial experimental parts.

– Leopold Stohwasser (Vienna), Peter Wieder (Jülich) and Norbert Dolfus (Jülich), for the crucial technical support during the set up of the experiments.

– *Hallendienst* of the *Experimentierhalle* (PSI), who had helped in the construction of the concrete shielding, moving the big parts and transporting the Liquid Helium dewars.

– The survey group from PSI for their meticulous work in the precise alignment of the setup at the πE5 area and accurate measurement of many parts of the experiment.

– Dr. Hans Grimmer, who have made possible the use of the SEIFERT® instrument.

– Uwe Flechsig (head of the beam optics group at the Swiss Light Source), who has kindly authorized the use of their optical profilometer to perform a second measurement of crystal radii. Veit Schoenherr and Sibylle Jaeggi, who have operated the profilometer.

The present work has been conducted at Paul Scherrer Institut and supported by a Ph.D. scholarship granted by the *Fundação para a Ciência e Tecnologia* (Lisboa, Portugal) through the POCI 2010 program.

> *"No love, no friendship, can cross the path of our destiny without leaving some mark on it forever."*
> Francois Mauriac (1885-1970)

To come to a different country, get used to new realities, culture and overcome the language barrier is by itself a huge challenge. A challenge which is only possible to be tackled with the support of the ones who love us. I can not say it was easy, but it would have been much harder or even unbearable without the love and friendship of those around me. I would like to expressed my gratitude to those who have been around me in the past four years:

– The members of the πH collaboration with whom I have worked and who ensured a great fellowship spirit during the beam times. It was always a pleasure to share a beer with you whatever for celebrating an experimental success or for releasing the frustration of a bad day.

– The collaborators of the μH Lamb-shift with whom I have my first contact with "big experiments" at PSI and who have shown me an excellent group atmosphere. A special thanks to Dr. Françoise Muhlhauser for helping me so much to improve my english at the very beginning of my stay. It was a honor to share my daily lunches at OASE with Dr. Franz Kottmann, who has transformed many ordinary meals in very interesting conversions about general topics. A word of admiration to *the non-paper man* Dr. Aldo Antognini (the latin side of Switzerland) and to *the most contagious laugher* Dr.^{2} Livia Ludhova (a slovak with italian soul) – GREAT SPIRIT. A special thanks also to Dr. Randolf Pohl for kindly have presented me with his nice pseudo-ugly black old furniture – black is cool and cooler if it is even for free! Wish the best for their further investigations.

– Anita Van-Loon, the secretary of the Laboratory for Particle Physics at PSI, who has always generously helped me to handle many bureaucracy items.

– The *Rinikers*: Christian Gruenzweig, Florian Piegsa and Murat Ay. My cherished flatmates with whom I have shared many unforgettable moments in Switzerland. On top of some natural differences we were able to build up strong friendship bonds which I believe and hope will remain for many years. A word of cordiality also to Melanie and Manuela.

– All the new friends that I have made at PSI. Besides science, the most remarkable thing from which one can profit by passing at PSI is the cultural exchange ensured by the worldwide origins of the scientific community. It is a truly rewarding experience which extends our horizons and can shape our appreciation of the world beyond our domestic frontiers. Some, who have touched me deeper, I would like to mention: Ahed Aladwan, Alessandra Bolsi, Fatima Gonzalez, Jorge Lobo-Checa, Juan Pablo Urrego, Marcos Gaspar, Marloes Steneker, Rossela Guerrieri, Stela Canulescu, Vladimir Strocov, Yuri Zaushitsyn and Yu Lung Chiu. I hope I can keep the friendship of all for long years.

– Irmhild, Leo's wife, who has always welcome me at their home with kindness. A special thanks for having always prepared excellent meals to restore my mental strength after the overwhelming scientific discussions with Leo! Some of these meals were true gastronomic experiences – the "strange" pumpkin soup will remain a delicious memory!

– The Atomic and Nuclear Instrumentation Group of Coimbra, my original group, whose members have always showed cordial hospitality during my visits at Coimbra and helped me with many formalities at the University and at the Portuguese Science National Foundation. Particularly I would like to mention Prof. Joaquim Santos, Dr. João Veloso, Fernando

Amaro, Cristina Monteiro, Elisabete Freitas, Paulo Gomes, Dr. Luís Panchorrinha (Pancho) and Dr. José Matias.

– My beloved parents who, despite the suffering from my absence, have always supported my choice. I would never be able to retribut the unconditional love and affection that they continuously give me. Mam! Dad! I love you!

– Os meus queridos pais, que apesar da dor da minha ausência, sempre apoiaram as minhas decisões. Nunca serei capaz de retribuir o amor e carinho incondicional que sempre me deram. Mãe! Pai! Amo-vos muito!

– Finally but not least, my beloved little princess Adriana. The precious gem, which like many great things in science and life, I unexpectedly discovered. The tenderness of your being has given me the strength I needed to face and overcome many problems and your love continuously rejuvenated my spirit. It was never easy to deal with the spatial distance that has kept us apart. However, day by day it became clear that is nothing compared to the proximity of our hearts. I am glad that our paths once crossed and we could walk together during the past two years. I wish our love endures with the passing years. I love you, my sweet little flower!

Abstract

Continuous experimental effort has been undertaken using the low-energy pion beam at the Paul Scherrer Institut (PSI), Switzerland, to extract with high precision the isospin scattering lengths of pion-nucleon strong interaction [116]. The experimental technique relies on the cyclotron trap and high resolution spectroscopy methods [77] to measure X-ray transitions feeding the ground state of pionic hydrogen and determine the strong interaction shift ϵ_{1s} and width Γ_{1s} of the fundamental level.

The extraction of Γ_{1s} faces particular difficulties as it is masked by Doppler broadening induced by Coulomb deexcitation. The interplay of the deexcitation mechanisms during the cascade of exotic hydrogen is very complex and not yet understood in detail although advanced cascade models exist [32, 33, 38]. Muonic hydrogen, which can be regarded as the twin system of pionic hydrogen can be used to improve our understanding of the cascade, because the μH system does not experience the strong interaction and, thus, any broadening of the X-ray transitions additional to the response function of the apparatus is related exclusively to the Doppler effect.

Results are reported from the dedicated μH experiment carried out at PSI by measuring X-rays of the $(3p - 1s)$ transition with a high-resolution crystal spectrometer. For the first time, the hyperfine splitting of the ground state of muonic hydrogen could be resolved. A Doppler effect broadening of the X-ray line was clearly identified and could be attributed to different Coulomb deexcitation steps preceding the measured transition.

The assumption of a statistical population of the hyperfine levels of the ground state was directly confirmed by experiment and measured values for the hyperfine splitting can be reported.

The results allow a decisive test of advanced cascade model calculations and establish a "model-free" method to extract the strong-interaction width from the pionic hydrogen data.

In addition, the characterization of the Si(111) crystal for the μH measurement is reported as well.

Sumário

Durante os últimos anos têm vindo a ser realizadas, no feixe de piões de baixa energia do acelerador de protões do Instituto Paul Scherrer (Suiça), experiências que visam a determinação do comprimento de dispersão em termos de isospin da interacção forte pião-nucleão com elevada precisão [116]. As técnicas experimentais baseiam-se na *cyclotron trap* e nos métodos de espectroscopia de alta resolução para medir transições radiativas (raios X) [77] e, deste modo, determinar o desvio ϵ_{1s} e a largura Γ_{1s} do estado fundamental do hidrogénio piónico causados pela interacção forte.

A determinação de Γ_{1s} levanta dificuldades acrescidas uma vez que é camuflada pelo efeito Doppler induzido pela desexcitação de Coulomb. A interacção entre os diferentes mecanismos presentes na cascata de desexcitação do hidrogénio exótico é bastante complexa e embora existam modelos avançados (ESCM) [32, 33, 38], muitos detalhes carecem de explicação. O hidrogénio muónico, que pode ser visto como um “sistema gémeo” do hidrogénio piónico, pode ser utilizado para melhorar o conhecimento acerca da cascata de desexcitação; sendo um sistema que não “sente” a força forte, a largura adicional das transições radiativas (raios X) que não é devida à função resposta do espectrómetro é devida exclusivamente ao efeito Doppler.

No presente trabalho apresentam-se os resultados da experiência realizada no PSI, cujo objectivo foi a detecção dos raios X da risca espectral $3p{-}1s$ do hidrogénio muónico com um espectrómetro de cristal de alta resolução. A estrutura hiperfina do estado fundamental do μH foi observada e resolvida pela primeira vez. O alargamento da linha espectral devido ao efeito de Doppler foi iniquivocamente identificado e pode ser atribuído a diferentes desexcitações de Coulomb que antecedem a deexcitação radiativa.

O preenchimento estatístico da estrutura hiperfina do estado fundamental foi confirmado experimentalmente, e apresentam-se os resultados para a separação entre os subníveis de energia do tripleto e do singleto.

Os resultados permitem testar os cálculos do modelo avançado da cascata de desexcitação (ESCM) e estabelecer um método independente de modelos teóricos para analisar os dados existintes em hidrogénio piónico e extrair o valor de Γ_{1s}.

A caracterização do cristal Si(111) utilizado nas medições efectuadas em μH é também disutida em detalhe.

Contents

List of Figures

List of Tables

Chapter 1

Introduction

In 1998 a collaboration which involved several institutes from different countries and different expertises proposed to measured the strong interaction shift and width of the ground state of pionic hydrogen (πH) at the Paul Scherrer Institut (PSI – Switzerland) with an accuracy of one order of magnitude better than previously known [108]. This should be achieved by combining high resolution crystal spectroscopy techniques with the cyclotron trap operated at a low high intensity and low momentum π^- beam line.

The main goal of this experimental effort is to extract the pion-nucleon scattering lengths for both isospin components (related to the measurable quantities) with an unprecedent precision. Hence, it constitutes a very important test of the fundamental theories in quantum chromodynamics at low energy, thus constraining future theoretical developments.

In order to accomplish the desired accuracy, several aspects related to the atomic cascade dynamics of the πH system needed to be clarified. Therefore, a measurement in muonic hydrogen (μH) was planned to overcome the lack of knowledge in the theoretical description of the cascade mechanisms of these exotic systems. A detailed discussion of the μH measurement and its analysis is the main subject of this work. In addition, a characterization of the spectrometer was planned by using narrow atomic spectral lines from highly charged ions.

A series of measurements were consequently planned and executed during the following years, with the first measurement of the strong interaction shift in πH being done in 2000 and concluded in 2001. The determination of the strong interaction width has started in 2001, carried on in 2002 and concluded in 2005. The μH experiment was done in 2004 and the characterization of the spectrometer was performed in several steps from 2002 till 2007. The strong interaction shift has been determined but the analysis related to the strong interaction width of the ground state of πH is still in progress, at a very advanced stage. On the other hand, the analysis of the μH data has been successfully accomplished in 2007.

The present work reports the measurement of an X-ray transition in muonic hydrogen feeding the ground state by using a high resolution crystal spectrometer. The characterization of the Si(111) crystal used is the second main subject of this work. A detailed overview about the experimental techniques, challenges, data analysis and results will be addressed. Furthermore, subsequent investigations on the crystal characterization, which were not initially foreseen but prompted by puzzling preliminary results, are additionally outlined.

1.1 Layout

The main stream of the ideas behind the theoretical development of the strong interaction at low energies is presented very briefly in ***Chapter 2***. The motivation for the pionic hydrogen investigations is resumed shortly and the relations that connect the scattering lengths with the measurable quantities are pointed out. The fundamentals of the hyperfine splitting of the ground state of muonic hydrogen are presented as well for the leading order term.

In ***Chapter 3*** the present knowledge about the atomic cascade of the light exotic atoms is addressed. The different mechanisms involved during the cascade as well as their interplay are discussed. Additionally, the evolution of the cascade model is presented together with its latest predictions for some measurable quantities. At the end of the chapter, the issues related to development of the kinetic energy during the cascade of the exotic system and their effect on the measurable X-ray transitions are pointed out. A simplified model, which was used in the analysis of the muonic hydrogen data to overcome the lack of theoretical knowledge on this topic, is presented.

The items related to high resolution spectroscopy with bent crystals are discussed in detail in chapter ***Chapter 4***. A short presentation of the most relevant aspects behind the theory of X-ray diffraction in crystals is given. The geometrical constraints of the image construction from a vertically extended and spherically bent crystal are carefully worked out. Furthermore, the impact of some geometrical parameters on the response function is studied by using the tracking routine developed inside the collaboration [114]. Finally, the spectrometer employed in all investigations is described.

Chapter 5 presents the investigations done on the characterization of the Si(111) crystal. A brief introduction about the electron cyclotron resonance ion sources is given. The experimental setup as well as the procedure to extract the response function of the spectrometer equipped with Si(111) is discussed in detail. The analysis of the data is meticulously explained together with the puzzling aspects which prompted further investigations on the characterization of the crystal. The results of these investigations are presented as well. A model to extrapolate the response function from the one measured at 3.1, 2.7 and 2.4 keV to the energy of the μH($3p-1s$) transition (2.25 keV) is delivered at the end of the chapter.

The μH experiment and the subsequent data analysis are discussed in ***Chapter 6***. The layout of the setup as well as the experimental routines are explained in detail. The logics of the analysis is presented step-by-step.

The results and conclusions of the present investigation are summarized in ***Chapter 7***. Two publications have already been originated directly from this work. One at *Review of Scientific Instruments* and a second to be submitted to *Physical Review Letters* for which the draft is under reviewing of the collaborators. A third publication about the characterization of the crystals with an ECRIT is foreseen.

Chapter 2

Theoretical background

The investigations on the muonic hydrogen μH constitute an important and crucial step of the measurement of the strong interaction shift (ε_{1s}) and width (Γ_{1s}) of the ground state of the pionic hydrogen system πH, which is the major goal of the πH collaboration [108]. The results obtained from this experiment will test the low energy approach to *quantum chromodynamics* about the strong interaction and constrain further theoretical development.

A detailed description of the theory about the pion-nucleon interaction is far from the scope of the present work. However, a brief insight into the main theoretical ideas which have stimulated the experimental activities in πH will be addressed. A deeper theoretical understanding can be found in the references mentioned.

2.1 Motivation

Prompted by the outstanding success of the predictions of *quantum electrodynamics* (QED), *quantum chromodynamics* (QCD) arose in the second half of the twentieth century as an expansion of QED in order to explain the strong interaction of quarks. QCD is a part of the standard model theory which is a gauge theory with a SU(3)$\otimes$SU(2)$\otimes$U(1) local symmetry [1, 2, 3, 4].

A gauge theory is based on the idea that systems can remain unchanged by applying a certain transformation. Hence, exhibiting global or local symmetries if they remain unchanged in time or not, respectively. Furthermore, according to Noether's theorem, for each continuous symmetry of the action of a physical system there is a conserved quantity. For instance, by translating a system in space the system remains unchanged, exhibiting a translational global symmetry which corresponds to linear momentum conservation. Thus, as QED is associated to the U(1) symmetry group and to electric charge conservation, QCD is associated with the SU(3) symmetry group and to the color conservation of quarks. The SU(2) symmetry is related to the weak interaction.

In a similar way as QED requires photons to mediate the electromagnetic interaction, strong interaction is mediated by gluons. Unlike the massless and neutral photons, gluons carry color. Several types of gluons exist which can couple among each other. This renders calculations hard to compute even when applied to simple systems. Moreover, QCD does not exhibit a linear behavior at different scales as QED does. The coupling constants, which evaluate the strength of the strong interaction, changes with distance, therefore named running coupling constants.

However, at very high energies the quarks can be treated as free particles because of the decreasing strength of the strong interactions as described by the running coupling constants. This is called asymptotic freedom and it allows to apply perturbative methods to QCD at large energies with great success.

At low energies, QCD becomes non-perturbative and none information can be extracted by the methods mentioned. Hence, a different method has been developed: the *chiral perturbation theory* (ChPT). ChPT is nowadays considered to be ***the*** theory to describe the strong interaction phenomena at low energies. ChPT is an effective field theory at low energy and introduces the quark masses as perturbation [5]. The general idea behind an effective field theory is, that it is not necessary to know all the physics of a process to make useful predictions about a specific part [6, 7]. In fact, ChPT resumes the quark world to the three lighter quarks (*up*, *down* and *strange*) which is sufficient to describe the pion-pion and meson-nucleon interaction.

Constructed upon the assumption of massless quarks, ChPT works best for the lightest quarks *up* and *down* combined with the lightest strongly interacting particle – the pion, and hence to describe the pion-pion interaction [8, 9]. On the other hand, when applied to the meson-nucleon interaction it is often denoted as *heavy baryon chiral perturbation theory* (HBChPT) [5, 4, 10].

Therefore, experiments involving pion-pion ($\pi\pi$) and pion-nucleon (πN) interaction are of major interest to test ChPT and HBChPT [77]. The measurement of the lifetime of the pionium ($\pi^+\pi^-$) system from the DIRAC experiment checks the predictions of the ChPT to the pion-pion interaction [11]. On the same way, the experiment performed by the πH collaboration [108] will allow accurate tests on the pion–nucleon interaction, thus testing HBChPT which constitutes the main motivation of the investigations on pionic hydrogen.

However, the determination of the experimental quantities in πH can be masked by the collisional interactions of the exotic systems with their surroundings, in particular for the extraction of strong interaction width of the ground state Γ_{1s}. The dynamics of these collisional processes is not yet fully understood. Here, the importance of the muonic hydrogen measurement, which is the main subject of the present work, is revealed. It constitutes a crucial part of the overall investigation in order to achieve the desired accuracy and will give important indications to overcome the intrinsic difficulties on the understanding of the atomic cascade dynamics in exotic hydrogen.

Here the measurements with kaonic systems like the ones intended by the DEAR and SIDDHARTA should be mentioned, as they involve the third lightest quark –the *strange* quark [12, 13].

2.2 Pion-nucleon interaction and pionic hydrogen

In the understanding of the strong interaction, experimentally available quantities play an important role as their determination tests the fundamental theories. The so-called *scattering lengths* make up that link. The scattering lengths are parameters describing the scattering at very short distance and low energy, roughly speaking when the wavelength of the incoming particle is too large to resolve the scattering center. Hence, they are defined at zero energy.

The scattering lengths of the $\pi\pi$ interaction can in principle be obtained via $\pi\pi$ scattering at higher energies by extrapolating to zero and by performing other important corrections [14]. However, experimental difficulties constrained the accuracy to values higher than the few percent level required to a decisive test of the ChPT [14]. On the other hand, the determination of the scattering lengths in πN systems does not suffer from that problems, despite their own intrinsic experimental difficulties, and constitute a milestone to test ChPT via its HBChPT expansion.

The πN processes experimentally accessible are the two elastic scattering reactions and the charge exchange reaction, with a respective scattering length being assigned to each one:

$$\pi^+ + p \longrightarrow \pi^+ + p \quad \Rightarrow \quad a_{\pi^+p\to\pi^+p} \tag{2.1}$$

$$\pi^- + p \longrightarrow \pi^- + p \quad \Rightarrow \quad a_{\pi^-p\to\pi^-p} \tag{2.2}$$

$$\pi^+ + p \longrightarrow \pi^0 + n \quad \Rightarrow \quad a_{\pi^+p\to\pi^0n} \tag{2.3}$$

The πN systems can be described in terms of isospin I. The isospin is a quantum number related with the strong interaction which describes particles with a similar mass as different states of the same particle. Therefore, the proton and the neutron form an isospin doublet of a nucleon with isospin $I = \frac{1}{2}$ and different components of the isospin projection $I_z = \frac{1}{2}$ and $I_z = -\frac{1}{2}$, respectively. On a similar way, the pion family π^-, π^0, π^+ are different states of an isospin triplet $I = 1$ with different isospin projection $I_z = -1, 0, 1$, respectively. Consequently each πN system is a superimposed state of the initial π and N states with a resultant isospin of $\frac{1}{2}$ or $\frac{3}{2}$.

Within the formalism of the quantum theory of scattering, at low energy (whith momentum $p \to 0$) the scattering lengths can be expressed in terms of the isospin [15, 16, 17]:

$$\begin{aligned} a_{\pi^+p\to\pi^+p} &= a_{3/2} \\ a_{\pi^-p\to\pi^-p} &= \frac{1}{3}(2a_{1/2} + a_{3/2}) \\ a_{\pi^+p\to\pi^0n} &= \frac{\sqrt{2}}{3}(a_{3/2} - a_{1/2}) \end{aligned} \tag{2.4}$$

And two basic parameters can be defined, related to the elastic scattering channels, the isoscalar(isospin-even) and isovector(isospin-vector) scattering lengths a^+ and a^-:

$$a^{\pm} = \frac{1}{2}(a_{\pi^+p\to\pi^+p} \pm a_{\pi^-p\to\pi^-p}) \tag{2.5}$$

$$a^{+} = \frac{1}{3}(a_{1/2} + 2a_{3/2}) \tag{2.6}$$

$$a^{-} = \frac{1}{3}(a_{1/2} - a_{3/2}) \tag{2.7}$$

Assuming that the isospin symmetry is exactly fulfilled, i.e. the masses of the *up* and *down* quarks are the same, the elastic channels are related to the charge exchange by:

$$a_{\pi^-p\to\pi^-p} - a_{\pi^+p\to\pi^+p} = -\sqrt{2}a_{\pi^+p\to\pi^0n} \tag{2.8}$$

Therefore, the isovector scattering length can be obtained directly from the charge exchange reaction:

$$a_{\pi^-p\to\pi^0n} = -\sqrt{2}a^- \tag{2.9}$$

and the isoscalar one from the elastic scattering channel involving the negative pion by using the isovector information:

$$a_{\pi^-p\to\pi^-p} = a^+ + a^- \tag{2.10}$$

The isovector part is of particular interest because it is directly related to the pion-nucleon coupling constant.

Experimentally, they can be obtained via a Deser-type formula [18] which relates the scattering lenghts with the strong interaction shift ε_{1s} and width Γ_{1s} of the atomic ground state of the pionic hydrogen:

$$\begin{aligned} \frac{\varepsilon_{1s}}{E_{1s}} &= -\frac{4}{r_B} a_{\pi^- p \to \pi^- p}(1+\delta_\varepsilon) \qquad (2.11) \\ \frac{\Gamma_{1s}}{E_{1s}} &= 8\frac{Q_0}{r_B}\left(1+\frac{1}{P}\right)\left[a_{\pi^- p \to \pi^0 n}(1+\delta_\Gamma)\right]^2 \qquad (2.12) \end{aligned}$$

E_{1s} being the binding energy of the ground state as predicted by QED, r_B the Bohr radius of the $\pi^- p$ system, Q_0 the π^0 momentum in the CMS system and P the Panofsky ratio (see page 33).

Correction parameters δ_ε and δ_Γ do not allow a direct extraction of the scattering lengths from the measurable quantities ε_{1s} and Γ_{1s}. They are of the order of a few percent and account for electromagnetic corrections and isospin breaking effects. Many efforts have been made in their calculation with several approaches available [19, 20, 21]. Within the framework of HBChPT calculations have been made up to fourth order.

Thus, it is desirable to obtain the strong interaction shift ε_{1s} and width Γ_{1s} of the atomic ground state in pionic hydrogen at least with an accuracy which is good enough to reach the order of the corrections and the precision of the calculations.

A detailed discussion about the physics of the pion-nucleon interaction and the pionic hydrogen experiment can be found in [8, 24, 25, 26, 77, 144] and references therein.

2.3 The hyperfine splitting of the ground state of the muonic hydrogen

The proton (as well as a neutron) also exhibits spin as an intrinsic property and consequently a magnetic moment:

$$\vec{\mu_p} = g_p \frac{e}{2m_p} \mathbf{S_p} \qquad (2.13)$$

e being the unitary charge, m_p the proton mass, $\mathbf{S_p}$ the proton spin operator and g_p the so-called g-factor of the proton which is a scaling factor determined experimentally as $g_p = 5.585694701(56)$ [22]. With the proton spin being one-half ($S_p = 1/2$)[§], the value of the magnetic moment in terms of nuclear magnetons is:

$$\mu_p = \frac{g_p}{2} \mu_N \qquad (2.14)$$

[§] for simplicy, along this section the quantum numbers will be denoted by the italic form of the corresponding quantum operators

μ_N being the nuclear magneton ($\mu_N = e\hbar/2m_p$).

Due to the mass relation between the proton and the electron, the nuclear magneton is close to 2000 times smaller than the Bohr magneton ($\mu_B = e\hbar/2m_e$) which renders the nuclear magnetism far less important compared to the electronic magnetism. Therefore, the magnetic interactions due the proton spin are very week. Nevertheless, a small perturbation in the energy levels of the hydrogen atom is accounted by the interaction between the magnetic moment of the nucleus and the magnetic dipole moment of the electron.

In the case of the $1s$ state of the hydrogen atom, the energy correction ΔH_{hs} on the Hamiltonian describing the atomic states is introduced in the following way [23]:

$$\Delta H_{hs} = \frac{4}{3} g_p \frac{m_e}{m_p} m_e c^2 \alpha_f^4 \left(1 + \frac{m_e}{m_p}\right)^{-3} \frac{1}{\hbar^2} \quad \mathbf{S_p}\cdot\mathbf{S_e} \tag{2.15}$$

α_f being the fine structure constant ($\approx 1/137$) and $\mathbf{S_e}$ the electron spin operator. By using (2.14) g_p is replaced by μ_p in nuclear magnetons in (2.15):

$$\Delta H_{hs} = \frac{8}{3} c^2 \alpha_f^4 \mu_p \frac{m_e^2 + m_p^2}{(m_e + m_p)^2} \frac{1}{\hbar^2} \quad \mathbf{S_p}\cdot\mathbf{S_e} = \mathcal{A} \quad \mathbf{S_p}\cdot\mathbf{S_e} \tag{2.16}$$

where $\mathcal{A}$ stands for all constant terms.

Similar to the total angular momentum of the electron (spin-orbit coupling, $\mathbf{J} = \mathbf{L} + \mathbf{S}_e$), a total momentum operator $\mathbf{F}$ can be attributed to this perturbation:

$$\mathbf{F} = \mathbf{S}_p + \mathbf{J} = \mathbf{S}_p + \mathbf{S}_e + \mathbf{L} \tag{2.17}$$

which in the case of the s state (orbital quantum number $L = 0$) is reduced to:

$$\mathbf{F} = \mathbf{S}_p + \mathbf{S}_e \tag{2.18}$$

thus,

$$S_p - S_e < F < S_p + S_e \quad \Rightarrow \quad 0 < F < 1 \tag{2.19}$$

which means that the hydrogen $1s$ state is degenerated in a singlet ($F = 0$, $F_z = 0$) and a triplet state ($F = 1$, $F_z = -1, 0, 1$). By squaring (2.18), $\mathbf{S_p}\cdot\mathbf{S_e}$ is found to be:

$$\begin{aligned} \mathbf{F}^2 &= \mathbf{S}_p^2 + \mathbf{S}_e^2 + 2\,\mathbf{S}_p\cdot\mathbf{S}_e \\ \mathbf{S}_p\cdot\mathbf{S}_e &= \frac{\mathbf{F}^2 - \mathbf{S}_p^2 - \mathbf{S}_e^2}{2} \end{aligned} \tag{2.20}$$

Therefore, the eigenvalues of the operator $\mathcal{A}\,\mathbf{S_p}\cdot\mathbf{S_e}$ are given by:

$$\frac{\mathcal{A}\hbar^2}{2}\left[F(F+1) - S_p(S_p+1) - S_e(S_e+1)\right] \tag{2.21}$$

and they only depend on F (S_p and S_e are equal to 1/2 for both triplet and singlet states). The energy shift of the ground state of the hydrogen is then:

$$\frac{1}{4}\mathcal{A}\hbar^2, \quad F=1 \tag{2.22}$$

$$-\frac{3}{4}\mathcal{A}\hbar^2, \quad F=0 \tag{2.23}$$

resulting in the hyperfine splitting:

$$\Delta^{hs} = \Delta H_{hs}^{F=1} - \Delta H_{hs}^{F=0} = \mathcal{A}\hbar^2 = \frac{8}{3}c^2\alpha_f^4\mu_p\frac{m_e^2+m_p^2}{(m_e+m_p)^2} \tag{2.24}$$

which holds in leading order for muonic hydrogen by replacing the electron mass (m_e) for the muon mass (m_μ). By performing the numerical substitution the leading order of the hyperfine splitting is 182.443 meV.

The precise theoretical value is obtained by applying higher order QED corrections together with the finite size of the proton. According to [161] and references therein, the hyperfine splitting is calculated to be 182.725 ± 0.062 meV which is the value used as reference in the evaluation of the μH($3p-1s$) transition.

Moreover, by assuming that the states $|F, F_z\rangle$ of the $1s$ energy level are equally fed in a μH($np-1s$) radiative transition, a statistical distribution 3:1 is expected for the triplet-to-singlet population. However, it can not be excluded that hyperfine interaction at excited states may change the statistical population.

Chapter 3

Cascade Processes in Light Exotic Hydrogen Atoms

Exotic atoms are formed by stopping negative particles (μ^-, π^-, K^-, $\overline{p}$, generally denoted by x^-) in matter. The particles are captured in outer shells and the highly excited atoms undergo a deexcitation process until the ground state is reached, a nuclear reaction takes place or a weak interaction occurs.

The cascade kinematics in exotic atoms formed with hydrogen is completely different from atoms with $Z \geq 3$. The atomic systems formed with hydrogen (x^-p) are electrically neutral, which allow them to penetrate deeper in the electron cloud of the surrounding hydrogen molecules.

The theoretical and experimental studies on the kinematics of the exotic hydrogen cascade have a long history. The first detailed calculations were performed by *Leon and Bethe* back in the sixties for π^-p and K^-p atoms [27]. Further theoretical developments resulted in a first *standard cascade model* (SCM) [28, 29, 30, 31] able to provide some good agreement with the experimental results. The subsequent work of *Jensen and Markushin* upgraded the SCM to the *extended standard cascade model* (ESCM) [32, 33] by including some important new features.

Despite all the theoretical developments, the kinematics of the exotic hydrogen cascade is not yet fully understood and some aspects remain unexplained. Particularly, the non-existence of reliable cross sections for some mechanisms in a molecular hydrogen target is a major drawback. The present work constitutes itself a test to the ESCM.

In this chapter, a description of the present knowledge of the cascade kinematics of the exotic hydrogen will be given.

3.1 Capture

The negative charged particles (μ^-, π^-, K^-, $\overline{p}$ ...) after being slowed down in the target matter to a kinetic energy of a few tens of eV are captured in the Coulomb field of the atoms/molecules. They become bound into highly excited states.

A study of the physics of the capture in hydrogen is described by *Cohen* and references therein [34, 35]. The probability of a charged particle to be captured at a certain n and l in atomic and molecular hydrogen and deuterium follows curves similar to the ones shown in figure 3.1 for the muon capture [35].

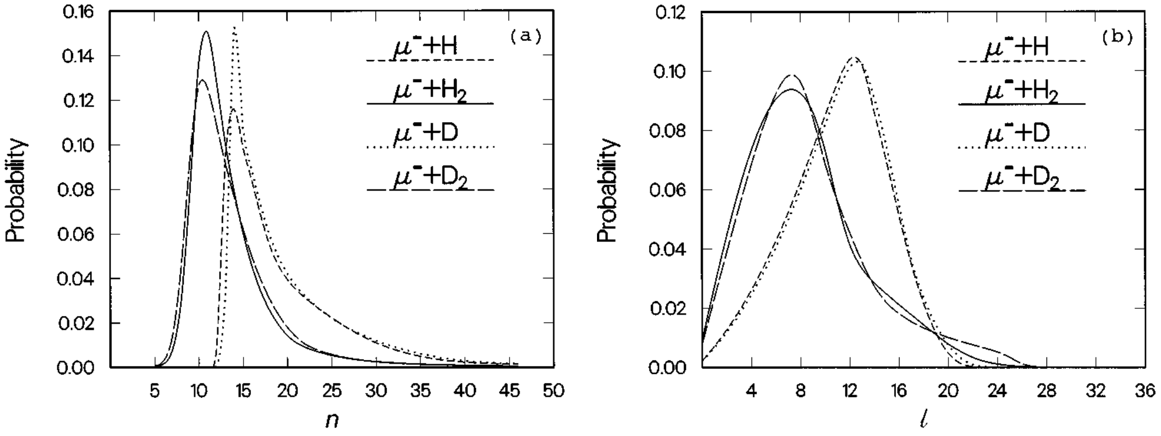

Figure 3.1: In (a) and (b) the n and l distributions are shown, respectively, for the μ^- capture by hydrogen and deuterium atoms and molecules [35].

The probability distributions for the capture by atomic hydrogen and deuterium targets would peak at:

$$n \approx \sqrt{\frac{\mu_{xp}}{m_e}} \tag{3.1}$$

n being the principal quantum number of the highly excited bound state where the capture occurs, m_e the electron mass and μ_{xp} the reduced mass of the x^-p bound system. x^- is a general negative charged particle.

That is the principal quantum number which corresponds to the exotic orbital whose overlap with the electronic ground-state is maximal with its binding energy being equal to the binding energy of the ground-state electron. For muons and pions, this happens to be n equal to 14 and 16, respectively.

The distribution falls abruptly for lower n. In this case, the additional binding energy should be carried away by the ejected electron as kinetic energy. However, according to the concept of adiabatic ionization [34], which describes the capture of heavy charged particles ($m >> m_e$), this is unlikely for the small energies involved. At higher n the distribution goes approximately with $\frac{1}{n^3}$.

The l distribution for atomic hydrogen and deuterium is almost statistical up to some peak, i.e., proportional to $2l+1$. Nevertheless, a modified statistical distribution $P_l \propto (2l+1)e^{\alpha l}$ is mostly used as an approximation to the initial population. The parameter α is fitted to the data and is approximately equal to 0.2 or less [36].

In molecular targets the capture occurs at slightly lower n and l, compared to the atomic targets. The distributions (figure 3.1) are shifted towards lower values and very large initial n are suppressed. The capture is more complex in molecular targets and the shift is mainly due to the molecular dissociation dynamics of the intermediate complex formed during the capture process [35].

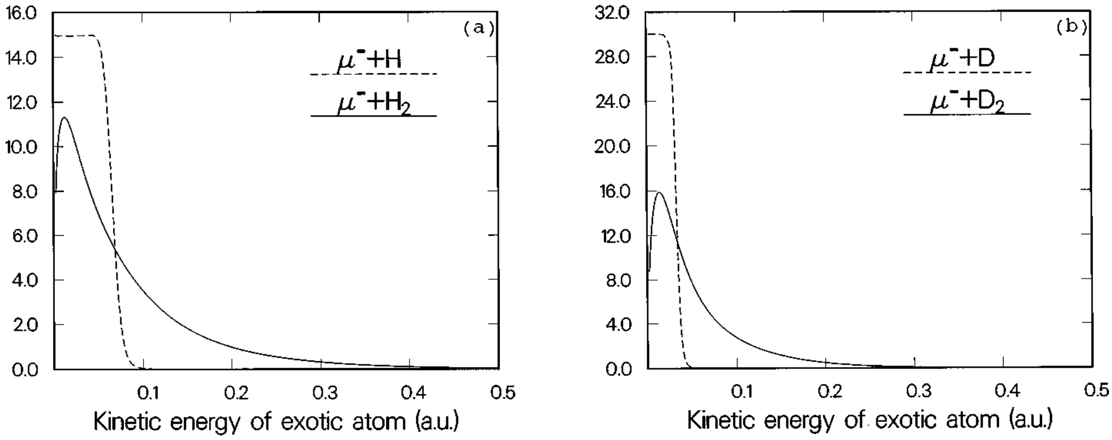

Figure 3.2: Distribution of the initial kinetic energy of (a) muonic hydrogen (μp) and (b) muonic deuterium (μD) formed in dense atomic and molecular targets, dashed and solid curves, respectively [35].

The kinetic energy of the exotic system formed in an atomic target, following the conservation of linear momentum, is given by:

$$E = \frac{m_{x^-}}{m_p + m_{x^-}} E_{x^-}^{lab} \tag{3.2}$$

m_{x^-} being the mass of the charged particle, m_p the proton mass and $E_{x^-}^{lab}$ the energy in the laboratory frame of the charged particle at the moment of capture.

The distribution of the initial kinetic energy for the muon capture in atomic and molecular hydrogen and deuterium is shown in figure 3.2, according to calculations [35] in atomic units (1 a.u. = 27.21 eV). As depicted in figure 3.2 the initial kinetic energy of the muonic atom formed is just a few eV.

For atomic targets the distribution is slightly broadened by the energy of the ejected electron and looks like a step function. In molecular targets, the exotic atom, after the collisional capture, has a broad angle distribution (for a given $E_{x^-}^{lab}$) as a result of the additional rotational and vibrational degrees of freedom of the molecules. Together with the dissociation dynamics of the intermediate complex and the capture cross sections which reaches to higher energies in molecular targets [35], it renders a kinetic energy of the exotic atoms (figure 3.2) with significantly higher energies possible (up to 5 times, compared to atomic targets).

3.2 Cascade mechanisms

After the exotic particle has been captured, several mechanisms compete during the deexcitation cascade. The cascade ends when the exotic particle reaches either the ground level or a weak decay (μ^-, π^-, K^-), or a nuclear absorption (π^-, K^-) or a annihilation ($\overline{p}$) process takes place.

The deexcitation mechanisms are either collisional or radiative. The **Auger emission**, **Coulomb deexcitation**, **Stark mixing** and **elastic scattering** are collisional mechanisms. Hence, opposite to the **radiative decay**, they have a strong dependence on the target density and on the kinetic energy of the exotic atom [30, 49, 32, 33].

The collisions of the exotic system x^-p with the hydrogen molecules can be formally written as:

$$(x^-p)_{n_i l_i} + \mathrm{H}_2 \longrightarrow (x^-p)_{n_f l_f} + X \tag{3.3}$$

where $X = \mathrm{H}_2$, H_2^*, H+H, H+p+e^-, etc. They play a very important role in the cascade history of the light hydrogen atoms.

3.2.1 Stark mixing

Since the exotic hydrogen atom is rather small on the atomic scale and electrically neutral, it can pass “freely” into the electron cloud of the neighboring hydrogen atoms and experience the Coulomb field of the proton. The strong electric field mixes the l

states at a given n of the exotic hydrogen. The mixing occurs according to the selection rules $\Delta n = \Delta m = 0$ and $\Delta l = \pm 1$ [37].

The Stark mixing can be considered as an elastic collision which does not conserve the l quantum number. Hence, it contributes to the deceleration of the exotic atom and thus influences the energy distribution along the cascade. In hadronic atoms it enhances the nuclear absorption by feeding the s- and p-states where the corresponding wave functions have a bigger overlap with the proton.

The mechanism is described by the following equations:

$$
\begin{aligned}
(x^- p)_{nl_i} + \mathrm{H}_2 \quad &\longrightarrow \quad (x^- p)_{nl_f} + \mathrm{H}_2^* && (3.4) \\
(x^- p)_{nl_i} + \mathrm{H} \quad &\longrightarrow \quad (x^- p)_{nl_f} + \mathrm{H} && (3.5)
\end{aligned}
$$

The Stark mixing can completely reshuffle the l states at the beginning of the cascade (high n). At that point, and at high densities, the Stark mixing rate Γ_{St} is large enough to allow a great number of transitions between l states during the typical collision time τ_{St} ($10^{-14}...10^{-13}$ s). This leads to a nearly statistical population of the l levels for a given n, with the initial state being “forgotten” by the exotic atom [27, 49, 77].

Its rate is given by the general expression for collisional processes:

$$\Gamma_{St} = \rho v \sigma_{St} \tag{3.6}$$

where ρ is the target density in number of atoms per unit volume, v the exotic atom velocity and σ_{St} the cross section of the Stark mixing.

This cross section can be calculated in a semiclassical framework [27], where the exotic system is assumed to have a classical movement in a straight line trajectory with a constant velocity through the electric field of the target atom. All the other variables are kept quantized. Yet, a more realistic and fully quantum mechanical treatment is desirable.

In the ESCM of *Jensen and Markushin* [38] a quantum mechanical framework is used for the lower excited states ($n = 2...5$) and a semiclassical approach for higher n, where the levels are so close they can be approximated by a continuum. This treatment turned out to be quite successful.

Beside Stark mixing, the exotic atoms suffer also other elastic collisions which conserve the quantum state. They contribute additionally to the deceleration of the exotic system.

3.2.2 Auger emission

In the Auger emission process the x^-p deexcitation occurs via an ionization of a neighboring H_2 molecule. The ejected electron carries away most of the transition energy. The following equation describes the mechanism:

$$(x^-p)_{n_il_i} + \mathrm{H}_2 \longrightarrow (x^-p)_{n_fl_f} + \mathrm{H}_2^+ + \mathrm{e} \tag{3.7}$$

Two approximations are used to calculate the cross sections of the process, namely the Born approximation [27], which approaches the total wave function by the incident wave function, and the eikonal approximation [40]. According to both, the transitions with the minimum change of the principal and angular quantum number which can ionize the molecule are favored, i.e. $\Delta n = 1$ and $\Delta l = -1$ ($\Gamma_{Au} \propto 1/\sqrt{\Delta_{n_in_f}}$ [27]). They show that the cross sections of the Auger mechanism increase with n till a certain level (n_c). This critical level corresponds to the maximum n for which a $\Delta n = 1$ transition provides enough energy to ionize the H_2 molecule. At higher n ($n > n_c$) the ionization is only energetically possible via transitions with $\Delta n > 1$ and the Auger cross sections decrease, in average, with n. Considering the ionization potential of the H_2 molecule (15.4 eV), for the μp and πp systems, n_c has the value of 7 and 8, respectively.

The rate of the Auger emission is calculated by equation (3.6) using the Auger cross sections. In the Born approximation the rates are independent of the kinetic energy [27]. In the eikonal approximation they show a weak dependence but with results very close to the ones in the Born approximation for $n \leq 6$ and kinetic energies in the order of 1 eV [40].

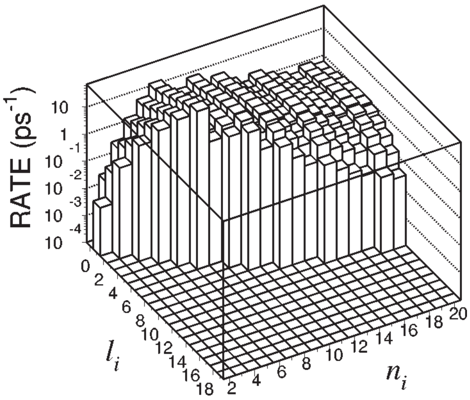

Figure 3.3: Auger emission rate for muonic hydrogen with the initial state n_il_i at LHD (Liquid Hydrogen Density, 1 LHD = 4.25 $\times 10^{22}$ atoms$\cdot$cm^{-3}) [49].

In figure 3.3 the Auger emission rate is shown as a function of the nl initial states in muonic hydrogen with a relatively high density ($4.25\ \times 10^{22}$ atoms$\cdot$cm^{-3}). The Auger rates were calculated using the Born approximation [27, 49].

3.2.3 Coulomb deexcitation

During a collision between an exotic system and hydrogen (atomic or molecular), the binding energy released from a change in the n state of the exotic atom can be converted into kinetic energy. This is the principle of the Coulomb deexcitation which is described by:

$$(x^- p)_{n_i l_i} + \mathrm{H}_2 \longrightarrow \left\{ \begin{array}{l} (x^- p)_{n_f l_f} + \mathrm{H} + \mathrm{H} \\ (x^- p)_{n_f l_f} + \mathrm{H}_2^* \end{array} \right. \tag{3.8}$$

$$(x^- p)_{n_i l_i} + \mathrm{H} \longrightarrow (x^- p)_{n_f l_f} + \mathrm{H} \tag{3.9}$$

The two or three atoms involved ($xp + \mathrm{H}$ or $xp + \mathrm{H}_2$) share the total kinetic energy, which can lead to a significant acceleration of the exotic system. Using the conservation of the momentum on the center of mass system (CMS):

$$\sum_i m_i v_i = const \tag{3.10}$$

the kinetic energy gained by the exotic system ($x^- p$) in a two-body Coulomb deexcitation is fixed in CMS to be:

$$T_{xp} = \frac{m_H}{m_{xp} + m_H} E_{n_i \to n_f} \tag{3.11}$$

where m_H and m_{xp} are the hydrogen and exotic hydrogen masses, respectively, and $E_{n_i \to n_f}$ the difference in the binding energy between the levels ($n_i > n_f$).

In the case of a molecular target, the gain in kinetic energy ranges from 0 (the two atomic hydrogens carry away all the energy available) to a maximum which is obtained by replacing m_H, in equation (3.11), by the mass of the hydrogen molecule ($2m_H$).

However, at the final part of the cascade, the binding energies involved are much larger than the H_2 dissociation energy. Hence, at that level, the kinematics is reduced to that of the two–body mechanism $xp + \mathrm{H}$ and the other hydrogen atom acts as a spectator.

The energies involved are rather small at the beginning of the cascade (for $\Delta n = 1$, see table 3.1). Nevertheless, the effect is cumulative and the kinetic energy of the exotic system can achieve much higher values if the deceleration mechanisms do not reduce the total energy gain. Moreover, for lower n transitions, the gains in kinetic energy can go up to several hundreds of eV and even to a keV for the muonic and pionic hydrogen systems, respectively.

Transition	T [eV]		Transition	T [eV]		Transition	T [eV]	
	μp	πp		μp	πp		μp	πp
			$11 \longrightarrow 10$	2.1	2.6	$6 \longrightarrow 5$	14.6	18.4
$15 \longrightarrow 14$		1.0	$10 \longrightarrow 9$	2.8	3.5	$5 \longrightarrow 4$	26.9	33.9
$14 \longrightarrow 13$	1.0	1.2	$9 \longrightarrow 8$	3.9	4.9	$4 \longrightarrow 3$	58.2	73.2
$13 \longrightarrow 12$	1.2	1.5	$8 \longrightarrow 7$	5.7	7.2	$3 \longrightarrow 2$	166.3	209.2
$12 \longrightarrow 11$	1.6	2.0	$7 \longrightarrow 6$	8.8	11.1	$2 \longrightarrow 1$	897.9	1129.5

Table 3.1: Gain in kinetic energy of the μp and πp systems by Coulomb deexcitation with $\Delta n = 1$ in collisions with atomic targets. The values are obtained considering the Coulomb binding energies of the exotic systems. They do not include the small corrections due to vacuum polarization, strong interaction, finite size effects and others.

Highly energetic πp atoms were first experimentally seen by *Czirr* [41]. The first calculations of the scattering cross sections of acceleration processes were done by *Bracci and Fiorentini* on their milestone work [28] where they named this kind of deexcitation mechanism as *Coulomb deexcitation*. The calculations were done in a semiclassical framework for μp in atomic hydrogen and the first rate predictions could be given.

A multicomponent structure of the kinetic energy distribution was directly observed in the the time-of-flight (TOF) spectrum of neutrons [42, 43]: the TOF spectra of the monoenergetic neutrons from the charge exchange reaction $\pi^- p \rightarrow \pi^0 n$ at rest turned out to be broadened by several Doppler contributions which correspond to different Coulomb deexcitation steps $n_i \rightarrow n_f$. A high kinetic energy component of 200 eV was identified and attributed to the $n = 3 \rightarrow 2$ transition in πp [44]. The kinetic energy distribution obtained through the TOF spectra of neutrons, measured in a wide density range [44, 45], are consistent with Coulomb deexcitation. Moreover, they confirmed the preference of $\Delta n = 1$ transitions, predicted by the calculations [28], but evidence for some $\Delta n = 2$ transitions has also been found.

Despite the experimental evidence of the Coulomb deexcitation, the TOF experiments could not provide useful information to be used in the πH studies [108]. They are performed in liquid hydrogen and other high densities and deal with the nuclear absorption which takes place predominantly from ns states with $3 \leq n \leq 5$. Therefore, the information possible to be extracted from the data is basically about the inner part of the cascade. On the other hand, in the πH and μH, the p state, from where the radiative transition $n_i p \rightarrow n_f s$ occurs, is fed by the outer states (higher l). This need for information about the outer part of the cascade prompted the Coulomb deexcitation studies in μH.

3.2.4 Radiative deexcitation

The radiative deexcitation is a non-collisional process, which follows the well known properties of the electrodipole transitions (E1). The exotic particle changes its n state (obeying to the selection rule $\Delta l = \pm 1$) with the binding energy carried away by a photon. The process is written by:

$$(x^- p)_{n_i l_i} \longrightarrow (x^- p)_{n_f l_f} + \gamma \tag{3.12}$$

The radiative rate in exotic hydrogen can be determined from the expression for the E1 spontaneous emission rate in hydrogen [27]:

$$\Gamma_\gamma = \frac{\mu_{xp}}{m_e} \Gamma_\gamma^{\mathrm{H}} \tag{3.13}$$

where Γ_γ^H is the spontaneous emission rate in hydrogen in the dipole approximation.

This approximation considers the atom as being a dipole, which radiates by creating an oscillating electrical field:

$$\vec{E}(\vec{r}, t) = \vec{\varepsilon} e^{i(\vec{k}.\vec{r} - \omega t)} \tag{3.14}$$

$\vec{r}$ being the position of the electron, $\vec{\varepsilon}$ the direction of the photon polarization and ω the angular frequency. The electric field is assumed to vary little in the phase over the spatial extension of the atom, considering the classical atomic size ($2a_0 \approx 1$ Å), thus the exponential part of electric field vector is approximated by one.

Under the dipole approximation the spontaneous emission rate in hydrogen is given by [50]:

$$\Gamma_\gamma^{\mathrm{H}} = \frac{4}{3} \frac{e^2 E^3_{n_i \rightarrow n_f}}{\hbar^4 c^3} \left| R_{n_i \rightarrow n_f} \right|^2 \tag{3.15}$$

where e is the electron charge, $E_{n_i \rightarrow n_f}$ the energy difference between the initial and final n states and $R_{n_i \rightarrow n_f}$ the dipole matrix element which can be written as:

$$R_{n_i \rightarrow n_f} = \left\langle \Psi_f^* \left| \vec{r} \right| \Psi_i \right\rangle \tag{3.16}$$

Ψ_i and Ψ_f being the wave functions of the initial and final n-states, respectively.

According to expression (3.15) the radiative deexcitation favors the maximum change in n, which maximizes $E_{n_i \rightarrow n_f}$. Yet, the dipole matrix element is lower for higher n resulting in a fast drop of the deexcitation rate with increasing n. For higher n, the rate can be rewritten in terms of n by averaging over all possible l sublevels [49]:

$$\Gamma_{\gamma,n} = \frac{1}{n^2} \sum_{n_f, l_f, l} (2l+1)\ \Gamma_\gamma \tag{3.17}$$

where n and l are the initial states. The term $2l + 1$ is the number of m sublevels. In the sum, the term Γ_γ varies with n_f according to equation (3.15). For instance, in terms of l, nine transitions are possible from the $n = 4$ level with four l substates statistically populated. The $4p$ ($l = 1$) has four deexciation channels: to $3s$, $2s$, $1s$ and $3d$. Using an index in Γ_γ to indicate the Δn, the term of the sum corresponding to $l = 1$ will be:

$$\sum_{n_f, l_f, 1} 3\ \Gamma_\gamma^{n-n_f} = 2 \times 3\Gamma_\gamma^1 + 3\Gamma_\gamma^2 + 3\Gamma_\gamma^3 \tag{3.18}$$

and by doing the same for the other possible l states, the sum for $n = 4$ will be:

$$\sum_{n_f, l_f, l} (2l+1)\ \Gamma_\gamma^{n-n_f} = 19\Gamma_\gamma^1 + 9\Gamma_\gamma^2 + 3\Gamma_\gamma^3 \tag{3.19}$$

Figure 3.4 shows the decrease of the radiative rate with increasing n in muonic hydrogen. The rate also increases for lower l, where the main contribution is the increase of possible transitions. As l decreases (till $l = 1$) new transitions with higher Δn are possible, according to the selection rule $\Delta l = \pm 1$.

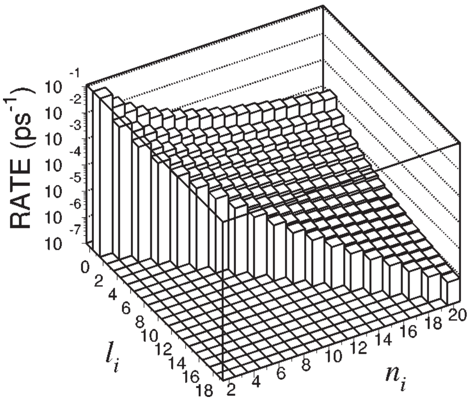

Figure 3.4: Radiative deexcitation rate for muonic hydrogen with the initial state $n_i l_i$ [49].

3.2.5 Competition between the mechanisms

The relative importance of the deexcitation mechanisms is correlated with the principal quantum number n. Yet, the cascade is dominated by different processes at different levels. Figure 3.5 shows a schematic representation of the atomic cascade in an exotic hydrogen system.

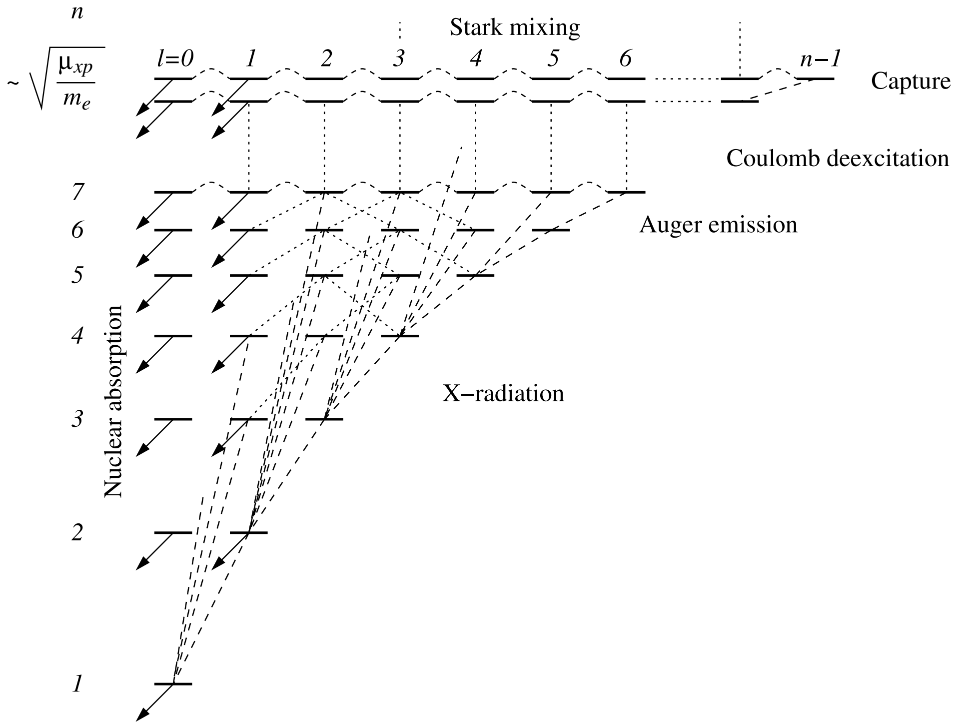

Figure 3.5: Schematic of the atomic cascade in exotic hydrogen. The nuclear absorption only takes place if the exotic particle is sensitive to the strong interaction (π, K, $\overline{p}$). Moreover, the strong interaction also induces a shift and width in the inner atomic levels.

Since long it is known that, in hadronic systems, the increase in target density leads to a drastic reduction in the X-ray yields (Day–Snow–Sucher effect) [47, 48]. It was understood as being due to the increase of collisions which enhances the Stark mixing rates and hence the feeding of the s and p states.

Leon and Bethe, in their pioneering work [27], by comparing the ratio between the Auger effect rate and the radiative deexciation rate have concluded that the radiative process can only dominate the cascade at low n or at very low target density when the collisional processes are reduced. That can be also illuminated by comparing the rates for Auger and radiative transitions in μH shown in figures 3.3 and 3.4, respectively.

The Stark mixing is the dominant process after the formation of the exotic system till relatively low n. However, it does not involve energy transfer. Considering only mechanisms with energy transfer, the Coulomb deexcitation is the dominant decay mechanism at higher n. With the decrease in n, the Auger effect becomes more important and the Coulomb rates decrease. At an intermediate stage, around n_c, the Auger emission dominates. In the lower n region the competition between those mechanisms is strong with the radiative deexcitation becoming more relevant and dominating at the latest steps of the cascade ($n = 3$, 2).

Moreover, for the hadronic systems, the nuclear absorption plays an important role, particularly at the lower cascade stage [51]. This is shown in figure 3.6. The figure presents the rates for the different cascade mechanisms in μH and πH at 80 mbar (10^{-4} LHD) and 3 bar, respectively, using the present knowledge [33, 46].

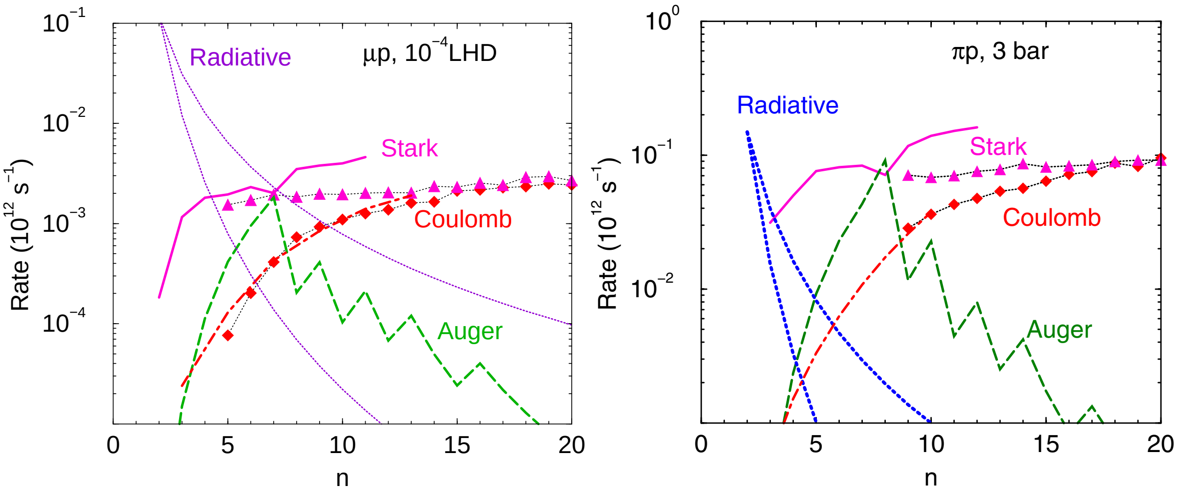

Figure 3.6: The l-averaged rates of the cascade mechanisms at a kinetic energy of 1 eV for muonic hydrogen at 80 mbar (left [33]) and pionic hydrogen at 3 bar (right [46]). The rates of the Coulomb deexcitation (filled diamonds) and Stark mixing (filled triangles) were calculated in the classical-trajectory model [33]. They are compared with the Stark mixing rate under the fixed field model (solid line) and the Auger emission rate (light dashed line) [38, 33, 27]. The Coulomb deexcitation rate for μH from *Bracci and Fiorentini* is depicted in dash-dotted line [28] and it was scaled for the πH case. The radiative $np \to 1s$ and $n(n-1) \to (n-1)(n-2)$ rates are shown in each plot with the bottom and upper dotted lines, respectively.

The figure demonstrates also the importance of the target density. A decrease in about two orders of magnitude is seen in the overall rates of the collisional mechanisms when the density is reduced from 3 bar to ∼0.1 bar. That enhances the relative importance of the radiative deexcitation, particularly at high n, where the Coulomb deexcitation rate reaches the same order of magnitude as the radiative deexcitation rate. Moreover, the Auger emission rates become smaller than the radiative ones. At even lower densities the collisional processes will be suppressed and the cascade will be purely radiative.

As the exotic system undergoes acceleration and deceleration mechanisms its kinetic energy is continuously changing. On the other hand, the cross sections of the different collisional mechanisms are kinetic energy dependent [32, 38]. Thus, the kinetic energy history of the exotic system is a key aspect in the cascade calculations, which was absent in the early models [27, 29] and introduced in the latest work only [32, 33].

At the lower stage of the cascade the Coulomb deexcitation is not fully understood [33, 51], where it is assumed to be enhanced by the hypothetic formation of resonant molecular states [52, 53]. Furthermore, the Stark mixing is still important at this stage [32, 33, 38, 51] shuffling the nl population at a certain n and promoting the nuclear absorption, which leads to a radiative yield decrease. Additionally, the exotic particle can still decay via weak interaction:

$$\mu^- \longrightarrow e^- + \bar{\nu_e} + \nu_\mu \tag{3.20}$$

However, due to its long life time compared to the cascade deexcitation times (∼2μs *vs* ∼ns), almost all the muons reach first the ground state.

Hence, the very strong interplay between the different mechanisms makes a reliable prediction of the cascade behavior very difficult, particularly at its final part.

Moreover, this interplay of mechanisms has also another important consequence. The measurement of absolute radiative yields at different target pressures could help to extract the physics behind the cascade mechanism. However, that is not an easy task due in part to the behavior of the different mechanisms with density.

The yield of a radiative decay is related with the rates for all the possible decay channels from the initial state. For a specific transition $n_il_i \to n_fl_f$ can be given by:

$$Y_\gamma^{n_il_i \to n_fl_f} = \mathrm{Pop}_{n_il_i} \frac{\Gamma_\gamma^{n_il_i \to n_fl_f}}{\sum_{j,n_f,l_f} \Gamma_j^{n_il_i \to n_fl_f}} \tag{3.21}$$

where $\mathrm{Pop}_{n_il_i}$ is the population of the initial state, $\Gamma_\gamma^{n_il_i \to n_fl_f}$ the radiative rate of the transition $n_il_i \to n_fl_f$ and $\sum_{j,n_f,l_f} \Gamma_j^{n_il_i \to n_fl_f}$ the sum of the rates of all the possible decay channels, with the subscript j standing for the different decay mechanisms. The quantity defined by the quotient is called branching ratio.

The density dependence of the radiative yields renders their direct measurement at high densities quite difficult due to the enhancement of the Stark mixing effect. That is a consequence of the collision rate dependence on the density as, contrary to these, the radiative rates are independent from density which makes the branching ratio to change with density. A hypothetical picture with all the rates changing with the density would result in approximately constant branching ratios.

3.3 Evolution of the Cascade model

It was always a very challenging task to provide a good cascade model which could correctly predict the different measurable quantities in exotic systems. As described in the previous section, the several decay channels involved and their interdependence renders the problem quite complex. Approximations were needed to reduce the degrees of freedom of the problem.

Standard Cascade Model

Leon and Bethe developed the first model which could fairly reproduce the experimental data [27]. They built in a description of the Auger emission, radiative deexcitation and Stark mixing. They also considered the strong interaction effects, shift and broadening of the energy levels, the Stark mixing and the role of nuclear absorption on the cascade history. However, the Stark mixing was restricted to transitions to the ns state from a statistically populated nl ($l > 0$) state, resulting in calculation of effective absorption rates.

The collisional processes were treated under a semiclassical approximation in order to simplify the differential equations resulting from a fully quantum mechanical formalism. Thus, some quantities were taken as classical and others were quantized. On their formalism, the motion of the vector between the proton of the hydrogen target and the center of mass of the exotic system was treated classically with a quantized direction and the exotic system was treated quantum mechanically. They calculated the Auger emission using the Born approximation and the Stark mixing using a fixed field model. The fixed field model assumed that as soon as the exotic system feels the electric field from the hydrogen target, its angular momentum m remains fixed in the field direction.

Based on previous results from *Day et al.* [47, 48] and *Wightmann* [54] it was assumed that the exotic system had a kinetic energy of about 1 eV when formed. As the decay times of the cascade were very short and elastic scattering would possibly be inefficient, due to being moderated by hydrogen molecules and not atoms, they assumed the system velocity to be constant and equal to the one at the initial n level through all the cascade. Moreover, no drastic changes were expected in the rates with kinetic energy. Anyhow, the initial kinetic energy could be used as a tuning parameter.

The data on cascade times, available at the time, could not be explained by Auger emission, which was found to be too slow at the initial n levels. To overcome this contradiction *Leon and Bethe* described the upper part of the cascade by the phenomenological mechanism named *chemical deexcitation* [27]. This would be a fast deexcitation mechanism, where the transition energy of the exotic system is transformed to dissociations and ro–vibrational excitations of the neighboring molecules, leaving the initial kinetic energy of the exotic system (of the order of 1 eV) essentially unchanged.

The work of *Leon and Bethe* [27] was later on refined by *Borie and Leon* [29] to consider the evolution of the orbital quantum number l due to Stark mixing. Additionally, a phenomenological parameter was introduced in the calculation of the Stark mixing rates, as rescaling factor. With this tuning parameter, the so called standard cascade model (SCM) could provide a fair description of many cascade properties of the exotic systems like the X-ray yields and the nuclear absorption fraction in the hadronic cases.

An important contribution to the development of the SCM was given by *Reifenröther and Klempt* in the late 80ies [31]. They used for the first time a classical Monte-Carlo method to follow the trajectories of the exotic system ($\bar{p}p$) in a collision with atomic hydrogen. The position and orientation of the exotic system during the collision were taken into account when calculating the electric field. Hence, the electric field was determined as function of time and the Stark mixing transition rates calculated based on that information. This constitutes a milestone, as in previous calculations the trajectories were taken as straight and an average of the electric field was used (fixed field model) [37].

Extended Standard Cascade Model

The view of the cascade was changed by the evidence from the TOF measurements [42, 43] that the exotic systems could have a structured distribution of the kinetic energy up to hundreds of eV. An extended standard cascade model (ESCM) was developed by *Markushin* [55] to include the evolution of the kinetic energy of the exotic system along the decay cascade. The initial ESCM included all the deexcitation mechanisms accepted in the SCM but considered the kinetic energy as time-dependent distribution rather than a tuning parameter.

The Coulomb deexcitation was assumed to be the mechanism responsible for the system acceleration and the respective rates were calculated based on the cross sections from *Bracci and Fiorentini* [28]. The phenomenological and not theoretically described assumptions on chemical dissociations were substituted by the Coulomb deexcitation picture. The multiple elastic scattering was additionally considered to cause the exotic atom deceleration. However, due to the lack of relevant cross sections the first ESCM was restricted to the lower part of the cascade ($n < 6$).

More recent developments by *Jensen and Markushing* [32, 33, 38, 56] resulted in a more consistent ESCM with an applicability extended to the higher part of the cascade. Under this approach the calculations are divided in two domains: a classical one at high n and a quantum mechanical one at lower n. For convenience the maximum rate of the Auger emission, which occurs at $n = n_c$ (see section 3.2.2), is used to separate the domains. Accordingly, the classical domain is defined at $n > n_c$, being $n_c = 7, 8$ and 12 for μp, πp and $\bar{p}p$, respectively.

On the classical approach, the hydrogen atoms and the exotic particles are assumed to be classical particles, with the electrons moving around the protons with a fixed charge distribution corresponding to its orbitals. Therefore, the scattering is calculated through a classical trajectory Monte-Carlo method. Within this method a list of possible transitions $n_i l_i T_i \longrightarrow n_f l_f T_f$ (T is the kinetic energy) for the relevant processes on this domain (Coulomb deexcitation, Stark mixing and elastic collisions) is created. The cascade takes this information directly into account by assuming the final state to be the initial state of the next collision [33]. Moreover, elastic collisions and Stark mixing are treated together with the same formalism and the chemical deexcitation is taken as another channel of the Coulomb deexcitation [32]. The scattering on molecular hydrogen targets is also considered.

In the lower part of cascade ($n \leq n_c$) the cross sections of the collisional mechanisms, besides the Auger emission, are calculated with a quantum mechanical framework which takes into account the energy shifts of the ns states due to vacuum polarization and strong interaction. A detailed description of this approach can be found in reference [57].

As the number of coupled second order differential equations used in the quantum framework grows with n^2, the quantum mechanical approach is rather complex for higher n. However, if the kinetic energy of the movement of the three-body system is large enough, it can be assumed classical. For muonic hydrogen, that energy is estimated to be less than 1 eV. Exotic atoms are known to have kinetic energies in the order of a few eV even at an early stage of the cascade.

Thus on the ESCM developments by *Jensen and Markushin* the full quantum mechanical calculation is restricted to the lowest levels $n \leq 5$, while the higher n of the lower cascade domain, $5 < n < n_c$, is treated semiclassically [32, 33].

To resume, the main features of the ESCM are:

- the evolution of the kinetic energy of the exotic system is taken into account right from the beginning of the cascade
- molecular effects are considered at higher n
- the chemical deexcitation is treated as a channel of the Coulomb deexcitation and is included in the calculations of the Coulomb cross sections
- the Stark mixing and the elastic scattering are treated under the same formalism
- the strong interaction and vacuum polarization effects are considered on the ns energy shift

A drawback of the ESCM is the non-inclusion of the molecular effects in the lower domain of the cascade. The formation of molecular resonant hybrid states from the scattering in molecular hydrogen targets is expected for excited $(x^-p)_n$ $(n > 1)$ states [58, 53]:

$$(x^-p)_{nl} + \mathrm{H}_2 \rightarrow \left[(x^-pp)_s pee\right]^* \rightarrow \left[(x^-pp)_{s'} pee\right]^* + \gamma \tag{3.22}$$

The resulting complex molecules $[(x^-pp)pee]^*$ could in principle decay by Auger emission, radiative or Coulomb deexcitation and even by back decay, i.e. returning to the initial exotic system plus hydrogen molecule. Moreover, hybrid Auger-Coulomb transitions are also admitted to occur [59]. Accordingly, at the present knowledge it is assumed that a major source of uncertainties at low n is the poor understanding of the Coulomb deexcitation on that domain. Therefore, better results are achieved for observables less sensitive to Coulomb deexcitation at low n, like kinetic energy distributions at low density [33, 56].

Despite the fact that the latest ESCM constitutes a huge leap forward in the cascade history predictions (compared to the SCM), the picture is far from being complete. Additional efforts should be made to extend the fully quantum mechanical framework to higher n and on the understanding of the molecular effects at lower n, particularly concerning the Coulomb deexcitation.

The present measurement of the $3p \rightarrow 1s$ transition in μH will give an indirect evidence of the kinetic energy distribution at the $3p$ state. Together with the measurements of the radiative yields, it can help to guide future development of the ESCM. More recently, *Jensen et al.* [60] have incorporated some new results on the collisional process [61, 62, 63] and have performed the full quantum mechanical calculations of the cross sections of the elastic, Stark and Coulomb mechanisms for $n \leq 8$. A better agreement with the experimental results on the K yields both on μH and πH was obtained.

For more details about the ESCM see references [32, 33, 38, 46, 56].

3.4 Some results from the ESCM in μH

3.4.1 Coulomb and Stark mixing cross sections

The calculations of the Coulomb cross sections using a classical approach and Monte-Carlo methods showed an increase of the cross sections with the inverse of the initial kinetic energy which is not as steep as predicted by *Bracci and Fiorentini* [28]. An approximate dependence of $1/\sqrt{T}$ was obtained in contrast to the $1/T$ dependence for low energies calculated by *Bracci and Fiorentini*. However, a fair agreement for initial kinetic energies above 1 eV was found. Moreover, the calculations showed that the Coulomb cross-sections are approximately twice as large if a molecular target is considered. In figure 3.7 the results are presented for an initial state $n_i = 13$.

In the case of the Stark mixing, the cross sections calculated with a molecular target are slightly higher than for an atomic target, being even lower at kinetic energies below 1 eV (see figure 3.7). Two effects may explain this observation: as the electric fields of the two hydrogens atoms in the molecule partly cancel each other it creates a considerable molecular screening; moreover, the fraction of the Coulomb cross-section in the total cross section is higher for the molecular target.

In collisions with atomic hydrogen the fixed field model overestimates the Stark mixing at lower energies (T<1 eV) but it shows a good agreement with the Monte-Carlo classical approach at higher energies. Considering molecular targets the agreement is only present at kinetic energies above 10 eV. Figure 3.7 shows the results for the Stark mixing cross sections using $n = 9$.

Considering the n dependence, the semiclassical model of *Bracci and Fiorentini*, which considers an atomic target, predicts a Coulomb deexcitation with a complete dominance of transitions with $\Delta n = 1$ [28]. The results from the Monte-Carlo classical approach, depicted in figure 3.8, show a more complex behavior.

The shape of the distribution of n_f depends on the initial n state. By decreasing n_i the distribution becomes narrower with less probability of big jumps in n. That is valid both for the molecular and atomic target cases, with $\Delta n > 1$ transitions being strongly enhanced by the molecular target.

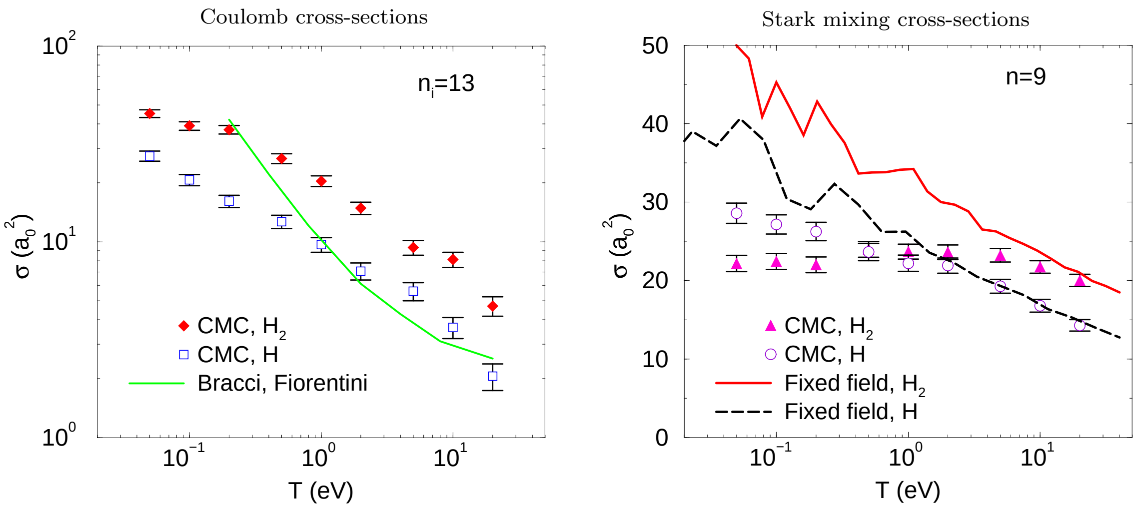

Figure 3.7: Energy dependence of the Coulomb (left) and Stark mixing (right) cross sections in μH according to the Monte-Carlo classical approach of the ESCM, in atomic units [32, 56]. The Coulomb cross sections were calculated for molecular (filled diamonds) and atomic (squares) hydrogen considering the initial state $n_i = 13$ and a statistical l distribution. The solid line is the semiclassical result from [28]. The Stark mixing cross sections were also calculated for molecular (filled triangles) and atomic (squares) hydrogen considering the initial state $n_i = 9$. The result of the fixed field model for molecular (solid line) and atomic target (dashed line) is also showed. The error bars are statistical and originated from the Monte-Carlo method.

In a molecular target, at higher n the transitions with $\Delta n > 1$ dominate the Coulomb deexcitation. For instance, for $n_i = 13$ the transitions with $\Delta n = 2, 3$ have the biggest chance to occur (see figure 3.8). This behavior changes with the decreasing of n_i, and the transitions with $\Delta n = 1$ become most probable, which is already the case for $n_i = 9$ (see figure 3.8). Anyhow, the transitions with $\Delta n > 1$ remain rather important being approximately 38% for $n_i = 9$.

With an atomic target, the Monte-Carlo classical approach showed that at higher n_i the dominance of transitions with $\Delta n = 1$ is not as overwhelming as predicted by *Bracci and Fiorentini* ($\sim$ 90% of the Coulomb cross sections). Furthermore, transitions with $\Delta n > 1$ have a significant weight which decreases rapidly with n. At $n_i = 13$ transitions with $\Delta n > 1$ constitute $\sim$ 40% of the total Coulomb cross section, decreasing to 19 % for $n_i = 9$ (see figure 3.8).

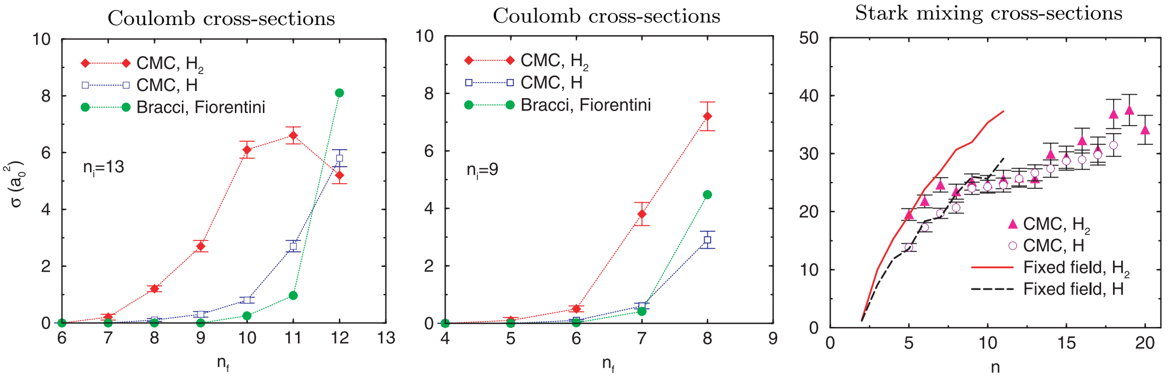

Figure 3.8: n dependence of the Coulomb (left and center) and Stark mixing (right) cross sections in μH according to the Monte-Carlo classical approach of the ESCM, in atomic units and averaged over l states [32, 56]. The n_f dependence of the cross sections for the Coulomb deexcitation were calculated for the initial states $n_i = 13$ (left) and $n_i = 9$ (center) considering a molecular (filled diamonds) and atomic (squares) hydrogen target. The filled circles show the classical result from [28]. The Stark mixing cross sections resulting for the molecular and atomic hydrogen target are depicted with filled triangles and circles, respectively. The fixed field model results are presented also for the molecular (solid line) and atomic target (dashed line). The three calculations were done for an initial kinetic energy of 1 eV in the laboratory system.

Concerning the Stark mixing dependence on the n state, a decrease with n is evident. At higher n, where the Coulomb deexcitation is more important, the fixed field model overestimates the Stark mixing, but in the lower part of the cascade the agreement with the Monte-Carlo classical model is quite good, particularly in the case of the atomic target (see figure 3.8).

3.4.2 X-ray K yields

The K radiative deexcitation rates are well known quantities. To relate the X-ray yields in exotic hydrogen with the respective rates, the influence of the other collisional mechanism, namely the Auger and Coulomb, needs to be considered [64, 39] as equation (3.21) indicates. In this way, the K-yields have a strong dependence on the density, which was already fairly explained by the SCM [29, 30]. Hence, by comparing the ESCM predictions with the experimental data available, the model is subject of test. For that, the μH system is the most suitable as the X-ray yields are not suppressed by strong absorption.

Experimentally, the radiative yield of a transition could be directly extracted from the relation:

$$Y_\gamma^{n_il_i \to n_fl_f} = \frac{N_X}{N_c\ \varepsilon\Omega\ T_r} \tag{3.23}$$

with N_X being the number of detected X-rays from the radiative transition $n_il_i \to n_fl_f$, N_c the number of exotic atoms formed, ε the detector's efficiency, Ω the solid angle and T_r the X-ray transmission between the target where the exotic atoms are formed and the detector.

An experiment to directly measure the absolute yields has one main difficulty: to exactly know the number of exotic atoms formed, N_c! This is overcome in πH by using the charge exchange reaction:

$$\pi^- p \to \pi^0 n, \quad \pi^0 \to \gamma\gamma \tag{3.24}$$

where the γ-rays are emitted back-to-back. The method is described in *Rusi et al.* [74] and consists in measuring the temporal coincident events of γ-rays with the X-rays from the transition of interest. The number of $\gamma\gamma$X coincidences is given by:

$$N(\gamma\gamma X) = N_c\ Y_\gamma^{n_il_i \to n_fl_f}\ \varepsilon\Omega\ T_r \frac{P}{1+P}\ \varepsilon_{\gamma\gamma} \tag{3.25}$$

$\varepsilon_{\gamma\gamma}$ being the efficiency of the $\gamma\gamma$ detection and P the Panofsky ratio which relates the cross sections between the two possible π^- nuclear decay channels: the charge exchange reaction (3.24) and the radiative capture ($\pi^- p \to \gamma n$). The Panofsky ratio is defined as follows:

$$P = \frac{\sigma_{\pi^- p \to \pi^0 n}}{\sigma_{\pi^- p \to \gamma n}} \tag{3.26}$$

It was measured to be 1.46 ± 0.1 by *Koller* and *Sachs* [75] in the fifties and remeasured in the seventies by *Spuller et al.* [76] who arrived at the value of 1.546 ± 0.009.

Within a probability close to 100% the π^- can only decay via weak interaction in a muon or via strong interaction by the two channels mentioned. However, by comparing with the cascade times involved and the rates of the strong interaction processes ($10^{12}\cdot\text{s}^{-1}$), the pion lives "forever" ($\approx$ 26 ns). Consequently, the weak decay can be neglected during the cascade and one can assume that all the pions which are capture will suffer nuclear absorption. Therefore, the total number of $\gamma\gamma$ coincidences detected will be:

$$N(\gamma\gamma) = N_c\ \frac{P}{1+P}\ \varepsilon_{\gamma\gamma} \tag{3.27}$$

The uncertainty from the number of pions captured is removed and the yields pinned down by determining the ratio:

$$\frac{N(\gamma\gamma X)}{N(\gamma\gamma)} = Y_\gamma^{n_i l_i \to n_f l_f}\ \varepsilon\Omega\ T_r \tag{3.28}$$

together with a proper background analysis.

In principle a similar method could be used in muonic hydrogen using the weak decay reaction of the muon:

$$\mu \to e^- + \bar{\nu}_e + \nu_\mu \tag{3.29}$$

However, the life time of the muon is very long ($\approx 2.2\ \mu$s) compared with the cascade times involved (ns) and beside that, to isolate the electrons from the muon decay would be extremely difficult as there would be many background electron emissions. Only relative measurements to the total radiative yields are therefore done.

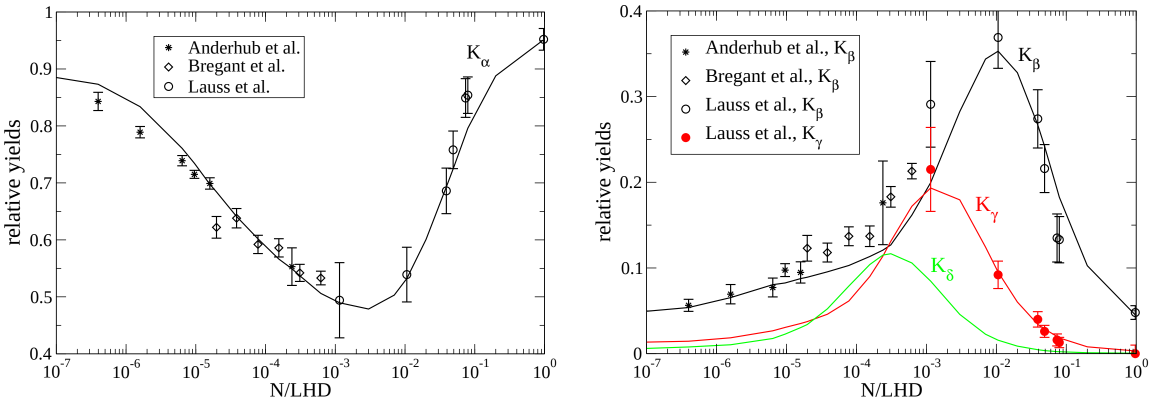

Figure 3.9: Comparison between the experimental X-ray K yields and the ESCM calculations as function of the target density in μH [60]. At the left the K$_\alpha$ is depicted. On the right the K$_\beta$, K$_\gamma$ and K$_\delta$ are plotted. The yields shown are relative to the absolute total K yield. The experimental data are from [65, 66, 67].

By using the most recent developments on the cascade kinematics, the K$_i$ yields ($i = \alpha, \beta, \gamma$ and δ) for μH were calculated from 1 LHD ($\sim$ 800 bar at 273 K) to 10^{-7} LHD ($\sim$ 0.1 mbar at 273 K) [60]. The results are depicted in fig 3.9 together with the experimental values.

Figure 3.9 shows a quite good agreement between the calculated and measured relative K yields, particularly for the K$_\alpha$ which presents a good agreement along all the density range considered. Unfortunately, no data is available for K$_\gamma$ below 10^{-3} LHD and for K$_\delta$ due to the very weak detection rates. In between 10^{-5} and 10^{-3} LHD the K$_\beta$ yields have some disagreement, possibly due to either theoretical and experimental reasons.

The values of the K$_i$ yields shown are relative to the absolute K$_{tot}$ (not depicted). The absolute K_{tot} yield is obtained by summing up all the absolute K$_i$ yields which have never been measured so far. According to the cascade calculations, K$_{tot}$ has a practically linear dependence on the density and varies steadily from very low density till 10^{-2} LHD, with values always higher than 95% [60]. At higher densities it suffers a fast decrease down till 40% at 1 LHD. This K$_{tot}$ supression can be explained by the quenching mechanism of the $2s$ metastable state.

A particle which arrives at the $2s$ state is “trapped”, as the $2s$ state has a long life time (in leading order the $2s \rightarrow 1s$ is a forbidden transition). It could only escape if the kinetic energy of the system allows a transition to the $2p$ by Stark mixing and consequently deexcitation to the ground state. However, the $2s$ state can decay ($2s \rightarrow 1s$) either radiatively or by Coulomb deexcitation. Therefore, the quenching mechanism can result in a suppression of the K_α yield and consequently the K_{tot} in case the rate of the non-radiative channel is significant. In fact, at low densities only a small fraction goes to this non-radiative $2s$ decay channel ($\sim$ 1% around 10^{-4} LHD [70]) but at pressures close to LHD this part becomes very significant [56].

Figure 3.9 exposes the opposite behavior of the relative K$_\alpha$ yield relatively to the others. It is maximum at very low and high densities and minimum at intermediate ones. It starts around 90% at 10^{-7} LHD, decreases with increasing density to approximately 50% at 10^{-3} LHD and increases again up to 94% at 1 LHD. On the other hand, the relative K$_\delta$, K$_\gamma$ and K$_\beta$ X-ray yields have their maximum at 10^{-4}, 10^{-3} and 10^{-2} LHD, respectively. In this density region, the relative intensity of K$_\alpha$ remains below 60%.

The density dependence of the yields can qualitatively be explained as follows. At very low densities the cascade is almost purely radiative, as seen in previous sections, and deexcites at low n through the circular states ($l = n - 1$). Therefore, almost all μ^-p systems undergo the radiative $2p \rightarrow 1s$ transition with the remaining $np \rightarrow 1s$ transitions being much weaker. With the density increasing the collisional processes become more efficient and the np states for $n > 2$ get more populated due to Stark mixing. Hence, the relative K$_i$ yields (i=β, γ, δ) increase with the consequent decrease of the K$_\alpha$.

At higher densities, above approximately 10^{-3} to 10^{-2} LHD, the collisional mechanisms $n \rightarrow n'$ ($n' < n$) dominate the cascade over the radiative deexcitations. Hence, the K$_i$ yields (i=β, γ, δ) decrease. Clearly, at these high densities, the radiative deexciations occur mainly via the $2p \rightarrow 1s$ transition. This results from two facts: first the collisional deexcitations to the $1s$ are strongly suppressed; second the $2p$ state is highly populated directly via the Coulomb mechanism or through the $2s \rightarrow 2p$ Stark transition.

Despite some aspects need still to be refined, at the present status, the ESCM can generally reproduce the measurements on the K X-ray relative yields. Moreover, the general behavior of the relative yields with the density can be understood by the competition amongst the different mechanisms during the atomic cascade.

3.4.3 Kinetic energy distribution

One of the main drawbacks on the first standard cascade models was the non inclusion of the kinetic energy variation during the deexcitation cascade. The ESCM includes this feature and indeed, it turned out to be very important: the collisional cross sections are velocity dependent and the exotic system does not remain thermalized after the capture by the proton. However, as mentioned previously, the strong competition between the various mechanisms renders the predictions very difficult. Despite some fair description by the existing ESCM the full picture still needs further investigations.

By analyzing the $\mu^- p$ diffusion times in hydrogen gas [68] and by means of TOF techniques [70, 71] the integrated kinetic energy distribution at the $1s$ state has been obtained. Experimental difficulties prompted the use of the integrated distribution instead of the differential one [70, 71]. Figure 3.10 shows the comparison between the calculated values within the ESCM and the experimental data from *Pohl* [70].

At these low densities, by using a molecular target to do the classical trajectory calculations on the upper levels, a fair agreement between the predictions of the ESCM and the experimental values is seen. When using an atomic target on the classical calculations, the foreseen increase of the kinetic energy with the density is much weaker and the agreement with the experimental results is poor.

From figure 3.10 one sees how the importance of the collisional processes increases with the density. At very low densities the probability to have energies higher than 20 eV is nearly 0. In contrast, for 4 and 16 mbar, 10 eV represents only 0.8 of the cumulative energy distribution and a fraction of about 0.05 is above 20 eV. The Coulomb deexcitation becomes more important at higher densities and more energy is gained by the system, leading to a more energetic final distribution.

Another indication about the dynamics between the different collisional mechanisms

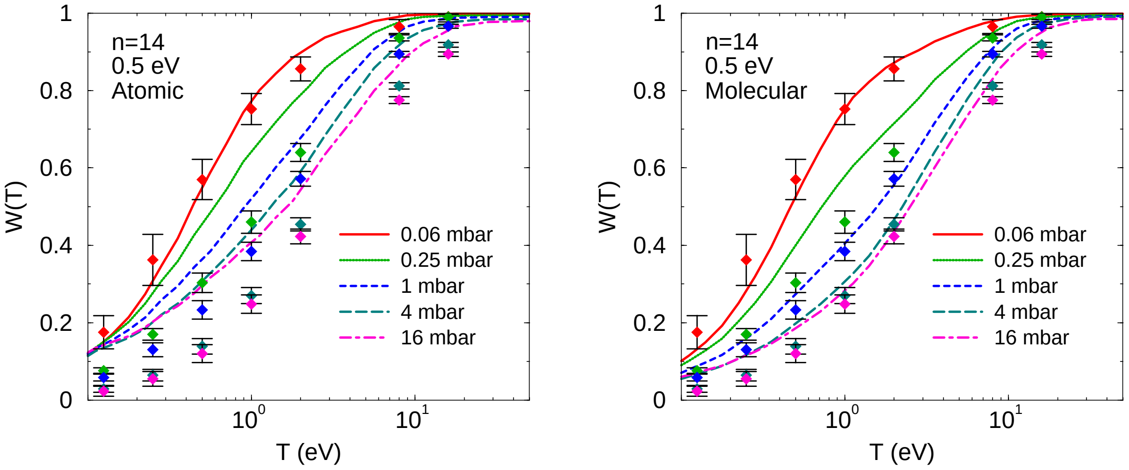

Figure 3.10: The results for the integrated energy distribution W(T) at the end of the cascade in μH from ESCM calculations and experiment are shown for comparison [33]. The experimental data are from [70]. On the ESCM calculations, $n_i = 14$ and $T_0 = 0.5$ eV was assumed. At the left, the ESCM curves were obtained using an atomic target for the classical-trajectory calculations at $n > 7$. At the right a molecular target was considered instead.

comes from how the median kinetic energy at the ground state varies with the density. Figure 3.11 shows this dependence for the $\mu^- p$ system within the range $10^{-8}...10^{-3}$ LHD (1 mbar $\sim 10^{-6}$ LHD).

The data are better described by using $n = 14$ together with $T_0 = 0.5$ eV or $n = 16$ with $T_0 = 0.25$ eV as initial conditions. The use of the atomic target in the classical calculations leads to an underestimation of the increase of the median energy. Indeed, to considerer the molecular structure on the CMC calculations is crucial to reproduce the data.

The median energy, when the cascade ends at the $1s$ state, grows from about 0.5 eV at very low density (10^{-7} LHD), up to a plateau of about 2.5 eV. Hence, it remains nearly constant between 10^{-5} LHD to 2×10^{-4} LHD. Above this density the median energy increases again.

This behavior can be explained with the competition between the several decay mechanisms. At low densities, the energy gain due to the Coulomb transitions with $\Delta n = 1...5$ in the classical domain ($n > 7$) dominates over the elastic collisions. Moreover, due to the strong absence of collisional mechanisms at densities $< 10^{-7}$ LHD the

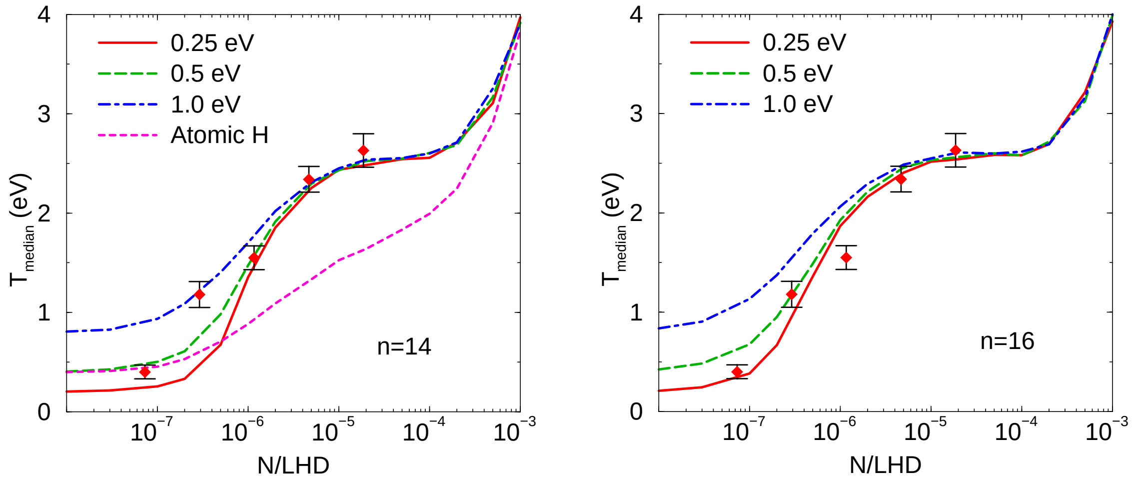

Figure 3.11: The density dependence of the median kinetic energy at the end of the cascade in μH [33]. The experimental results are from [70, 72] for 0.06, 0.25, 1, 4 and 16 mbar (1 mbar$\sim 10^{-6}$ LHD). The ESCM calculations were performed with $T_0 = 0.25, 0.5$ and 1 eV and assuming the cascade starting at $n = 14$ (left) and $n = 16$ (right). A molecular target was assumed in the classical calculations at higher n. The calculation with an atomic target is shown with dashed line (left plot) for which a $T_0 = 0.5$ eV was assumed.

exotic system roughly keeps its energy during the cascade. Therefore, the mean energy increases until the Auger transitions have some dominance in the intermediate region, which happens around 10^{-5} LHD. With increasing density, the Coulomb deexcitations at $n < 8$ are enhanced. Thus, the median energy increases and is basically determined from the competition between the accelerating and decelerating mechanisms at $n < 8$. The initial kinetic energy is almost forgotten.

The kinetic energy gain of the exotic systems have a direct impact on the measured spectral lines. The movement of the exotic system at the instant of the radiative emission causes a line broadening by Doppler effect. Figure 3.12 shows an example of the expected broadening by Doppler effect in the muonic hydrogen $K_{\alpha,\beta,\gamma}$ lines.

The spectral lines have quite pronounced tales which are particularly extended for K_α. For radiative transitions to the ground state with lower Δn more energetic Coulomb deexcitations are available. Table 3.2 clarifies the situation. Assuming the energy gain by Coulomb deexcitation with $\Delta n = 1$, the corresponding energy shifts by Doppler effect of the subsequent radiative transitions are presented. The $n = 3 \rightarrow 2$

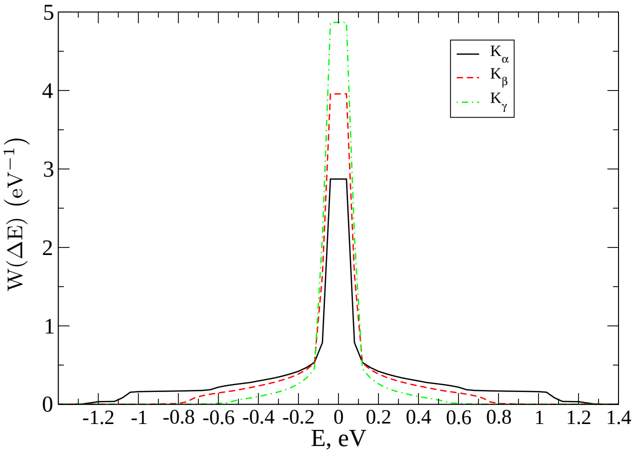

Figure 3.12: The expected broadening of the K lines by Doppler effect due to the kinetic energy gain during the $\mu^{-}p$ cascade at 10 bar. Coulomb transitions with $\Delta n = 1, 2$ were considered [60].

Coulomb transition which leads to an energy gain of about 166 eV can induced a Doppler shift up to ±1.1 eV on the measured K_{α}.

By taking into account the existent information about the cross sections for the different cascade mechanisms the ESCM is able to provide a theoretical prediction for the kinetic energy distribution at the instance of the radiative transitions. In figure 3.13 the kinetic energy distributions are shown for the $K_{\alpha,\beta,\gamma}$ transitions in μH at 10 bar ($\sim 1.3 \times 10^{-2}$ LHD).

The complex structure of the kinetic energy distribution is revealed. Peaks corresponding to Coulomb deexcitations with $\Delta n > 1$ can occur directly or by steps with

spectral line	max Energy shift [eV]	Coulomb deexcitation $\Delta n = 1$	
		transition	kinetic Energy gain [eV]
K_{α}	±1.1	$3 \rightarrow 2$	166.3
K_{β}	±0.75	$4 \rightarrow 3$	58.2
K_{γ}	±0.54	$5 \rightarrow 4$	29.6
K_{δ}	±0.41	$6 \rightarrow 5$	14.6
K_{ϵ}	±0.32	$7 \rightarrow 6$	8.8

Table 3.2: Energy shift (as defined in the text) of the $\mathrm{K}_{\alpha,\beta,\gamma,\delta,\epsilon}$ lines by Doppler effect due to Coulomb deexcitation with $\Delta n = 1$ in μH.

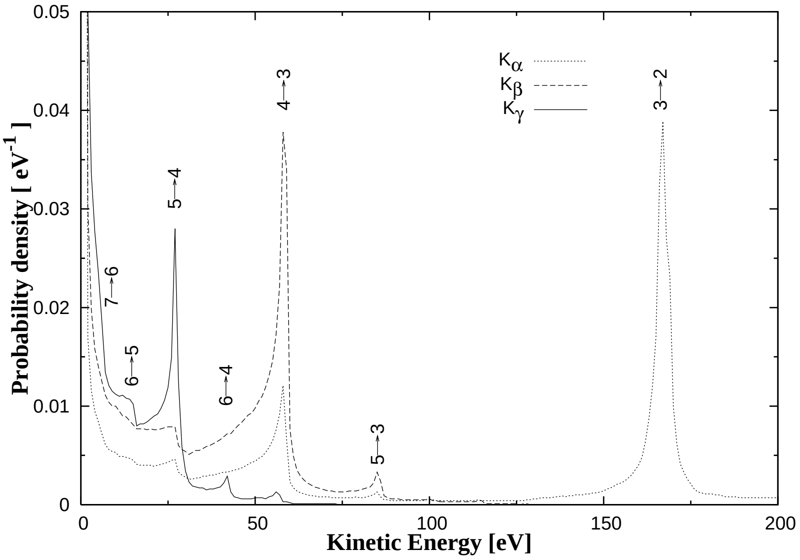

Figure 3.13: The probability density of the kinetic energy at the instant of the K_α, K_β and K_γ transitions in μH at 10 bar ($\sim 1.3 \times 10^{-2}$ LHD). The data were obtained with the latest ESCM version by *Markushin* and *Jensen* [32, 33, 38, 46]. It is plotted in energy steps of 1 eV. A kinetic energy of 0.5 eV was assumed in the laboratory frame *ab initio* and 10^7 exotic systems were tracked. The Coulomb deexcitation transitions $n \rightarrow n'$ corresponding to the peaks are indicated.

the kinetic energy being accumulated. The extended tails have their origin in the deceleration by multiple elastic collisions.

The ESCM predicts a probability of about 0.22, 0.36 and 0.60 to have a kinetic energy less than 2 eV at the time of the K_α, K_β and K_γ transitions, respectively (not depicted as figure 3.13 is cut at a maximum probability of 0.05). This low energy component may result when Coulomb deexcitations occur only at high n (n>10) with the exotic system proceeding via radiative deexcitation where the energy gain remains frozen. Another possible channel is elastic collisions which decelerate the high energy states produced by Coulomb deexcitation. The combined treatment of the cross sections of elastic scattering and Coulomb deexcitation is still under debate and can lead to much different results. However, the mentioned high probabilities indicate the importance of this region and the need to understand better the mechanisms which result in such low kinetic energies.

In figure 3.14 the kinetic energy distribution at the moment of the K_β transition is

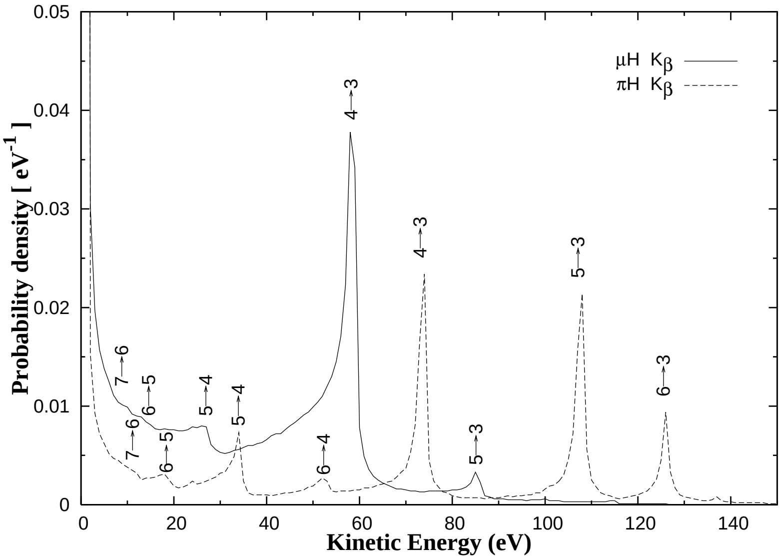

Figure 3.14: Comparison between the probability distributions of the kinetic energy at the K_β decay instant for πH and μH at 10 bar. A kinetic energy of 0.5 eV in the laboratory frame was assumed *ab initio* and 10^7 systems were tracked. The Coulomb deexcitation transitions corresponding to the peaks are indicated.

compared for πH and μH at 10 bar. The structures for both kinetic energy distributions look about similar. However, for πH the peaks are more pronounced relative to the tails. This should result from the faster πH cascade, where the strong interaction plays an important role. In this faster cascade the elastic collisions are less frequent and their importance declines.

3.5 Approximate model for the kinetic energy distribution

The complex structure of the kinetic energy distribution can be approximated by rectangular boxes. These have the advantage to be straightforward to handle in a fit routine, where their number, limits and relative weights can be treated as free parameters. Moreover, it is a “model free” approximation as it is not biased by the predictions of the cascade kinematics routine. Hence, it can be used as an alternative to the ESCM predictions and in a test of the cascade model.

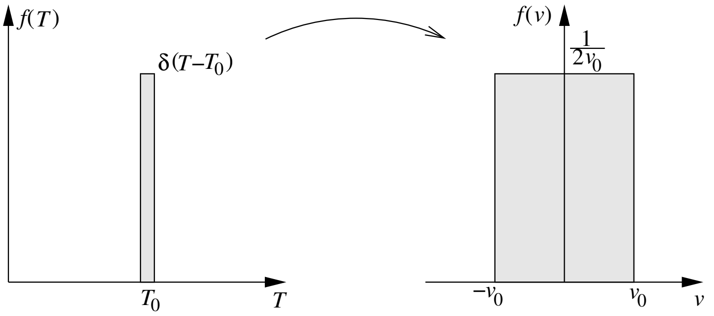

Figure 3.15: Correspondence between a δ-like kinetic energy distribution and the correspondent box like velocity distribution. The maximum of the velocity distribution is given by $\frac{1}{2v_0}$.

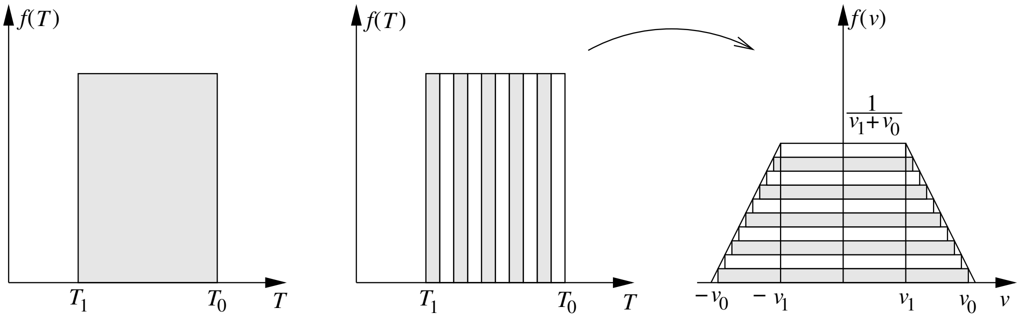

Figure 3.16: Correspondence between a box-like kinetic energy distribution and the correspondent trapezoidal velocity distribution. The rectangular shape of the energy distribution can be approximated by δ-like functions corresponding to velocity boxes which are piled up and generate a trapezoid. The top of the trapezoid is at $\frac{1}{v_1+v_0}$.

Assuming δ-like peaks in the kinetic energy distribution, i.e., $\delta(T - T_0)$, T_0 being the energy where the δ-peak is located, the relation between this energy and the exotic system velocity is given by:

$$v_0 = \sqrt{\frac{2T_0}{m_{x^-p}}} \tag{3.30}$$

A δ-like peak will correspond to a rectangular box on the 1-dimensional velocity distribution extending from $-v_0$ to v_0 (see schematics of figure 3.15). On the other hand, a rectangular box within the limits $[T_0 : T_1]$ $(T_1 > T_0)$ can be regarded as a sum of δ-like functions, each one corresponding to a rectangular box on the velocity distribution. Adding up all the boxes, a trapezoid is obtained. Hence, a rectangular box on the energy distribution is transformed to a trapezoid structure on the velocity distribution (see figure 3.16). For more details check [73].

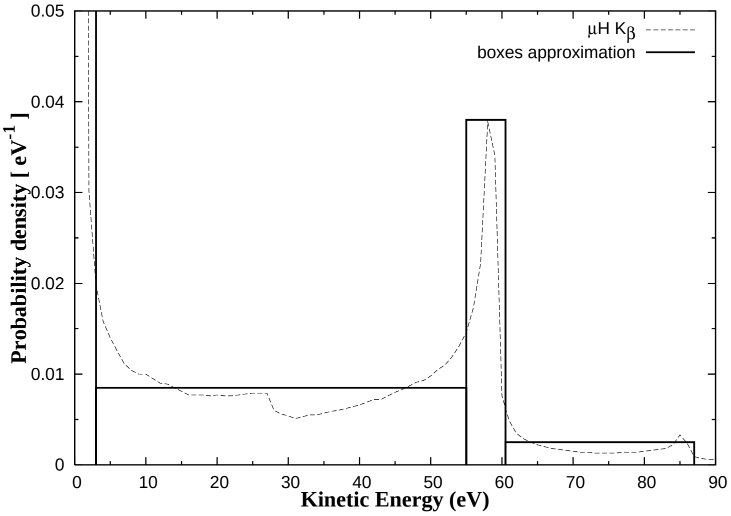

Figure 3.17: Example of a box approximation of the kinetic energy distribution at the instant of the K_β decay in μH at 10 bar. A kinetic energy of 0.5 eV in the laboratory frame was assumed *ab initio* and 10^7 systems were tracked.

The complex structure of the energy distribution is approximated by rectangular boxes which correspond to trapezoid velocity distributions.

Figure 3.17 gives an example of a box approximation of the kinetic energy distribution for K_β in μH at 10 bar. Four boxes with different sizes are used to approximate the complex structure.

Chapter 4

High Resolution X-ray Spectroscopy

Precision measurements of X-rays from light exotic atoms demand high resolution spectroscopy techniques, which can be realized by X-ray diffraction (XRD). As the energies involved are low (few keV) Bragg spectrometers equipped with spherical bent crystals together with position sensitive detectors are used [77].

The setup of these experiments entails several important constraints related to the spectrometer which can reduce the accuracy. Therefore, the understanding of some key aspects of X-ray diffraction theory and the geometrical behavior of bent crystal spectrometers is essential.

This chapter presents a brief introduction into some aspects of the theory of X-ray diffraction. The geometry of the Bragg spectrometers with spherical bent crystals will be addressed as well. The spectrometer used by the πH collaboration will be described together with the data acquisition system. Simulations of the spectrometer behavior will be presented and discussed.

4.1 Elements of X-ray diffraction

4.1.1 Bragg diffraction

In November 1912, following the discovery of X-ray diffraction on crystals by *Max von Laue* [78], *William Lawrence Bragg* in collaboration with his father *William Henry Bragg* presented to the *Cambridge Philosophical Society* his interpretation of *Laue*'s work [79].

For X-rays with sharply defined wavelengths and certain incident directions on crystalline materials, intense peaks from scattered radiation were observed. *Bragg* explained these peaks by regarding a crystal made out of atomic parallel planes. He assumed that the X-rays were specularly reflected, i.e with the angle of reflection equal to the angle of incidence in each plane, and he required constructive interference. In this way, *Laue*'s conditions for diffraction could be reformulated into what became known as *Bragg's law*:

$$m\lambda = 2d \sin\theta_B \tag{4.1}$$

where m is the order of diffraction (an integer), λ the incident radiation wavelength, d the distance between the crystal planes and θ_B the incident angle (Bragg angle).

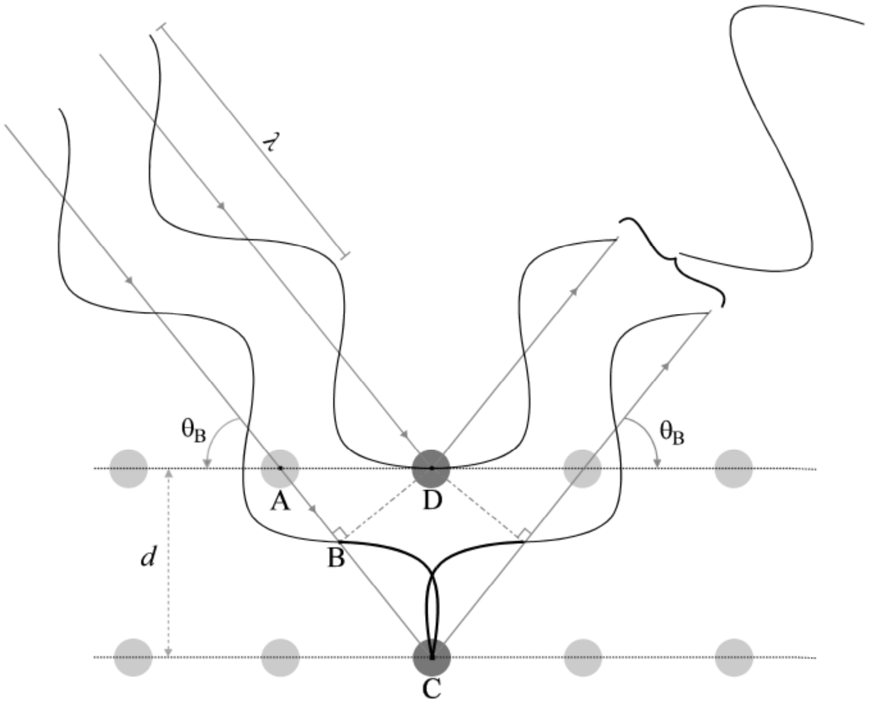

Figure 4.1: Classical construction of the Bragg diffraction of two incoming linearly polarized electromagnetic waves on adjacent crystal planes. The electric field vector is depicted, which is assumed to be π-polarized.

In a classical view, an electromagnetic wave is composed of electric and magnetic vectors perpendicular to each other and to the direction of propagation. By approaching an atom the electric field exerts a force on the electronic cloud. The electrons accelerate and radiate another wave with the same frequency and phase shifted by π. This is known as *Elastic* or *Rayleigh Scattering.*

Bragg's law assumes constructive interference: X-rays scattered from two adjacent crystal planes will have the same phase when the difference between their paths is a multiple of their wavelength.

The idea is shown in Figure 4.1. An X-ray is scattered on the atom marked with D, in the top crystal plane. Another one is transmitted to the consecutive plane and scattered on C. The difference between the paths traveled by the two waves is $2\overline{BC}$. The distance $\overline{BC}$ is given by the difference between $\overline{AC}$ and $\overline{AB}$.

Rewriting $\overline{DC}$ by d gives:

$$\begin{aligned}
\overline{AC} &= \frac{d}{\sin\theta_B} && (4.2)\\
\overline{AD} &= \frac{d}{\tan\theta_B} && (4.3)\\
\overline{AB} &= \overline{AD}\cos\theta_B = \frac{d}{\tan\theta_B}\cos\theta_B \\
&= \frac{d\cos^2\theta_B}{\sin\theta_B} = \frac{d}{\sin\theta_B}\left(1-\sin^2\theta_B\right) \\
\overline{AB} &= \frac{d}{\sin\theta_b} - d\sin\theta_B && (4.4)
\end{aligned}$$

thus:

$$\begin{aligned}
\overline{BC} &= \overline{AC} - \overline{AB} = \frac{d}{\sin\theta_B} - \frac{d}{\sin\theta_b} + d\sin\theta_B \\
\overline{BC} &= d\sin\theta_B && (4.5)
\end{aligned}$$

The path difference is twice this value. Clearly, to have maximal constructive interference, within this length an integer number of wavelengths of the incoming X-rays is possible as well. This number m defines the order of the Bragg diffraction and can only change by varying the Bragg angle accordingly:

$$\frac{m}{\sin\theta_B} = \frac{2d}{\lambda} = constant \tag{4.6}$$

Hence, Bragg scattering for higher orders is only possible when $\theta_B < 30°$ for the first order. As $\sin 30° = 0.5$, that would imply a second order at $\theta_B = 90°$ which is the angular limit for Bragg scattering.

4.1.2 Similarities between Bragg and optical diffraction

Despite the maximum constructive interference, which leads to a very intense and narrow peak, other constructive interferences are also possible corresponding to phase differences ranging from 0 to π. Those should result in a large number of less intense peaks seen at different scattered angles, for the same angle of incidence. However, they are not visible.

In fact, the scattering of X-rays on atoms in successive lattice planes leads to a similar interference pattern as for light striking a diffraction grating. Considering *Fraunhofer diffraction* where the position of the observation is far compared to the slit/aperture size so that spherical waves at that location can be considered to have a planar nature, the intensity of each point of the interference pattern induced by the diffraction grating is proportional to the following function:

$$f(x) = \frac{\sin^2 Nx}{\sin^2 x} \tag{4.7}$$

where N is the number of slits.

The function $f(x)$ reaches the maximum at integer multiples of π and is zero at integer multiples of $\pi/2$. The maximum value of $f(x)$ is N^2. Figure 4.2 shows $f(x)$ around π for N=10 and 500 . For low N smaller peaks are visible but with increasing N they tend to become narrower and quasi coincident with the maximum interference peak. For high N, $f(x)$ has narrow peaks for integer multiples of π and is basically zero elsewhere. In the example, the width of the maximum peak changes, approximately, from 0.28 rad (16°) for $N = 10$ to 5.5 mrad (0.3°) for $N = 500$.

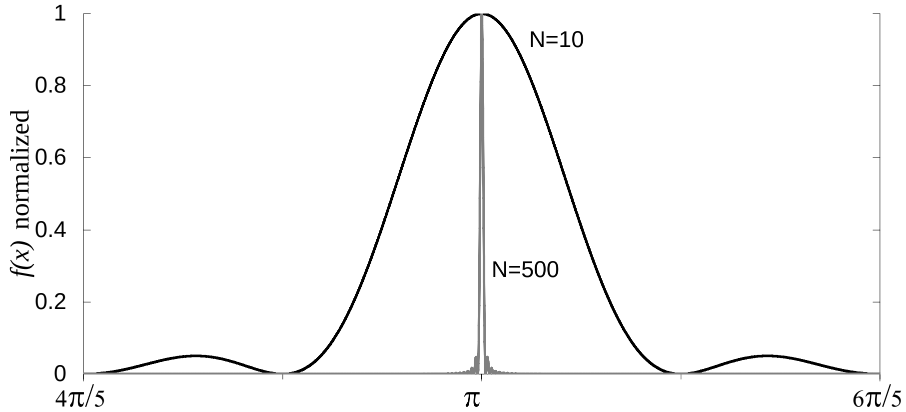

Figure 4.2: The function $\frac{\sin^2 Nx}{\sin^2 x}$ for $N = 10$ (bold) and $N = 500$ (gray) which constrains the intensity of the diffraction pattern on a diffraction grating. The functions were normalized to a maximum of 1.

Each crystal plane can be regarded as a slit in a diffraction grid distant $2d$ from the following slit. An X-ray beam can penetrate deeply into the crystal and can be reflected along tens of thousands of crystal layers which can be considered to be a three dimensional diffraction grating with a very high number of slits. This leads to very sharp and intense peaks, the *Bragg reflection*. In chapters 3 and 4 of *Warren* [80] an analytical treatment of the intensity of the Bragg reflection is presented and its relation with $f(x)$ is explained in detail.

4.1.3 The kinematical and dynamical approach

For very high N various effects constrain the width and the shape of the Bragg reflection. The refraction of the X-rays entering the crystal's medium, their photoelectric absorption by the material and the thermal motion of the atoms in the lattice, for instance, have an important influence on the shape of the Bragg reflection. A proper mathematical treatment on the reflection and transmission of the incoming waves by the crystal layers can predict the intrinsic shape of the Bragg reflection [80, 81]. Two major approaches are used for deduction: the *kinematical theory* and the *dynamical theory* which were first developed by *C.G. Darwin* in 1914 [82, 83].

Under the kinematical view, a real crystal is composed of small (in the order of some d) and ideal perfect crystal grains, also called mosaic blocks, which have a narrow distribution of the relative angular orientations, ranging typically from 0.01° to 0.1° (*Nielsen*, section 4.5.1 [81]) as depicted in figure 4.3.

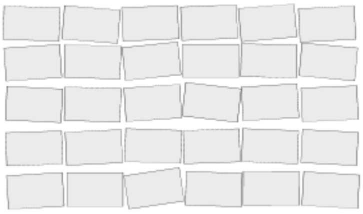

Figure 4.3: Schematic of the kinematical view of a crystal formed by ideal crystals of small dimensions and a narrow distribution of orientations.

An X-ray beam is very weakly reflected in each crystal layer and the total reflected beam is a sum over the total number of planes crossed by the incoming beam. In that way, for a perfectly collimated incoming beam, the accumulated intensity of the Bragg reflection corresponding to a plane with Miller indices (h,k,l) is achieved by rotating the macroscopic crystal and fulfilling the Bragg condition for all single crystal blocks.

Due to the crystal's mosaicity the kinematical approach does not consider the possible Bragg back-scattered X-rays from the Bragg reflected beam. The small differences in the blocks orientation renders the back-scattering unlikely outside the block where the Bragg scattering occurred. If the back-scattered X-rays cannot be ignored one enters the dynamical domain.

The dynamical treatment takes into account a second reflected beam which will have the direction of the primary one (figure 4.4). As the intensity of a second reflected beam on a single layer is small, the effect only becomes relevant for a large number of planes. This happens in highly perfect crystals where the kinematical approach fails completely as multiple scattering needs to be considered.

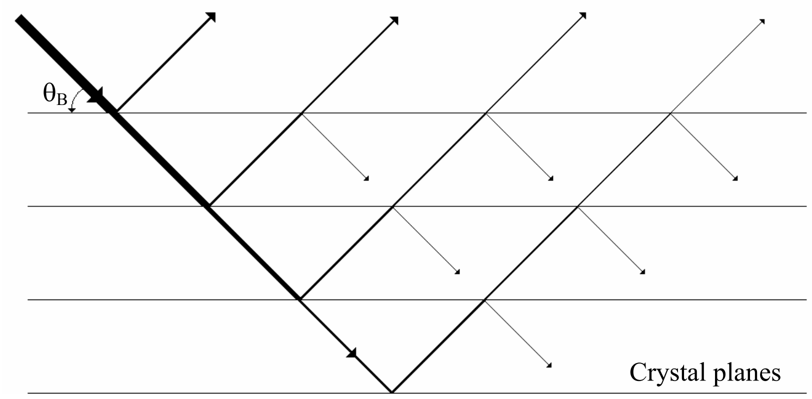

Figure 4.4: Illustration of the Bragg scattering in dynamical view. The Bragg reflected beam can be back-scattered creating a secondary and weaker beam.

The reflectivity curve

A detailed mathematical treatment for both kinematical and dynamical approaches to the scattering of X-rays in crystals can be found in references [80, 81].

The scattering is considered in terms of interactions between the electric fields describing the incoming and outgoing X-rays. According to the Bragg scattering theory, a crystal can scatter a small "bandwidth" of wavenumbers Δk. Hence, by considering a fixed Bragg angle, the reflection does not take place only for X-rays where k fulfills the Bragg condition $(\frac{m\pi}{d\sin\theta_B})$ but also for other X-rays with a small offset Δk. However, the intensity of the reflected X-rays decreases with the offset.

The reflectivity at each crystal layer is very tiny [81]. The kinematical approach calculates the total intensity of the reflection by summing up all the small contributions at different depths. A reflectivity curve is obtained as function of the relative offset of the wavenumber($\zeta = \Delta k/k$) [80, 81]. The maximum is not achieved for $\zeta = 0$ but is slightly shifted (ζ_0) because of refraction inside the crystal. An example for Si(111) is depicted in figure 4.5.

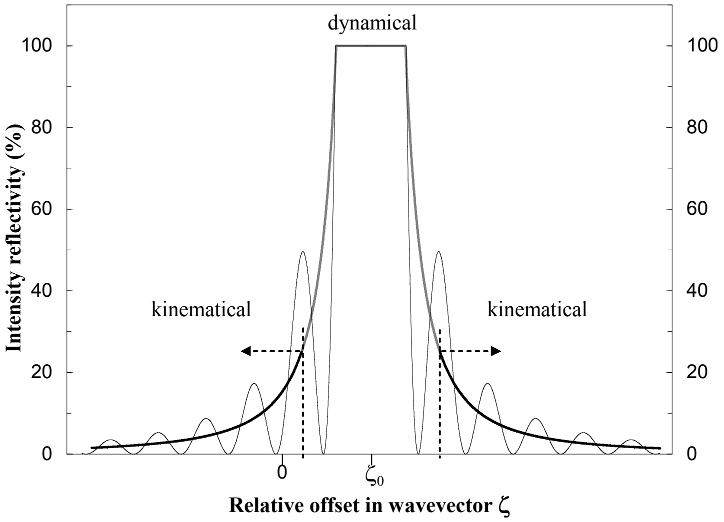

Figure 4.5: Example of a reflectivity curve under the kinematical approach. It was calculated for Si(111) by considering 1.5×10^4 layers and first order reflection according to [81]. The thicker curve is an approximation to the thinner one, with the kinematical region plotted in black and the dynamical one plotted in gray. No absorption or polarization effects were taken into account. The curves are top clipped due to the maximum reflectivity physically possible, i.e. 100%.

As shown in figure 4.5 the reflectivity curve is formed by several peaks. By increasing N the peaks get closer and closer and the curve can be approximated by its mean value (bold line in figure 4.5). However, for higher N the central peak becomes higher and narrower and it needs to be clipped due to the physical limit of the intensity reflectivity (100%). The approximation breaks down. The kinematical approach is only valid for relatively low number of layers. Nevertheless, even at high N it can remain valid at regions far from the central position.

In the case of highly perfect crystals the dynamical theory works better as it considers the multiple scattering inside the crystal (Fig. 4.4). Moreover, it has intrinsically embedded the constraint to not allow a value for the reflected intensity higher than 100%. In fact, the approach predicts a broad region of wavevectors where the intensity of the reflectivity is maximum (100%) — *total reflection region.* A comparison between the reflectivity curve predicted acording to the kinematical and dynamical theories is shown in figure 4.6 for Si(111). The curve obtained from the dynamical theory is known as *Darwin curve.* The depicted curves differ significantly in the central region where the admitted relative shift in the wavevector is small. Yet, by allowing higher relative shifts the kinematical theory becomes a better approximation of the Darwin curve. In the formalism of the dymamical theory, ζ is changed to another variable η so that the Darwin curve is centered at $\eta = 0$ and the total reflection region is limited by $-1 < \eta < 1$ [80]. This variable is denoted by x in [81].

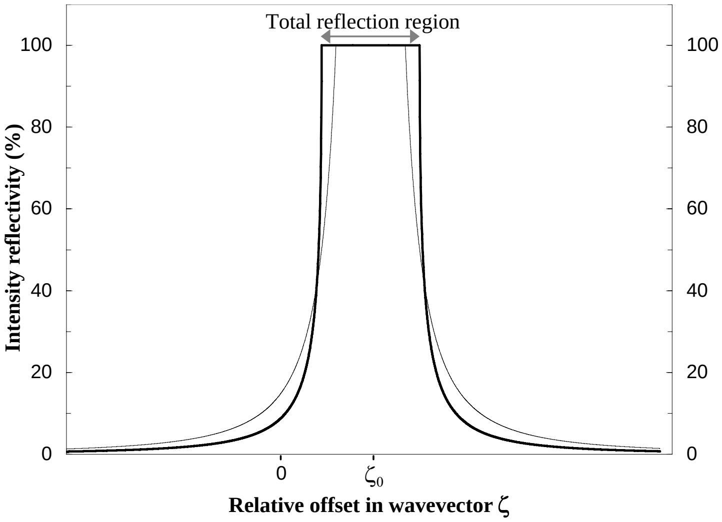

Figure 4.6: The Darwin curve in Si(111) for a first order reflection is plotted in bold. The thinner curve is its correspondent kinematical reflectivity curve. The top flat region of the Darwin curve is known as region of total reflection. The curves were calculated according to [81]. No absorption or polarization effects were taken into account.

Additionally to Bragg scattering, the X-rays also suffer photoelectric absorption inside the crystal, being therefore attenuated. Consequently, a reduction in the intensity of the reflectivity which scales with the energy of the scattered X-rays is expected. In fact, the expansion of the dynamical theory so that it incorporates the photoelectric absorption [81] reveals an asymmetric attenuation of the Darwin curve relative to its center (see figure 4.7a). The attenuation is more pronounced for positive and larger ζ (Δk), i.e. in the direction of smaller k (lower energies). The impact of the photoelectric absorption is enhanced for X-rays with lower energies (see the difference between 8 and 3 keV in Fig. 4.7).

The Darwin curve can be regarded as an intrinsic property of the crystal as long as photoelectric absorption is neglected. It only depends on the parameters of the crystal's unit cell and is a function of the relative offset of the wavenumber (ζ) admitted in the incoming wave. Therefore, it is independent of the wavelength of the X-rays [80, 81]. In fact, this holds by assuming that the structure factor of the unit cell F used in its calculus is a crystal parameter. This is an approximation as F varies slightly with the wavelength of the X-rays. However, this small dependence can be neglected as it comes from small dispersion corrections to the atomic form factors used in the determination of F.

Nevertheless, the Darwin curve can be depicted in an angular mode by relating ζ with $\Delta\theta_B$. The relation is found by differentiating Bragg's equation (4.1) with respect to θ_B ($d\lambda/d\theta_B$):

$$\frac{\Delta\lambda}{\lambda} = \frac{\Delta\theta_B}{\tan\theta_B} = \frac{\Delta k}{k} = \zeta \tag{4.8}$$

where the energy dependence is intrinsically accounted by the $\tan\theta_B$ term. Three examples of the angular form of the Darwin curve are depicted in figure 4.7b. It shows that, the lower the energy the more deviates the angular position of the maximum intensity reflectivity from θ_B. Moreover, for lower energies the angular form of the Darwin curve shows a stretched profile with long tails. The angular form of the Darwin curve is know as *rocking curve* due to the experimental technique used to determine it: by rocking/rotating the crystal [134].

A very important parameter of the Darwin curve is its width (FWHM) as it is a key constraint for the resolution of a XRD system. Following the dynamical theory, it is given by [81]:

$$\zeta_D^{\text{FWHM}} = \frac{3\sqrt{2}}{\pi}\left(\frac{d}{m}\right)^2 \frac{r_0\,|F|}{v_c} \tag{4.9}$$

where d is the crystal lattice spacing, v_c the volume of the unit cell, r_0 the classical electron radius ($\approx 2.82 \times 10^{-5}$Å) and F the structure factor of the unit cell. The FWHM of the Darwin curve (w_D^{FWHM}) is:

$$w_D^{\text{FWHM}} = \zeta_D^{\text{FWHM}} \tan\theta_B \tag{4.10}$$

Once more, by assuming the approximation that $|F|$ is a crystal parameter, ζ_D^{FWHM} is also a crystal parameter. On the other hand, the angular width of the curve increases with increasing wavelength (smaller energies) as θ_B becomes larger, limiting the resolution of a X-ray diffraction (XRD) spectrometer.

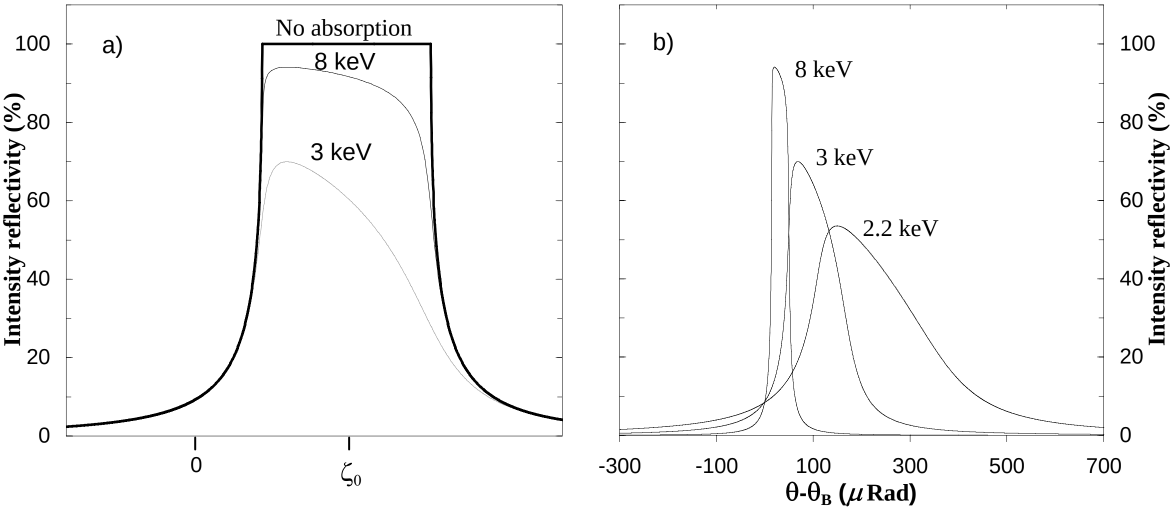

Figure 4.7: a) Effect of the absorption in the Darwin curve of Si(111) at 8 keV and 3 keV for the first order reflection. b) Angular form of the Darwin curve at 2.2 keV, 3 keV and 8 keV considering the absorption in Si(111) for the first order reflection. The curves were calculated according to [81]. No polarization effects were taken into account.

The penetration depth: extinction and absorption

Along its path inside the crystal, the X-ray beam becomes weaker and weaker till total annihilation. Beside being partially reflected at each crystallographic plane the X-rays can also suffer photoelectric absorption.

The depth that the X-ray penetrates into the crystal, considering only attenuation by reflection, is named *extinction depth* (Λ). According to [81] the dynamical theory predicts it to be:

$$\Lambda = \frac{1}{4\sqrt{1-\eta^2}} \frac{m}{d} \frac{v_c}{r_o|F|} \tag{4.11}$$

where the polarization was omitted.

The value of Λ varies along the *Darwin curve* as it depends upon η. Therefore, in a calculation of the extinction depth the value of η has to be specified. As $\eta \to \pm 1$, the square root tends to 0 and the extinction depth diverges to infinity. Thus, for $|\eta| \geq 1$ only the photoelectric absorption contributes to the total penetration depth of the incident photons. At the middle of the *Darwin curve*, where $\eta = 0$, the extinction depth becomes:

$$\Lambda = \frac{1}{4}\frac{m}{d}\frac{v_c}{r_0|F|} \tag{4.12}$$

The electric field vector has two polarization components and the extinction depth depends on polarization. The component parallel to the plane of incidence or scattering plane is named *p-like* (stands for parallel) and the component perpendicular to this plane is termed *s-like* (stands for *senkrecht*, german word for perpendicular). X-rays with a p-like electric field vector are said to be *p-polarized*, *π-polarized*, *tangential plane polarized* or to be a *transverse-magnetic* (TM) wave. Opposite, with a s-like electric field vector the X-rays are *s-polarized*, *σ-polarized*, *sagital plane polarized* or to be a *transverse-electric* (TE) wave. An unpolarized X-ray beam has 50% of each component. Figure 4.8 clarifies the situation.

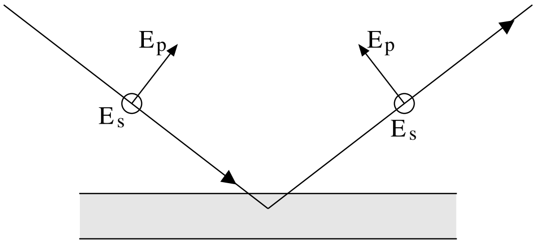

Figure 4.8: The polarization of the electric field vector of a plane wave. The p-component is parallel to the scattering plane, which is defined by the incoming and outgoing X-rays. The s-component is perpendicular to the scattering plane.

By introducing in (4.11) a polarization factor, the effect of beam polarization is included in the extinction depth formalism:

$$\Lambda = \frac{1}{C}\frac{1}{4\sqrt{1-\eta^2}}\frac{m}{d}\frac{v_c}{r_0|F|} \tag{4.13}$$

$$\Lambda = \frac{1}{4C}\frac{m}{d}\frac{v_c}{r_0|F|}, \quad \eta = 0 \tag{4.14}$$

where C is the polarization factor. In the dynamical theory it is given by [88]:

$$C = \begin{cases} 1 & \text{for } \sigma \text{ polarization (perpendicular to the scattering plane)} \\ |\cos(2\theta_B)| & \text{for } \pi \text{ polarization (parallel to the scattering plane)} \\ \frac{1}{2}[1+|cos(2\theta_B)|] & \text{for an unpolarized beam} \end{cases} \tag{4.15}$$

On the other hand, there is a characteristic absorption depth λ_D associated to the photoelectric absorption. The mean free path of a photon inside a material (λ_P) is inversely proportional to the linear attenuation coefficient (μ_a) and is a material property which depends upon the photon energy. In Bragg scattering the photons need to cover twice the same distance without being absorbed to reach again the crystal surface. The absorption depth is then related to the mean free path and hence to the linear attenuation coefficient according to:

$$\lambda_D = \frac{\lambda_P \sin\theta_B}{2} = \frac{\sin\theta_B}{2\mu_a} \tag{4.16}$$

Taking both attenuation effects in consideration, the total penetration depth of an X-ray beam hitting a crystal is obtained by adding the inverse of the extinction depth and the inverse of the absorption depth[89]:

$$\frac{1}{\lambda_T} = \frac{1}{\Lambda} + \frac{1}{\lambda_D} \tag{4.17}$$

This equation will be needed later for the interpretation of the ECRIT results.

4.2 Bent crystal Bragg spectrometers

Since the pioneering work of *Laue* and *Bragg* about diffraction in crystallographic materials [78, 79] the XRD experienced an enormous theoretical and experimental development. Now it is one of the most powerful non-intrusive material analysis techniques.

Very high resolution spectra in the X-ray region can be obtained via XRD, outperforming the energy dispersion X-ray techniques. Typical resolving powers ($\lambda/\delta\lambda$) of the order of 1000 to 10000 are achieved with common XRD setups and it is even possible to exceed 100000 for flat single- or multiple-crystal arrangements [90, 91]. Hence, the X-ray diffraction techniques have become a very important tool in highly accurate X-ray applications, such as crystallographic studies, monochromatization of synchrotron light sources, or atomic and molecular physics with exotic atoms.

4.2.1 The Johann geometry

Bragg spectrometers equipped with flat crystals are not suitable for applications with a spatially extended X-ray source with low rate, which is the case in the field of exotic atoms. Instead, cylindrically and spherically bent crystals, which enhance the X-rays intensity owing to the focusing properties, are used.

A remark from *Wagner* [92] delayed the development of diffraction spectrometers equipped with bent crystals for more than a decade. *Wagner* stated that for an extended curved surface it would be impossible to fulfill simultaneously the two requirements of the Bragg condition: emission angle = incident angle (specular reflection) and constant deflection angle.

Figure 4.9 illustrates the situation. In a circle with a radius equal to $\overline{MO}$, any triangle BP_iA (above AB) defines a constant angle Φ. However, the angles of BP_i and P_iA against the tangent to the circle at P_i are different, i.e. $\theta_i \neq \theta_{i+1}$.

This incompatibility is only valid for optical reflecting surfaces. It was first recognized by *DuMond and Kirkpatrick* [93] who identified the possibility to overcome the problem for crystals. The technical solutions were provided later on by *Johann* [94] and *Johansson* [97]. Figures 4.9 and 4.10 clarify the main ideas of the solution provided by *Johann*.

In figure 4.9 an optical reflection from B at C will pass through A. The triangle OBC has an right angle at B. By rotating the structure $OBCA$ around O the point C describes an arc with a radius equal to the diameter $\overline{OC}$ with reflection points $C_1, ...C_i$. In figure 4.9 the structure was rotated with a step of 5°. The reflected rays, as well as the incident rays, are tangential to a circle with radius $\overline{OA} = \overline{OB}$. This circle is called "caustic circle". A similar construction would be obtained by rotating the structure $OBCA$ to the right!

By cylindrically bending a crystal in the way the crystal planes follow the curvature defined by $C_1...C_i$, a partial focusing is obtained to a circle with a diameter equal the bending radius $R_c = \overline{OC}$. This circle is named *Rowland circle* and the geometry is known as *Johann setup*. The defocusing introduced by the Johann setup is rather small and can be well controlled in practical applications by chosing appropriate dimensions for the crystal size and its radius.

The Johann setup is depicted in detail in figure 4.10. According to it, the Bragg reflected X-rays are focused near a point (D in figure 4.10) placed on the Rowland circle and is given by the focusing condition $\overline{CD} = R_c \sin\theta_B$. The Rowland circle only touches the crystal at its middle point C. The focusing condition is defined from that position and only the X-rays Bragg reflected at C will pass through D. The X-rays fulfilling the Bragg condition at any outer parts of the crystal will have a trace which will intersect the Rowland circle in the neighborhood of D (following the caustic circle, see figure 4.9). Therefore, it leads to an asymmetric aberration in the direction of the higher energies, i.e. smaller Bragg angles, as seen in figure 4.10, leading to the so-called *Johann broadening*, which will cause a shift of the measured Bragg reflection,

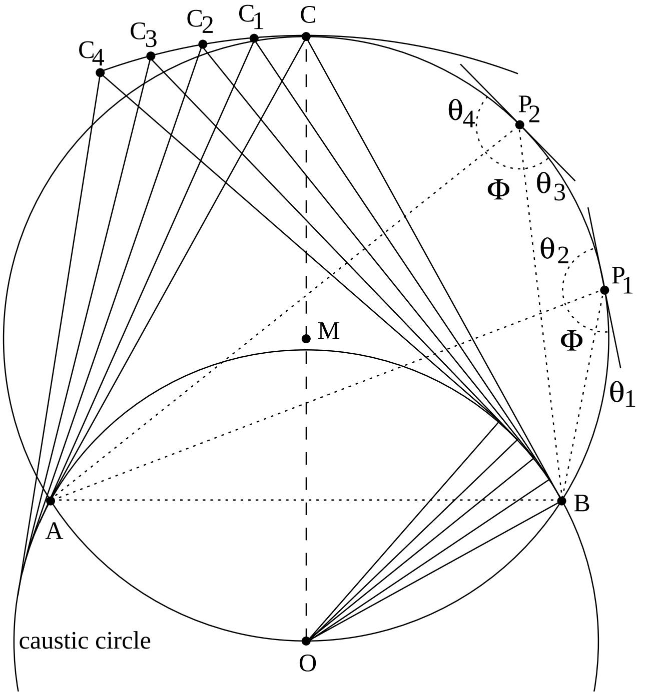

Figure 4.9: An optical reflection on a curved surface with radius $\overline{OC}$ leads to rays tangential to a caustic circle. A spatial concentration of the rays is achieved at points of the circle with radius $\overline{OM} = \frac{1}{2}\overline{OC}$.

the *Johann shift*. The geometrical aberration will be discussed in a section 4.2.3.

An alternative geometry, proposed by *Johansson* [97], overcomes the geometrical Johann broadening. The angle Φ in figure 4.9 is identified in the language of Bragg reflection with the Bragg angle θ_B: $\Phi = \pi - 2\theta_B$. By grinding the surface of the bent crystal with a grinding radius equal to the half of the bending radius, the crystal surface is tangent to the Rowland circle and the Bragg planes always touch it. As consequence the *Johansson geometry* fulfills the focusing condition independently of the X-rays striking point at the crystal (Fig. 4.11). However, the difficulties of the machining are enormous.

The Johann setup was initially described using cylindrically bent crystals. Nevertheless, it can be extended to spherically bent crystals which further enhances the intensity by a partial vertical focusing [95].

Moreover, the Johann broadening and shift can be quantified and kept smaller compared to the crystal intrinsic resolution by choosing appropriate dimensions for the crystal width (b, see figure 4.10) compared to R_c ($R_c >> b$). The width of the active

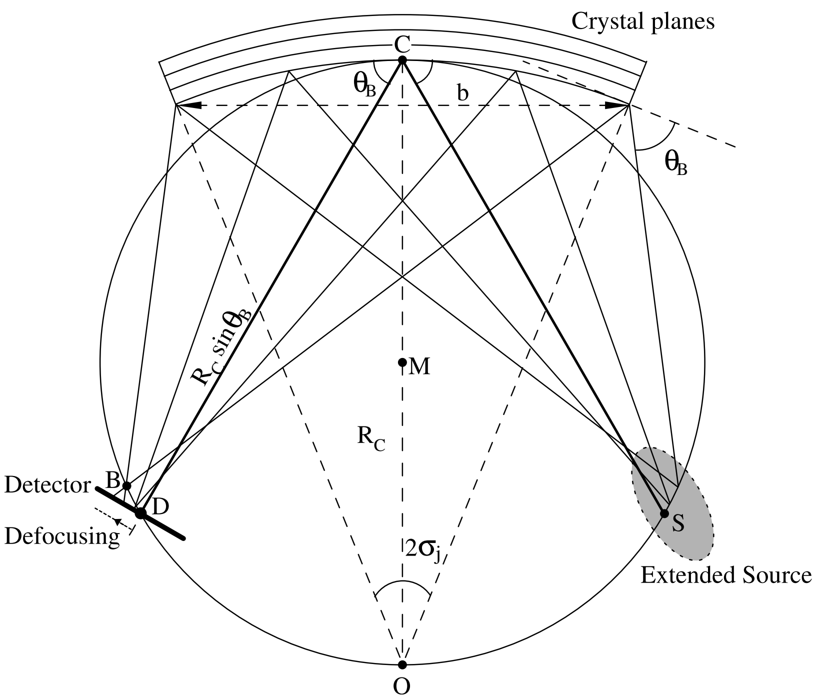

Figure 4.10: The Johann geometry. A cylindrically bent crystal with a radius $R_c = \overline{OC}$ will focus the incoming X-rays, which fulfill the Bragg condition, from an extended source to the neighborhood of a point distant $R_c \sin\theta_B$ from the crystal center C. This distance corresponds to the focusing condition and is on a circle centered in M with a diameter equal to the bending radius. The circle is named *Rowland circle*. The reflections from the outer regions of the crystal lead to a defocusing which can be quantified relatively to the crystal opening angle σ_j [94]. The detector is perpendicular to CD.

crystal area can easily be controlled by placing apertures in front of the crystal limiting the width of the crystal's reflection region.

4.2.2 Vertical focusing with spherically bent crystals

In a 3-dimensional view the Bragg condition defines an infinite admittance cone for each position of its vertex on the crystal's surface. The angle between the tangent plane to the crystal surface at the vertex and the lateral surface of the admittance cone is the Bragg angle. Thus the cone's opening angle ξ is twice $(90 - \theta_B)$. Consequently, an arbitrary cone base at a certain distance from the vertex will be parallel to the tangent

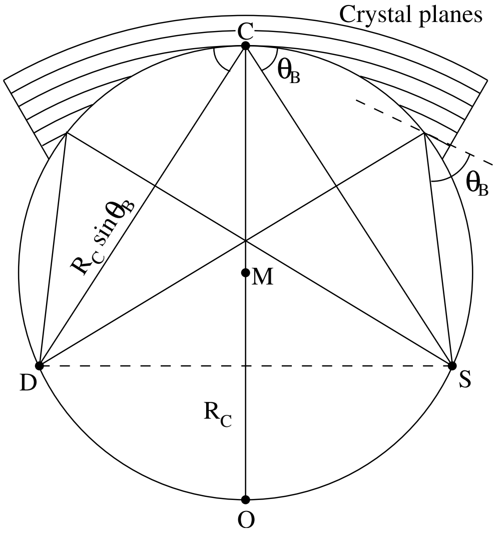

Figure 4.11: The Johansson geometry. The grinding of the crystal prevents the geometrical distortion seen in the Johann geometry.

plane. Therefore, the Bragg condition is fulfilled for an income and corresponding outgoing X-ray on the cone's lateral surface and in antipode positions. Figure 4.12 clarifies the concept.

Point-like source *vs* extended crystal

Figure 4.12 shows the vertical focusing considering a point-like source. The center of the crystal C will be the vertex of an admittance cone which passes through S. The focusing condition $R_c \sin\theta_B$ defines the position of the detector plane. Hence, an X-ray coming from S and hitting the crystal at C will be detected at D.

On the other hand, an admittance cone with its vertex at C' can be constructed by rotating the first one like a pendulum with its fixed point vertically aligned with C and at a distance R_C from it. The second cone can be extended so that it intersects the previous one at a position close to S. By considering that the crystal radius is much larger compared to its dimensions the second cone is just slightly tilted. Therefore, for sake of simplicity, the intersection can be assumed to pass very near to S. In practice, the source would need to have some finite size in order both cones would intersect it.

Within this approximation, the distance $\overline{SC'}$ is slightly larger than $\overline{SC}$. As consequence, the detector plane will not cut the outgoing X-ray $C'I$ at I (at the same distance from C' as S) but at I'.

So, the vertical extension of the spherically bent crystal will result in a curved 2-dimensional spectrum line out of a point-like source. The upper and lower crystal extension (positive and negative y) will create the upper and lower part of the line (positive and negative x_D) respectively. As depicted in the figure, facing the crystal, the curvature of the line will be to the right, i.e. in the negative side of x_D (detector coordinate system).

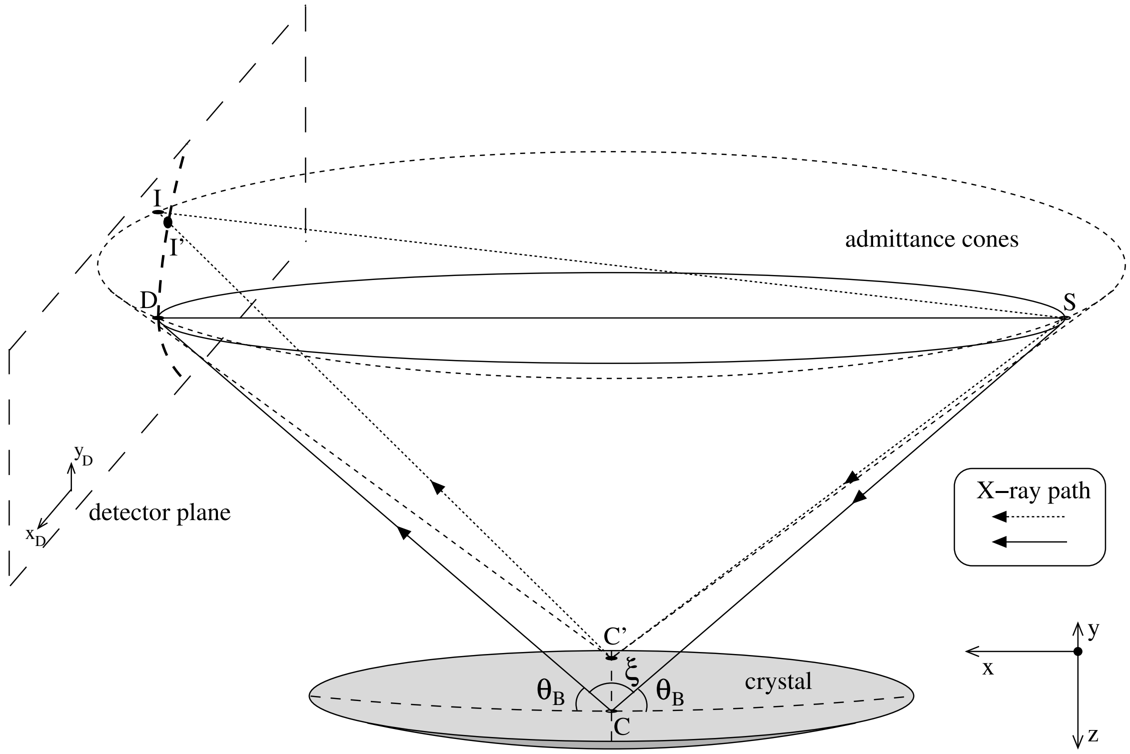

Figure 4.12: Perspective view of the effect of the vertical extension of a spherically bent crystal using a point-like source. The admittance cones with vertexes at C and C' are drawn as solid and dashed lines, respectively. The admittance cone with vertex at C' is an approximation valid for large crystal radius compared to the crystal dimensions. The detector plane is depicted in long dashed lines and is perpendicular to the direction CD. The position D is given by the focusing condition $R_c \sin\theta_B$. The 2-d spectrum line is drawn as medium-long bold dashed line.

The positive and negative line extensions can be estimated, in leading order, for a given θ_B and vertical crystal extensions with the source placed on the Rowland circle at a distance given by the focusing condition. Figure 4.13 shows the geometrical construction of the positive line extension.

The line extension d= $\overline{DI'}$ is twice the hight e (see figure), which is related to the distance h between O and N by:

$$\mathrm{e} = \mathrm{h} \tan\phi \tag{4.18}$$

where ϕ is the angle between OC and OC'. The angle ϕ and the distance h are given by:

$$\phi \approx \frac{\mathrm{a}}{R_c} \approx \sin\phi \approx \tan\phi \tag{4.19}$$

$$\mathrm{h} = \mathrm{f} \cos\theta_B \tag{4.20}$$

a is the positive vertical extension of the crystal and f the distance from O to S:

$$\mathrm{f} = R_c \cos\theta_B \tag{4.21}$$

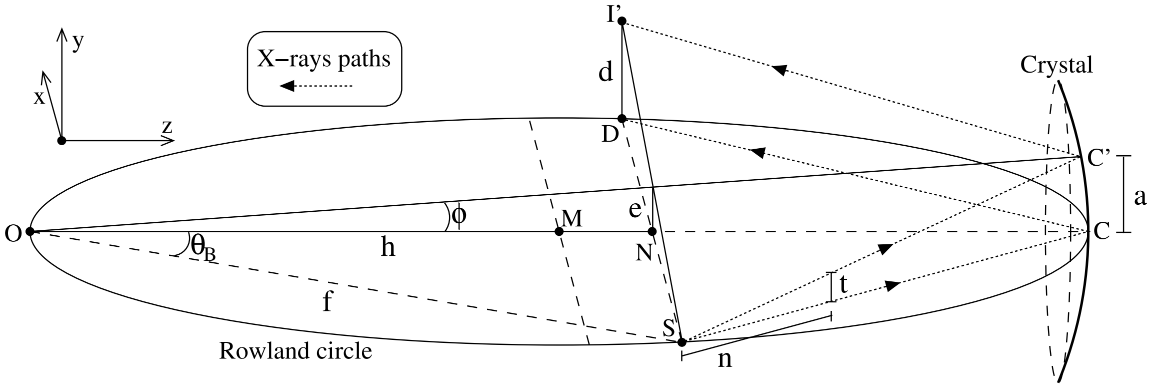

Figure 4.13: Perspective view of the geometrical construction of the spectral line vertical extension from a point–like source. The Rowland circle with center at M is depicted to clarify the geometrical relations. O is the origin of the coordinate system.

Therefore the positive line extension becomes:

$$\begin{aligned} \mathrm{d} &= 2\mathrm{e} = 2\mathrm{h}\tan\phi = 2\mathrm{f}\cos\theta_B\tan\phi = 2R_c\cos^2\theta_B\tan\phi \\ \mathrm{d} &= 2a\cos^2\theta_B \end{aligned} \tag{4.22}$$

The same could be done for the lower part of the spectral line considering the negative vertical extension of the crystal. For a symmetric vertical crystal extension, equation (4.22) holds also with a and d being the total vertical extension of the crystal and spectral line, respectively.

By moving the point-like source inside the Rowland circle the Bragg condition is only fulfilled at point C along the vertical direction. To create the same effect as a point-like source at S, at a distance n from S the source needs to have a vertical extension t given by the triangular relation (see figure 4.13):

$$\mathrm{t} = \frac{\mathrm{a{\cdot}n}}{R_c \sin\theta_B} \tag{4.23}$$

In case the source has a smaller vertical extension, the effect would be the same as a point-like source at S using a vertical crystal extension a' given by:

$$\mathrm{a'} = \frac{R_c \sin\theta_B\ \mathrm{t}}{\mathrm{n}} \tag{4.24}$$

By placing the point–like source outside the Rowland circle the above relations hold, but the lower part of the source ($y < 0$) would be responsible for the upper part of the reflection on the detector plane ($y > 0$).

Point-like crystal *vs* extended source

To study the effect of the vertical focusing from a vertical extended source, one can start to consider a point like crystal, i.e. consider only X-rays striking the crystal at its center C. Figure 4.14 shows the construction of the spectral line under the mentioned conditions.

In figure 4.14 the detector plane is placed perpendicular to the direction given by CD. An X-ray which passes at S' and strikes the crystal at C fulfilling the Bragg condition will be reflected along the direction CD' and will intersect the detector plane at I'. The distance S'C and CD' are equal. Point I' will have a bigger y coordinate than D'. On the other hand, the intersection of the direction S'C with the source plane (not depicted) will have a symmetric y compared to I'. Thus, the lower part of the source ($y < 0$) will create the upper part of the spectral line ($y > 0$) and vice-versa.

Therefore, an extended source will be reproduced on the detector plane with symmetric y coordinates, with the curvature being defined by the intersection of the admittance cone with the source and detector planes.

Placing the source inside or outside of the Rowland circle will enhance or limit the effect. Calling l the distance to the crystal center C of an arbitrary position of the source plane (always perpendicular to SC), and y_2 the height of the source to create the same effect as a source placed at S with height equal to y_1, the following triangular relation can be written:

$$l = \frac{y_2}{y_1} R_c \sin\theta_B \tag{4.25}$$

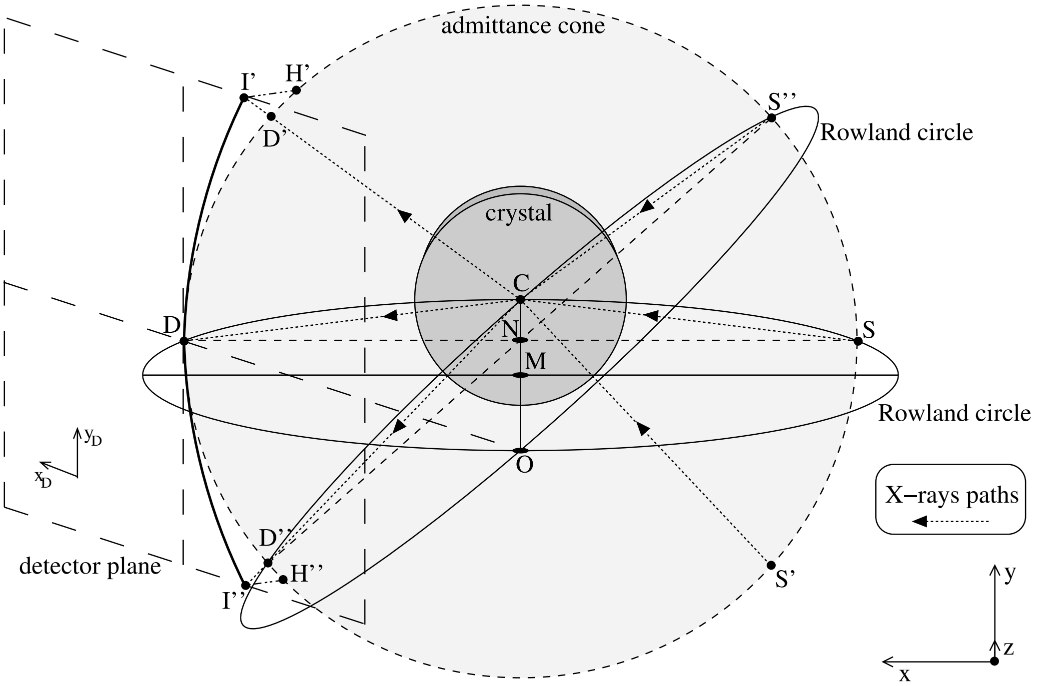

Figure 4.14: Perspective view of the geometrical construction of the spectral line from a vertically extended source and a point-like crystal. In dashed line is depicted the base of the admittance cone generated by the revolution of the triangle CNS around the axis CO. The detector plane is in long dashed lines and is perpendicular to the direction CD at D. The spectral line generated by the vertically extended source using only the crystal center C is in solid bold line.

Yet, inside the Rowland circle a shorter vertical source extension can produce the same vertical extension on a spectral line as a source placed at the Rowland circle. Outside the Rowland circle the source needs to be higher.

Extended crystal *vs* extended source

The two approaches can be combined in order to obtain the vertical focusing of a vertically extended source using a vertically extended crystal. The top view of the geometrical construction which helps to understand the concept is shown in figure 4.15.

The tilt of the admittance cone with the vertex in C' was neglected. The total vertical extension of the spectral line can be regarded as partly $(\mathrm{Y}_\mathrm{D}^+)$ due to the vertical extension of the source $(\mathrm{Y}_\mathrm{S}^-)$ using a point-like crystal at C and partly (d) due to a point-like source placed at the negative extremity of the source and using the total

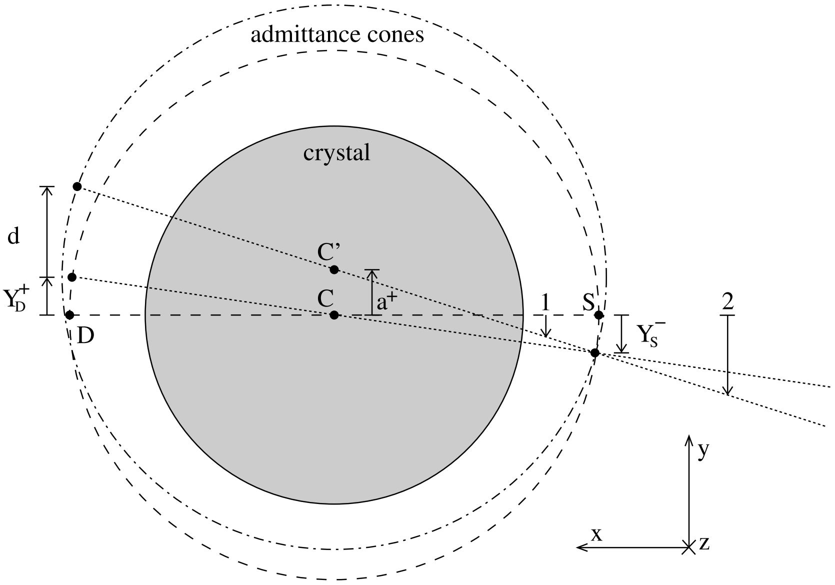

Figure 4.15: Top view of the geometrical construction of the vertical spectral line extension from a vertically extended crystal and source. The bases of the admittance cones with vertex in C and C' are indicated in dashed and point-dashed lines, respectively. The projections of the X-ray paths against the plane (x, y) are indicated as pointed lines. The tilt of the cone with vertex at C' was neglected.

vertical positive crystal extension (a^{+}). Hence, $\left|\mathrm{Y}_{\mathrm{D}}^{+}\right| = \left|\mathrm{Y}_{\mathrm{S}}^{-}\right|$ and d is given by equation (4.22).

The limits of the source define the limits of the image (image height). Therefore, to use only the points S and S+$\mathrm{Y}_{\mathrm{S}}^{-}$ is sufficient to determine the positive half of the height of the image (y =$\mathrm{Y}_{\mathrm{D}}^{+}$+d). Any point between S and S+$\mathrm{Y}_{\mathrm{S}}^{-}$ at the source will lead to a Bragg reflection between D($y = 0$) and y =$\mathrm{Y}_{\mathrm{D}}^{+}$+d.

Moreover, the curvatures due to the two different approximations — point-like source *vs* extended crystal and extended source *vs* point-like crystal — are similar and can be considered to overlap.

By calling Y_{im} the total reflection extension on the detector plane and using the minus and plus signs to indicated negative and positive y coordinates, respectively, one can write in leading order:

$$\begin{aligned}
\mathrm{Y_{im}} &= \left|\mathrm{Y_{im}^{+}}\right| + \left|\mathrm{Y_{im}^{-}}\right| \\
\mathrm{Y_{im}} &= \left|\mathrm{d}^{+}\right| + \left|\mathrm{Y_{D}^{+}}\right| + \left|\mathrm{d}^{-}\right| + \left|\mathrm{Y_{D}^{-}}\right| \\
\mathrm{Y_{im}} &= \left|2\mathrm{a}^{+}\cos^{2}\theta_{B}\right| + \left|\mathrm{Y_{S}^{-}}\right| + \left|2\mathrm{a}^{-}\cos^{2}\theta_{B}\right| + \left|\mathrm{Y_{S}^{+}}\right| \qquad (4.26)
\end{aligned}$$

For a symmetric crystal and vertical source extension, expression (4.26) can be simplified to:

$$\mathrm{Y_{im}} = 2a\cos^{2}\theta_{B} + \mathrm{Y_{S}} \qquad (4.27)$$

where a is the total vertical crystal extension and $\mathrm{Y_S}$ the total vertical source extension. This is valid for a source placed in the Rowland circle.

It is clear from figure 4.15 that a source place outside the Rowland circle (position 2, for instance) needs to have a larger vertical extension to produce the same image height as the source with height $\mathrm{Y_{S}^{-}}$ at S. Inside the Rowland circle at a position not far from it (position 1, for instance) the vertical extension of the source, needed to produce the same effect as the source at S, is smaller than $\mathrm{Y_{S}^{-}}$. Nevertheless, expression (4.27) gives a fair approximation of the height of the image for positions near the Rowland circle and can be used in leading order.

4.2.3 Angular corrections of bent crystals spectrometers

Effect of refraction on the Bragg law

The simple Bragg law [79] does not take into account the index of refraction of the crystal material. Therefore, a small correction needs to be done in order to have a more correct relation between the X-rays wavelength and the Bragg angle measured at the exterior of the crystal.

When an X-ray penetrates a crystal it suffers a change in its wavelength due to refraction (Fig. 4.16). Assuming the Bragg law holds inside the crystal and the new wavelength is λ', the Bragg angle will become θ'_B and the Bragg law can be rewritten as:

$$n\lambda' = 2d\sin\theta'_{B} \qquad (4.28)$$

Considering that the optical principles of refraction can be extended to X-rays, the wavelength and Bragg angle inside the crystal can be related with the correspondent values at the exterior of the crystal:

$$n_r = \frac{\lambda}{\lambda'} = \frac{\cos\theta_B}{\cos\theta'_B} = 1 - \delta \qquad (4.29)$$

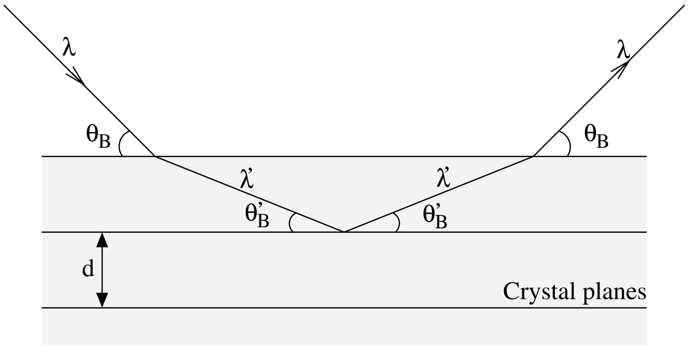

Figure 4.16: The effect of the refraction on the Bragg reflection. The X-rays change slightly their wavelength inside the crystal.

where δ is the decrement of the index of refraction n_r. Working out expressions (4.28) and (4.29) in order to eliminate the index of refraction and the primed quantities, one arrives at a corrected Bragg law ([98], chapter 6), considering that the refraction index for X-rays is close to unity i.e. $\delta \approx 0$:

$$n\lambda \approx 2d \sin\theta_B \left(1 - \frac{\delta}{\sin^2\theta_B}\right) \tag{4.30}$$

Further details can be found in *Chantler and Deslattes* [90].

Geometrical corrections

The geometrical defocussing entailed by the Johann setup due to the horizontal crystal extension is as large as the horizontal crystal opening angle $2\sigma_j$ (Fig. 4.10). According to *Eggs and Ulmer* [95] the maximum broadening on the Rowland circle ($du = \overline{DB}$) is given in leading order by:

$$du = R_c \frac{\sigma_j^2}{2} \cot\theta_B = \frac{1}{8}\frac{b^2}{R_c} \cot\theta_B \tag{4.31}$$

where $b = 2\sigma_j R_c$ is the horizontal crystal extension.

In angular terms, the maximum angular broadening, considering only the horizontal crystal extension, is [95]:

$$\Delta\theta_b = \frac{\sigma_j^2}{2} \cot\theta_B = \frac{1}{8}\frac{b^2}{R_c^2} \cot\theta_B \tag{4.32}$$

Additionally, the source dimensions and the height of the crystal also introduce an extra angular variation. The maximum angular broadenings due to these two factors are respectively, according to *Eggs and Ulmer* [95]:

$$\Delta\theta_z = \frac{z^2}{R_c^2 \sin 2\theta_B} \tag{4.33}$$

$$\Delta\theta_a = \frac{1}{128}\frac{a^4}{R_c^4}\cot^3\theta_B \tag{4.34}$$

where z is the height of the source and a the vertical crystal extension. The geometrical broadening due to the crystal height can be neglected in most practical applications [95]. Therefore, the maximum Johann broadening becomes the sum of two contributions:

$$\Delta\theta_J = \Delta\theta_b + \Delta\theta_z \tag{4.35}$$

A detailed description on how to calculate the average broadening caused by a cylindrical crystal is given by *Zschornack et al.* [96]. In leading order it corresponds to an integration of the Johann broadening over the cylindrical crystal width divided by that width:

$$C_{JohannCyl} = \frac{\frac{1}{8}\frac{\cot\theta_B}{R_c^2}\int_0^b b^2 \, \mathrm{d}b}{b} \tag{4.36}$$

and hence:

$$C_{JohannCyl} = \frac{1}{3}\Delta\theta_b \tag{4.37}$$

By working in leading order, a calculus similar to the one expressed by equation (4.36) can be carried out to find approximately the average Johann broadening for a spherical crystal surface.

A cylindrical surface with a reflecting area limited to a circle causes the same Johann broadening as a spherical surface, the circle radius being equal to the one of the spherical calotte. On both situations, the horizontal crystal extension varies along the vertical crystal axis and the integration should be done also over the vertical crystal extension. The variables x and y will be the horizontal and vertical coordinates, respectively. An uniform reflectivity is assumed over the whole crystal surface.

The Cartesian coordinates (x,y) can be written in polar coordinates (r,ϑ) to simplify the subsequent integration:

$$x = r\cos\vartheta \tag{4.38}$$

$$y = r\sin\vartheta \tag{4.39}$$

$$\frac{\mathrm{d}y}{\mathrm{d}\vartheta} = r\cos\vartheta \Rightarrow \mathrm{d}y = r\cos\vartheta \, \mathrm{d}\vartheta \tag{4.40}$$

The average Johann broadening $J(y)$ for an infinitesimally high strip ($\mathrm{d}y$) at a coordinate y will be $\frac{1}{24}\frac{\cot\theta_B}{R_c^2}[2x]^2$, where $2x$ is the strip length. The weight $w(y)$ of each strip $\mathrm{d}y$ is, in its turn, the reflecting area ($2x\mathrm{d}y$).

The average broadening ($C_{JohannSph}$) for the circular area is then given by the weighted average of the average broadenings of the strips at height equal to $y = r\cos\vartheta$ and length $2x = 2r\sin\vartheta$. In other words it is the sum of all the infinitesimal strip contributions divided by the total area, thus:

$$C_{JohannSph} = \frac{\int J(y)w(y)\ \mathrm{d}y}{\int w(y)\ \mathrm{d}y} \tag{4.41}$$

where $\int w(y)\mathrm{d}y$ is obviously the circle's area and thus, equal to πr^2. Inserting the limits for a circle with a diameter equal to b, it becomes:

$$C_{JohannSph} = \frac{\int_{-b/2}^{b/2} \frac{1}{24}\frac{\cot\theta_B}{R_c^2}(2x)^2\ 2x\ \mathrm{d}y}{\pi\frac{b^2}{4}} \tag{4.42}$$

by changing $\frac{1}{24}\frac{\cot\theta_B}{R_c^2}$ for K, and using (4.38) and (4.40) the integral becomes:

$$\begin{aligned}\int_{-\pi/2}^{\pi/2} K(2r)^2\cos^2\vartheta\ 2r\cos\vartheta\ r\cos\vartheta\ \mathrm{d}\vartheta = \\ = 8Kr^4\int_{-\pi/2}^{\pi/2}\cos^4\vartheta\ \mathrm{d}\vartheta\end{aligned} \tag{4.43}$$

The integral is solved by making use of the double-angle identity:

$$\cos^2\vartheta = \frac{1+\cos 2\vartheta}{2} \tag{4.44}$$

thus:

$$\begin{aligned}8Kr^4\int_{-\pi/2}^{\pi/2}\cos^4\vartheta\ \mathrm{d}\vartheta &= 8Kr^4\int_{-\pi/2}^{\pi/2}[\cos^2\vartheta]^2\ \mathrm{d}\vartheta = \\ = 8Kr^4\int_{-\pi/2}^{\pi/2}\left[\frac{1+\cos 2\vartheta}{2}\right]^2\ \mathrm{d}\vartheta &= 8Kr^4\int_{-\pi/2}^{\pi/2}\frac{1}{4}\left[1+\cos 2\vartheta\right]^2\ \mathrm{d}\vartheta = \\ = 8Kr^4\int_{-\pi/2}^{\pi/2}\frac{1}{4}\left[1+2\cos 2\vartheta+\cos^2 2\vartheta\right]\ \mathrm{d}\vartheta &= 8Kr^4\int_{-\pi/2}^{\pi/2}\frac{1}{4}+\frac{2\cos 2\vartheta}{4}+\frac{1}{8}\left[1+\cos 4\vartheta\right]\ \mathrm{d}\vartheta = \\ = 8Kr^4\int_{-\pi/2}^{\pi/2}\frac{3}{8}+\frac{\cos 2\vartheta}{2}+\frac{\cos 4\vartheta}{8}\ \mathrm{d}\vartheta &= 8Kr^4\ \frac{3\pi}{8} = 3\pi Kr^4\end{aligned} \tag{4.45}$$

By inserting the result in (4.42) and introducing the value of $r = \frac{b}{2}$:

$$C_{JohannSph} = \frac{3\pi Kr^4}{\pi r^2} = 3Kr^2 = \frac{3}{4}Kb^2 \tag{4.46}$$

and finally by substituting K:

$$C_{JohannSph} = \frac{1}{24}\frac{\cot\theta_B}{R_c^2}\frac{3}{4}b^2 = \frac{1}{4}\frac{b^2\cot\theta_B}{8R_c^2}$$

which according to (4.32) can be rewritten:

$$C_{JohannSph} = \frac{1}{4}\Delta\theta_b \tag{4.47}$$

In principle, with the described approach it is possible to calculate the average Johann broadening of any crystal surface parametrization in leading order, even asymmetric surfaces.

The use of spherically bent crystals with partial vertical focusing properties introduces an additional vertical aberration. Over a two-dimensional position detector, a reflection line takes a curved shape along the vertical direction (discussed in the previous section) which broadens and shifts the line (see Fig. 4.17). It can be corrected as follows.

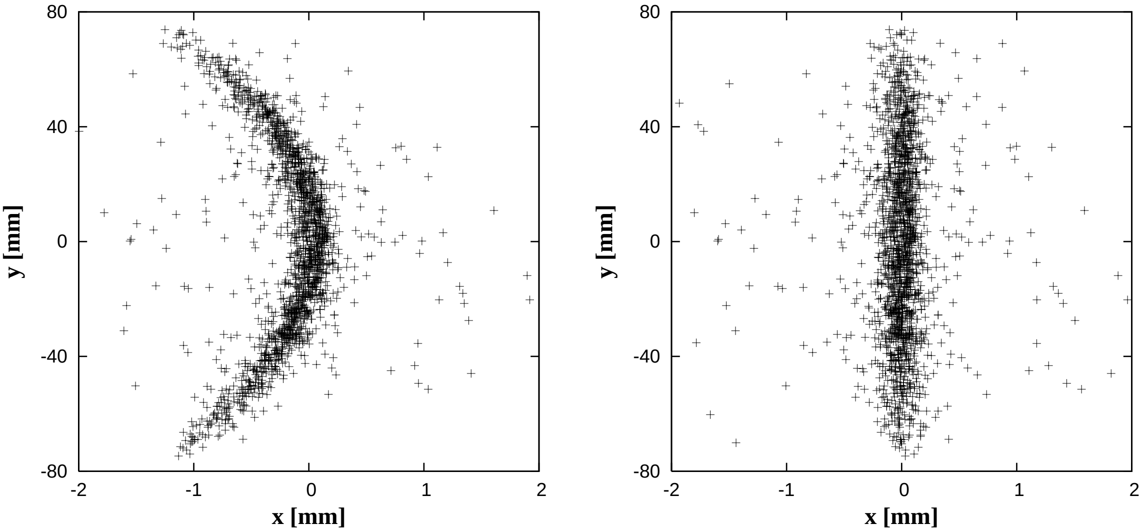

Figure 4.17: Simulated spectrum of 3.104 keV X-rays using a spherically bent Si(111) crystal with $R_c \approx 2985$ mm, a diameter equal to 100 mm and a width b=60 mm. The detector is placed at the position given by the focusing condition and centered at (x,y)=(0,0). The effect of the spherical bending on the vertical line shape is shown at the left. The spectrum after curvature correction is shown at the right.

The line can be parameterized and fit with a second order polynomial $x = Ay^2 + By + C$. To restore the vertical form of the line, the position of the events $(x_i; y_i)$ has to be changed to $(x_i - Ay_i^2 - By_i; y_i)$. The effect of the curvature correction is shown in Fig. 4.17.

Other corrections

Besides the corrections presented, there are other ones which might be needed to be considered. One of those is related to the variations of the crystal lattice parameter d. The bending process causes a slightly variation of d along the crystal depth which will result in a line broadening. The effect depends upon the elastic properties of the crystal material [99]. A dependence of d on temperature can also be considered [100]. However, it is negligible for small variations in temperature as the thermal expansion coefficient for silicon is of the order of 10^{-6} K^{-1} [105] and the impact of the relative variation of d on the Bragg angle is given by:

$$\frac{\mathrm{d}\theta_B}{\mathrm{d}d} \Rightarrow \Delta\theta_d = -\frac{\Delta d}{d}\tan\theta_B \tag{4.48}$$

In practice the temperature variation is about a few kelvin. More details about other second order corrections can be found in *Chantler and Deslattes* and in *Cembali et al.* [90, 99].

4.2.4 Response function

A very important point of the data analysis in high-resolution spectroscopy is the determination of the response function of the spectrometer at the energy of interest. The XOP package [84] delivers the response function of a flat crystal at a given energy for both linear polarizations, σ and π. For an unpolarized beam the response function is assumed to be the sum of the curves for each polarization (see e.g. Fig. 4.18).

By interpreting the XOP output as a probability density function of the reflection angle around the Bragg one and inserting it in a tracking routine which simulates the geometrical constraints of the experimental setup, the theoretical response function of the spectrometer at a certain energy can be obtained.

Yet, non-linear surface distortions caused by the bending and polishing processes are not excluded to contribute to an extra broadening of the response function. In fact, experiments revealed a response function broader than theoretically expected [102]. Therefore, the spectrometer response function has to be experimentally determined.

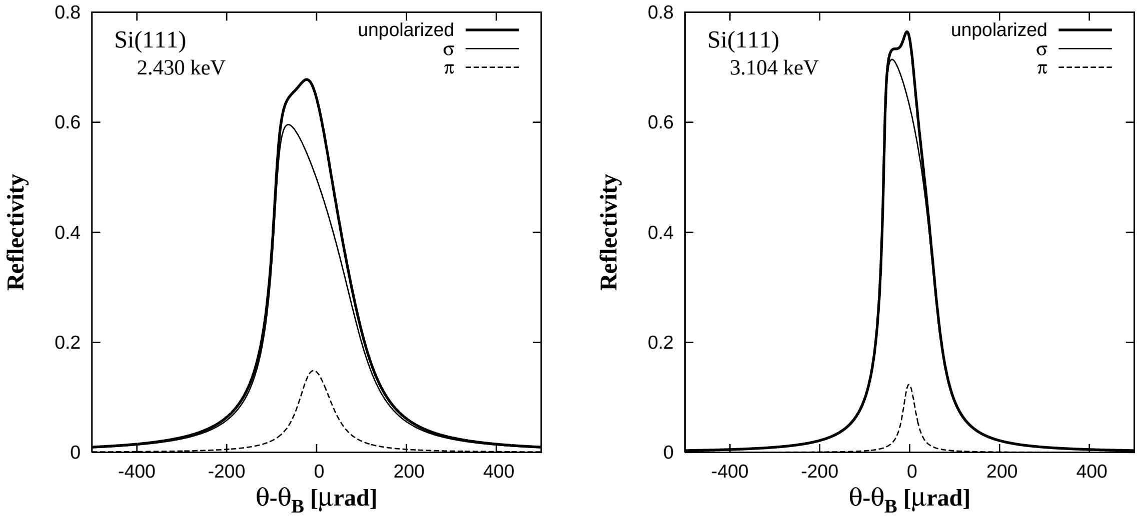

Figure 4.18: Rocking curves of a Si(111) 0.3 mm thick crystal, for 3.104 keV (He-like Ar M1) and 2.430 keV (He-like S M1) at 300 K obtained with XOP [84]. The total rocking curve is shown in bold as the sum of the σ polarization (solid normal black) and the π polarization (dashed). See table 5.9 in page 151 for more details about the FWHM of the rocking curves for the energies studied.

To do that, the use of X-ray transitions lines with widths considerably smaller than the expected response functions is compulsory. Light exotic atoms could provide such lines but must be discarded because of the low count rate and the high statistics needed.

The M1 X-rays from Helium-like ions are a very good alternative as they have a suitable line width and can be produced by plasma sources with very high intensity. In addition the low kinetic energy of the ions in electron cyclotron resonance sources (less than 1 eV [106, 107]) results in a negligible Doppler broadening. Around 3 keV the Doppler effect contributes to an additional broadening of about 40 meV, which compared to the typical response function of our spectrometer at that energy ($\approx$ 450 meV [102]) is about one order of magnitude smaller.

The M1 X-rays from Helium-like sulfur, chlorine and argon, with energies 2.430, 2.757 and 3.104 keV [109], respectively, can be used to extract the response functions at the aimed πH transitions, namely the $2p-1s$ (2.436 keV), the $3p-1s$ (2.886 keV) and the $4p-1s$ (3.043 keV) [108].

Contrary to the mentioned πH transition lines, the μH$(3p-1s)$ transition, object of the present dissertation, does not have an easily accessible M1 Helium-like ion which overlaps its energy (2249.46 eV [110]). Helium-like phosphor could provide a suitable M1 line (2.12 keV [109]), but available phosphor gases, like the phosphor pentafluoride (PF_5) and the phosphine (PH_3) are corrosive and very toxic. PH_3 is even extremely inflammable. Thus, to get the response function at the energy of the μH($3p-1s$) transition an extrapolation based on the results for the other M1 lines needs to be done.

The extra broadening attributed to surface distortions is pinned down by comparing the measured response functions with the ones provided by the tracking routine. A good agreement with the experimental data can be found by convoluting Gaussians with the theoretical response functions [102]. Thus, the imperfect nature of the crystal can be modeled through a Gaussian whose width is determined experimentally. By including the Gaussian broadening in the tracking routine a response function very close to reality is obtained.

The experimental determination of the response functions at the desired πH transitions as well as the extrapolation for the μH($3p-1s$) will be discussed in chapter 5.

4.2.5 Dispersion and energy resolution

The dispersion is the ability of the spectrometer to separate small wavelength differences. Like the energy resolution it is an important quantity to characterize the performance of a bent crystal Bragg spectrometer.

To deduce the angular and energy dispersion one first considers the Johann geometry described in figure 4.10 (page 59). The distance from the detector to the crystal is given the symbol Y. The direction along the detector ($\perp$ to DC) is x. Hence, one can write:

$$dx = -Y d\theta_B \tag{4.49}$$

where the minus sign is purely conventional, it defines the direction of dx. dx is positive when x increases which means that θ_B decreases.

The energy derivative with respect to the wavelength is given by:

$$\frac{dE}{d\lambda} = \frac{-hc}{\lambda^2} = -\frac{E}{\lambda} \tag{4.50}$$

where h is the Planck constant and c the velocity of light in vacuum. Thus, one can write:

$$\frac{dE}{E} = -\frac{d\lambda}{\lambda} \tag{4.51}$$

According to the differential Bragg relation (4.8) (page 53) and equation (4.49) this becomes:

$$\frac{dE}{E} = -\cot\theta_B d\theta_B = -cot\theta_B \frac{-dx}{Y} \tag{4.52}$$

which finally can be rearranged to the energy dispersion relation:

$$\frac{dx}{dE} = \frac{Y}{E}\tan\theta_B \tag{4.53}$$

For the particular case where the Bragg reflection is placed on the Rowland circle (at D) the distance to the crystal Y is given by the focus condition $R_c \sin\theta_B$ and equation (4.53) is rewritten:

$$\frac{dx}{dE} = \frac{R_c}{E}\sin\theta_B \tan\theta_B \tag{4.54}$$

which is a good approximation in the vicinity of D [108].

The energy resolution of the bent crystal spectrometer depends in leading order on the intrinsic resolution of the crystal in a flat configuration. It is predicted by the perfect crystal theory, according to what was described in section 4.1.3 (page 53), and by including second order corrections. However, as described in previous sections, the bent nature of the crystals introduces a geometrical broadening and thus additional contributions to the energy resolution. These are related with finite sizes of the crystal (width) and source (height) [95]. Moreover, the imperfect nature of the crystals introduces an extra broadening. The contribution from the crystal height [equation (4.33)] can be neglected, as mentioned previously. The energy resolution is then the quadratic sum of all the individual contributions and can be written in the following form:

$$\left(\frac{\Delta E}{E}\right)^2 = \left(\frac{\Delta E}{E}\right)^2_{Cry-Int} + \left(\frac{\Delta E}{E}\right)^2_{Cry-W} + \left(\frac{\Delta E}{E}\right)^2_{Src-H} + \left(\frac{\Delta E}{E}\right)^2_{Cry-Imp} \tag{4.55}$$

Taking into account the differential Bragg equation (4.8), the relation (4.51) and the angular FWHM of the Darwin curve (4.10) the intrinsic resolution, omitting the minus sign, will be given in leading order by:

$$\left(\frac{\Delta E}{E}\right)_{Cry-Int} = \left(\frac{\Delta\theta_B}{\tan\theta_B}\right) = \left(\frac{w_D^{FWHM}}{\tan\theta_B}\right) = \frac{3\sqrt{2}}{\pi}\left(\frac{d}{m}\right)^2 \frac{r_0\,|F|}{v_c} \tag{4.56}$$

The two relevant geometrical contributions follow similarly from equation (4.32) and (4.33)

$$\left(\frac{\Delta E}{E}\right)_{Cry-W} = \frac{b^2}{8R_c^2}\cot^2\theta_B \tag{4.57}$$

$$\left(\frac{\Delta E}{E}\right)_{Src-H} = \frac{z^2}{2R_c^2 \sin^2\theta_B} \tag{4.58}$$

The fourth contribution which comes from crystal imperfections needs to be extracted from a comparison between the experimental resolution and the Monte Carlo simulation, as discussed in the previous section and to be shown in later chapters.

An important tool to pin down the intrinsic resolution as well as the response function (rocking curve) of a crystal are the available software packages like XOP [84] or DIXI [101] where the crystal theory as well as some important corrections are built in.

4.3 Quantification of geometrical constraints by X-ray tracking

A Monte-Carlo tracking routine was developed inside the πH collaboration [114]. It is a very important tool in the data analysis and serves as well for a better understanding of the behavior of the bent crystal Bragg spectrometer. The simulation routine, named XTRACK [114], takes the rocking curve and the experimental geometrical constraints to provide reliable response functions. As already mentioned in 4.2.4, the possibility to add an additional Gaussian broadening, which models the crystal's imperfectness, is also built in.

In the following studies the 3.1 keV is used as example because it corresponds to the measured transition energy from M1 He-like ions (chapter 5) where the effects are more visible.

4.3.1 The impact of the crystal reflecting area on the response function

As discussed in section 4.2.3, the finite size of the crystal limits the resolution of the spectrometer. However, by reducing the crystal reflecting area the count rate is reduced as well. That can render a measurement in exotic spectroscopy very time consuming because of already low count rates typical for the exotic atoms. Hence, the reflecting area should be tuned in order to maximize the count rate without degrade significantly the resolution.

By using the tracking routine, the impact of this geometrical constraint on the response function of the spectrometer can be clarified. Figure 4.19 shows a comparison between the flat crystal response function from XOP [84] at 3.104 keV (θ_B=39.56°) and

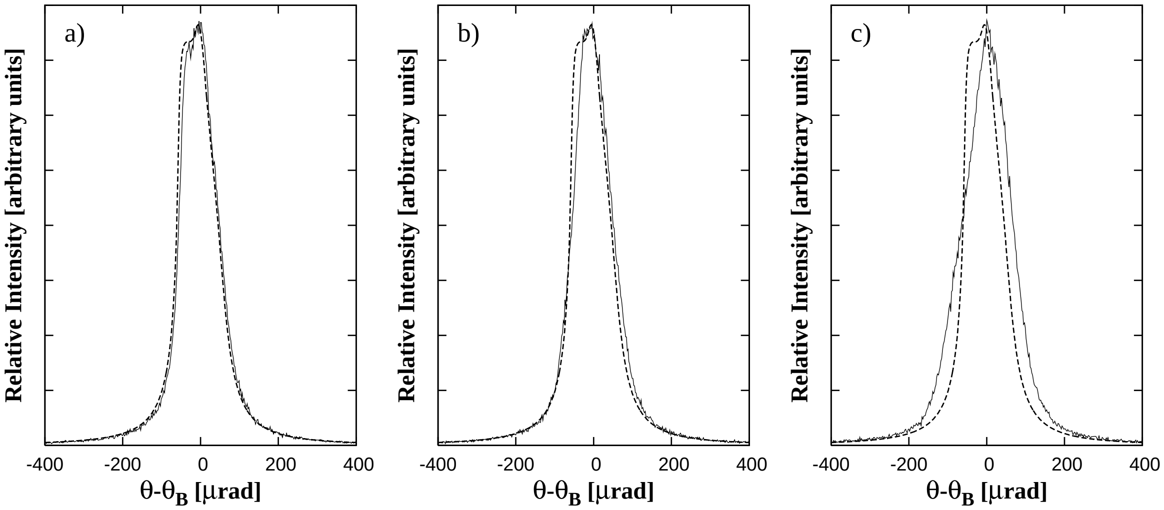

Figure 4.19: The response functions obtained with XTRACK for a Si(111) bent crystal with different reflecting areas (solid lines) are compared to the rocking curve given by XOP [84] for a flat Si(111) crystal (dashed lines). a) Circular reflecting area with 40 mm diameter. b) Rectangular reflecting area 60 mm wide and 95 mm high. c) Circular reflecting area with 95 mm diameter. The response functions for the bent crystal were normalized to the rocking curve.

different response functions obtained with XTRACK by changing the crystal reflecting area. A circular area with 40 mm and 95 mm diameter and a rectangular area 60 mm wide and 95 mm high were studied.

By simple visual inspection of figure 4.19 it is clear that the rectangular reflecting area leads to a line distortion which is only slightly larger than for 40 mm diameter where the response function is roughly similar to the rocking curve of the crystal. On the other hand, by using a circular reflecting area with 95 mm diameter, which is almost the whole crystal, the response function gets considerably distorted.

In fact, the rough check of the FWHM of these response functions confirms the previous observation. The FWHM of the response function obtained with 40 mm diameter reflecting area is nearly the same as the FWHM of the rocking curve (within $\pm 1\mu$rad). It differs by only ∼4 μrad (∼15 meV) from the one which corresponds to the rectangular reflecting area depicted in figure 4.19 b). The FWHM of the response function for the 95 mm diameter reflecting area is ∼512 meV, ∼25% larger than the FWHM of the rocking curve (∼410 meV) which represents a considerable line distortion.

Therefore, around 3 keV, the 60×95 mm (H×V) rectangular reflecting area is a good choice. It leads to a negligible distortion in the response function with a reflection area about 70% of the whole crystal but 4.5 times bigger than the circular 40 mm solution.

At the μH$(3p-1s)$ energy transition (2.248 keV, θ_B=61.58°), the impact of the reflecting area on the response function is expected to be rather small, as the equations in section 4.2.3 allow to predict from the $\cot\theta_B$ factor. This factor decrease fast for increasing θ_B: a change in the Bragg angle from ∼39.56° at 3.104 keV ($\cot\theta_B \approx 1.21$) to ∼61.58° at 2.248 keV ($\cot\theta_B \approx 0.54$) results in a major decrease of the angular broadening [see equation (4.32)].

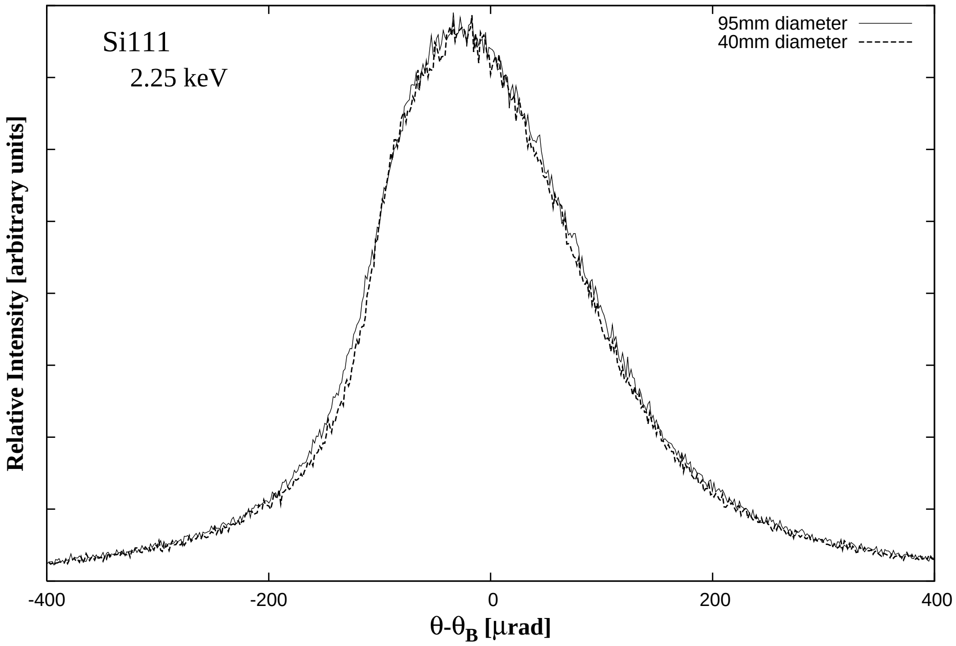

Figure 4.20: The comparison between the response functions calculated with XTRACK at 2.25 keV of the Si(111) bent crystal with a 40 mm diameter reflecting area (dashed line) and with 95 mm diameter reflecting area (solid line) is shown. The lines were normalized for direct comparison.

The response functions at 2.248 keV obtained with a circular reflecting area 40 and 95 mm diameter are shown in figure 4.20. The XTRACK simulations show a very small difference between these two response functions. A rough FWHM determination indicates a difference of the order of 7 μrad between them, which means ∼9 meV. The response function obtained with the 40 mm diameter reflecting area corresponds, in first order, to the rocking curve which has a FWHM of about 255 meV.

Therefore, the use of almost the whole crystal maximizes the reflecting area with a negligible distortion in the response function.

4.3.2 Effect of the source dimensions on the response function

The Bragg condition and the Johann/Johansson geometry establish that an X-ray reaching the detector was emitted from a curved and vertical source region limited by the admittance cone which is as narrow as the reflection width. A Bragg reflection at the detector is a mirrored image (possibly vertically extended) of the source region for a specific Bragg angle. Figure 4.21 shows the source distribution of more than 55000 events which fulfilled the Bragg condition at 3.104 keV (a vertical collimation at the source of 4 mm was used). One can see that the events come from a very narrow horizontal region with width of about 300 μm.

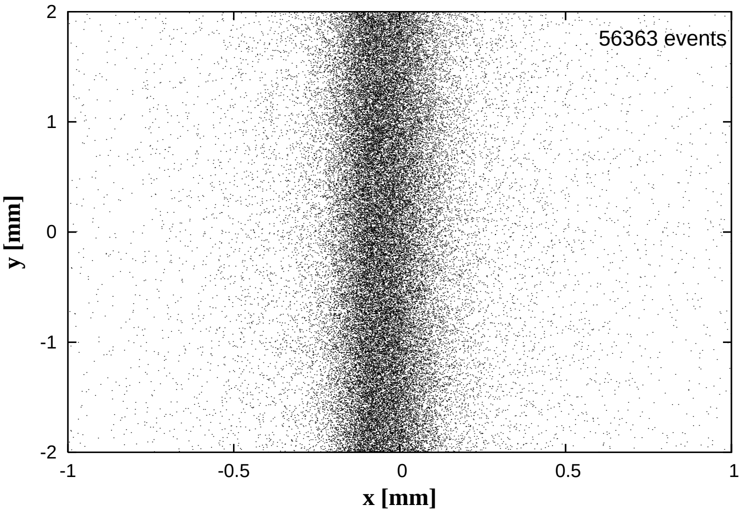

Figure 4.21: Monte-Carlo simulation of the source distribution of the events which fulfilled the Bragg condition at 3.104 keV. A source collimator with an height of 4 mm and a width of 200 mm was assumed.

Because the base of the admittance cone at the vertical source plane has a very big radius compared to the vertical collimator opening ($\sim$ 1500 mm *vs* 4 mm, for R_c $\sim$3000 mm and $\theta_B \sim 40°$), the vertical source region looks basically straight. However, it should be noted that it is just a part of a vertical curved region.

Accordingly, the vertical source collimator width does not influence the line shape, unless it truncates the line distribution at the source. The collimator width limits the possible range admitted for the Bragg angles. It defines as well the source region which is possible to scan for a given Bragg angle (target scan).

On the other hand, the vertical dimensions of the collimator can influence the Bragg reflection shape, as predicted in section 4.2.3. For Bragg angles ranging from 40° to 60° the distortion should be similar, as the $\sin 2\theta_B$ factor is nearly one for all possible cases. The simulation tracking routine helps to quantify the expected distortion as well as it clarifies the effect on the two-dimensional Bragg reflection. In figure 4.22 the 3.104 keV Bragg reflections at the detector as well as the response functions obtained by using a vertical source collimation of 1 mm and 100 mm are compared. An extended source wider than the 100 mm collimator was used.

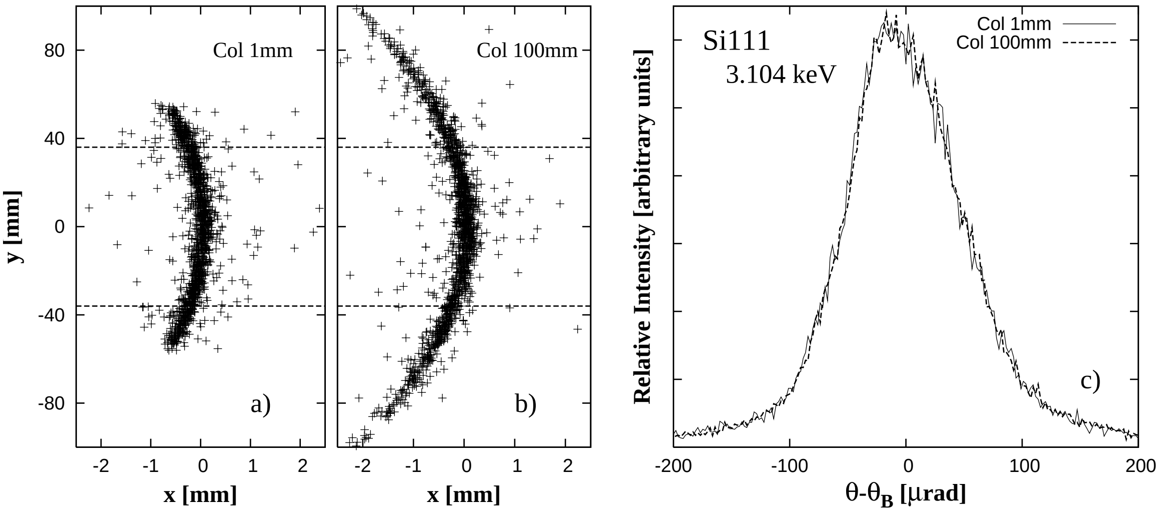

Figure 4.22: The 3.104 keV Bragg reflections at the detector from the bent Si(111) crystal simulated with 1 mm (a) and 100 mm (b) vertical collimation are compared. The horizontal dashed lines in a) and b) are the vertical limits of our CCD detector (72 mm high). The respective normalized response functions are depicted in (c), after curvature correction, in solid (1 mm) and dashed (100 mm) lines. A 60mm×95mm reflecting area from the Si(111) bent crystal and an extended source wider than 100 mm were used.

As the figure shows and already discussed in section 4.2.2, the source collimator's height limits the Bragg reflection vertical extension. Nevertheless, considering our crystal and detector dimensions, even a narrow collimator of only 1 mm height will lead to a Bragg reflection that would extend to outside of the detector's area. In fact, for the mentioned collimator and crystal extension, 1 mm and 95 mm, respectively, and $\theta_B \approx 39.6°$, equation (4.27) predicts a Bragg reflection vertical extension around 114 mm, confirmed by figure 4.22a.

As only the inner part of the line overlapping with the vertical size of the CCD detectors (indicated in figure 4.22) will be used, no significant differences are foreseen for the response functions. Figure 4.22c shows exactly that. Basically no difference in the response functions from a fine source collimation (1 mm) to the extreme case of a very open source (100 mm) is observed.

At the μH$(3p-1s)$ transition energy the reflection height is significantly reduced. For a point-like source expression (4.27) predicts a vertical line extension around 42 mm using a 95 mm vertical extended crystal ($\theta_B \approx 61.6°$) which is barely half of our detector's height (72 mm). Figure 4.23c confirms the predicted value. To use the full capacity of the detector a source collimator's height that exceeds approximately 30 mm should be used. Figures 4.23 compares the 2-dimensional spectra obtained with different collimation's height at $\sim$ 2.25 keV [μH$(3p-1s)$ transition energy].

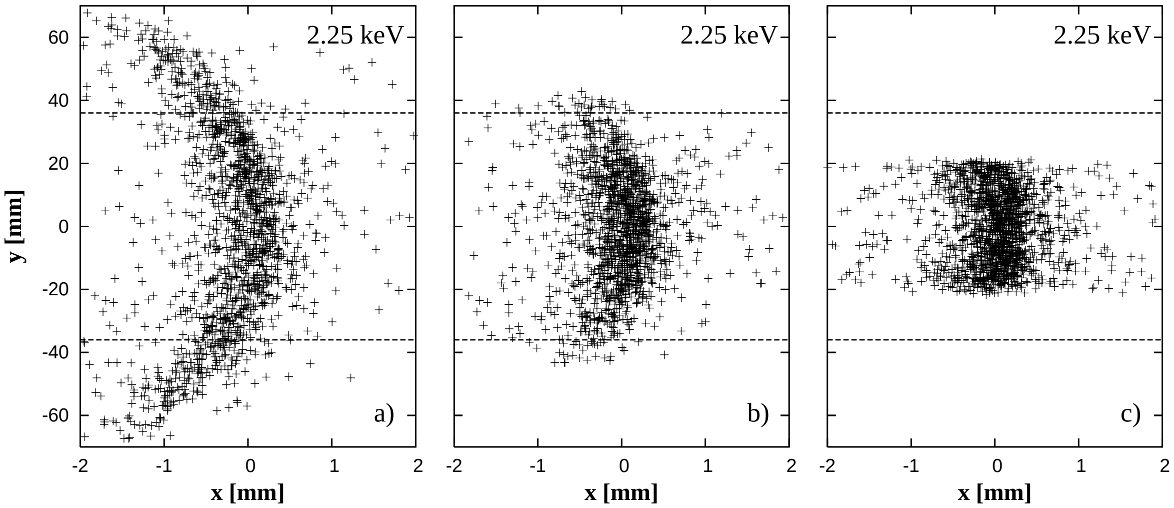

Figure 4.23: Simulated 2-dimensional spectra at ~2.25 keV from the Si(111) bent crystal with different source height collimation: a) 100 mm; b) 50 mm; c) 1 mm. A rectangular 60×95 mm reflecting area from the Si(111) bent crystal and a horizontally extended source wider than 100 mm were used. The dashed lines are the detector's vertical limits.

Despite the height limitation, within the detectors limits, it could be shown that, still at this energy ($\sim$ 2.25 keV), the response functions obtained with a 1 mm source collimation height and with any bigger than this one, have no significant difference.

Therefore, from the point of view of the reflection broadening, no particular restrictions are needed to be taken in the source collimator width nor height. This is an important feature on exotic atoms experiments which suffer from low count rates, allowing to possibly open the source collimation.

4.3.3 The influence of a crystal's position offset in the response function

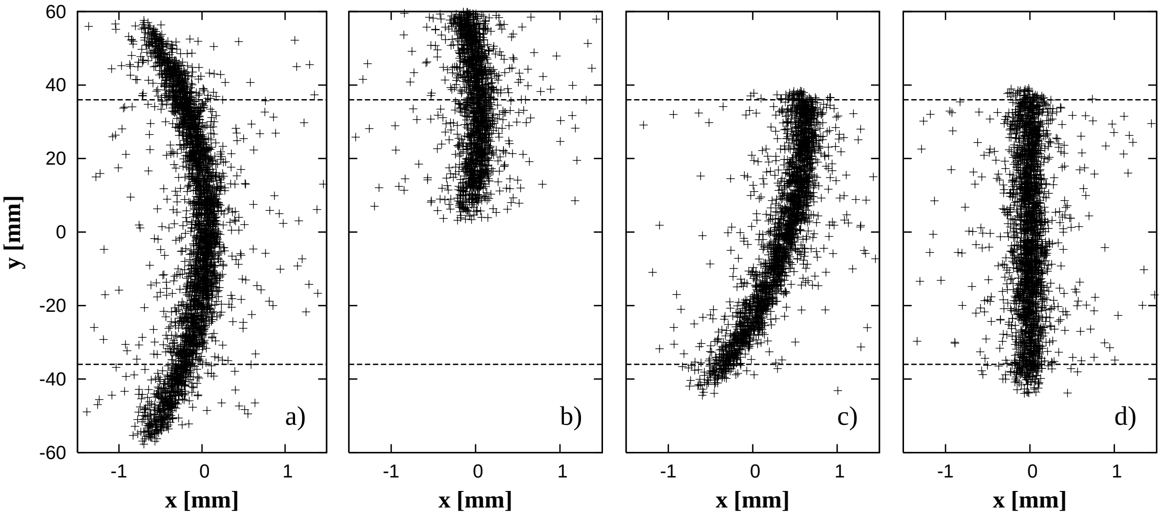

Figure 4.24: Effect of a vertical crystal center displacement of 30 mm in the 2D spectrum at 3.104 keV. A source collimator 4 mm high and a 60×95 mm reflection area were used. The horizontal dashed lines are the vertical limits of the detector's area. The (0;0) coordinate is the central position of the detector plane. a) Normal reflection over the detector without any crystal displacement. b) Reflection got with a 30 mm vertical crystal center offset. c) situation after b) spectrum has been tilt-corrected, the vertical centering being restored. d) The verticality of the reflection in c) is restored by applying the curvature correction algorithm.

The grinding of a glass lens to the desired curvature radius is a delicate process. It would be desirable that the center of a concave glass lens coincides with the deepest point of the surface. However, small displacements of several millimeters can not be avoided or excluded. On the spectrometer geometry such displacements act like if the crystal would be vertically/horizontally misaligned (in the crystal holder and behind the mask which limits the reflecting area) relative to the detector system.

The tracking routine helps to predict and understand the effect of any crystal vertical/horizontal displacement. In figure 4.24 the impact of a 30 mm vertical crystal offset in the 2-dimensional spectrum at 3.104 keV is shown. The reflection is shifted upwards by the same amount and is not anymore vertically centered at the detector. Moreover, it is partially cut at its bottom part which can lead to statistics losses at lower energies if the collimator is not opened enough and the vertical extension of the reflections are smaller than the detector's height.

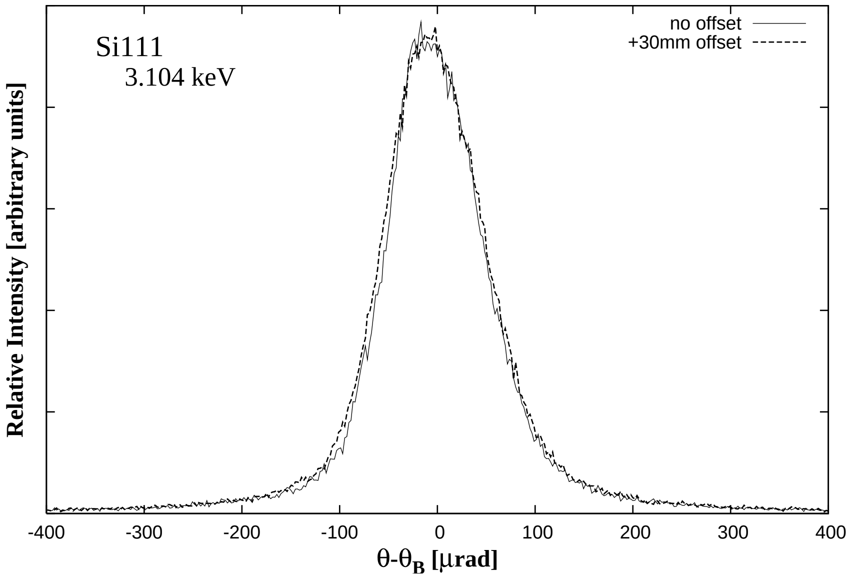

Figure 4.25: Normalized response functions of the bent Si(111) at 3.104 keV with and without vertical offset are depicted. The response function obtained without any crystal displacement is in solid black. The dashed line represents the one obtain with a vertical 30 mm crystal center offset. A small difference is seen, which corresponds to less than 3 μrad in the FWHM.

By using the vertical tilt steering system of the crystal holder the reflection can be replaced at the detector center. After this tilt correction, the line would show up a slightly more pronounced curvature. By performing a curvature correction on the tilted and cut reflection, the verticality of the reflection can be restored without causing any significant horizontal shift.

In fact, the vertical crystal offset leads to a negligible broadening of the response function, after tilt correction. Figure 4.25 shows a comparison between the response function of the spectrometer at 3.104 keV without any crystal offset and with a vertical 30 mm offset. The difference between them is very small. A rough FWHM determination quantifies it to be less than 3 μrad ($\sim$11 meV) which is negligible compared to the total FWHM ($\sim$110 μrad).

On the other hand, a horizontal offset of the crystal center (δx) causes a horizontal shift of the reflection over the detector given by $\delta x \cdot \sin \theta_B$ as shown by figure 4.26. The figure compares the response functions without any offset and with 30 mm offset. No difference between the response functions is seen.

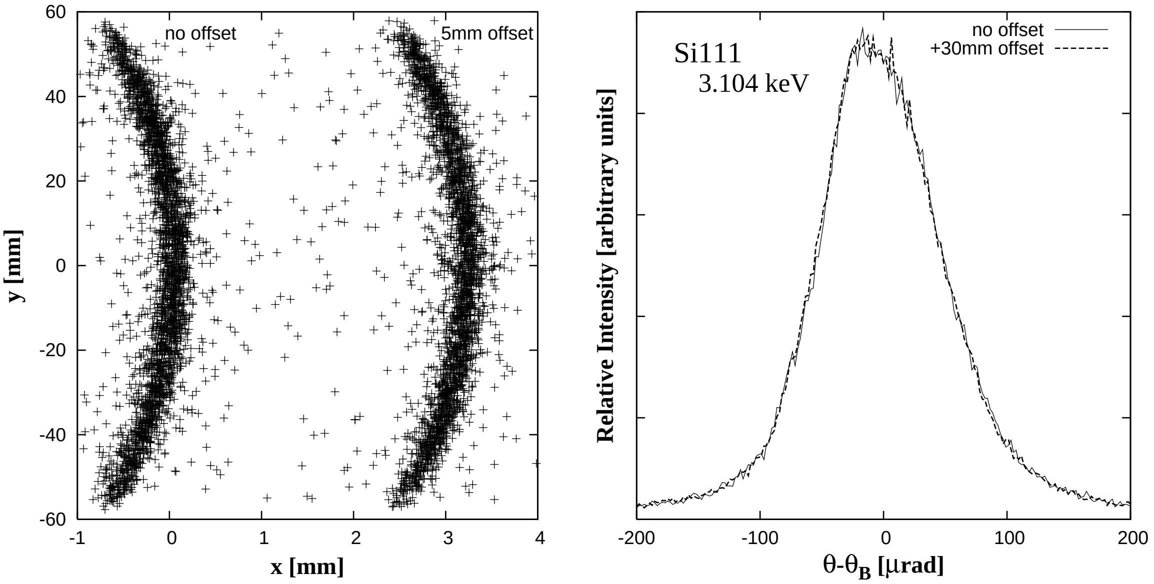

Figure 4.26: Impact of a horizontal crystal center offset on the 2-dimensional Bragg reflection — at the left; and response function of the Si(111) bent crystal at 3.104 keV — at the right. The response functions were normalized. For the 2-dimensional Bragg reflection comparison 5 mm offset was used. A more extreme 30 mm offset (dashed line) was used for the response functions comparison.

Additionally, an offset of 3 cm is quite extreme and would correspond to a very rough fabrication/setup error, which is very unlikely to happen. In practice crystal center displacements larger than 10 mm can be excluded. Around this value, the already minor impacts will be even smaller and completely unimportant.

Considering a displacement of the crystal holder relative to the CCD detector, the described behavior would be the same, despite the fact that no statistics would be lost when a vertical offset would occur. Similar results would be obtained at the μH$(3p-1s)$ transition energy.

Therefore, offsets smaller than 10 mm in the crystal center position, as well as on the relative position of the crystal holder to the detector will not affect the measurements. The spectrometer geometry showed to be quite immune to this kind of systematic errors.

4.3.4 The response function *vs* the distance crystal-detector

Deviations from the nominal focus position ($R_c \sin\theta_B$) will lead to a spectrum line distortion due to defocalization. Actually, small deviations from the focus up to 2 mm can not be avoided. The simulation routine clarifies the impact of small deviations from the nominal focus of the detector position. A positive or negative value of the detector's shift from the nominal focus means towards or away from the crystal, respectively.

The simulation of the response function with the detector shifted by +2 mm from the nominal focus shows basically no line distortion. Opposite, an impact of a +10 mm shift is already very prominent on the line's shape. The response function gets considerably broader with a much bigger distortion on the high energy side ($\theta - \theta_B < 0 \Rightarrow$ smaller angles). Figure 4.27) a shows the direct comparison.

Moreover, the response functions obtained with symmetric detector's shifts, towards and away from the crystal, are similar. Thus, the line distortion will only depend upon the nominal shift value and not on the direction. This is stressed in figure 4.27b).

Therefore, even if small detector's shifts from the focus, of the order of a millimeter, do not introduce an important distortion, it grows rapidly with the nominal shift value. The behavior of this effect is similar at other energies where the arguments hold as well.

4.3.5 Study of the focusing condition

In the Johann geometry, due to geometrical aberration, the focusing condition given by $R_c \sin\theta_B$ is only approximately correct. In fact, a careful geometrical drawing (see picture 4.10, page 59) supports the idea that the focus, defined as the position where

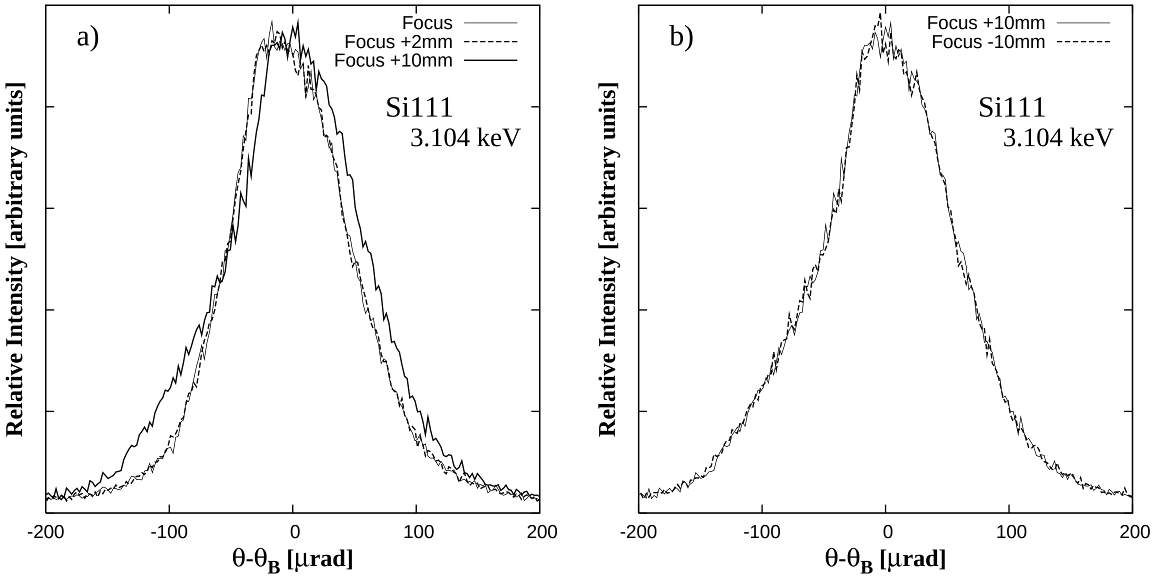

Figure 4.27: Comparison between the simulated response functions of the Si(111) bent crystal at 3.104 keV obtained with different positions of the detector. a) The response function at the nominal focus (solid line) is compared to the one obtained with a 2 mm (dashed line) and 10 mm (bold line) shift in the direction of the crystal. b) The response functions corresponding to shifts of 10 mm towards the crystal (solid line) and away from it (dashed line) are depicted. A rectangular 60×95 mm reflecting area and a 4 mm high source collimator were used.

the spectral line is thinnest, should be slightly shifted inside the Rowland circle, toward the crystal (detector plane at B and $\perp$ to CD in figure 4.10).

By making use of the simulation routine one can test the applicability of the focusing condition to the bent crystal Bragg spectrometer used. High statistics spectra can be simulated by setting the detector plane (always $\perp$ to CD, see figure 4.10) at several positions around the position given by the focusing condition. Several moments of the horizontal distribution can be evaluated to characterize the events at the detector plane.

To estimate the x coordinate around which the distribution spreads the *mean* was used and to characterize the width of the distribution over x the common *variance* and its square root, the *standard variation* were applied. As third estimator to characterize the width of the distribution, the *average deviation* was used:

$$\mathrm{ADev}(x_1...x_N) = \frac{1}{N}\sum_{j=1}^{N}|x_j - \overline{x}| \tag{4.59}$$

where N will be the total number of events, $\overline{x}$ and x_j the mean of the x coordinates and the x coordinate of an arbitrary event, respectively, at the detector plane in the detector coordinate system.

The average deviation is claimed to be a more robust estimator than the variance, as it was verified that higher power moments are generally less robust than lower power ones in broad distributions ([113], section 13.1). The variance is a second order estimator given by:

$$\mathrm{Var}(x_1...x_N) = \frac{1}{N-1}\sum_{j=1}^{N}(x_j - \overline{x})^2 \tag{4.60}$$

involving the sum of quadratic differences. Therefore, the average deviation looks to be more suitable to characterize the width of the x distribution of the Bragg reflections. In the detector coordinate system, the origin (0;0) is the intersection between the detector plane and the direction CD perpendicular to it (check figure 4.10, page 59).

In figure 4.28 the results for four different moments of the x distribution are depicted as function of the detector shift from the position given by the focusing condition $R_c \sin\theta_B$. The simulated distributions were performed for the M1 He-like Ar energy transition (3.10418 keV), using a Si(111) crystal with a bending radius close to 2985 mm. A source collimator 4 mm high and a 60×95 mm reflecting area were used. 98525 events were obtained at the detector plane from 10 million initial trials.

The mean of the distribution shows a linear trend in the order of a tenth of μm per millimeter, which corresponds to 0.0025 pixel/mm. Hence, there is a small asymmetry for symmetric detector shifts, which is very tiny and thus negligible.

The rocking curve has a slight tail in the direction of negative x (lower energies, $\theta - \theta_B > 0$), as shown in figure 4.18 (page 72) for instance. In principle that would be sufficient to explain the distribution's mean at $x < 0$. However, the geometrical broadening when the detector is shifted away from the focus is more pronounced at the higher energy side ($x > 0$), as made clear in figure 4.10 (page 59). Thus, it would be expected that the mean would vary around a minimal value when shifting the detector plane around the focus.

Yet, the right side of the crystal (facing the crystal) is closer to the source, and the probability to be hit is higher than the left side, due to the bigger solid angle. By moving the detector away from the crystal, the X-rays leaving from the right side of the crystal are registered with larger x opposite to the X-rays leaving from the left side which lead to events having smaller x (see figure 4.10 on page 59).

Consequently, the mean value of the distribution changes from a negative x to a positive one, by moving the crystal away from the crystal, as the crystal's right side starts to be responsible for the hits with positive x.

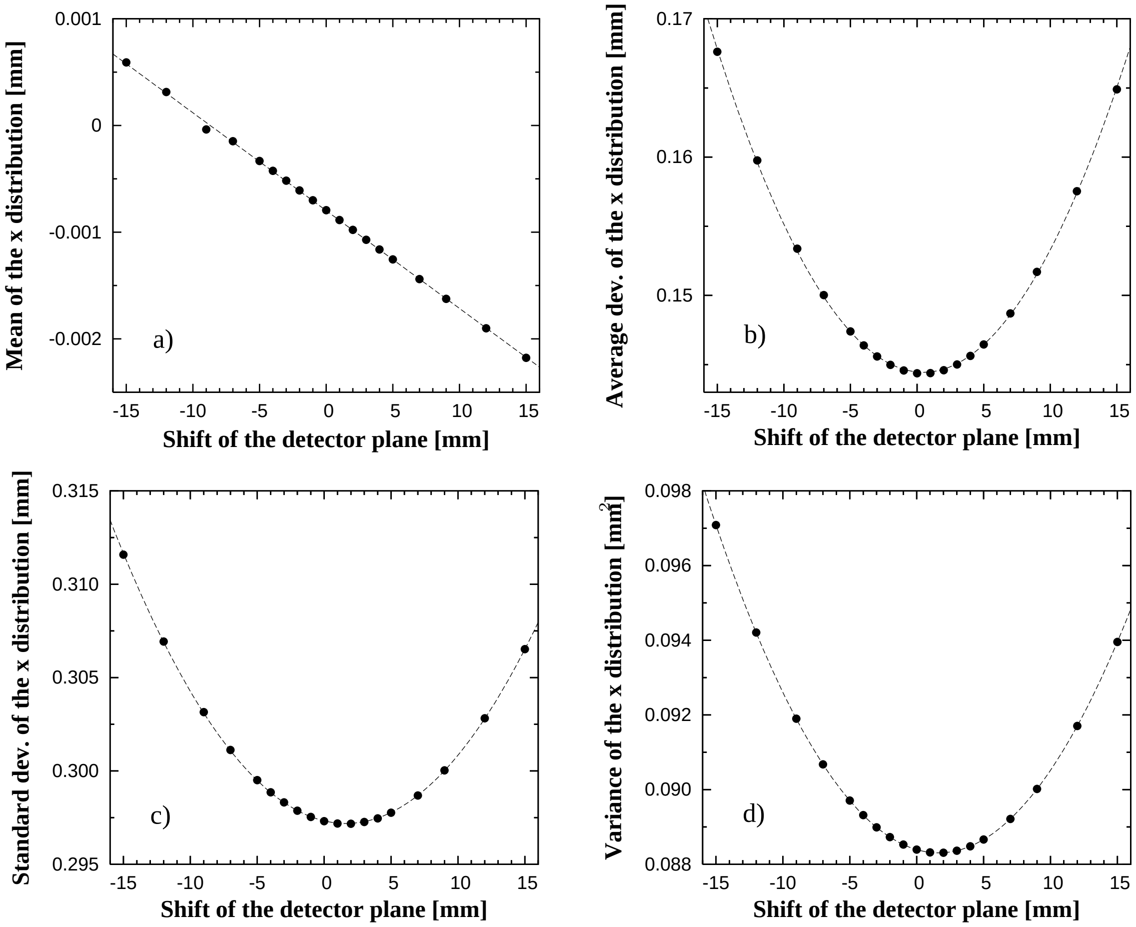

Figure 4.28: The trend of the mean (a), average deviation (b), standard deviation (c) and variance (d) of the x distribution at the detector plane are depicted against its shift from the nominal focus given by $R_c \sin\theta_B$. In dashed lines are the linear fit (a) and the quadratic fit to the calculated moments.

Concerning the other three estimators which evaluate the width of the distribution, they all exhibit a quadratic behavior, where the minimum should in principle correspond to the focus. By fitting a second order polynomial, the shift that minimize the estimators were ∼0.5 mm and ∼1.6 mm for the average deviation and variance, respectively. Obviously the result for the standard deviation is the same as for the variance.

The result shows that the focusing condition given by $R_c \sin\theta_B$ can be applied to the bent crystal Bragg spectrometer. It is correct within less than 2 mm, or even with about 0.5 mm when considering only the most robust width estimator, which for the purpose is good enough.

4.4 The crystal spectrometer

The bent crystal Bragg spectrometer used in all the experimental set–ups at PSI is composed of three main parts : the cyclotron trap, the crystal chamber and the detector cryostat, arranged in a rigid mode and connected through vacuum pipes to avoid X-ray absorption. Figure 4.29 shows a schematic top view of the PSI spectrometer.

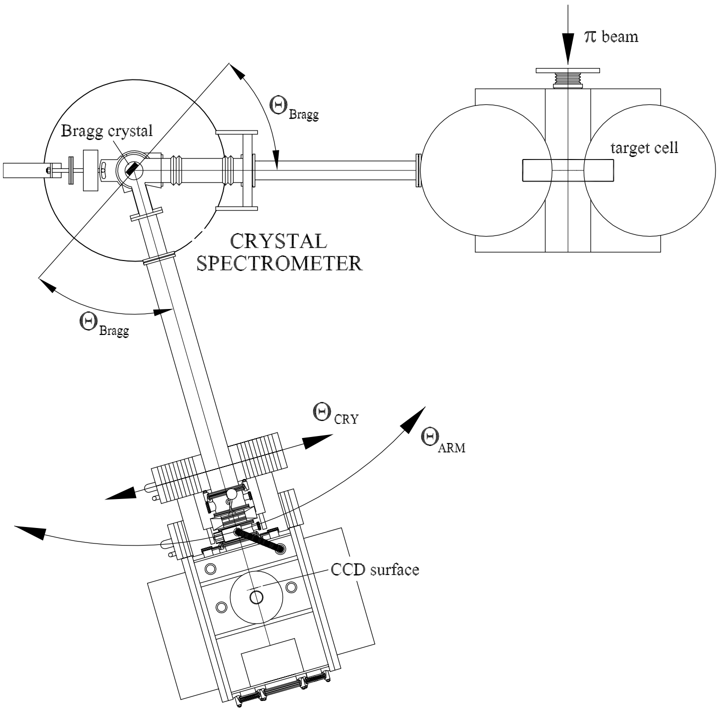

Figure 4.29: Top view of the crystal spectrometer. The angles Θ_{ARM} and Θ_{CRY} define the angular settings of the spectrometer. The Bragg angle is taken between the crystal backplane and the incoming and outgoing X-rays.

The cyclotron trap provides a high stop rate in a target cell from a negative particle beam. This enables the measurement of X-rays with relatively high intensity from the deexcitation of exotic atoms. Moreover, the cyclotron trap can be modified into a Electron Cyclotron Resonance (ECR) ion source allowing atomic X-ray spectroscopy of high charged ions. More details about both configurations will be given in the dedicated chapter 5 and chapter 6.

4.4.1 Crystal details and spectrometer tuning

The crystal used in the μH($3p-1s$) experiment was a Si(111) which has better resolution and higher reflectivity than an alternative solution with suitable energy acceptance: Quartz($10\bar{1}$) [102]. The Si(111) crystal is 0.3 mm thick, has 100 mm diameter and is mounted by optical contact on a high quality cylindric glass lens. The glass lens is 30 mm thick, has a diameter of 120 mm and one of its bases is ground into a spherical shape with the desired radius. Figure 4.30 shows the crystal mounting. Specially cut and polished to preserve its reflection properties, the crystal is carefully bent against the ground face and takes its spherical form. The radius to which the lens is ground, which determines the bending radius of the crystal, is close to $R_c = 2985$ mm. The cutting, polishing and bending processes were performed by *Carl Zeiss, Inc.*, Oberkochen, Germany.

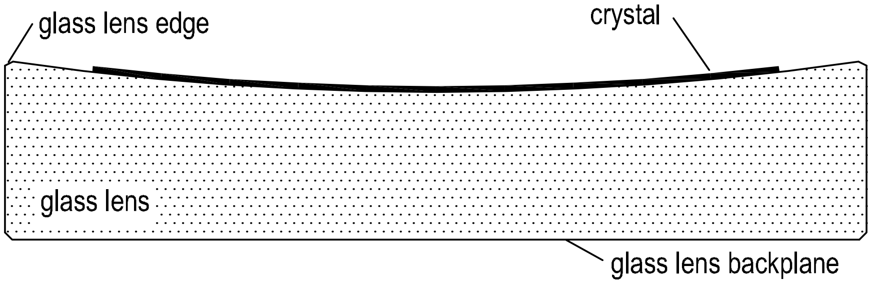

Figure 4.30: Lateral section view of the crystal mounting design. The thin crystal disc is pressed against the thick glass lens, previously ground, to take a spherical shape. Due to the mirror finished surfaces the crystal remains attached to the lens by molecular forces. The sharp glass edges are removed to avoid edge cracks. The curvature and the crystal thickness are to scale.

The crystal is mounted in a holder which allows its vertical tilt for vertical adjustment of the Bragg reflection over the detector (Fig. 4.31). Aluminum apertures can be placed in front of the crystal to define the active reflection area. The crystal holder can be rotated from outside the vacuum system by a shaft. This can be done independently or together with the detector chamber, defining the angles Θ_{CRY} and Θ_{ARM} (Fig. 4.29). This idea is unique for this kind of spectrometers and it was developed at *Jülich* to allow the scan of the target region [115]. All the angular movements are remotely controlled by step motors and high precision angular encoders (resolution of 0.2 seconds of arc). The vertical axis of the crystal holder is aligned to ±0.1 mm with the angular encoder.

Figure 4.31: Photo of the crystal holder together with a Si(110) crystal at its side. The Si(111) crystal looks similar.

To change the energy acceptance of the apparatus by $\Delta\theta_B$ both angles (Θ_{ARM} and Θ_{CRY}) need to be changed. When changing Θ_{ARM} the crystal rotates together with the detector's chamber. Hence, Θ_{ARM} should be moved twice $\Delta\theta_B$ and Θ_{CRY} shifted $\Delta\theta_B$ in opposite direction (see Fig. 4.29 for better understanding of the procedure).

By changing only Θ_{ARM} (Θ_{CRY} and the Bragg reflection over the detector are kept fixed) different source regions are analyzed (target scan). A movement in Θ_{CRY} implies a change in the observable spectral region as well as in the source region. To control some small instabilities, the value of Θ_{CRY} is continuously monitored and readjusted by a feedback loop with a ceramic piezo-electric element. It has already been seen that stresses generated by the rigid connection between the detector's cryostat and the crystal's chamber could lead to mechanical long-term instabilities out of the piezo range [112]. In order to decouple the crystal's chamber from the detector's cryostat and avoid the stresses a bellows compensator was installed between them (figure 4.33).

4.4.2 Detection system

The detector system is based on an array of two columns of three CCDs with a total sensitive area of 48×72 mm. The CCDs used in the assembly were developed for 1...10 keV large area detection in X-ray astronomy missions (CCD22) [104, 103].

CCD22 are high-resistivity devices with a depletion depth approximately 30 μm. These chips have 600×600 square pixels with a side length of 40 μm at room temperature. Each pixel has an energy resolution of 160 eV at 3 keV. The gaps between the six CCDs and their orientation were measured with an accuracy of about 0.8 μm and 50 μrad to be less than 500μm and 7 mrad, respectively [104, 105]. CCD22 has very good quantum-efficiency (QE) in the designed energy region increasing from $\sim$75% at $\sim$2 keV to a maximum of 90% around 4 keV [103, 104]. Figure 4.32 shows the used CCD-detector assembly.

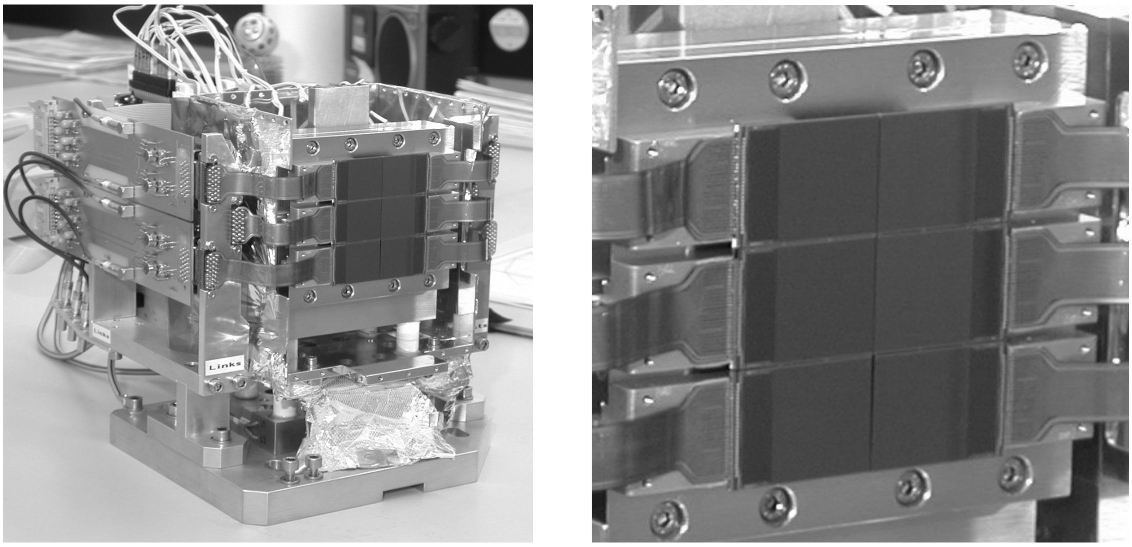

Figure 4.32: Picture of the detector system prior to installation inside the vacuum cryostat. At the left a general view of the system with its cold-finger holder and part of read-out electronics. At the right the array of the six CCDs is zoomed.

In order to decrease the operation noise, mainly due to dark current, the CCDs are mounted on a cold-finger cooled with liquid nitrogen. A closed loop control keeps the CCDs temperature at -100 ± 0.5°C [104]. A thermal dependence of the pixel size was verified with high accuracy and the pixel size at the operation temperature (-100°C) was found to be 39.9775 ± 0.0006 μm [105].

The cold-finger holder is sitting on a high-precision translation table from which it is thermally isolated. The crystal-detector distance is then remotely adjustable to match the crystal focusing condition in a 86 mm range with a precision of 0.2 mm [104]. Figure 4.33 presents a detailed section view of the stainless steal vacuum tight cryostat which houses the whole detector mounting. The cryostat is placed on a polished granite table and can be air-lifted, permitting its easy movement on the table and therefore θ_{ARM} adjustments by a step motor. Several electronic elements placed inside and outside the cryostat carry out the operation of the CCDs through a custom designed software running on an IBM compatible PC. A more detailed information about the characterization and operation of the detector system can be found in Ref. [103, 104, 105].

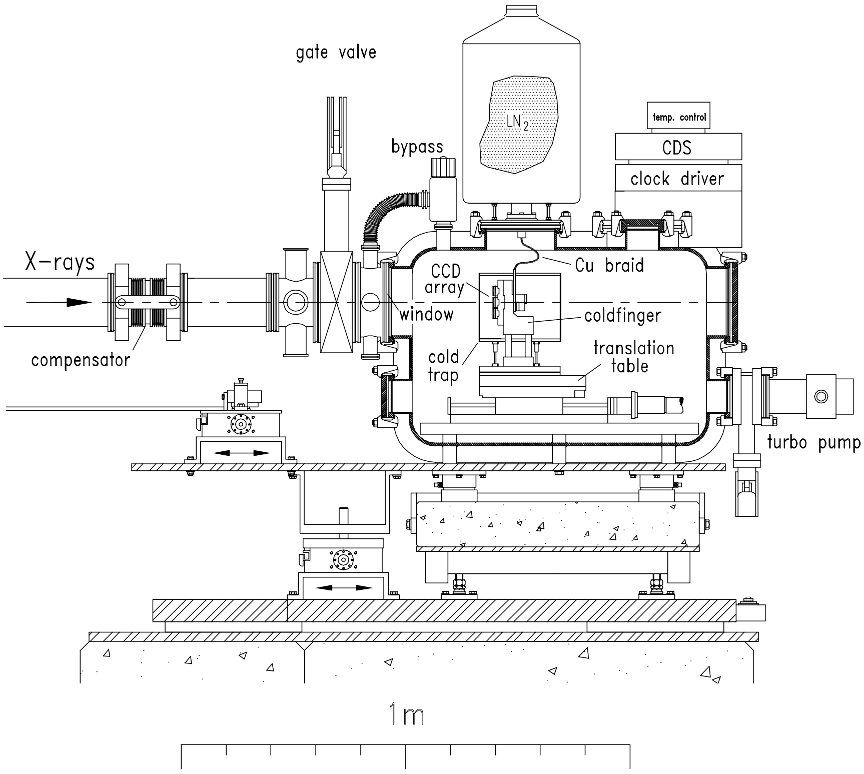

Figure 4.33: Schematic view of the detector vacuum cryostat.

4.4.3 Data processing

The data is collected by exposing the CCD array to the X-rays which are Bragg reflected from the crystal. The detector system acts as a camera which takes successive pictures, named frames, with an exposure time of about 1 min. The energy of an X-ray is converted to a charge when it hits a pixel. After a frame, the read-out system stores the position of the pixels which were hit and their charge with the pixels being cleared. A column of pixels corresponds to the same x and therefore to one angular position.

Cluster analysis

The X-rays in the few keV region (< 4 keV) are mainly converted in the depletion region ($\sim$30 μm thick) of the pixel and cause a single event on it. Additionally, if the absorption occurs near the pixel edge the charge can be split between two adjacent pixels. In contrast, highly energetic photons can penetrate deeper into the CCD substrate, beyond the depletion region, i.e. in the field free region. In this case, the charge can diffuse freely along the substrate and eventually be collected in several pixels producing a multi-pixel cluster event (see fig. 4.34). Partial or total recombination is also possible with consequent charge losses. High energetic particles can additionally create tracks on the CCD.

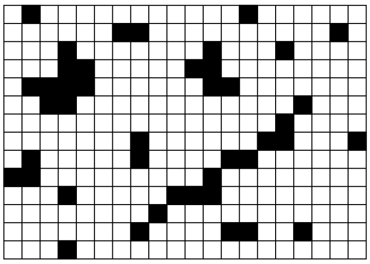

Figure 4.34: Schematic view of a typical charge distribution over the CCD pixels. The few keV X-rays produce the single and double pixel events. Higher energy X-rays originate larger clusters according to their energy. Tracks along the CCD area are created by high energetic particles.

Therefore, a cluster analysis is mandatory to separate the “good events” from higher order clusters and reduce the background. The CSDCLUSTER program, used in the raw data processing, separates the data by cluster size allowing not only the correct treatment of the few keV X-rays but also higher energy X-rays (5-12 keV) which produces clusters of 5-15 pixels.

The huge impact of the cluster analysis on reduction of the background of the μH data can be seen in figure 4.35 which shows the energy spectrum of one of the CCDs. The reduction is about a factor of 1000.

However, in the case of the ECRIT, the source intensity is so high that a great number of "good" events is registered in contiguous pixels which would be wrongly identified as clusters. Consequently, the cluster analysis would lead to a dramatic reduction in the peak intensity and it should be turned off. In fact, a reduction to about 25% of the total peak intensity was seen by using cluster analysis. Therefore, the illumination was arranged in the way that only a few percent of the pixels were hit per frame.

Energy cuts

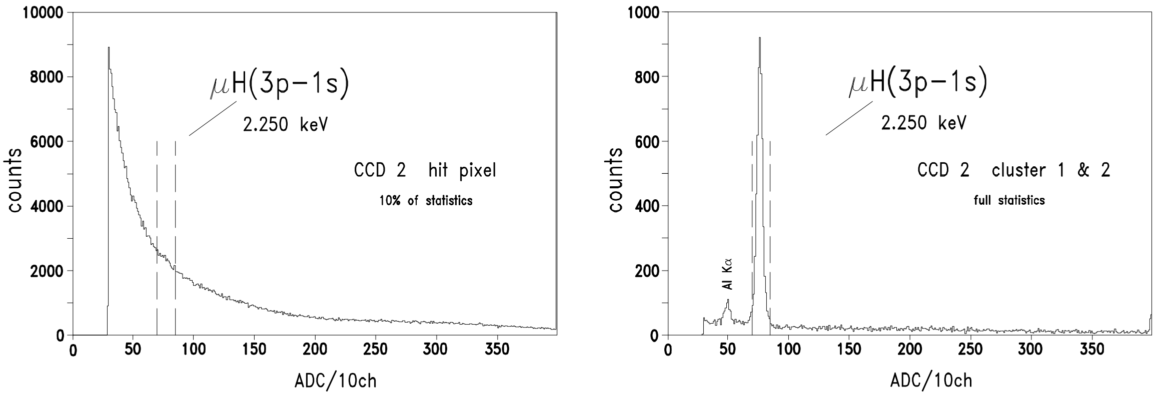

Figure 4.35: Examples of the energy spectra for one of the CCDs obtained during the measurement of the μH$(3p-1s)$ X-rays: at the left before cluster analysis and at the right by considering only clusters with 1 and 2 pixels. The energy spectrum presented at the left has only 10% of the statistics. The selected energy cuts are indicated by dashed vertical lines. A binning factor of 10 was applied. Each ADC channel corresponds roughly to 3 eV for CCD2.

Further background reduction is achieved by applying energy cuts to the raw data. The cuts are set according to the energy region of interest by inspecting the energy spectra. This is done individually for each CCD as the gain is slightly different. A previous energy calibration with a 6 keV ^{55}Fe source determines the gain and the noise level for each chip.

Figure 4.35 shows how the energy cuts are selected from the energy spectra of the CCDs. All pixels which contained charge corresponding to an energy out of the region of interest are rejected.

Bad pixel map

Another feature that must be taken into account are the damaged, faulty pixels. In case of internal damage, pixels can contain charge without being hit by a photon. These are called “hot pixels” and have to be rejected in the analysis. This is done by setting a minimum number of hits which declares a pixel as faulty and registering its position in a bad pixel map (BPM). The threshold was set in an iterative way. After a first BPM has been created, the effects on the spectrum should be checked, and the threshold for the BPM changed accordingly until a good compromise between the background reduction and the losses of good events is achieved.

Relative position and orientation of the CCDs

The position and orientation of the CCDs relative to each other is also considered in the raw data processing. This was measured by a dedicated experiment [105] and serves as input in CSDCLUSTER which processes the respective corrections of the spectra.

Curvature correction

To produce a correct position spectrum a curvature correction must be performed. As described in section 4.2 the spherical profile of the crystal induces an image at the detector plane which has a curved shape leading to a broadening of the one-dimensional spectra.

The CSDCLUSTER parameterizes the curve by a second order polynomial and uses the algorithm referred to on page 71 to restore the line shape. Inside the program this needs to be done iteratively. A first parameterization of the curve is performed after a selection of the region of interest. In a second step, a narrowed region aligned with the curved reflection is selected and the parameterization is redone until it converges. Figure 4.36 shows an example of a curvature correction done with CSDCLUSTER.

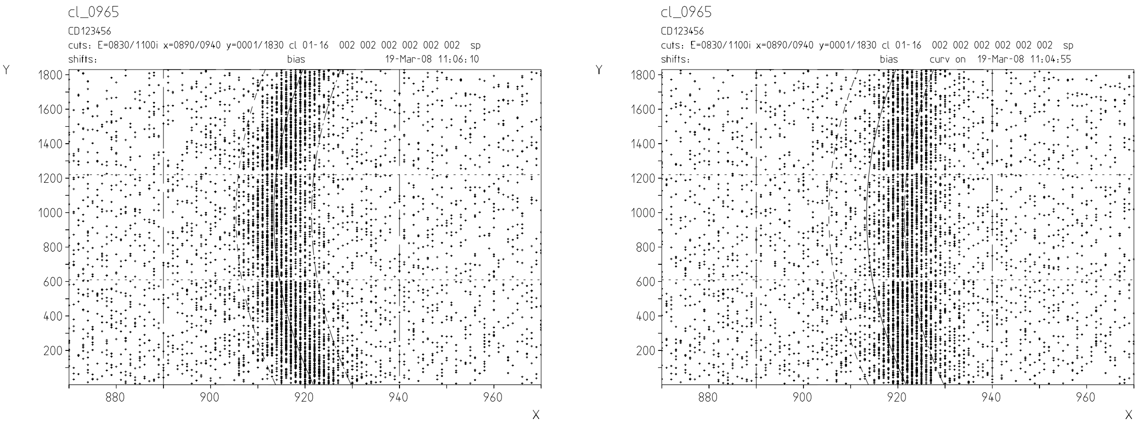

Figure 4.36: An example of the curvature correction using the CSDCLUSTER program is shown for the He-like Chlorine M1 line. At the left the two-dimensional spectrum of the line before the curvature correction and at the right after the correction. The long dashed vertical lines limit the region of interest selected for the first iteration. The short dashed curved lines limit the region of interest for the next parametrization iterations. The solid curved line defines the curvature of the M1 reflection. The horizontal dashed lines are the limits of the 3 CCDs where the spectral line is.

Multiple hit analysis

In the presence of a relatively intense source, the exposure time might be too long and it is possible that during a frame a pixel is hit more than once by photons with similar energy. In this situation the energy deposited in the pixel is double and according to the energy cuts discrimination the pixel will not be taken into account to build the position spectrum.

Multiple hits are negligible in the exotic atom experiments (less than 1 good event per frame) but it was seen to contribute to a loss up to 15% of the statistics in the ECR ion trap experiment (about 100 good events per frame). Accordingly, a double and even triple hit analysis should be performed. The double and triple hit spectrum is obtained by setting the energy cuts around the double and triple energy of interest, respectively. The final position spectrum is the sum of the single hit spectrum with twice the double hit spectrum and three times the triple hit spectrum. Figure 4.37 shows an example of a spectrum with multiple hit events obtained during the ECRIT data acquisition.

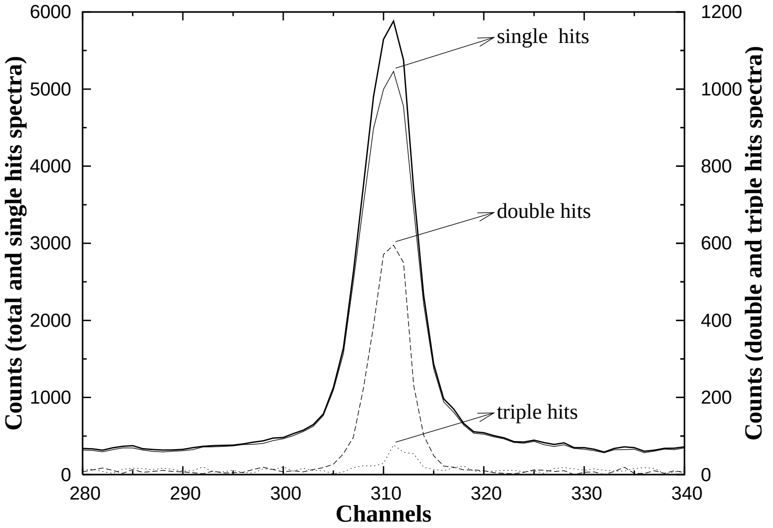

Figure 4.37: The spectrum of the M1 transition in He-like argon is shown in solid bold. The spectra of the single, double and triple hits are depicted for comparison in solid, dashed and dotted lines, respectively. The double and triple hit spectra are depicted with respect to the right y-axis. The double and triple hit events corresponds to approximately 11% of the total spectrum.

Chapter 5

Characterization of the Si(111) bent crystal labeled Z13

The characterization of the bent crystals used in the Bragg crystal spectrometer is a key issue of the high precision spectroscopy in both pionic and muonic experiments at PSI [77, 108, 116].

One of the fundamental aspects is to determine the response function of the crystal at the energies of interest, which, as discussed in section 4.2.4, needs to be experimentally done by using appropriated X-ray lines. The knowledge of the response function of the crystal will allow to unfold the kinetic energy effect in the μH$(3p-1s)$ spectrum which constitutes an important step in the πH(Γ_{1s}) analysis.

An electron cyclotron resonance ion trap (ECRIT) was set up to determine the response function of the crystals which were used in the pionic and muonic hydrogen measurements. The Si(111) crystal named Z13 was the one used to measure the μH$(3p-1s)$ X-ray transition. In the present chapter, the ECRIT device is described as well as the experimental strategy and analysis to pin down the response function of Z13 at the μH$(3p-1s)$ transition energy.

However, during the first data analysis some difficulties emerged to interpret the results. An incorrect mechanical setting by a few millimeters from the assembling of the vacuum tubes and other mechanical elements was considered as a possible source of error. An accurate measurement by optical means was performed to determine the distance between the crystal and the linear table on which the detector moves. It resulted in the exclusion of this possibility.

As consequence, alternative explanations were sought and further investigations of the crystal properties were taken up. A check of the value for the crystal radii provided by *Carl Zeiss*® was considered. Moreover, the possibility that the crystal surface might not be parallel to the Bragg planes was additionally taken more seriously.

Indeed, the orientation of the Bragg planes to the crystal surface and its radius of curvature can constrain the focal position of the spectrometer and lead to a detector misplacement. However, despite these items were not considered during the former μH and πH measurements, any possible correction can be posteriorly applied. The crystals were always placed in the holder with the same orientation. Furthermore, the accurate knowledge of these two parameters can avoid such errors in future experiments.

Hence, the full characterization of the Si(111) crystal entails the determination of its response function, the relative orientation of the Bragg planes to the surface and its curvature.

In the present chapter the asymmetric cut angle is discussed in detail. The value for the curvature radius obtained from the ECRIT data analysis is a byproduct and is compared to an optical measurement and the value provided by the manufacturer *Carl Zeiss*®.

5.1 The ECRIT experiment

In order to determine the response function of a crystal at a certain energy, the measurement of an X-ray line with a similar energy and considerably smaller width than the expected response function is mandatory. This excludes the use of fluorescence X-rays which have natural line widths of the order of eV, incompatible with the few hundreds of meV of the expected response function of the spectrometer [102]. In contrast, exotic atoms can provide suitable lines. For instance, the natural width of the πNe($6h \rightarrow 5g$) transition ($\approx$ 4.5 keV) is 12 meV [117]. However, the poor count rate and the high statistics needed render the results difficult to interpret.

Alternatively, Electron Cyclotron Resonance (ECR) ion sources can provide very intense X-ray lines, from highly charged ions, with suitable natural width. The M1 transitions in He-like ions formed with low to medium Z atoms are lines having an energy of a few keV and negligible natural width ($<<$ 1meV [108]). Moreover, positive ions have a rather small kinetic energy inside the ECR ion source ($<$ 1 eV [106]), which for X-ray energies around 3 keV leads to a Doppler broadening less than 50 meV (one order of magnitude smaller than the expected response function).

In He-like ions the magnetic-dipole transitions (M1) are clean lines because neighboring satellite lines, which could influence the line shape, have low intensity. The M1 from He-like ions produced in ECR ion sources are therefore perfect candidates to determine the response function of Bragg crystals in the few keV range. In figure 5.1 an illustration of the decay scheme of the He-like ions with medium Z is given.

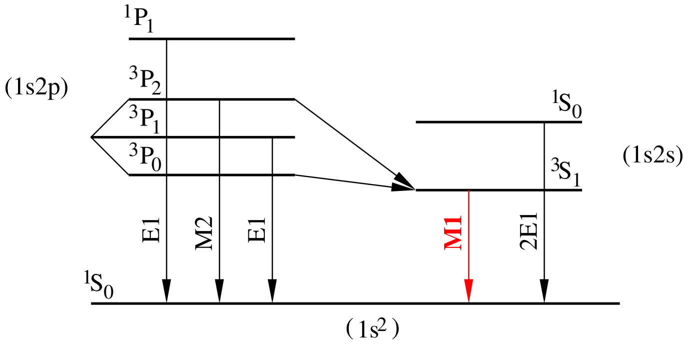

Figure 5.1: Illustration of the decay scheme of the $1s2p$ and $1s2s$ states in He-like ions.

5.1.1 Electron Cyclotron Resonance Ion Sources and Traps

The first electron cyclotron resonance ion source (ECRIS) was developed in 1971 by *R. Geller* and his collaborators [118] to produce high intensity ion beams of highly charged states. An atomic plasma created by the electron cyclotron resonance of free electrons and confined inside a magnetic field can be used as well as an intense X-ray source.

The ECR ion sources became a relatively low-cost apparatus and are used in many accelerator machines. Moreover, together with a high resolution spectrometer the ECR ion sources allow a wide range of spectroscopy studies in atomic, plasma and ion-surface interaction physics. Commercial versions of ECR ion sources are available [119, 120].

The core of the ECR ion source is a vacuum chamber, which acts as microwave cavity, embedded in two groups of magnets: two solenoids magnets and a multipole magnet (see figure 5.2). The free electrons present inside the chamber are accelerated by high frequency radiation. These high energetic electrons collide with the surrounding atoms and induce a very strong ionization by progressively stripping the atoms from their electrons. The plasma is formed by the free electrons and the highly charged ions in many different charge states. The ions can be extracted from the plasma by applying a high potential to the vacuum chamber, creating a highly charged ion beam.

The axial confinement is determined by a longitudinal so-called mirror field which can be obtained with two sets of solenoids or permanent magnets (fig. 5.2). Along the chamber axis, the magnetic field has a minimum value at the center of the vacuum chamber and two maxima which define the limits of the confinement.

To confine the electrons radially, a hexapole or other multipole structure is used. The multipole, generally made of rare earth permanent magnets, induces a radial

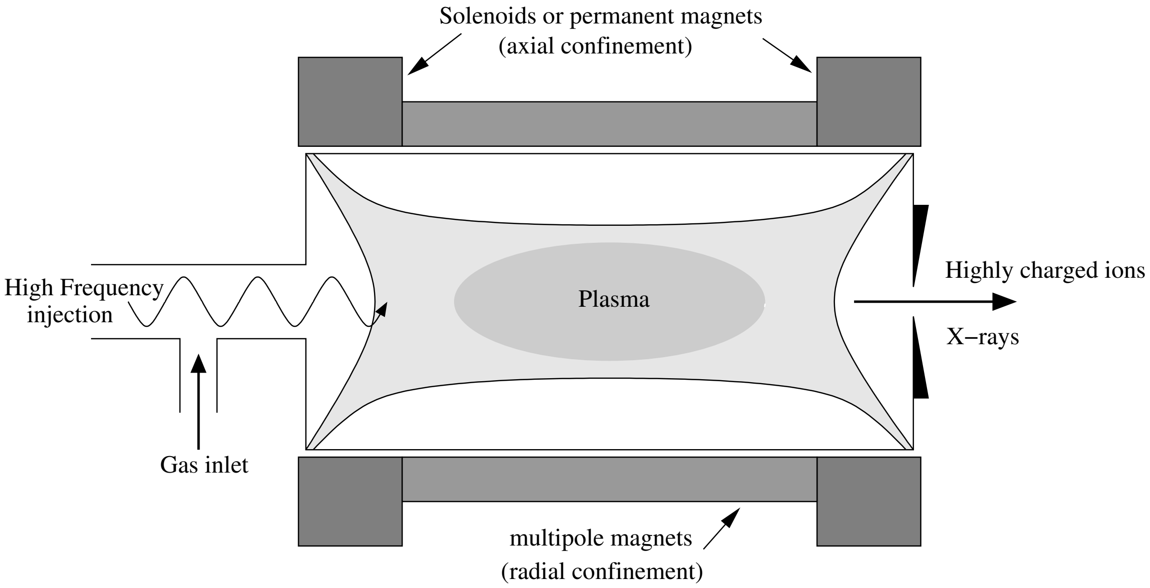

Figure 5.2: General scheme of an ECR ion source. The two sets of magnets generate a magnetic bottle which confines the plasma (electrons plus ions). The highly charged ions generate X-rays with different energies from the various transitions available. By applying an electric field, the ions can be extracted into a highly charged ion beam.

magnetic field with a minimum at the longitudinal axis of the chamber. In figure 5.3 an illustration of the magnetic field along the vacuum chamber axis is shown together with the radial field lines created by a hexapole element.

The basics of the particle confinement can be worked out by taking the geometry of the magnetic field (B) which is generated only by the two coils (see figure 5.4). This is the simpler magnetic confinement and it is named *magnetic bottle* or *magnetic mirror* which traps the particles in a "magnetic well" (figure 5.3).

In the absence of an electric field ($\vec{E} = 0$), a particle with charge q and a velocity $v_\perp$, perpendicular to a uniform magnetic field $\vec{B}$ experiences a force given by:

$$F_B = qv_\perp B \tag{5.1}$$

As the magnetic force is perpendicular both to the velocity and to the magnetic field, the charged particle will move in a circular orbit "tied" to a magnetic field line. The radius of this gyro-orbit is called *cyclotron radius*, *gyroradius* or *Larmor radius* and is given by:

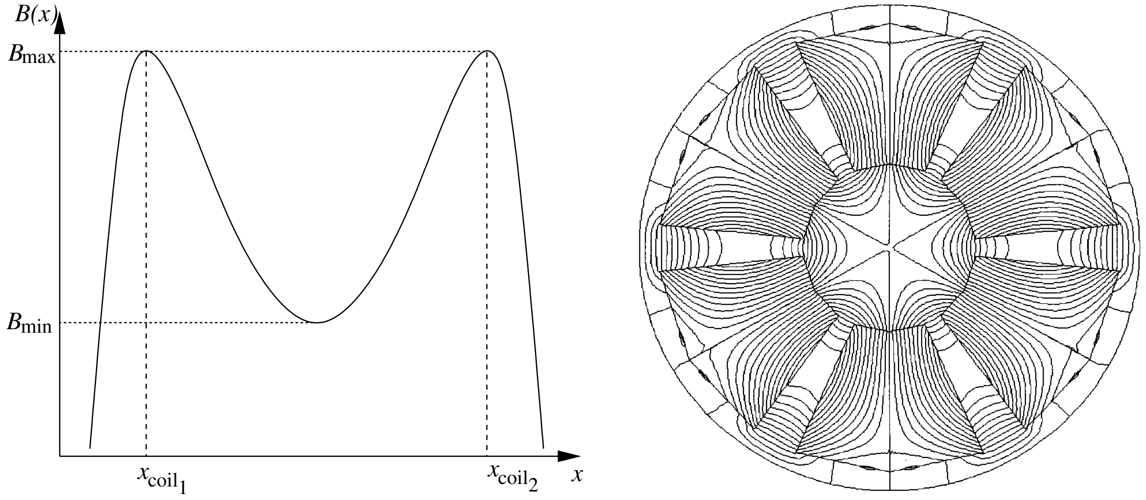

Figure 5.3: At the left the general shape of the magnetic field (B) along the longitudinal axis of the ECR ion source is depicted. B is maximum at the axial coordinate of the coils and minimum at the half distance between them. At the right, an example of the radial B-field lines created by a hexapole is depicted [124]. The field is minimum at the center.

$$\rho_L = \frac{mv_\perp}{|q|B} \tag{5.2}$$

where m is the mass of the particle with charge q. By taking the energy in eV and the magnetic field in kG, the Larmor radius can be rewritten in centimeters for electrons and ions [119]:

$$\rho_L^e = 0.0035\frac{\sqrt{E_e}}{B}[\mathrm{cm}] \tag{5.3}$$

$$\rho_L^i = 0.16\frac{\sqrt{AE_i}}{z^+B}[\mathrm{cm}] \tag{5.4}$$

A and z^+ being the atomic number and the ion charge state, respectively. For the same energy and field strength the Larmor radius is much smaller for the electron as it scales with the square root of the mass ratio. For instance, in a ECR ion source, by considering a typically mean energy of 10 eV and a minimum field of 2 kG, the electrons have a mean Larmor radius of about 0.06 mm and a Ar^{+16} about 0.9 mm. It should be pointed that at the beginning of the ionization process the Larmor radius is much larger. For instance, an Ar^{+1} ion (E_K =10 eV) will have a mean Larmor radius close to 15 mm. Consequently, only the ions with low kinetic energies will remain inside the magnetic mirror and suffer further ionization. This helps to explain the observed small kinetic energies of the positive ions inside the ECR ion source (< 1 eV [106]).

If the charged particle has a velocity with an arbitrary orientation to the magnetic field the resulting trajectory is a helix and the velocity can be subdivided in two components:

$$v = v_\perp + v_\parallel \tag{5.5}$$

where $v_\parallel$ is the component parallel to $\vec{B}$ and $v_\perp$ is perpendicular to $\vec{B}$. Considering a magnetic field along the x direction: $v_\perp = \sqrt{v_y^2 + v_z^2}$ and $v_\parallel = v_x$. The magnetic force $q\vec{v} \otimes \vec{B}$ causes the components of the perpendicular velocity to change in time but the parallel component remains constant. On the other hand, the perpendicular velocity defines a magnetic moment given by:

$$\mu_p = \frac{mv_\perp^2}{2B} = \frac{E_{K\perp}}{B} \tag{5.6}$$

$E_{K\perp}$ being the perpendicular component of the kinetic energy.

Despite the magnetic field in a magnetic bottle is not constant in space, it varies slowly and several adiabatic invariants can be defined. An adiabatic invariant follows from considering an action integral of a mechanical system. If p_i and q_i are the generalized canonical momenta and coordinates, for each coordinate which is periodic the action integral J_i is defined by:

$$J_i = \oint p_i dq_i \tag{5.7}$$

with the integration being calculated over a complete cycle of the coordinate q_i. The action integrals of a system are constant. Moreover, if the properties of the system which are not related with the periods of motion are changed slowly compared to these periods, the action integrals remain also constant [136]. Such changes are called *adiabatic changes.*

In the case of a charged particle inside a magnetic bottle, the action integral for the gyro-motion is:

$$J = \oint \vec{p}_\perp d\vec{\rho}_L \tag{5.8}$$

where $\vec{\rho}_L$ is the canonical coordinate ($|\vec{\rho}_L| = \rho_L$) and $\vec{p}_\perp$ the perpendicular component of the canonical momentum $\vec{p} = m\vec{v} + q\vec{A}$, with $\vec{A}$ being the magnetic vector potential. By performing the integration over the circular path $2\pi\rho_L$ the action integral will be (*Jackson* section 12.6 [137]):

$$J = \pi|q|B\rho_L^2 = \frac{\pi}{|q|}\frac{p_\perp^2}{B} = \frac{2\pi m}{|q|}\mu_p \tag{5.9}$$

The adiabatic invariance of J means that the flux of the magnetic field through the surface defined by the gyro-motion is constant. Therefore, if B varies slowly in space the Larmor radius will increase according to (5.9). Hence, the quantities $B\rho_L^2$, $p_\perp^2/B$ and μ_p are adiabatic constants.

Admitting in first approximation that the charged particles inside the magnetic bottle move without collisions in vacuum and without external forces, the total kinetic energy is constant during their helical trajectory around the field lines. The particles can not gain energy from a non-time-varying field and the total energy has only a kinetic component:

$$E = E_{K\|} + E_{K\perp} = \frac{1}{2}m(v_\|^2 + v_\perp^2) \tag{5.10}$$

The adiabatic constants of the movement (5.9) require that as B varies along the field lines $v_\perp$ changes accordingly by transfering the kinetic energy between its parallel and perpendicular components.

The magnetic field is minimum at the middle point between the coils and maximum at the axial position of the coils. Moving from the center towards the coils, the charged particles face the increase of B by increasing $v_\perp$ and reducing $v_\|$. When $v_\|$ reaches zero, the particle stops its longitudinal movement, changes its direction and is reflected in the direction of the minimum B. Therefore, it can not access regions where $B > E/\mu_p$. The bouncing condition $v_\| = 0$ at the B maximum position defines the confinement:

$$\mu_p > \mu_{trap} = \frac{E}{B_{max}} \tag{5.11}$$

All particles which satisfy this inequality will be trapped in the field line between the coils. The trapped particles will describe a periodic motion between two points called *mirror points*. By taking μ_p given by equation (5.6) at the central position ($B = B_{min}$) and put it into the inequality (5.11), the confinement condition can be rewritten in terms of the ratio between the velocity components:

$$\frac{|v_\||}{|v_\perp|} < \sqrt{\frac{B_{min}}{B_{max}} - 1} \tag{5.12}$$

This inequality defines a “loss cone” in the velocity space such that any particle in it $\left(v_\perp < \sqrt{\frac{B_{min}}{B_{max}} - 1}\ v_\|\right)$ will not be bounced at the mirror point and will escape from the system.

The quantity B_{min}/B_{max} is named *mirror ratio* and is a characteristic of the ECR ion sources. Higher values define an higher efficiency of the electron confinement. Depending on the magnets’ characteristics, the mirror ratio ranges typically from 1 to 5. Obviously, charged particles with a velocity parallel or nearly parallel to the magnetic field lines can not be trapped. Moreover, as collisions always occur, some diffusion and scattering out of the magnetic confinement region is expected which leads to some plasma leakage. The figure 5.4 shows a schematic of the magnetic mirror geometry.

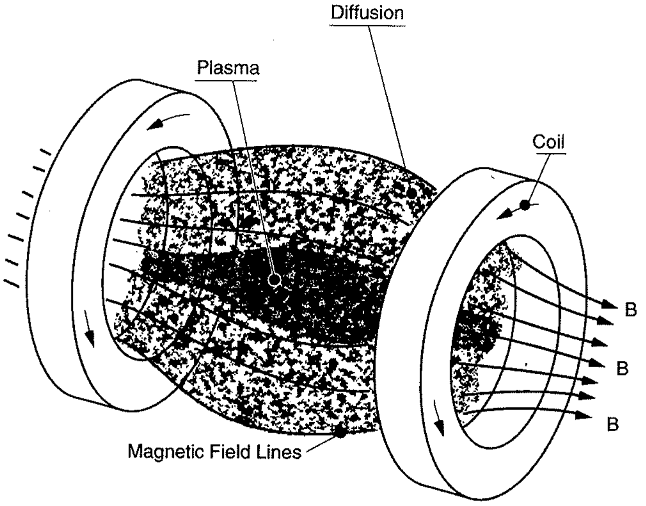

Figure 5.4: The particles are trapped between the magnetic coils along the B field lines creating the plasma. However, the geometry also exhibits some drifting across the field lines [119].

In fact the plasma confinement is even more complex and implies a strong diffusion. The plasma is a kind of fluid and does not behave like free particles. The concave shape oriented inwards (figure 5.4) results in possible plasma instabilities. To create an extended B minimum region destroying that bad curvature shape solves the problem. This can be done by inserting a hexapole in between the coils. The hexapole modifies the concavity of the field lines which become outwards oriented (see fig 5.2) and leads to plasma stability. This type of confinement (axial+radial) is named *minimum-B* configuration [119].

The magnetic field inside the chamber is a superposition of both axial and radial magnetic fields. For a given magnetic field $\vec{B}$, the electrons have a cyclotron resonance frequency from their gyro-motion defined by:

$$\omega_c = \frac{eB}{m_e} \tag{5.13}$$

where e and m_e are the charge and mass of the electron. In order to accelerate the electrons and induce the gas ionization, an electromagnetic wave with a high frequency (HF) which matches ω_c is injected inside the chamber. It is clear that the resonance state is only achieved on a magnetic equipotential surface. The fast electrons, confined inside the magnetic bottle, periodically cross the resonance surface which favors the confinement as they are accelerated in the direction perpendicular to the magnetic field [119]. The stronger the magnetic field, the higher is the resonance frequency of the electrons which is matched by the HF, leading to larger plasma density and ionization possibilities [121]. A resonance frequency of the order of 5-20 GHz (microwaves) matches a typical magnetic field of 0.2-0.8 T.

Nested shells of resonance surfaces can be produced by injecting different HF which increases the probability to heat up the electrons [124, 123]. Higher HF will match resonance frequencies in the outer regions where the magnetic field is higher.

The density of free electrons in the plasma can be enhanced by inserting an electron donator inside the vacuum chamber. That can be accomplished with a polarized electrode or by coating the chamber walls with a secondary-electron emitter as alumina, for instance [122]. The ionization of the injected gas is a collisional process and can be described by:

$$X^{n+} + e^- \rightarrow X^{(n+1)+} + 2e^- \tag{5.14}$$

Obviously, the kinetic energy of the electrons should be at least equal to the ionization energy of the X^{n+} ion to obtain the next ionization level $X^{(n+1)+}$. Taking argon as an example, to obtain Ar^{17+} a population of “hot” electrons with kinetic energy of at least 4.12 keV (ionization energy of the Ar^{16+}) should exist in the plasma.

In the plasma region coexist different populations of particles: cold ions, hot electrons and the thermal electrons. The cold electrons are mainly present in the outer regions of the plasma and the hot electrons in the plasma core. The particles can gain kinetic energy from collisional processes and be scattered into the loss cone, leaving the plasma region. The frequency of the collisions between electrons is similar to the one of electron-ion collisions and different from the frequency of the ion-ion collisions ($\upsilon_{ee} \approx \upsilon_{ei} \neq \upsilon_{ii}$) [119]. Therefore, a plasma potential is created by the difference in the collision frequencies.

In the outer regions $\upsilon_{ei} > \upsilon_{ii}$ is valid and the thermal electrons are more easily scattered into the loss cone which builds up a positive potential of the order of few tens of volts [119]. This potential traps the thermal electrons and balances the electron losses. On the other hand, at the plasma center $\upsilon_{ii} > \upsilon_{ei}$ is valid resulting in the fast scattering of the ions into the loss cone. Therefore, a depression in the plasma potential is created by the hot electrons which attract the positive ions into this region. The system is kept in equilibrium by ambipolar mechanisms. Figure 5.5 shows the typical shape of the plasma potential.

The number of highly charged ions produced from the main gas can be further enhanced by adding a lighter gas into the plasma. Using again argon as example, oxygen gives the best results as support gas [120, 138], in particular the heavier isotope ^{18}O. Compared to oxygen ^{16}O, ^{18}O leads to an increase of about 25% in the Ar^{14+} ion population inside the plasma [138].

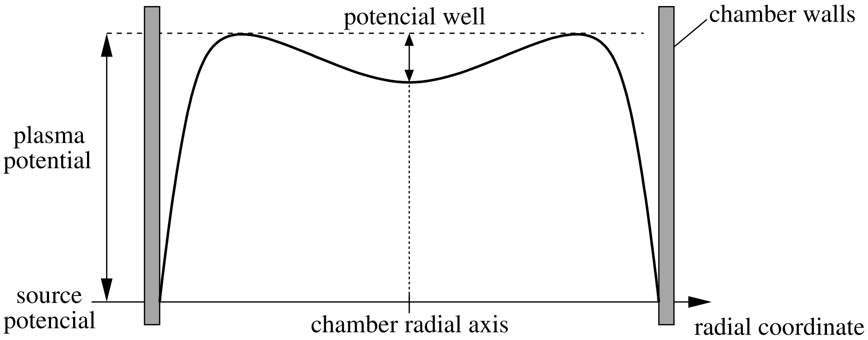

Figure 5.5: Typical shape of the plasma potential due to the electrons and positive ions distribution. The hot electrons are trapped closer to the axis and create a potential well which attracts the ions towards the center [119].

This gas mixing effect is explained by the cooling of the heavier ions by the low mass ions. Therefore, it increases the confinement time of the ions from the main gas and maximizes the probability of additional collisions with the electrons and higher ionization levels. This explanation is most widely accepted [122].

The gas pressure ranges typically between 10^{-5} to 10^{-7} mbar depending on the application. Lower pressures avoid electron recombination with the ions and sustain the production of highly charged ions. On the other hand, higher pressures are used to obtain an intense beam from low charged ions.

5.1.2 Experimental setup

By modifying the existent cyclotron trap, used in the exotic atom experiments, it was possible to achieve an ECR ion trap configuration (ECRIT). Special iron blocks were inserted (field forming iron in figure 5.6) and a NdFeB hexapole magnet (AECR-U-style) with an open structure was brought inside the vacuum chamber (see figure 5.6). A 6.4 GHz power regulated emitter provided the HF waves needed [123].

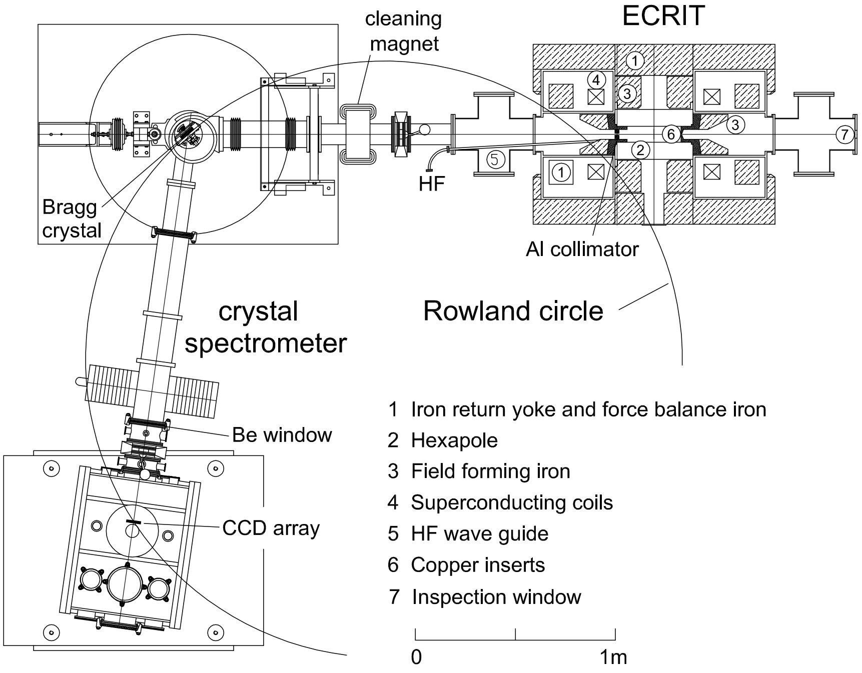

Figure 5.6: Schematic of the setup with the main parts of the ECRIT indicated.

The hexapole is 300 mm long and has an inner diameter of 90 mm and an outer diameter of 240 mm. The permanent field at its inner faces (radius=45 mm) is about 1.2-1.4 T [124]. The hexapole was cooled by a continuous and forced flow of demineralised water. A stainless steel tube with an inner diameter of 85 mm, 0.4 mm thick and a length of 265 mm which is limited by copper insertions comprised the plasma chamber. The tube was perforated at the hexapole gaps by a series of 2.5 mm diameter holes to increase the conductance of the vacuum pumping.

The magnetic field parameters of this ECRIT configuration guaranteed a mirror ratio of about 4.3 along the chamber. This very high ratio ensures a high efficiency of the electron confinement and consequently a high ionization probability. A copper insertion guided the HF into the plasma chamber.

Three turbomolecular pumps and a cryogenic pump (1000 $\mathrm{l \cdot s^{-1}}$) provided a reference pressure (without plasma) inside the chamber of about 3×10^{-8} mbar. The gas injection was done radially by UHV precision leak valves through the gaps of the open structure of the hexapole and the surveillance of the gas mixture was performed by a quadrupole mass spectrometer.

As main gases, Ar, $CHClF_2$ and SO_2 were used to produce highly charged argon, chlorine and sulphur, respectively. Molecular oxygen was employed as support gas with a mixing ratio around 1:9 [102]. The total pressure inside the plasma chamber was about 3...4.5×10^{-7} mbar.

The Bragg spectrometer equipped with a Si or Qu crystal, the detection system (described in section 4.4) and a cleaning magnet placed at about 1 m of the crystal position complete the setup. The magnet was installed in order to reduce the background caused by a huge amount of high energetic electrons seen in first ECRIT operations [102]. The distance between the center of the trap and the crystal was about 2200 mm. The length of the vacuum tubes connecting the crystal chamber with the detector cryostat was varied to fulfill the focusing condition for each He-like M1 transition.

A beryllium window (not depicted in figure 5.6) was placed between the cleaning magnet and the valve which couples the ECRIT to the spectrometer (near the HF guide in figure 5.6). The window separated the vacuum in the spectrometer from the plasma pressure inside the ECRIT chamber. A bypass system (also not depicted in figure 5.6) ensured that the window does not explode when the spectrometer is vented and the valve closed.

The CCD detector was protected against the plasma light by a 30 μm thick beryllium window installed in front of the CCD cryostat. In order to reduce the background and avoid the CCDs overloading, a collimator made of copper in a frame of densimet®(machinable tungsten alloy) was placed 150 mm away from the chamber center. Aperture windows of 28 mm(h)×4 mm(v) for argon and 28 mm(h)×1 mm(v) for the other two gases were used. To control the exposed area of the crystal, several aluminum apertures with circular and rectangular shapes and different opening dimensions were available to be placed in front of the crystal.

Some important aspects of the ECRIT setup are resumed in the table 5.1.

Gas	M1 He-like	E [eV]	θ_B [degrees]	Θ_{ARM} [degrees]	dispersion [pixel·eV^{-1}]	$R_c \sin\theta_B$ [mm]	Cry-LTab [mm]
Ar	Ar	3104.18	39.5635	79.12	12.66	1899.5	1855
$CHClF_2$	Cl	2756.85	45.8221	91.64	19.96	2138.8	2100
SO_4	S	2430.34	54.4424	108.88	34.95	2426.1	2349

Table 5.1: Some important aspects of the ECRIT setup with the Si(111) crystal. The value measured at *Zeiss*® for R_c (2982.2 mm) together with the lattice spacing of Si(111) ($d = 6.2708322$ Å) from XOP[84] were used in the calculations.

5.1.3 Spectrometer alignment and source tuning

Alignment

Despite the spectrometer being equipped with very accurate angle encoders, it can not be set to a specific absolute angle. For Johan type spectrometers the absolute energy calibration is done by comparison to a well know calibration line. Thus, a reference spectral line, whose Bragg angle is known, should be found first.

In practice the spectrometer mechanics was first set up at an angle close to the Bragg angle corresponding to the spectral line which would be used as reference. The reflection condition of the crystal was established by means of a laser: a general purpose laser was flanged to the trap so that it shone along the longitudinal axis of the trap; the crystal holder was kept loose and manually adjusted; when hit at its center the crystal should reflect the incoming beam along the longitudinal axis of the vacuum tubes which connected the crystal chamber to the detector's cryostat; once this condition was met the holder was fixed.

After a M1 X-ray line was identified, the spectrometer was arranged in order to place the M1 line in the middle of one of the two CCD columns of the detector.

A vertical alignment of the M1 line was additionally performed. This was done by tilting the crystal so that the reflection is vertically centered at the detector. In order to simplify the alignment, the height of the M1 reflection was reduced such that the whole vertical extension of the line would be "seen" by the detector. This was accomplished by limiting the height of the active area of the crystal to 20 mm with an appropriate aluminum plate.

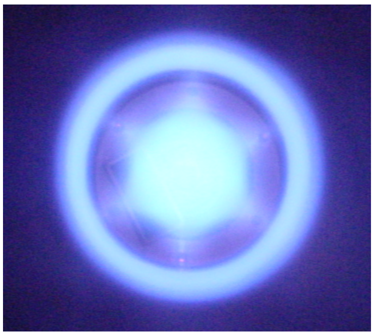

Figure 5.7: Picture of the plasma star inside the ECRIT chamber. The ions follow the field lines of the hexapole (see figure 5.3 on page 103).

HF power and total pressure scan

A careful tuning of the HF power and the pressure of the gases inside the chamber was performed in order to maximize the X-ray intensity without compromising the stability of the source. These conditions were first tuned by visual inspection to initiate the plasma production inside the chamber (see figure 5.7).

Afterwards, the impact of the total pressure and the HF power on the M1 intensity was studied. Only one parameter was varied at each scan. The total pressure was changed either by varying the pressure of the main gas or the pressure of the support gas (O_2). Figure 5.8 shows some examples of the HF power and total pressure scans. As expected, a strong dependence of the M1 intensity both on total pressure and on HF power is seen.

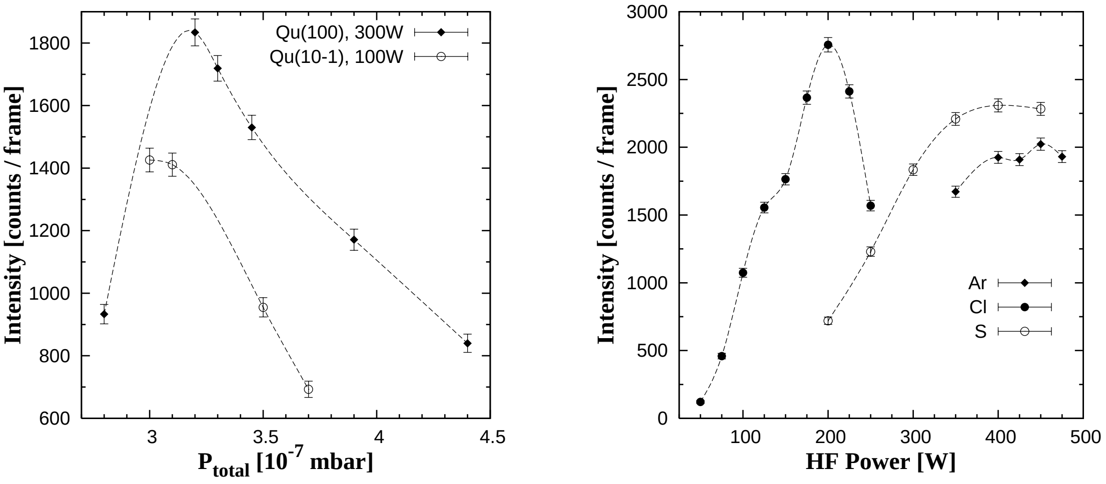

Figure 5.8: Typical pressure and power scans. The total pressure scans shown were obtained with sulfur. A direct comparison of the intensities should not be done as the experimental conditions were different: in one case a Qu($10\bar{1}$) crystal and HF power of 100 W were used and in the other a Qu(100) crystal and a HF power set to 300 W. The same holds for the the power scans. The argon scan was obtained with a Qu($10\bar{1}$) crystal and a total pressure about $4.3{\times}10^{-7}$ mbar. The chlorine and sulfur data were both collected with the total pressure set to $3.2{\times}10^{-7}$ mbar using a Si(111) and a Qu(100) crystal, respectively. The argon and chlorine data were scaled by a factor 6 and 2, respectively. The dashed lines serve to guide the eye.

An optimum total pressure of about $3...4.5{\times}10^{-7}$ mbar was found for all three main gases (Ar, Cl and S), with some small variations from different HF power. The pressure of the main gas inside the chamber was one order of magnitude higher than for oxygen.

The intensity of the M1 lines increases with power followed by saturation or fast drop (see figure 5.8). The increase in power leads to a higher number of energetic electrons, however it also increases the probability that some electrons escape from scattering. After a certain value, a greater fraction of the high energetic electrons produced escape and consequently less highly charge states are created. In the case of the argon, the plasma was getting unstable at powers close to 500 W.

The ionization energies of $2s$ state electrons of the Li-like argon, chlorine and sulfur are about 918, 809 and 707 eV [139], respectively. An increase of the HF power with the ionization energy would be expected as higher energetic electrons are needed to strip the Li-like ions from its 2s electron. The final He-like ions could later be excited to higher spin-orbit coupling states and deexcitate via a M1 transition to the ground state.

In fact, this idea did not hold. Sulfur showed a similar result as argon, both with the double of the optimum power of chlorine. That might be related to the injection of molecular gases inside the ECRIT to obtain the He-like chlorine and sulfur. The presence of extra atoms could modify the plasma dynamics. However, the results can not be easily compared as the chamber conditions might have changed every time the main gas was changed and the ECRIT vented. Moreover, an improvement of the intensity with time was also registered which was attributed to the cleaner environment inside the plasma chamber.

Scan of the longitudinal B field

The dependence of the intensity of the M1 transition on the current of the superconducting coils was additionally studied. For the present work the current was initially set to 50 A. A fine tuning was performed by changing it in steps of 0.25 A up to 52.75 A. Figure 5.9 shows a non-trivial dependence. Within the studied range, the M1 intensity oscillates between two distinct maxima and a minimum.

As already mentioned before, the resonance condition (5.13) is only fulfilled in a magnetic equipotential surface which has an ellipsoidal shape [119, 124]. For a certain ω_{HF} injected, it is always possible to find an equipotential surface where the resonance condition is fulfilled if $B_{min} < \frac{m_e}{e}\omega_{HF} < B_{max}$. Therefore, by increasing the magnetic field the plasma only ignites after a threshold is reached: $B \rightarrow B_{max} > \frac{m_e}{e}\omega_{HF}$. On the other hand, the plasma production is cut off when B is too high, i.e. $B \rightarrow B_{mim} > \frac{m_e}{e}\omega_{HF}$.

The dependence shown in figure 5.9 can be explained by the dimensions of the equipotential surfaces. Inside the chamber, the HF wave would behave like a steady wave being reflected at the chamber walls. Therefore, the resonance would be favored if the resonance surface would have dimensions of the HF wavelenght λ_{HF}. A higher number of hot electrons would be generated when the ellipsoid axes matches better λ_{HF} or multiples of it. At the limit, a sphere with a radius equal to $N\lambda_{HF}$ would be ideal. In fact, closer to the chamber center the ellipsoidal surfaces are less extended and more symmetric.

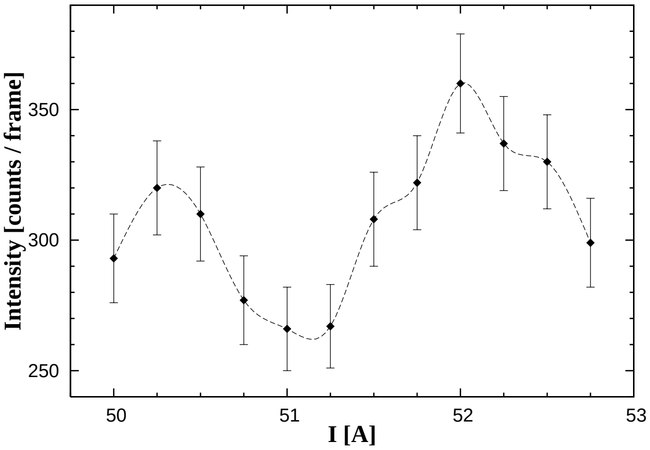

Figure 5.9: The dependence of the He-like Argon M1 intensity on the current intensity of the superconducting coils is depicted. The data was obtained with a Qu(10$\bar{1}$) crystal and a total pressure of about 4.1×10^{-7} mbar. The dashed line is to guide the eye.

Hence, current intensities of about 50.25 A and 52 A in the superconducting coils will lead to magnetic equipotential surfaces, where the resonance condition is fulfilled, which matches better multiples of λ_{HF}. A frequency of 6.4 GHz corresponds to a wavelength of 4.6 cm. The higher the current intensity, the higher the magnetic field and the resonance condition will be fulfilled in a surface closer to the chamber center and consequently more symmetric. This explains the higher M1 intensity for a current of 52 A.

Source scan

The volume of the source which can be “seen” by the crystal depends on the focusing condition as the distance between the target and the crystal is always fixed (2200 mm). Within the ECRIT setup the center of the source was never exactly at the expected focus ($R_c \sin\theta_B$). The distance from the expected focus was approximately -150, 80 and 375 mm for the M1 He-like argon, chlorine and sulfur, respectively*. The active crystal area and the collimator placed in front of the source give additional geometrical constraints. The sketch in figure 5.10 clarifies the ECRIT geometry with respect to the source.

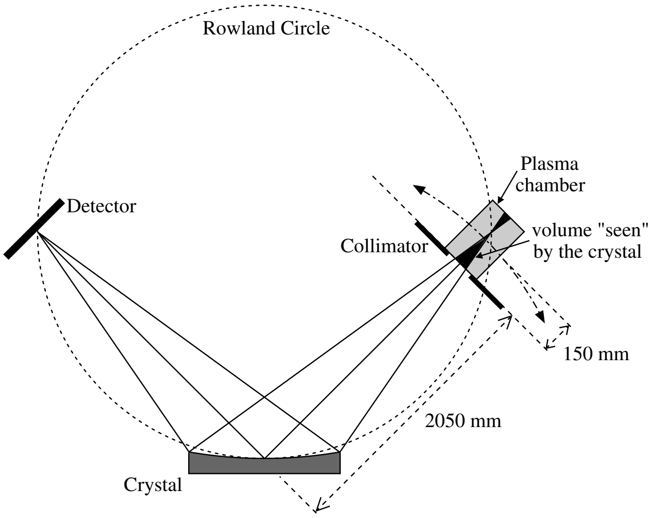

Figure 5.10: Schematic of the ECRIT geometry with respect to the source region “seen” by the crystal. The dimensions of the crystal, source and collimator’s opening are oversized to make the effect visible. The geometrical defocusing is neglected. The dash-dotted arc represents the translation of the source region “seen” by the crystal when detector and crystal are rotated together, i.e. varying Θ_{ARM}.

Moreover, the region of the source which is “seen” by the crystal depends on Θ_{ARM}. Thus, a source scan is another important aspect. When Θ_{ARM} is changed, the detector is rotated together with the crystal, keeping θ_B fixed, and the source region which fulfills the Bragg condition experiences a translation (dash-dotted arc in figure 5.10). By varying Θ_{ARM},the distribution of He-like ions inside the target can be studied

---

*The minus sign indicates the direction away from the crystal, i.e. outside the Rowland circle based on the M1 intensity. The distance to the crystal (2050 mm) and the width (28 mm) of the collimator permits a source scan within a $47'$ range around the nominal $\Theta_{ARM} = 2\theta_B$ (Bragg condition fulfilled at the plasma chamber's center). Figure 5.11 shows two typical source scans obtained.

The figure reveals that the distribution of He-like ions is higher at the center of the plasma chamber and decreases to the outer region. This confirms the possible existence of a highly charged population in the center of the plasma [125].

The source scan obtained with lower HF power shows a practically constant distribution along the scan region. The fast drop at the edges can be due to the collimator edges. The dominant behavior might be explained based on the plasma potential (see page 108 and fig. 5.5). The number of high energetic electrons naturally decreases with the HF power injected which results in a less pronounced depression of the plasma potential at the center. Consequently the attraction force on the positive ions will be weaker resulting in a freer diffusion and smoother distribution.

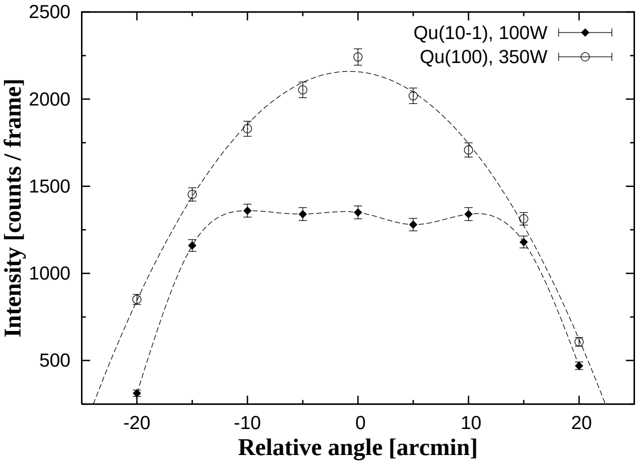

Figure 5.11: Typical source scans with low and high HF injected power. The data was collected with sulfur and a total pressure of 3.2×10^{-7} mbar by using a Qu(100) and Qu($10\bar{1}$) crystals. The data is plotted relative to the nominal $\Theta_{ARM} = 2\theta_B$. The dashed lines are to guide the eye.

As already mentioned, by increasing the HF power, more electrons with high energy are produced but a greater fraction escape by scattering from the outer regions of the plasma. This can also explain the shapes of the target scan. By injecting higher HF power the fraction of positive ions produced in the outer regions is less and the X-ray intensity is higher at the center.

5.1.4 Data acquisition to characterize the crystals

Once the spectrometer and source parameters were optimized, two sets of measurements were performed by changing two different aspects of the geometry: the distance of the detector from the crystal and the active area of the crystal. The analysis of this data will lead to the determination of the response function of the spectrometer at the energies of interest.

The data collected for the studies described in the previous section had just a satisfactory statistics to allow an optimization of the different parameters through an online analysis. Typically, spectra with 5 to 10 frames were sufficient. However, the determination of the response function of the spectrometer requires a more careful analysis, thus higher statistics. At least 40 frames spectra were recorded.

Several spectra were taken with the detector placed at different distances from the expected focus. The position of the detector was changed in steps of 3 mm within a range of 24 mm. Such a focal scan allowed the direct determination of the focal position, reducing the error of a misplacing due to its calculation based on several geometrical parameters. Moreover, it permitted to double check the geometry.

By performing an analysis during the data acquisition of the FWHM of the M1 lines, a first estimation for the focal position could be obtained. Such an analysis was done by fitting a Gaussian profile as the proper analysis could not be done during the run. The final result can only be determined in a refined analysis by using the correct line profile, i.e. response function.

Secondly, the detector was moved to the focal position found and the active area of the crystal was modified by placing aluminum plates with different aperture shapes and sizes in front of it. This allowed a study of the impact of the active crystal area on the response function. Thus, the distribution of the uniformity along the frontal area of the crystal is checked.

An example of a highly charged argon spectrum obtained during the ECRIT measurement is presented in figure 5.12. The most intense transitions from Be-like, Li-like and He-like argon are identified. The spectrum was taken near the focal distance for the M1 transition and the ECRIT and spectrometer optimized to maximize its intensity.

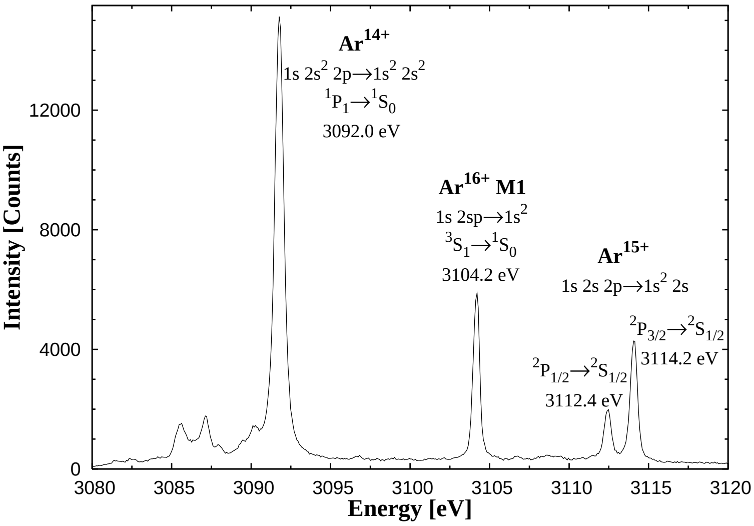

Figure 5.12: Example of a He-like argon spectrum taken with Si(111) near the focal distance of the M1 transition. A rectangular aperture 60 mm wide and 95 mm high was used to limit the reflecting area of the crystal. The experimental conditions were optimized to maximize the M1 intensity. The major transitions are identified according to the energies provided in *Martins et al.* and *Costa et al.* [140, 141]. The energy scale was obtained using the energy dispersion around the M1 transition which is 79 meV·pixel^{-1}.

5.2 Relative orientation of the lattice planes

A crystal disc is produced by cutting it with a saw from crystal material. It is subsequently polished. The process is done in the way the final disc has the optical surface parallel to the desired crystal planes. A deviation from paralelism of less than $1'$ was assumed inside the πH collaboration for long time (until 2005). However, this assumption became increasingly suspicious. The appearance of vertical misalignments of the Bragg reflections after a careful laser alignment was never understood. Moreover, discrepancies from the expected focal lengths, which in some cases reached almost ten millimeters, were also puzzling.

In fact, the precise knowledge of the orientation of the lattice plans may be lost during the disc manufacturing, particularly due to the difficulty of the alignment of the sawing machine. Small errors in the determination of the orientation of the bulk material can also not be excluded. Thus, a detailed investigation of the relative orientation of the lattice planes became mandatory and is described in the following sections.

5.2.1 Miscut in flat crystals

Asymmetrically cut crystals are extensively used in radiation beam lines of synchrotron facilities. They are employed in monochromators in order to modify the beam divergence [127, 126]. The asymmetric cut angle, also named miscut, is characterized by an angle α between the optical surface of the crystal and the lattice planes (see figure 5.13).

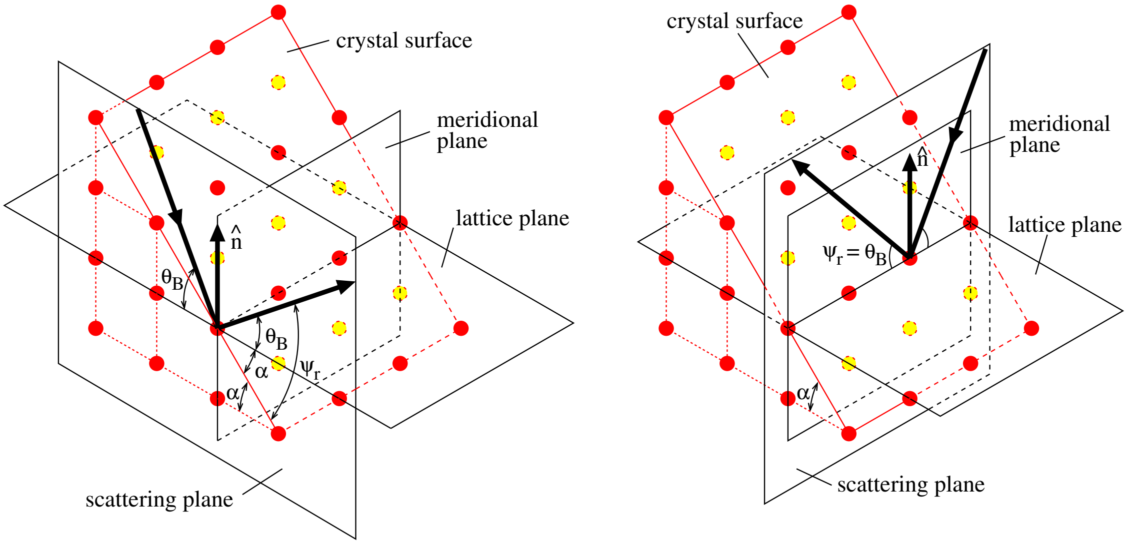

a) b)

Figure 5.13: The figure shows a schematic representation of the Bragg reflection in asymmetric cut crystals. The direction of the scattering vector is indicated by n̂; a) the scattering plane is perpendicular to the meridional plane, the effect of the miscut is maximum and the measured reflected angle will be $\Psi_r = \theta_B + \alpha$; b) the scattering plane is parallel to the meridional plane, no effect is visible, $\Psi_r = \theta_B$.

The Bragg angle is an absolute parameter given by the Bragg condition. However, experimentally it needs a reference plane to be determined. In a flat crystal, the optical surface will be that reference. Hence, if the optical surface is parallel to the lattice planes the angle between a Bragg reflection and the optical surface will coincide with θ_B. This does not hold in the presence of a miscut and the angles are decoupled.

For an asymmetrically cut crystal, the angle between a Bragg reflection and the crystal surface is related with the Bragg angle through:

$$\Psi_r = \theta_B \pm \alpha \tag{5.15}$$

depending on the position of the source relative to the crystal surface. In fact, this is only valid for a particular orientation of the crystallographic planes, i.e., when the plane of dispersion which contains the incoming and reflected beam, is perpendicular to the meridional plane. The meridional plane is defined at each hit point (on the optical surface) to contain the scattering vector (normal to the lattice planes) and the intersection between the surface and the lattice plane. Figure 5.13 clarifies the geometry.

An arbitrary orientation of the incoming beam to the surface plane is equivalent to a rotation around the scattering vector by an angle φ. The effective miscut α' can then be obtained as the projection $\alpha \cos\varphi$ and equation (5.15) generalized accordingly:

$$\Psi_r = \theta_B + \alpha \cos\varphi \tag{5.16}$$

In case the meridional plane is parallel to the scattering plane, which corresponds to $\varphi = 90°$ or $270°$, no effect is seen as $\Psi_r = \theta_B$ (figure 5.13b).

5.2.2 Miscut implications in the Johann geometry

After cutting, the spherically bent crystals are shaped by forcing thin discs into glass lenses previously ground. Therefore, in the presence of an asymmetric cut angle, it is expected that it will be constant over the whole surface of the bent crystal.

In the presence of a miscut, the focal distance given by $R_c sin\theta_B$ is not anymore valid which implies a redefinition of the focal distance to include the orientation of the lattice planes relative to the surface. The Guinier's focusing condition for cylindrically bent crystals [128] establishes that distances between the crystal (C), detector (D) and source (S) are given by (see figure 5.14):

$$\overline{CD} = R_c \sin(\theta_B + \alpha) \tag{5.17}$$

$$\overline{SC} = R_c \sin(\theta_B - \alpha) \tag{5.18}$$

which corresponds to the situation sketched in figure 5.13a) and follows the Guinier's convention, where a positive angle corresponds to a larger crystal-detector distance.

Similar to the situation described in the previous section, equations (5.17) and (5.18) are only valid for a particular orientation of the lattice planes. To consider all possible

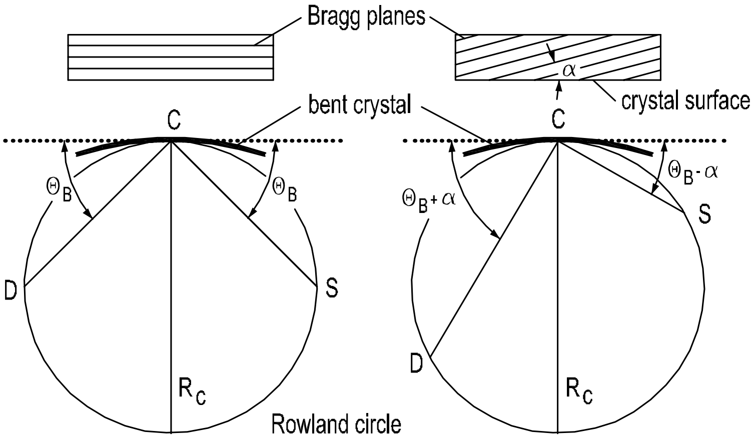

Figure 5.14: Bragg reflection and focusing condition without and with a miscut α for a bent crystal setup in the symmetry plane. The left drawing sketches the symmetric Bragg case and the right drawing the asymmetric one for a miscut orientation φ=0° [128, 129]).

situations, the effective miscut α' as the projection $\alpha\cos\varphi$ should be introduced and the distance crystal-detector rewritten:

$$\begin{aligned} \overline{CD} &= R_c \sin\left(\theta_B + \alpha\cos\varphi\right) \\ \overline{CD} &= R_c \sin\theta_B \cos\left(\alpha\cos\varphi\right) + R_c\cos\theta_B \sin\left(\alpha\cos\varphi\right) \end{aligned} \tag{5.19}$$

Assuming a small miscut ($\alpha < 1°$), which is generally the case for the crystals used, the focal distance will become:

$$\overline{CD} = R_c \sin\theta_B + R_c\cos\theta_B \sin\left(\alpha\cos\varphi\right) \tag{5.20}$$

The separation between the usual focussing condition and the term due to the asymmetric cut angle is clear in equation (5.20). As expected, a meridional orientation ($\varphi = 90°$ and 270°) will not lead to any change in the focal distance as it eliminates the miscut effect. Nevertheless, due to the three-dimensional geometry of the spherically bent crystal, such an orientation will lead to a reflection above or below the symmetry plane as figure 5.15 shows. Despite it can be corrected by tilting the crystal, it can additionally induce a top-bottom asymmetry of the reflection.

The figure 5.15 shows how a Bragg reflection is affected by the orientation of an asymmetric cut crystal. The detector was placed at the focal condition in the absence of a miscut. The simulation was obtained with XTRACK.

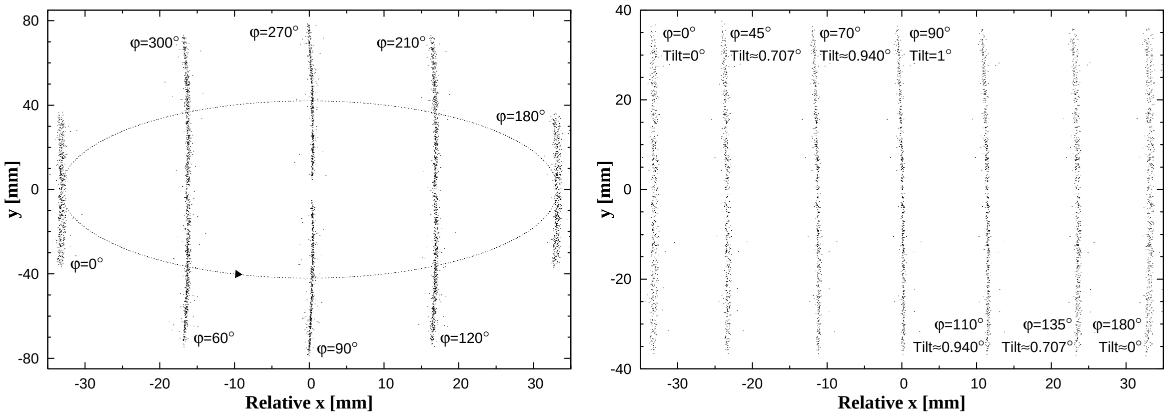

Figure 5.15: Simulation of a Bragg reflection of the M1 He-like Ar transition with about 550 events obtained with an asymmetric cut Si(111) crystal (R_c=2982 mm, α=1°). The active area of the crystal was reduced to 60 mm width and 95 mm height. The detector was placed at $R_c \sin\theta_B$ and the horizontal coordinate is measured from the position where the reflection would be in the absence of a miscut. Negative x correspond to larger angles, thus to the direction of the smaller energies. At the left 8 lines corresponding to a different φ are plotted without tilt correction. The dashed line corresponds to the translation of the center of the reflection on the detector. At the right the crystal was tilted by $\alpha \sin\varphi$.

The centroid of the reflection describes an ellipse over the detector as the orientation of the miscut is changed. As predicted by equation (5.20) the focal distance changes with φ. Accordingly, a line broadening can be noticed as function of the horizontal coordinate of the line centroid (see plot at the right in figure 5.15). To restore the line shape and replace the reflection at its central position the detector should be shifted by $R_c \cos\theta_B \sin(\alpha\cos\varphi)$ and the crystal rotated by an angle equal to $-\alpha\cos\varphi$ around the vertical axis.

The figure also shows that the vertical displacement caused by the miscut orientation is corrected by tilting the crystal by a value of $\alpha\sin\varphi$. Moreover, the small top–bottom asymmetry would disappear after the curvature correction.

The importance of a precise determination of both the miscut and its orientation is revealed by the following example. For a Si(111) crystal and X-rays of the $3p-1s$ transition in πH (2.89 keV) the Bragg angle is $\theta_B = 43.2°$. A miscut as small as 0.1° results in a change in the focal length of about 4 mm, 0.2% for $R_c \approx 2980$ mm. If such a miscut is ignored and the detector is placed at the supposed focal position, the displacement of the focus broadens the line by about $10''$ (considering 60 mm as the horizontal extension of the crystal). This is to be compared to the intrinsic resolution of the Si(111) crystal which is about $26''$ at the mentioned energy.

5.2.3 First experimental evidence of an asymmetric cut angle in our bent crystals

A finite cut angle will change the focal distance according to (5.20) which can be rewritten as follows:

$$\mathcal{F} = R_c \sin\theta_B + R_c \cos\theta_B \sin\left[\alpha \cos\left(\Phi - \Phi_0\right)\right] \tag{5.21}$$

$\mathcal{F}$ being the focal distance, Φ the crystal rotation measured to an arbitrary reference mark placed on the rim of the glass lens and Φ_0 the miscut orientation relatively to that mark. Hence, by measuring the focal distance function of the crystal orientation Φ the miscut α and its orientation Φ_0 can be extracted.

This was first done during the ECRIT run of summer 2005 to characterize new quartz crystals. The crystals had been cut in order to use the plane $(1\bar{2}10)$ as the diffraction plane. After the spectrometer has been tuned, the focal position of the M1 transition line in He-like argon ($\theta_B \approx 54.386°$ [84]) was determined for different crystal orientations Φ.

The crystal was rotated manually without removing it from the crystal holder by loosing the fixing screws. Several marks corresponding to different rotation angles were previously made on the rim of the glass lens to support this procedure. Obviously, to accomplish this operation the spectrometer needed to be vented every time the orientation was changed.

For each crystal orientation several high statistics spectra were recorded with the detector placed at different distances from the crystal. In order to determine the FWHM as a function of the detector-crystal distance, a Gaussian profile was fit to the spectra. Despite not being the correct line profile, it is sufficient for this purpose. The focal distance for each orientation was then found by calculating the mininum of a third order polynomial fit to the data. There is no theoretical reason for choosing such a function beyond the fact that it serves the purpose of finding the minimum and provides a good fit to the data. In figure 5.16 an example of such a fit is shown for Z23, one of the two Qu$(1\bar{2}10)$ crystals, and two different orientations: $\Phi = 0°$ and $\Phi = 180°$.

A quite large change in the focal distance was observed by rotating the crystal. A maximum change of about 30 mm was registered for both Qu$(1\bar{2}10)$ crystals (Z22

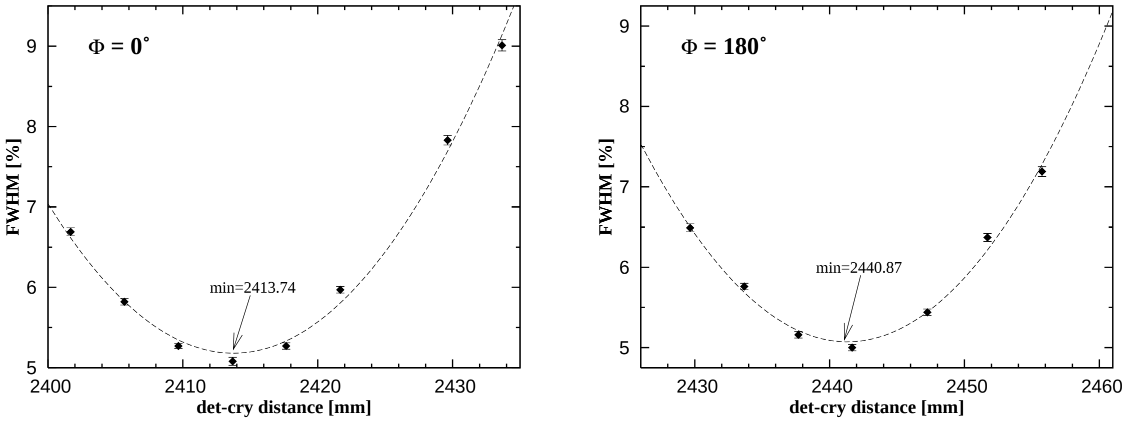

Figure 5.16: Two examples of the determination of the focal distance for different orientations of Qu($1\bar{2}10$) Z23 are shown. The FWHM of the gaussian profile fit to the spectra is plotted in function of the detector-crystal distance. The minimum FWHM corresponds to the focal position and was found by fitting a third order polynomial to the data points. The error bars are fit errors.

and Z23) as shown in figure 5.17. This indicated the presence of a relatively large miscut. Indeed, by fitting (5.21) to the focal distances the following results (given in degrees) were obtained: $\alpha = 0.49 \pm 0.01$, $\Phi_0 = 206.8 \pm 1.2$ for Z22 and $\alpha = 0.50 \pm 0.03$, $\Phi_0 = 162.3 \pm 5.4$ for Z23. The errors are fit errors. From the manual setting of the crystal orientation a few degrees can be considered as a systematic error on Φ_0.

The results depicted in figure 5.17 show a very good agreement between the fit function and the focal distances for different crystal orientations. In the case of Z23, even four experimental points are enough to get a quite good fit but with larger fit errors. In order not to bias the results, the crystal radius R_c was let as a free parameter, particularly because at that moment the crystal radius was not under control. The fits have delivered a crystal radius about 3...4 mm larger than the one measured by Zeiss® which was puzzling. This issue will be discussed in a forthcoming section.

This was the first experimental evidence of the presence of an asymmetric cut angle in the bent crystals owned by the collaboration. It led to the characterization of the other crystals with respect to the miscut and its orientation and to the inclusion of these parameters in the analysis routine. Despite the ECRIT measurement turned out to be very accurate and a straightforward method to perform such a determination, it is also very time-consuming and demands quite a lot of manpower to set up and operate it. Moreover, dedicated measurements to determine the response function of the Si(111) and Qu($10\bar{1}$) crystals (the ones of interest for the πH and μH experiments) have already been done. An alternative solution was desirable.

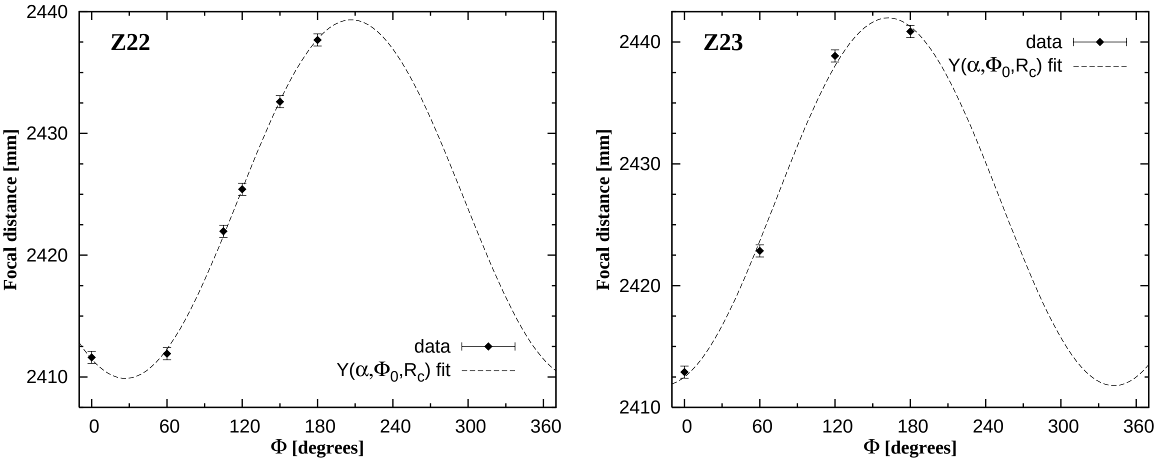

Figure 5.17: Results of the focal distance as function of the crystal orientation for Z22 and Z23. The dashed line is the fit to the data of the function (5.21) by leaving R_c, α and Φ_0 as free parameters.

5.2.4 Miscut angle determination

The techniques for determining the asymmetric cut angle and its orientation within crystal blocks are well established [130], in particular for measuring the orientation of epitaxial layers and implantation profiles [131, 132, 133]. They use X-ray diffraction methods to measure angle differences and/or rocking curve widths, among other quantities. These techniques are well adapted to flat specimens [134] and other special shapes of crystal material [135] but can not be easily extended to a spherically bent crystal setup.

In a spherically bent crystal, already mounted, to measure the miscut angle by angle difference would depend on the hit point. However, there is always a point where the bent surface is parallel to the reference plane defined by the glass lens backplane and if its position is known the X-ray diffraction techniques can be used. For this point the name of *critical point* was chosen (Fig. 5.18).

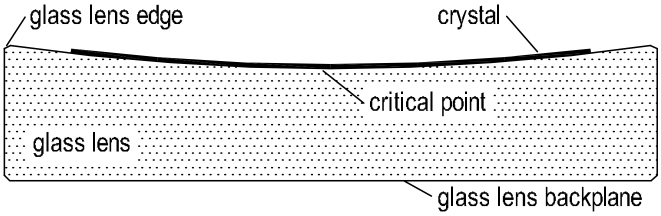

Figure 5.18: Cross section of crystal mounting showing the critical point [129]. The curvature and crystal thickness are not to scale.

Method

A technique to extend the miscut determination by X-ray diffraction to already mounted bent crystals was developed [129]. It is based on a laser alignment of the crystal and subsequent use of an angle difference method.

The critical point is always the lowest point at the surface, but in practice does not coincide with the geometrical center of the crystal mounting. Therefore, it needs to be found. This can be done by means of a laser beam reflected from the crystal onto a screen. When rotating the crystal lens, the position of the reflected light remains unchanged if the critical point is on the axis of rotation, as is required by this method (see figure 5.19). Otherwise, the reflected spot describes an ellipse. The closer the critical point to the rotation axis, the smaller the ellipse axes. At the limit, when both coincide, the ellipse reduces into a spot.

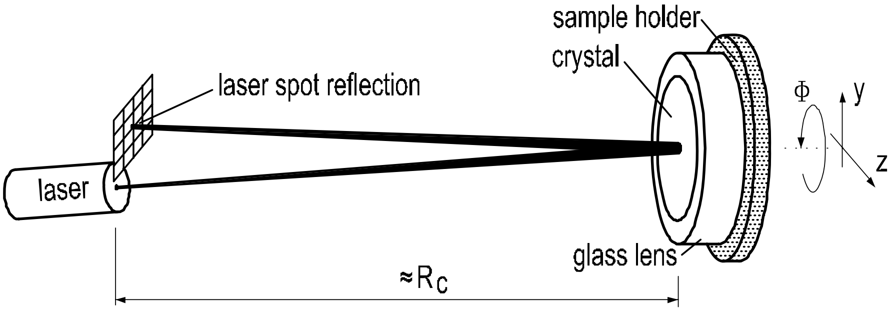

Figure 5.19: Sketch of the crystal alignment to position the critical point onto the holder rotation axis [129].

During this procedure the laser as well as the rotation axes are kept fixed and the sample holder, together with the crystal lens clamped on it, is moved along the y and z coordinate (figure 5.19). Once the critical point is found no further tilt adjustment is needed.

The accuracy of this alignment depends on the distance from the screen to the crystal. In addition the laser spot diameter can limit the accuracy. Placing the laser's aperture at a distance R_c the crystal acts as a concave mirror and will focus the reflected beam also at that distance.

In the absence of any miscut ($\alpha = 0$), an X-ray beam hitting the crystal surface at the critical point is Bragg reflected under the angle $\Psi_r^0 = \theta_B$, whatever the rotation angle. In the case of an asymmetric cut crystal, the reflection angle Ψ_r varies periodically around Ψ_r^0. The angles Ψ_r^0 and Ψ_r are relative to the sample holder surface which coincides to the backplane and is parallel to the crystal surface at the critical point. The relation is given by:

$$\Psi_r = \Psi_r^0 + \alpha \cos(\Phi - \Phi_0) \tag{5.22}$$

which follows from (5.16) and where $\varphi = \Phi - \Phi_0$ is the miscut orientation. The angle Φ is measured relative to an arbitrary reference mark placed on the rim of the glass lens. The phase Φ_0 is the orientation of the miscut with respect to the reference mark. The miscut and its orientation (α,Φ_0) are then obtained through a fit of the $\Psi_r(\Phi)$ curve.

Within this method, almost no restriction for the Bragg angle arises because any diffraction angle accessible by the diffraction spectrometer can be used. Noteworthy, the method can also be applied to the measurement of the miscut at any point of the crystal surface, by using a holder capable of tilting the crystal.

Measurement

The measurement was performed with a SEIFERT® XRD 3003 PTS high-resolution X-ray diffraction spectrometer, which provides a collimated monochromatic beam of Cu K_α X-rays (8.041 keV). The SEIFERT® spectrometer allows a very versatile fine adjustment of the sample in space with the *zero* of all coordinates being possible to be reset. Figure 5.20 shows a schematic of the possibilities. The X-ray beam was collimated to 1 mm in width and 1 cm in height at the source side. The collimator width at the detector was set to 0.5 mm. Both, source and detector windows were about 20 cm from the crystal.

A spectrometer-sample alignment was first performed. The alignment sequence is illustrated in figure 5.21. In a first step the spectrometer is aligned. The crystal was moved away from the beam path and the Θ_{ARM} was reset to *zero* at the position where the intensity of the direct irradiation of the detector is maximum (step 1 in Fig. 5.21).

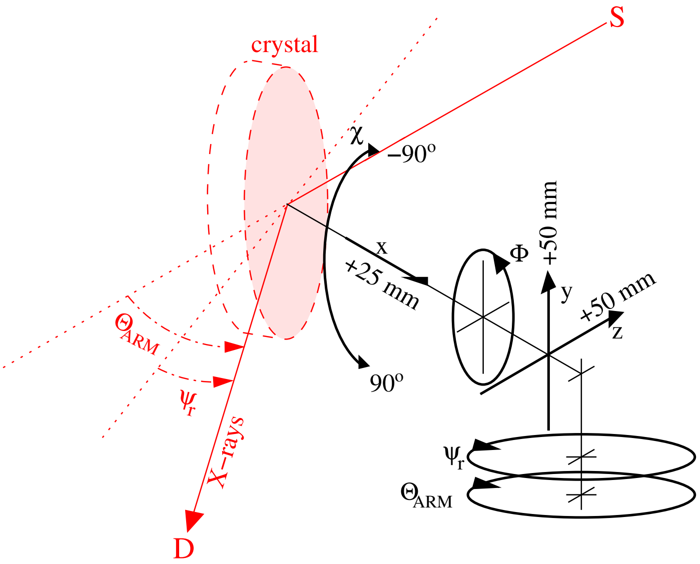

Figure 5.20: Adjustment scheme of the SEIFERT® spectrometer. The relative placement of the crystal, source (S) and detector (D) are indicated in gray. Rotations around the y axis of the crystal and the detector are denoted by Ψ_r and Θ_{ARM}, respectively. The source is not a movable part. The angles Φ and χ defined crystal rotations around the x and z axes, respectively.

In a second stage the orientation of the x position of the sample is adjusted iteratively. The beam should be cut by the glass lens edges by half of its intensity (step 2 in Fig. 5.21). The angle Ψ_r is reset to zero at this position. Afterwards, the crystal is moved in front to correct the depth (step 3 in Fig. 5.21). Otherwise, the X-rays would not hit the critical point. For instance in the case of Silicon crystals, the glass lens has a depth of 0.6 mm at the critical point (from the curvature radius and lens diameter) and the crystal is 0.3 mm thick. So, the mounting should be moved by $0.6 - 0.3 = 0.3$ mm in order to align the critical point with the beam. The Quartz crystals, with the same R_c and lens diameter (approximately) are only 0.2 mm thick and so they should be moved by $\Delta x = 0.4$ mm .

The optical alignment (see figure 5.19) was done with a general-purpose gas laser (660 mm). The light spots were about 6 and 0.5 mm on the crystal surface and on the screen catching the reflected laser beam, respectively.

The spectrometer was initially set to $\Psi_r = \theta_B$ and $\Theta_{ARM} = 2\theta$. In order to easily find the Bragg reflection wider slits (2-3 mm) were used. A source scan was performed and the slits changed. To minimize the error in not hitting the critical point, a fine adjustment in x was performed. The holder was fixed at the x position which maximized the intensity.

The measurement proceeded by taking $\Psi_r(\Phi)$ in steps of $\Delta\Phi = 45°$. For each Φ an alignment in χ was additionally performed: an iterative scan in χ and Ψ_r was done in order to maximize the intensity; the value of Ψ_r, which corresponded to the intensity maximum, was registered. A set of 13 crystals were successfully characterized with this method.

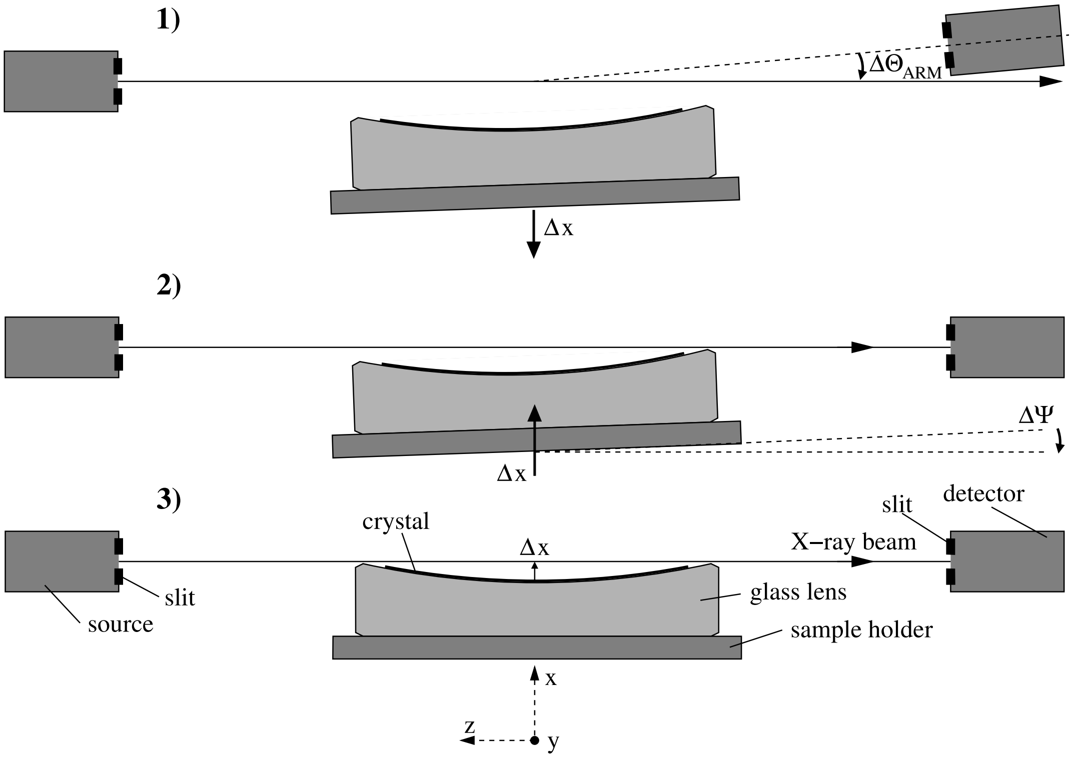

Figure 5.21: Schematic top view of the alignment sequence of the crystal-SEIFERT® spectrometer.

Results

The miscut and its orientation (relative to a mark in the glass lens rim) were then extracted by fitting (5.22) to the data. Figure 5.22 shows the fit for the Si(111) crystal as well as two other examples of a relatively small and large miscut, Si(110) and Qu($1\bar{2}10$), respectively. The fit to the predicted cosine behavior is almost perfect.

There is a small offset on the $\Psi_r(\Phi_0)$ curves, which are not vertically centered at

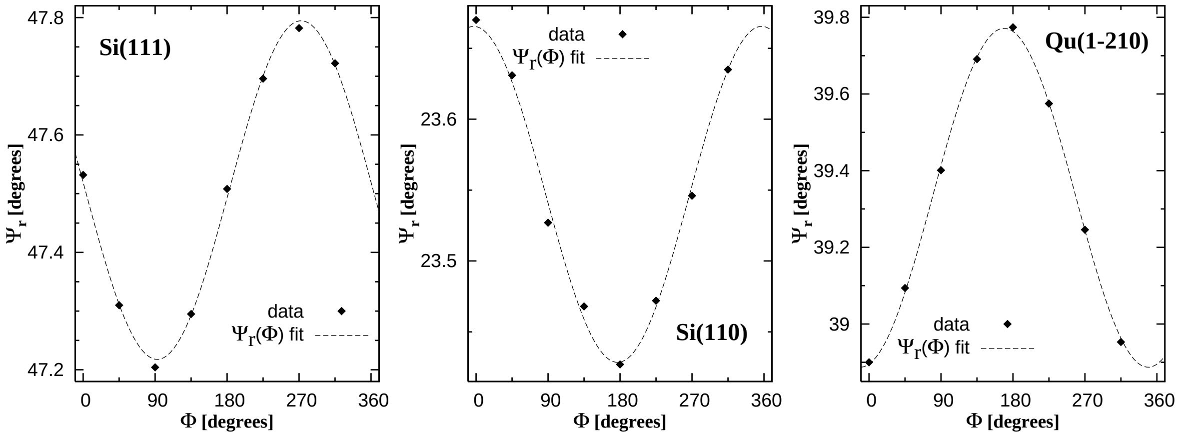

Figure 5.22: Variation of the reflection angle Ψ_r for the Bragg diffraction of the Cu K_α line in 3rd order in Si(111) crystal and in 2nd order in Si(110) and Qu($1\bar{2}10$) crystals, corresponding to θ_B = 47.53° [84], 23.67° [84] and 39.41° [84], respectively. The dashed line corresponds to the fit according to equation (5.22). The outliers in Ψ_r are about 0.001° (of the size od the dots). The small discrepancies seen on the figure are not understood.

the corresponding Bragg angle θ_B. In the case of the Si(111) and Si(110) crystals this is due to a reset of $\Psi_r(0°)$ to $\Psi_r(0°) = \theta_B$ at the beginning of the measurement sequence. Such reset was not done with the Qu($1\bar{2}10$) crystal. Here, the small deviation from θ_B ($\approx$ 0.1°) may be due to an asymmetry on the glass lens whose edge might not be parallel to the backplane, as the alignment crystal-spectrometer requires. However, this fact has no impact in the extraction of the values for α and Φ_0. It represents just a phase in the fit function (5.22).

The results for all the 13 crystals characterized are resumed in table 5.2. They are grouped by crystal planes with the labels being indicated. No optical alignment was performed with Z6 and Z23. In the case of Z6, the optical alignment could not be done as its surface did not reflect the laser beam but dispersed it. This was a result of a former attempt to improve the crystal reflectivity by a physical treatment applied to the surface. On the other hand, Z23 was the first crystal characterized and the alignment was not foreseen. The miscut of Z23 and Z22 was already known at the time from the previous ECRIT measurement and Z23 was selected to validate the present method. As the result agreed inside 1.5 standard deviations with the result obtained with the ECRIT, the angle difference method was validated and the alignment problem postponed.

Crystal	Bragg plane	θ_B [degrees]	order	α [degrees]	$\mathbf{\Phi_0}$ [degrees]
Z13–Si	**(111)**	**47.53**	**3rd**	$\mathbf{0.29 \pm 0.01}$	$\mathbf{-87.4 \pm 1.2}$
Z14–Si	(111)	47.53	3rd	0.30 ± 0.01	-45.6 ± 1.3
Z6–Si	(111)	47.53	3rd	0.19 ± 0.01	4.5 ± 1.6
Z15–Si	(110)	23.67	2nd	0.12 ± 0.01	-3.0 ± 2.0
Z30–Si	(110)	23.67	2nd	< 0.05	
Z31–Si	(110)	23.67	2nd	< 0.04	
Z5–Si	(100)	34.60	4th	0.63 ± 0.01	-174.4 ± 0.4
Z9–Qu	(100)	46.42	4th	< 0.05	
Z10–Qu	(100)	46.42	4th	< 0.05	
Z11–Qu	(100)	46.42	4th	< 0.05	
Z20–Qu	$(10\bar{1})$	43.73	3rd	< 0.05	
Z21–Qu	$(10\bar{1})$	43.73	3rd	< 0.05	
Z23–Qu	$(1\bar{2}10)$	39.41	2nd	0.44 ± 0.01	169.0 ± 0.7

Table 5.2: Results with the fit error of the miscut measurement using an angle difference technique together with the optical alignment described. The errors consider only the fit errors.

The quartz crystals, apart from the $(1\bar{2}10)$ one (Z23), have relatively small miscuts ($< 0.05°$) which can be neglected in most of the applications. Relatively large miscuts were identified among the silicon ones, particularly for Z5. The Si(111) labed Z13, which was the crystal used in the μH$(3p - 1s)$ experiment, has a significant and not negligible miscut. However, its orientation is almost parallel to the meridional plane, thus it does not affect the focal position (see equations (5.22),(5.20) and Fig. 5.13). The "twin" crystals Z13 and Z14, fabricated at the same time, showed the same miscut.

Accuracy of the method

In addition to the fit error, experimental uncertainties must be considered. The hit position of the collimated X-ray beam may deviate from the critical point by the step width of the y-z movement, which was about 0.5 mm. The angle between the tangent to the optical surface (at the hit position) and the backplane will contribute to a systematic error ($\Delta\alpha$) in the measurement of the miscut angle α (see figure 5.23). This resulted in ellipses with an axis up to 4 mm. Accordingly, the systematic error in the miscut angle can be estimated by:

$$\Delta\alpha = \frac{1}{2}\arctan\frac{\frac{1}{2}H}{L} \tag{5.23}$$

H and L being the distance between two reflections after a crystal rotation of 180° and the distance crystal-screen, respectively. The illustration of figure 5.23 clarifies the geometrical construction. Within the maximum ellipse axis found (4 mm) $\Delta\alpha$ is approximately 0.02° ($L \approx 3$ m). The error is dominated by the limitation in the step width on y-z as the laser spot (at the laser window) is less than 1 mm.

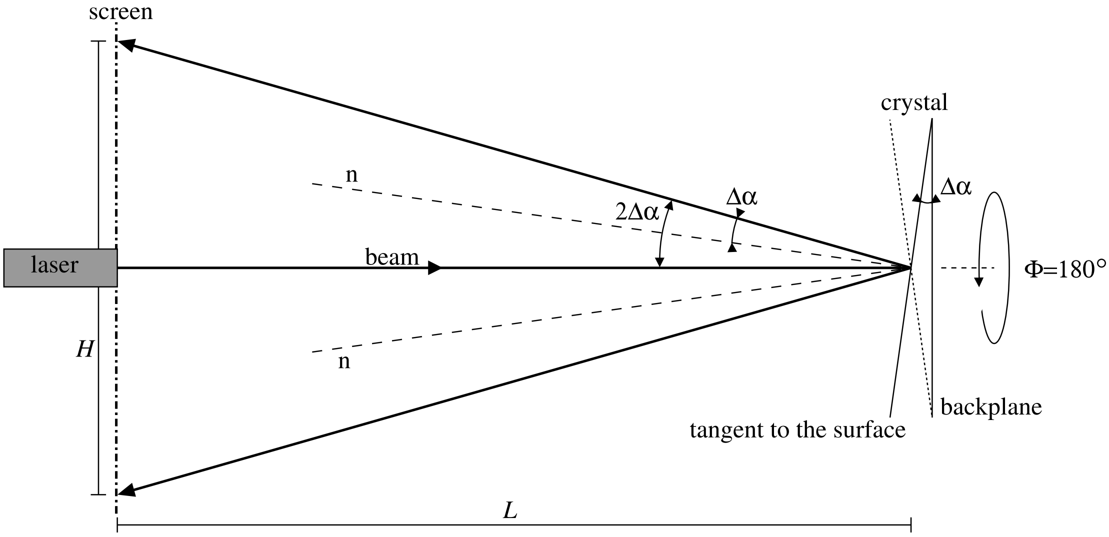

Figure 5.23: Illustration of the geometrical construction to estimate the systematic error in the miscut angle α. The direction n is perpendicular to the crystal surface at the hit position. H is the distance between two reflections at the screen after a 180° rotation. In the present setup $L = 3000$ mm and $H < 4$ mm.

As mentioned, the orientation angle Φ_0 is measured against a reference mark on the glass lens rim. The accuracy $\Delta\Phi_0$ for the mounting of the glass lens on the sample holder was better than 2°.

The fact that the results are pinned down by fitting a simple cosine function renders a specific adjustment of the meridional plane unnecessary, which is of great advantage. Obviously the accuracy of the method scales linearly with the dimensions of the laser setup. In the case of very small asymmetric cut angles (< 0.1°) the accuracy can be increased by adding data points to the fitting curve, as far as mechanical limitations appear.

5.3 Analysis of the ECRIT data

As discussed in section 4.2.4, the total response function of a Bragg spectrometer equipped with a spherically bent crystal consists of three main contributions: response function for a perfect and flat crystal, the geometry of spherical crystals and a Gaussian. The first is provided by XOP [84]; XTRACK modifies it with the geometry for spherical bent crystals; the Gaussian needs to be found by comparing the XTRACK simulation of the experimental spectra with the ECRIT data.

For a given energy, with all the geometrical constraints under full control, any ECRIT spectrum taken with the detector at any position could possibly be used to pin down the Gaussian broadening. The Gaussian which models the imperfect nature of the crystal should not depend on the position of the detector. However, during the experiment it could not be excluded that unjustified assumptions were made. As an example, the detector could be placed out of the assumed position. During the analysis, that difference would be associated to the Gaussian broadening resulting in an increase/decrease of it, depending on the direction of the detector's shift. Therefore, the Gaussian was extracted after a careful analysis of the focal distance. The analysis strategy and the results for the Si(111) crystal are presented in detail.

5.3.1 Strategy of analysis

The first step of the analysis was to determine a preliminary Gaussian broadening. For that, the spectra taken at the focal position, found during the data acquisition, were used. For each ion-like argon M1 transition, a spectrum at the nominal focus (considering R_c provided by *Zeiss*® and the orientation of the Bragg planes) was simulated with XTRACK and compared to the data ones. A first result for the Gaussian was obtained.

In the subsequent stage, for each energy considered, the spectra taken at different positions of the detector were used. By using the Gaussian broadening previously determined, several spectra were simulated with the detector placed at different positions in steps of 0.5 mm. Each spectrum taken with the detector shifted from the supposed focus was compared to the simulated ones around that position. A χ^2 distribution as function of the detector's position (simulated) was obtained. By fitting a third order polynomial, the minimum χ^2 and its corresponding simulated detector's position were determined. Consequently, for each energy the final result of the focal distance was considered to be the weighed mean of the values found for the different positions of the detector which is given by:

$$\mathcal{F} = \frac{\sum_i f_i \frac{1}{(\Delta f_i)^2}}{\sum_i \frac{1}{(\Delta f_i)^2}} \tag{5.24}$$

where f_i is the focal distance found when fitting spectrum number i recorded with the CCDs shifted from the focus. Δf_i is the respective error which was estimated according to:

$$\Delta f_i^{\pm} = \left| Y_i(\chi^2_{min}) - Y_i(\chi^2_{min} \pm 1) \right| \tag{5.25}$$

$Y_i(\chi^2_{min})$ corresponding to the focal distance f_i. Usually the errors are approximately symmetric.

The error on the weighed mean $\mathcal{F}$ is estimated to be:

$$\frac{1}{(\Delta\mathcal{F})^2} = \sum_i \frac{1}{(\Delta f_i)^2} \tag{5.26}$$

Once again, the choice of a third order polynomial has no theoretical support but it provides a very good fit and only serves the purpose of finding the minimum of the χ^2 distribution.

Once the focal distance was known it was compared to the one determined during the data acquisition. The difference was taken as a detector displacement from the focus. The spectra taken at the supposed focal distances were again analyzed with the displacement of the detector taken into account in the simulations.

In principle, this analysis sequence should be done iteratively till no difference is seen in the Gaussian broadening. However, one iteration turned out to be sufficient. After the focal distance was obtained for the first time no significant change in the Gaussian broadening was seen and the result was therefore taken as final value for the Gaussian broadening. A flowchart of the strategy of the analysis is presented in figure 5.24 .

As indicated by (5.25) the slower the χ^2 changes with the detector's position the bigger is the error on the determination of the focal distance. As shown in section 4.3.5 the geometrical broadening of the response function varies approximately quadratic with the detector's shift from the focus. Moreover, the effect is approximately symmetric around the focus. Therefore, the method will be more sensitive by using spectra taken at bigger distances from the focus. Additionally, simulations with shifts symmetric to "shift 0" would lead to similar results as the method is ill-defined around the focus. Hence, spectra with the detector supposedly shifted more than 5 mm were used.

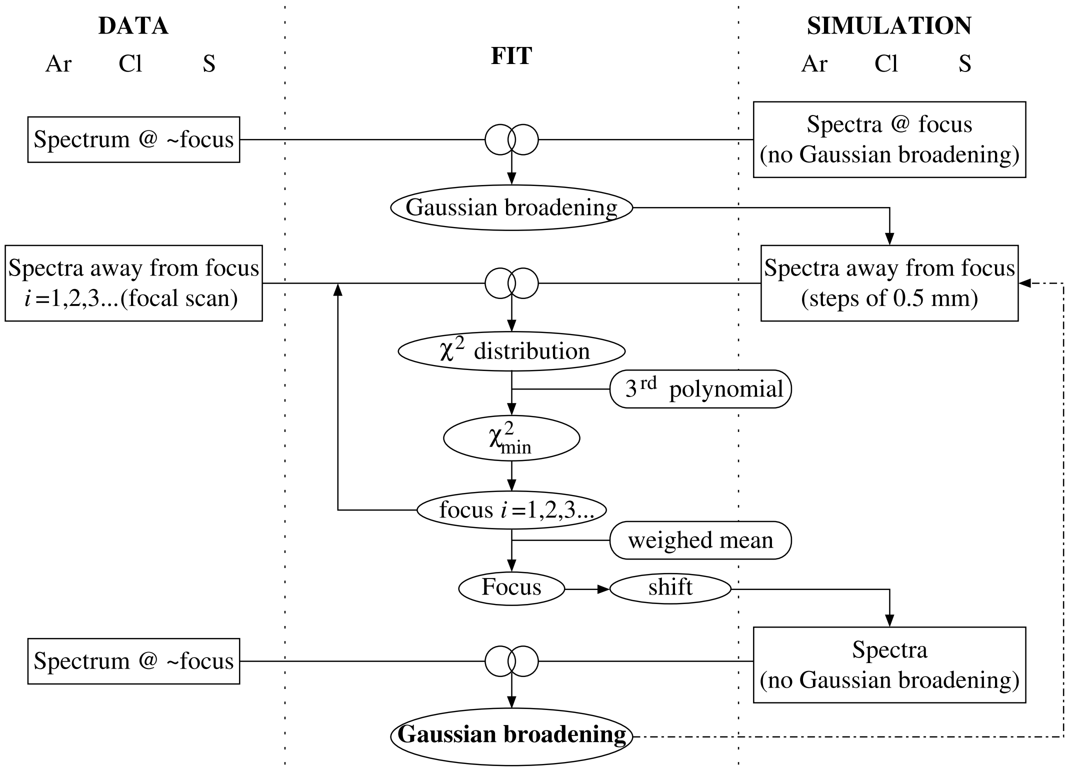

Figure 5.24: Flowchart of the strategy of the analysis to determine the Gaussian broadening of the response function at different energies. The three different sets of data (He-like argon, He-like chlorine and He-like sulfur) were evaluated independently with the same strategic method.

5.3.2 The analysis routine

To perform the data analysis a series of software routines with different purposes were used: XOP [84], XTRACK, CURVSORT, FOLDGT and MINUIT. The XTRACK, CURVSORT and FOLDGT routines were developed inside the πH collaboration [114] and MINUIT is a fitting routine from CERN based on the least squares method [143] which was accordingly modified to fulfill the specific purpose of the ECRIT and exotic atoms data [142].

As mentioned already in earlier sections, the XOP [84] package provides the response function of a flat and perfect crystal for the energy of interest. This is used as input in XTRACK which additionally takes into account the geometry of the experimental setup to simulate the experimental conditions. Its output is the (x,y) positional spectrum at the detector position. By using a mathematical software like GNUPLOT the curvature parameters of the spectrum are obtained. A second order polynomial is fit to the two-dimensional spectrum.

As input, the CURVSORT routine takes the two-dimensional spectrum and the parameters of the correction curve. Once the curvature of the two-dimensional spectrum is corrected its projection over the horizontal direction of the detector will comprise the theoretical response function (ThRF) of the given geometry of the spectrometer for a certain energy.

The ThRF is simulated with a horizontal step size of 0.1 pixel. In order to minimize the statistical errors of the simulation, the ThRF is determined with more than 200000 events which compares to the typical ECRIT spectra with one order of magnitude less statistics. Only the events registered in between the vertical limits of the detector size are taken into account to construct the ThRF, i.e. -36 mm< y <36 mm (zero corresponds to the position at the detector plane horizontally aligned with the crystal's center).

The FOLDGT routine folds the ThRF with Gaussians of different widths. During the analysis, a range between 2 and 120 μrad for the Gaussian width and a step size of 2 μrad were used. Therefore, FOLDGT produces 60 different convolutions of the ThRF with a Gaussian. These output functions are subsequently used by MINUIT as fit functions to the data. The figure 5.25 shows a flowchart of the analysis routine.

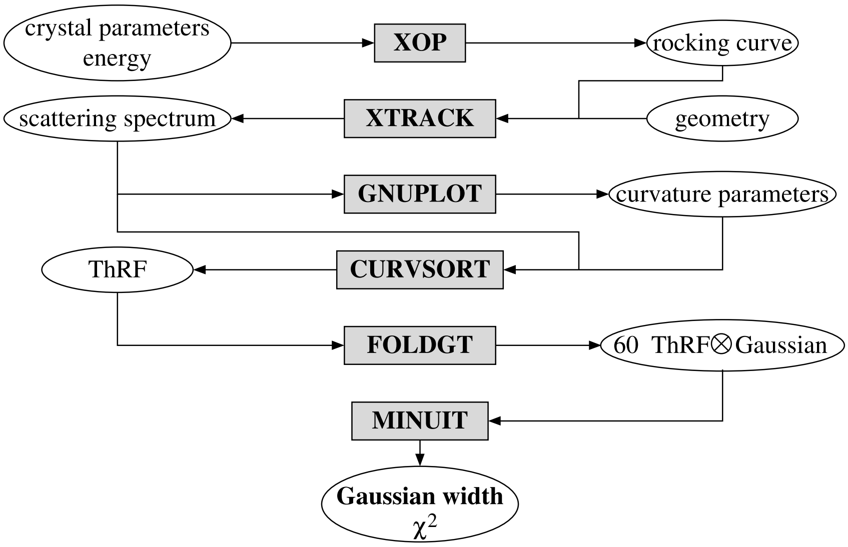

Figure 5.25: Flowchart of the analysis routine. Several routines are needed to simulate and prepare the function used to fit the ECRIT data.

The MINUIT is a powerful fit tool but to be properly used some limitations of the routine should be known. MINUIT is very sensitive to small changes on the initial conditions (start values) as the χ^2 minimization can lead to local minima. Hence, an exhaustive scanning of the initial conditions should be done until a consistent minimum χ^2 is obtained as well as reasonable errors in the fit parameters.

To perform the fit of the ECRIT data up to four free parameters are needed: peak position, scale factor, Gaussian width and background. The background was assumed to be constant.

A reduction of the free parameters reduces the sensitivity to the initial conditions. During the analysis of the focal distance, the Gaussian width was fixed and only three parameters were kept free. However, it was also possible to reduce the number of free parameters to three during the extraction of the Gaussian width. The peak-to-background ratio is very high in the ECRIT data and the fit turned out not to be too sensitive to small changes in the initial conditions of this parameter. Therefore, in a first approach all parameters were let free and small changes in the initial conditions for the background were induced until a consistent value for it was obtained. The background was then fixed and a fit with only three free parameters was performed.

5.3.3 Results

The data available for each gas were analyzed by following the strategy and routine described. In total 8, 6 and 4 spectra taken at different positions away from the supposed focus (found during the data acquisition) were analyzed to extract the focal position of the M1 helium-like argon, chlorine and sulfur, respectively. As well, for the different gases, several spectra taken at the supposed focus were available to extract the Gaussian broadening with two different shapes of the crystal active area.

In figure 5.26 some examples of the fits to the spectra are presented for the three M1 He-like ions acquired at the supposed focus. The figure shows also an example of a M1 He-like Ar defocused and the respective fits with ThRF simulated with the detector placed at different positions.

The quality of the fits of the spectra taken at the supposed focus are very good when no detector's shift is considered in the ThRF simulation. However, for all three gases the M1 He-like ion revealed a small perturbation above the background at its base on the high energy side (see figure 5.26 near the energies 3104.75, 2757.25 and 2430.75 eV for Ar, Cl and S, respectively). The effect is small but might indicate the presence of very weak satellite lines. Regarding the fits, this perturbation lead to a general increase of the χ^2 value but neither the focal position nor the Gaussian broadening determinations were affected.

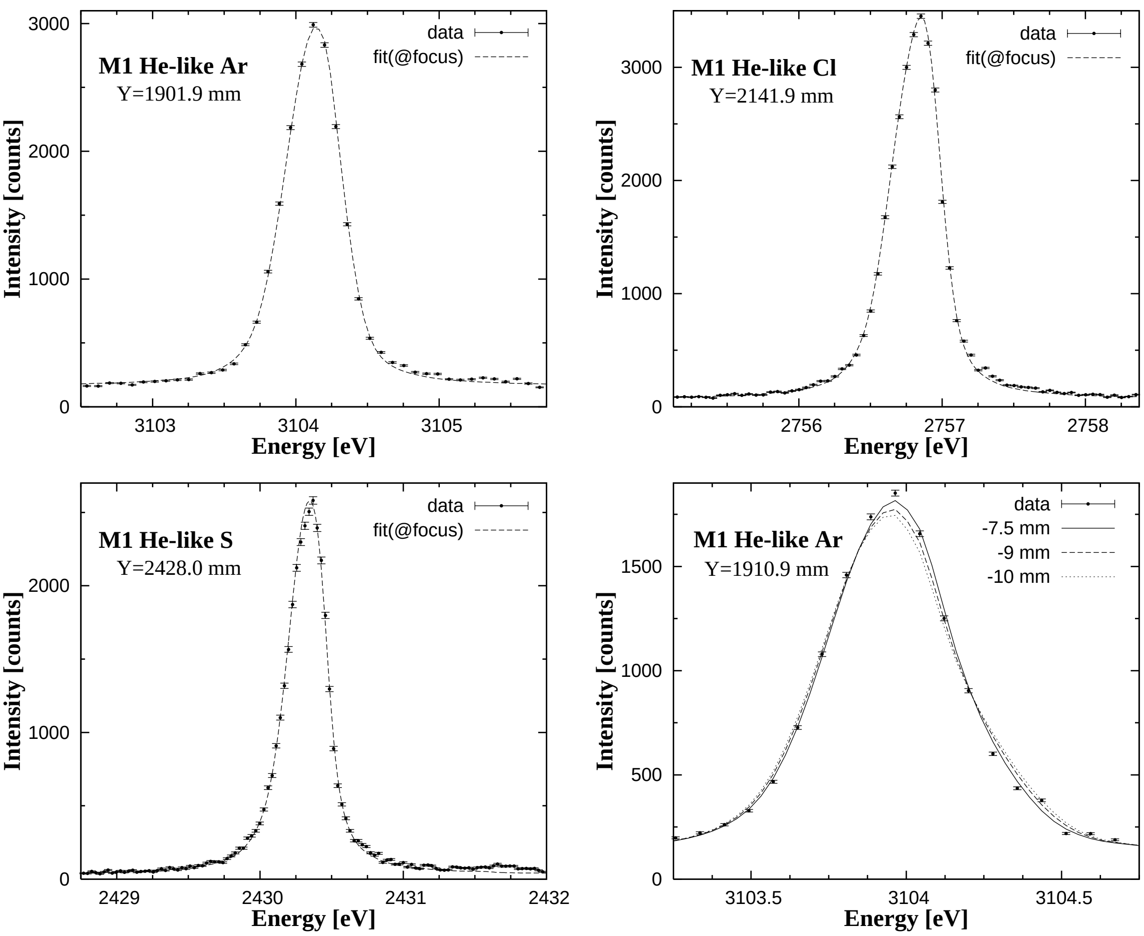

Figure 5.26: Examples of the fits of the M1 He-like lines taken at the focus found by the analysis done during the data acquisition. The ThRF of the Si(111) crystal (Z13) was simulated at the focus. An example of a defocused M1 He-like Ar fit with ThRF simulated with different detector's shifts is also presented. The energy scale was set to give the energy of the M1 lines at the position of lines' peak with the detector placed at the focus.

The fourth example given in the figure 5.26 shows how the fit reacts to a change in the detector's shift used to simulate the ThRF. When an adequate shift is used to simulated the ThRF the fit becomes very good, as can be seen in the example when using a shift of -7.5 mm which led to the best fit of the presented spectrum.

Two examples of the method to determined the focal position are presented in figure

5.27 for a defocused M1 He-like argon line. The figure shows the distributions of the χ^2 when using different detector's shifts to simulate the ThRF as well as its third order polynomial fit. The fits are almost perfect. For direct comparison, the same detector's shift and χ^2 ranges in the x, y axis were used in both examples.

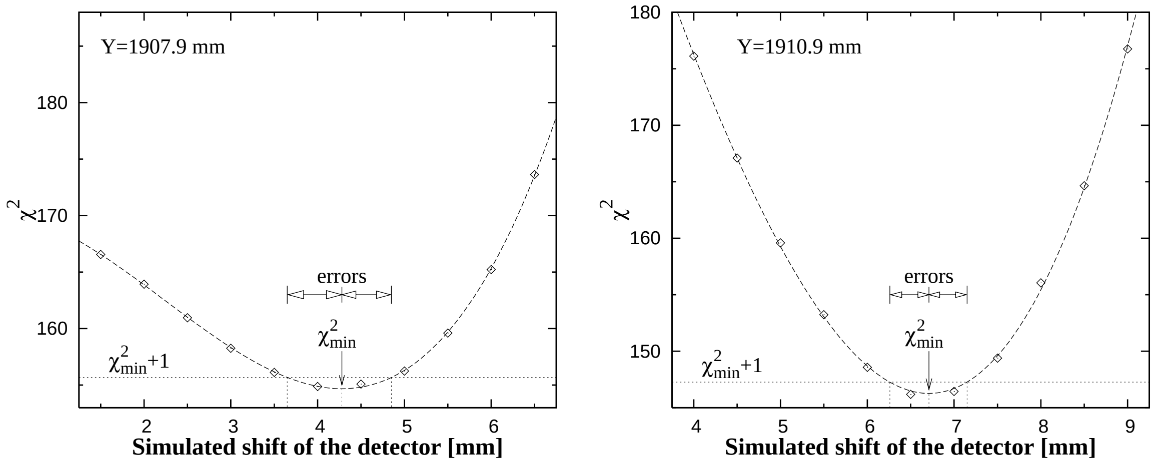

Figure 5.27: Examples of the method to determine the focal position. The χ^2 distributions of the fit of two different defocused spectra of the M1 He-like Ar are shown. The dashed lines are third order polynomial fits to the distributions. The dotted lines indicate the χ^2_{min} (shift) and the error limits.

The lower sensitivity of the fit closer to the focus is also highlighted in figure 5.27. For each distribution presented, the χ^2 varies slower at the side of smaller detector's shifts. Moreover, the χ^2 in general varies slower for the spectrum taken closer to the focus which leads to a wider distribution and bigger error bars, as depicted in the figure.

The results of the focal distance analysis are resumed in the table 5.3 on page 141 and schematically presented in figure 5.28.

Within less than 1 mm the weighed mean for the focal distance agrees with the value calculated during the data acquisition which indicates that the method to extract the focal distance based on the FWHM of a Gaussian fit to the spectra is indeed quite good.

On the other hand, the final results for the focal distance differ by about 2 mm from the nominal and initially expected value. The increase of the error on the focal distance with the decrease of the energy can be explained by the higher dispersion at lower energies. As the dispersion increases, the spectra becomes less sensitive to changes in the detector position. Therefore, the χ^2 distribution curves become less sensitive to the simulated detector's shift and the estimated error of the determination of the focal distance increases.

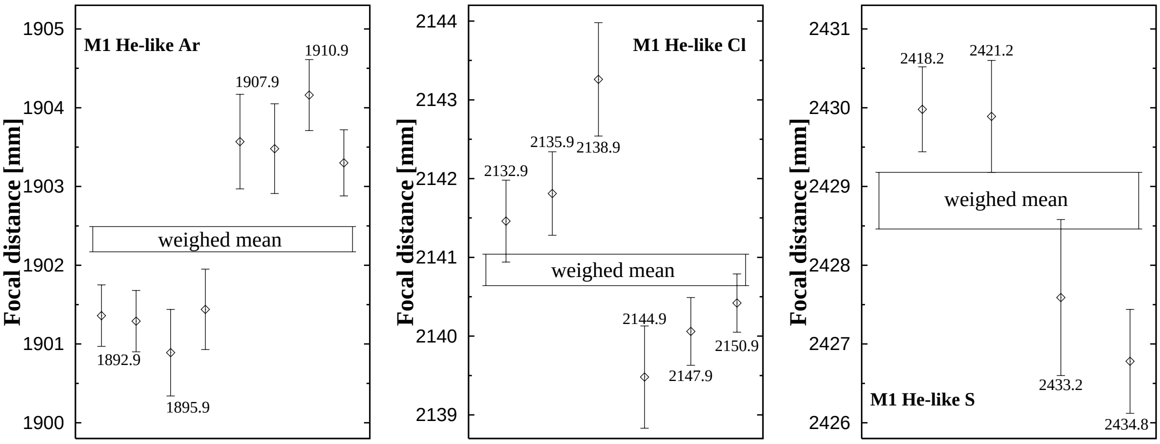

Figure 5.28: Results of the analysis of the ECRIT data regarding the focal distances. The detector position for each spectrum used is indicated near the result. The weighed mean is depicted by a box whose vertical limits corresponds to the estimated error. For direct comparison the range of the axes of the focal distance is the same for all data sets and equal to 5.5 mm.

The results show a relatively large deviation from the mean, systematically above 1.5σ. Moreover, looking to figure 5.28, they seem to be grouped in two sets: one using the spectra taken with the detector placed after the focus and the other one before the focus. For each hypothetic group, the results agree within the errors, but the agreement is rather poor between the two groups. A similar behavior was also seen in the determination of the response function of the Quartz crystals Z20 and Z21 done separately [144]. Comparable results were obtained in a first analysis without considering the asymmetric cut angle and prompted its investigation.

Such a behavior is rather striking and puzzling. This is especially the case after the miscut and the crystal-detector distance have been accurately measured and taken in account. A larger radius than the one measured by Zeiss® could explain the results. This led to the investigations about the crystal radius described in the next section.

The Gaussian broadening was then extracted by taking the relative displacement

data				**fit results**		
M1 He-like	nominal $\mathcal{F}$ [mm]	supposed $\mathcal{F}$ [mm]	Y [mm]	f_i [mm]	$\mathcal{F}$ [mm]	dev from $\mathcal{F}$ [σ]
Ar	1900.1	1901.9	1910.87	1903.30±0.42	$\mathbf{1902.33 \pm 0.16}$	2.31
				1904.16±0.45		4.06
			1907.85	1903.48±0.57		2.02
				1903.57±0.60		2.07
			1895.87	1901.44±0.51		1.75
				1900.89±0.54		2.67
			1892.86	1901.29±0.39		2.67
				1901.36±0.39		2.49
Cl	2139.2	2141.9	2150.86	2140.42±0.37	$\mathbf{2140.84 \pm 0.20}$	1.14
			2147.87	2140.06±0.43		1.81
			2144.87	2139.48±0.65		2.09
			2138.89	2143.26±0.72		3.36
			2135.86	2141.81±0.53		1.83
			2132.89	2141.46±0.52		1.19
S	2426.5	2428.0	2434.78	2426.78±0.66	$\mathbf{2428.84 \pm 0.34}$	3.12
			2433.22	2427.59±0.99		1.26
			2421.24	2429.89±0.71		1.48
			2418.22	2429.98±0.54		2.11

Table 5.3: Results of the analysis of the focal distances using different defocused spectra. The nominal focus is given by equation (5.21) when using the values of the miscut and its orientation of Z13 and the curvature radius measured by *Zeiss*® which is 2982.2 mm. The supposed focal distance is the one found by the analysis done during the data acquisition.

of the detector to the focal positions found for each energy into account in the ThRF simulations. The table 5.4 presents the results for two different active areas of the crystal which were used: a rectangular one with 60 mm width and 95 mm height and a circular one with 40 mm diameter.

The use of a smaller and more centered active area of the crystal leads to a smaller Gaussian broadening. As the Gaussian models the imperfect nature of the crystal, it is acceptable to explain this result by a hypothetic increase of the imperfections towards the outer regions of the crystal's surface. Regarding the behavior of the broadening versus the energy no conclusions can be directly deduced from the table. A careful interpretation of the Gaussian broadening and its energy dependence will be presented in an upcoming section.

M1 He-like	E [eV]	**Gaussian broadening (FWHM)**					
		60×95 mm			$\emptyset$40 mm		
		[pixels]	[μrad]	[meV]	[pixels]	[μrad]	[meV]
Ar	3104.18	1.6 ± 0.1	$\mathbf{32.77 \pm 2.21}$	123.1 ± 8.3	1.4 ± 0.1	$\mathbf{30.22 \pm 2.29}$	113.5 ± 8.6
Cl	2756.85	2.2 ± 0.1	$\mathbf{40.95 \pm 2.07}$	109.7 ± 5.5	1.9 ± 0.1	$\mathbf{34.63 \pm 2.40}$	92.8 ± 6.4
S	2430.34	3.4 ± 0.2	$\mathbf{56.53 \pm 2.99}$	98.2 ± 5.2	3.1 ± 0.2	$\mathbf{51.42 \pm 3.57}$	89.3 ± 6.2

Table 5.4: Gaussian broadening of Z13 at different energies obtained via the analysis of the ECRIT data. The bold values are obtained directly from the fitting routine. The conversion into pixels and millielectronvolts was done by considering the dispersion at the position where the detector was placed.

5.3.4 Investigations on the curvature radius

The curvature radius can be estimated as a byproduct of the focal distance analysis by modifying (5.21) accordingly:

$$R_c = \frac{\mathcal{F}}{\sin\theta_B + \cos\theta_B \cdot \sin\left[\alpha \cdot \cos\left(\Phi - \Phi_0\right)\right]} \tag{5.27}$$

where $\mathcal{F}$ is the weighed mean from the focal distance analysis for each gas. As all the other quantities are known, R_c is directly calculated. On the ECRIT setup Φ=0°.

The error is estimated by applying the error propagation theory to (5.27). As the error on $\mathcal{F}$ dominates over the errors of α and Φ_0, the last ones are left out which simplifies the error formulation. The error on R_c is then given by:

$$\Delta R_c = \frac{\Delta\mathcal{F}}{\sin\theta_B + \cos\theta_B \cdot \sin\left[\alpha \cdot \cos\left(\Phi - \Phi_0\right)\right]} \tag{5.28}$$

The final result for the curvature radius and its error is the weighed mean of the values found using each gas [see equations (5.24) and (5.26] on page 134 for the formulation). The results are resumed in table 5.5 and a schematic view depicted in figure 5.29.

The weighed mean obtained for the curvature of Z13 differs by about 3 mm from the radius measured by *Zeiss*® through mechanical means. Although the discrepancy is less than 0.1% it is rather puzzling and it was systematically observed also with the Z20 and Z21 Qu(10$\bar{1}$) crystals [144] and again with the Qu(1$\bar{2}$10) crystal labeled Z22 [145].

According to the focal distance relation (5.21) a change in the crystal radius δR_c will consequently cause a change in the focus given by:

M1 He-like	$\theta_\mathbf{B}$ [degrees]	$\mathcal{F}$ [mm]	$\mathbf{R_c^i}$ [mm]	$\mathbf{R_c}$**(weighed mean)** [mm]	**dev from mean** [σ]
Ar	39.5639386	1902.33 ± 0.16	2985.85 ± 0.25	$\mathbf{2985.17 \pm 0.17}$	2.7
Cl	45.8225983	2140.84 ± 0.20	2984.40 ± 0.28		2.8
S	54.4430162	2428.84 ± 0.34	2985.04 ± 0.42		0.3

Table 5.5: Results for the curvature radius of Z13 based on the focal distance analysis of the ECRIT data. The Bragg angle was taken from XOP [84].

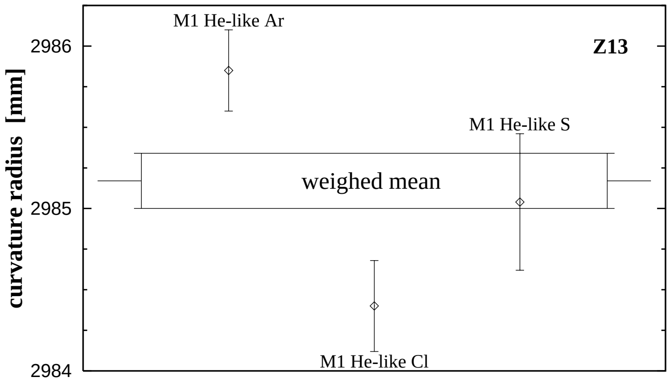

Figure 5.29: Schematic view of the results for the curvature radius of Z13 obtained via the focal distances analysis of the ECRIT data. The weighed mean is depicted by a box whose vertical limits correspond to the estimated error.

$$\delta\mathcal{F} = \delta R_c \cdot \sin\theta_B + \delta R_c \cdot \cos\theta_B \sin\left[\alpha\cos\left(\Phi - \Phi_0\right)\right] \tag{5.29}$$

Hence, a 3 mm mistake on the crystal's radius would lead to a shift in the focal distance of about 1.9 mm, 2.2 mm, 2.4 mm and 2.6 mm concerning the M1 He-like Ar, M1 He-like Cl, M1 He-like S and μH$(3p - 1s)$ transition energies, respectively. Such shifts would not have, in principle, a significant impact on the line broadening as they are comparable with the uncertainty on the definition of the focus ($\sim$ 2 mm, recall section 4.3.5). Moreover, during the setup the value given by (5.21) is merely indicative and the determination of the focus is granted by the data analysis.

The situation observed prompted further investigations to check the validity of the value given by *Zeiss*®. Thus, a third measurement of the radius was performed at PSI by using a dedicated device available at one of the support laboratories of the Swiss

Light Source (SLS) at PSI.

The device is an optical-type profilometer which was customer designed to measure curvature radius of tens of meters. Therefore, considering the comparably small radius of Z13, an accuracy limit of about 1 mm is expected.

The profilometer consists of a box where a laser, several optical elements and a CCD detector are mounted. The box moves along the longitudinal direction towards a fixed mirror mounted in front of it. Briefly, the apparatus works as follows: two perpendicular double beams exit the moving box which will be reflected back to the box by the fixed mirror and the sample surface, respectively; hence, by moving the box, one of the laser beams is driven along the surface of the sample and by comparing the translation of its reflection with the reference beam, the curvature radius of the sample surface is determined. The calculation is automatically done by the dedicated software of the profilometer.

A total of 41 measurements were performed, each corresponding to a different scanned region of the surface of Z13. The results are presented in the histogram of figure 5.30 .

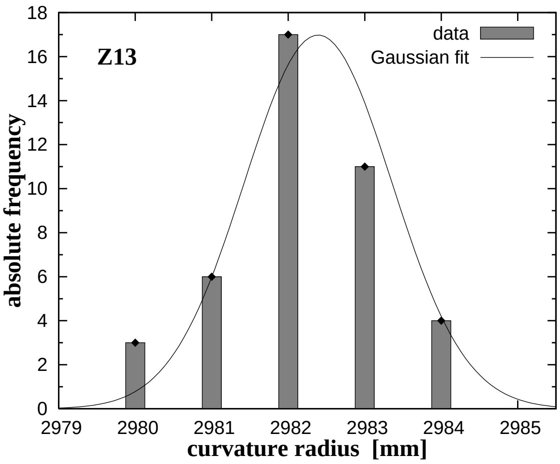

Figure 5.30: Histogram of the results of the radius of curvature of Z13 obtained with an optical profilometer. A total of 41 measurements were done. The solid curve is a fit to the distribution of a Gaussian.

Despite the results show a small variation, the fair quality of the Gaussian fit suggests that this is only a statistical effect. The final result for the curvature radius of Z13 is assumed to be the simple mean of the distribution, whose standard deviation is taken as the error. Therefore, the result is:

$$R_c(\mathrm{Z13}) = 2982.2 \pm 1.1 \text{ mm}$$

A similar result is obtained by fitting a Gaussian to the distribution, i.e 2982.4±1.0 mm. The Gaussian curve is described by the function:

$$f(x) = \frac{A}{\sigma\sqrt{2\pi}} \exp - \frac{(x-\bar{x})^2}{2\sigma^2} \tag{5.30}$$

A being the total number of events, $\bar{x}$ their mean and σ their standard deviation.

The result perfectly agrees with the value from *Zeiss*® and so the puzzle remains. It might be possible that both values (2982.2 mm and 2985.2 mm) are correct and have different natures. The first one was measured by optical and mechanical means and thus it corresponds to the curvature radius of the surface of the crystal. On the other hand, the second one comes from an X-ray measurement and is therefore related to the curvature of the crystal planes. Despite it is assumed that crystal planes follow the curvature of the surface it can not be excluded that second order effects on the mechanical bending process cause a discrepancy of 0.1%. In fact, this is a rather small deviation, only revealed due to the very accurate nature of the ECRIT measurement. In conclusion, in first order the crystal planes follow the curvature of the surface.

5.3.5 Study of the effect of Gaussian broadening and of the background in the focal analysis by using Monte-Carlo techniques

The strategy of the focal analysis relies on an initial first value for the Gaussian broadening which is determined by assuming that the focal position found during the measurement is close to its final value. Obviously, if the assumed focal position is wrong by a few millimeters it would lead to a Gaussian broadening larger than in reality as the defocussing would not be taken into account on the simulated fit function. Another unknown limitation of the method which would cause the extracted Gaussian to be smaller than its real value, is also not excluded.

In case a larger FWHM of the Gaussian would be considered in the focal analysis, less geometrical broadening on the ThRF (smaller detector's shifts on the ThRF simulations) would be needed to guarantee a good fit of the defocused spectra. Hence, by using negatively defocused spectra (direction away from the crystal) a negatively shifted focal distance would be obtained. On the same way, by using the positively defocused spectra (direction to crystal) a positively shifted focus would be registered. In fact, the M1 He-like Ar analysis shows this behavior (see figure 5.28).

On the other hand, an underestimation of the Gaussian broadening would cause the opposite behavior. A negatively shifted focus would be achieved by using the spectra which were positively defocused and a focus positively shifted would be obtained with the spectra negatively defocused. This behavior was seen in the focal analysis of the M1 He-like Cl and S spectra (see figure 5.28).

Additionally, the sensitivity of the spectra to the defocusing increases with the detector's shift. Consequently, close to the focus the same change in the detector's position originates less geometrical broadening due to defocussing. Therefore, by using the same wrong Gaussian, the focal analysis of the less defocused spectra would deliver a result for the focal distance more far away from its real value. This is clearly seen on the results of the analysis of the M1 He-like Cl (see figure 5.28).

Accordingly, a possible wrong assumption for the FWHM of the Gaussian on the focal analysis would possibly explain the systematic deviation of the results from the mean. In order to quantify this hypothesis, a focal analysis of simulated Ar spectra obtained via Monte-Carlo routines was performed. The spectra were simulated with statistics and background similar to what was experimentally observed. All the geometrical constraints of the experimental setup with Z13 were taken into account.

Impact of the focus' assumption on the FWHM of the Gaussian broadening

The first study quantifies the direct influence of a wrong assumption of the focal distance on the extraction of the Gaussian broadening. Several spectra with different detector displacements from the focus and a Gaussian FWHM of 34 μrad were simulated. The spectra were analyzed in the same terms as the real data by assuming all spectra taken at focus. The results are resumed in table 5.6 and figure 5.31.

This study demonstrates that in the case of the M1 He-like Ar transition, a wrong assumption of about 1.5 and 4 mm on the focal position results in a value for the FWHM of the Gaussian broadening larger by 2 and 10 μrad, respectively. However, by taking into account the results of the focal analysis of the experimental data (section 5.3.3), a wrong assumption on the focal position by more than 2 mm is unlikely. Nevertheless, the use of a Gaussian broadening larger by a few μrad during the focal analysis is quite acceptable.

Impact of the Gaussian broadening on the focal analysis

The second study aimed to clarify the impact of the FWHM of the Gaussian broadening on the focal analysis [146]. Four spectra of the M1 He-like Ar transition were produced via Monte-Carlo techniques with the detector shifted by 9,6,-6 and -9 mm from the focal position. The simulated data had statistics and background similar to those with a Gaussian broadening of 34 μrad.

Monte-Carlo data detector's shift [mm]	**Gaussian FWHM [μrad]**	**ΔFWHM [μrad]**	χ^2
-4.0	44.17	2.61	117.236
-3.0	40.09	3.80	114.106
-2.0	37.57	2.97	115.988
-1.0	35.29	3.04	114.369
0.0	**33.95**	**3.08**	**108.852**
1.0	34.21	3.18	110.450
1.5	35.36	3.07	105.712
2.0	35.85	3.02	104.178
3.0	38.97	3.06	112.261
4.0	42.81	2.69	112.858
5.0	47.87	2.49	123.906

Table 5.6: Results for Gaussian broadening by considering a wrong assumption of the focal distance of the M1 He-like argon. The spectra were produced by Monte-Carlo techniques with statistics and background similar to those observed in the experimental data. A FWHM of 34 μrad was considered for the Gaussian.

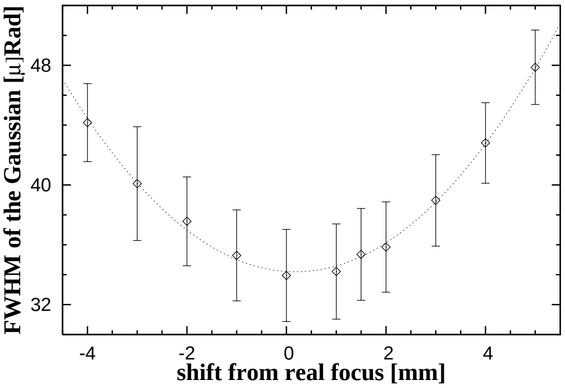

Figure 5.31: Correlation between the FWHM of the Gaussian broadening and the defocusing of the M1 He-like Ar line. The dashed curve is a line to guide the eye and is a fit to the results of a second order polynomial. The data was obtained via Monte-Carlo techniques. The numerical results as well as further details are presented in table 5.6 and in its caption.

Therefore, three sets of analysis were done by using different Gaussian broadenings on the derivation of the fit function: 33.95, 36 and 44 μrad. The first one is the value obtained via an analysis similar to the one performed on the experimental data. The results are resumed in table 5.7 and a schematic view is given in figure 5.32.

Gaussian FWHM [μrad]	defocussing [mm]	**fit results**		
		$\mathcal{F} - f'_i$ [mm]	$\mathcal{F} - \mathcal{F}'$ [mm]	dev from $\mathcal{F} - \mathcal{F}'$ [σ]
33.95	-9	-0.24 ± 0.37	-0.13 ± 0.21	0.29
	-6	-0.71 ± 0.51		1.13
	6	-0.13 ± 0.47		0.01
	9	0.32 ± 0.39		1.16
36.00	-9	-0.35 ± 0.38	-0.12 ± 0.22	0.61
	-6	-0.83 ± 0.52		1.37
	6	0.02 ± 0.48		0.29
	9	0.43 ± 0.43		1.41
44.00	-9	-0.88 ± 0.42	-0.10 ± 0.24	1.87
	-6	-1.62 ± 0.61		2.50
	6	0.79 ± 0.56		1.58
	9	1.01 ± 0.44		2.51

Table 5.7: Results of the analysis of the focal distance for the M1 He-like Ar transition by using data produced with Monte-Carlo techniques. The data were generated with statistics and background similar to what was experimentally observed. All the geometrical constraints of the setup with the Z13 crystal were considered. $\mathcal{F}$ indicates the focal distance given by expression (5.21) and $\mathcal{F}'$ and f'_i the values found through the analysis.

As in the analysis of the experimental data, the results are grouped in two sets whose agreement gets poorer when the Gaussian broadening becomes wronger. Anyhow, it is clear that despite the deviations of the results from the weighed mean increase, neither the weighed mean nor its statistical error are significantly affected. Moreover, the deviations from the mean only start to be significant and comparable to what was seen in the analysis of the experimental data (section 5.3.3, table 5.3, page 141) for a Gaussian broadening with an additional FWHM of about 10 μrad. However, it is hardly acceptable and rather doubtful that the extraction of the Gaussian FWHM from the experimental data is wrong by more than 2 μrad, particularly by an amount of the order of 10 μrad. This would mean that the detector would be wrongly placed by about 4 mm (figure 5.31).

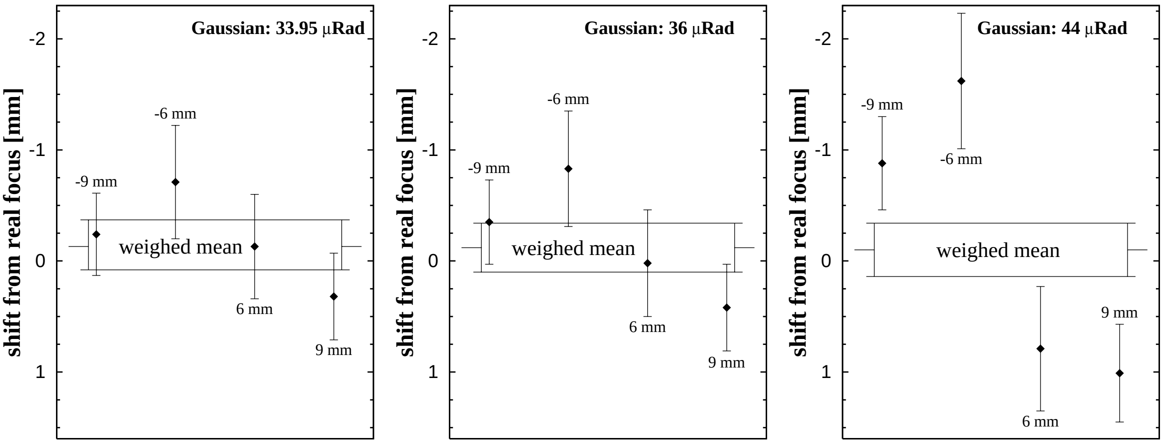

Figure 5.32: Schematic view of results of the analysis of the focal distance for the M1 He-like Ar transition by using data generated with Monte-Carlo techniques. The weighed mean is depicted by a box whose vertical limits correspond to the estimated error. Further details are given in table 5.7 and in its caption.

Impact of the background on the analysis of the focal distance

The influence of the background on the analysis of the focal distance of the M1 He-like Ar transition was also quantified by using the Monte-Carlo data. The analysis was done by using only two defocused spectra (-6 and -9 mm) and the background was assumed to be 5% larger/smaller than in reality. The FWHM of the Gaussian broadening was fixed on 33.95 μrad. The results are resumed in table 5.8.

This demonstrates that a wrong estimation of the background level by ±5% can not explain the deviations from the mean which have been seen in the analysis of the focal distance, although it leads to a significant change on the deviations. The deviations are still about half of the values registered on the experimental data analysis. Additionally, a wrong estimation of the background by ±5% is already rather unlikely. Therefore, a wrong background assumption can also be excluded as the explanation of the behavior of the results of the analysis of the focal distance.

Conclusions

Although the behavior of the results for the focal distance was confirmed by the analysis of the Monte-Carlo data, a background effect turned out to be much less pronounced and within errors. Additionally, no reasonable explanation was obtained

defocusing [mm]	table 5.7		assumed background [%]	$\mathcal{F} - f'_i$ [mm]	dev from $\mathcal{F} - \mathcal{F}'$ [σ]
	$\mathcal{F} - f'_i$ [mm]	dev from $\mathcal{F} - \mathcal{F}'$ [σ]			
-9	-0.24 ± 0.37	0.29	$+5$	-0.45 ± 0.54	0.59
			-5	-0.01 ± 0.36	0.33
-6	-0.71 ± 0.51	1.13	$+5$	-0.91 ± 0.51	1.44
			-5	-0.39 ± 0.49	0.36

Table 5.8: Results of the a partial analysis of the focal distance of the M1 He-like Ar transition by using Monte-Carlo techniques and considering a background level ±5% different from its real value. The analysis was done by using a FWHM of 33.95 μrad for the Gaussian broadening. $\mathcal{F}'$ corresponds to the weighed mean on table 5.7.

to justify the large deviations from the mean which were seen in the analysis of the experimental data. Therefore, the puzzle remains but apparently does not disturb the extraction of the focal distance. Facing the lack of other possibilities, the only explanation remaining is the underestimation of the errors by the χ^2 method.

5.4 Interpretation of the Gaussian broadening and extrapolation to 2.25 keV

The ineffective layer model

The results for the Gaussian broadening resumed in table 5.4 (page 142) might point to a direct correlation with the X-ray energy. By looking to the values in μrad they suggest an inverse proportionality with energy, which indeed could be used. However, a careful analysis reveals that, in μrad, despite the Gaussian broadening increases with the decrease of the energy, the relative increase in the response function is approximately the same (around 5%). The various contributions for the response function (RF) should be added quadratically:

$$\mathrm{FWHM}_{RF} = \sqrt{\mathrm{FWHM}^2_{ThRF} + \mathrm{FWHM}^2_{G}} \tag{5.31}$$

The numerical values are presented in table 5.9.

As the FWHM of the ThRF is typically three times higher than the one of the Gaussian, the relative weight of the Gaussian contribution on the FWHM of the RF is about 1/20:

$$
\begin{aligned}
\frac{\mathrm{FWHM}_{RF}-\mathrm{FWHM}_{ThRF}}{\mathrm{FWHM}_{RF}} &= \frac{\sqrt{\mathrm{FWHM}_{ThRF}^2+\mathrm{FWHM}_G^2}-\mathrm{FWHM}_{ThRF}}{\sqrt{\mathrm{FWHM}_{ThRF}^2+\mathrm{FWHM}_G^2}} \\
&= \frac{\sqrt{\mathrm{FWHM}_{ThRF}^2\,(1+1/9)}-\mathrm{FWHM}_{ThRF}}{\sqrt{\mathrm{FWHM}_{ThRF}^2\,(1+1/9)}} \\
\frac{\mathrm{FWHM}_{RF}-\mathrm{FWHM}_{ThRF}}{\mathrm{FWHM}_{RF}} &= \frac{\sqrt{10/9}-1}{\sqrt{10/9}} \approx 0.051 \approx \frac{1}{20} \qquad (5.32)
\end{aligned}
$$

	Energy	[eV]	3104.18	2756.85	2430.34
FWHM	rocking curve (XOP)	[μrad/meV]	109.4/411.0	134.4/360.0	170.6/296.4
	ThRF (XTRACK)	[μrad/meV]	112.0/420.8	136.4/365.4	167.6/291.2
	Gaussian (data analysis)	[μrad/meV]	32.8/113.5	41.0/109.7	56.5/98.2
	RF (ThRF$\otimes$Gaussian)	[μrad/eV]	116.7/438.5	142.4/381.5	176.9/307.3
	Relative increase ($\frac{RF-ThRF}{ThRF}$)	[%]	4.2	4.4	5.5

Table 5.9: Impact of the Gaussian broadening in the response function (RF) of crystal Z13 by using an active area of 60 × 95 mm. The FWHM of the rocking curve, ThRF and RF were calculated (in μrad) by a Gaussian fit, which at the focus is a fair description of the lines. The values in meV were deduced by considering the dispersion at the position where the detector was placed during the data acquisition.

Therefore a relatively large error on the extrapolation of the FWHM of the Gaussian broadening is rather acceptable and will not have a significant influence on the RF at the μH$(3p-1s)$ transition energy.

Following the observations presented on table 5.9 a correlation of the total response function with the energy can be tried. In fact, the penetration depth, which is related with the energy, offers a better physical interpretation of the Gaussian broadening.

As described in section 4.1.3, a Bragg reflection is constructed by thousands of reflections along the beam path by crossing the successive crystal planes. The FWHM of the ThRF can be fairly related to the penetration depth (λ_T) by considering an inverse proportionality with an unknown constant $\mathcal{K}$ (not necessary the same for different θ_B):

$$\mathrm{FWHM}_{ThRF} = \mathcal{K}\frac{1}{\lambda_T} \qquad (5.33)$$

In this way, an increase on the FWHM_{ThRF} would be associated with a decrease in the depth reached by the X-rays, i.e. less crystal planes are crossed and thus a smaller number of individual reflections occur.

A microscopic roughness of the surface and/or small changes in the interplanar distances (d) at the superficial planes caused by stresses during the fabrication are plausible to create an *ineffective layer* at the surface of the crystal. Along the length of this layer ($\mathcal{L}$) the incoming waves would be attenuated but the resulting Bragg reflections would follow different directions, hence, not contributing to the amplitude of the nominal outgoing waves. The ineffective layer would be a physical property of each crystal and independent of the X-ray energy.

Therefore, the ineffective layer would reduce the penetration depth to an *effective penetration depth* (λ_{T_e}) where the individual Bragg reflections contribute to total Bragg reflection. This would result in an additional broadening of the ThRF. A relation similar to (5.33) can be written to correlate the FWHM$_{RF}$ with λ_{T_e}:

$$\mathrm{FWHM}_{RF} = \mathcal{K}\frac{1}{\lambda_{T_e}} \tag{5.34}$$

Naturally, the length of the ineffective layer is given by:

$$\mathcal{L} = \lambda_T - \lambda_{T_e} \tag{5.35}$$

Recalling the considerations on section 4.1.3 (page 54) and considering that in case the extinction depths for both polarizations are known (Λ_σ,Λ_π), the total extinction depth(Λ) for an unpolarized beam is given by:

$$\frac{1}{\Lambda} = \frac{1}{2\Lambda_\sigma} + \frac{1}{2\Lambda_\pi} \tag{5.36}$$

The length of the hypothetical ineffective layer of Z13 can be calculated from the data available. The calculations, as well as the data of interest and their origin are presented in table 5.10.

The error on the extraction of the Gaussian broadening is assumed to dominate the error on the FWHM$_{RF}$. Hence, the errors on the FWHM of the response function, effective penetration depth and on the length of the ineffective layer are estimated by the theory of error propagation and are given by:

$$\Delta\mathrm{FWHM}_{RF} = \frac{\mathrm{FWHM}_G \cdot \Delta\mathrm{FWHM}_G}{\sqrt{\mathrm{FWHM}_G^2 + \mathrm{FWHM}_{ThRF}^2}} \tag{5.37}$$

$$\Delta\mathcal{L} = \Delta\lambda_{T_e} = \frac{\mathcal{K}}{\mathrm{FWHM}_{RF}}\Delta\mathrm{FWHM}_{RF} \tag{5.38}$$

The final result for the length of the ineffective layer is taken to be the weighed mean of the values achieved with the different gases.

physical quantity	*origin*	**M1 He-like Ar**	**M1 He-like Cl**	**M1 He-like S**
E [eV]	[110]	3104.18	2756.85	2430.34
θ_B [degrees]	XOP [84]	39.5639386	45.8225983	54.4430162
Λ_σ [μm]	XOP [84]	0.725	0.733	0.752
Λ_π [μm]	XOP [84]	3.843	25.537	2.323
Λ [μm]	(5.36)	1.220	1.425	1.136
μ_a [cm^{-1}]	XOP [84]	2081.47	2856.76	3968.44
λ_D [μm]	(4.16)	1.530	1.255	1.025
λ_T [μm]	(4.17)	**0.679**	**0.667**	**0.539**
		60×95 mm		
FWHM$_{ThRF}$ [μrad]	XTRACK	112.0	136.4	167.6
$\mathcal{K}$ [μrad$\cdot\mu$m]	(5.33)	76.0480	90.9788	90.3364
FWHM$_{RF}$ [μrad]	(5.31)	116.7 ± 0.6	142.4 ± 0.6	176.9 ± 0.9
λ_{T_e} [μm]	(5.34)	0.652 ± 0.004	0.639 ± 0.003	0.511 ± 0.003
$\mathcal{L}$ [nm]	(5.35)	**27 ± 4**	**28 ± 3**	**28 ± 3**
	weighed mean	**28 ± 2**		
		$\emptyset$40 mm		
FWHM$_{ThRF}$ [μrad]	XTRACK	109.5	131.0	164.4
$\mathcal{K}$ [μrad$\cdot\mu$m]	(5.33)	74.3500	87.3770	88.6116
FWHM$_{RF}$ [μrad]	(5.31)	113.6 ± 0.6	135.5 ± 0.6	172.3 ± 1.1
λ_{T_e} [μm]	(5.34)	0.655 ± 0.004	0.645 ± 0.003	0.514 ± 0.003
$\mathcal{L}$ [nm]	(5.35)	**24 ± 4**	**22 ± 3**	**25 ± 3**
	weighed mean	**24 ± 2**		

Table 5.10: Calculations of the penetration depth, effective penetration depth and ineffective layer of Z13 under the model described within the text.

A small difference is seen between the results obtained with the different active areas. Although the difference is small and not significant within the errors it can be interpreted by admitting that the values obtained for $\mathcal{L}$ are an average of $\mathcal{L}$ over the crystal's surface. It is expected that the crystals have better surface properties at the center which would lead to a less pronounced Gaussian broadening. Therefore, the ineffective layer near the center would be thinner than on the outer part of the crystal's disc. As a larger area of the outer region is exposed to the incoming beam when using the 60 × 95 mm aperture, the value of $\mathcal{L}$ is naturally higher.

An overall consistency is observed among the results which gives a stronger validity to the model. Moreover, a picture of a 2×2 mm^2 area around the crystal center taken with an interferometric microscope from ZIGO® revealed a rough surface within a range tickness of 16 nanometers [145]. This is in fair agreement with the estimated length of the ineffective layer.

Extrapolation of the FWHM of the Gaussian for 2.25 keV

In order to extrapolate the Gaussian broadening for the μH($3p - 1s$) transition energy a calculation similar to the one described in table 5.10 was performed by taking $\mathcal{L}$ as a known constant. The results and main data are presented in table 5.11.

physical quantity	*origin*	**60×95 mm**	**∅40 mm**
E [eV]	[110]	2249.46	
θ_B [degrees]	XOP [84]	61.5165029	
Λ_σ [μm]	XOP [84]	0.775	
Λ_π [μm]	XOP [84]	1.421	
Λ [μm]	(5.36)	1.003	
μ_a [cm^{-1}]	XOP [84]	4831.99	
λ_D [μm]	(4.16)	0.910	
λ_T [μm]	(4.17)	**0.477**	
FWHM$_{ThRF}$ [μrad]	XTRACK	208.4	202.0
$\mathcal{K}$ [μrad·μm]	(5.33)	99.4068	96.354
$\mathcal{L}$ [nm]	table 5.10	28 ± 2	24 ± 2
λ_{T_e} [μm]	(5.35)	0.449 ± 0.002	0.453 ± 0.002
FWHM$_{RF}$ [μrad]	(5.34)	221.4 ± 1.0	212.7 ± 0.9
FWHM$_G$ [μrad]	(5.31)	**75 ± 3**	**67 ± 3**

Table 5.11: Results of the extrapolation of the Gaussian broadening at 2.25 keV for Z13 based on the ineffective layer model.

The error on the Gaussian broadening is obtained again by applying the error propagation theory. According to the previous estimate for the error in $\mathcal{L}$ it follows:

$$\Delta\lambda_{T_e} = \Delta\mathcal{L} \tag{5.39}$$

$$\Delta\mathrm{FWHM}_{RF} = \frac{\mathcal{K}}{\lambda_{T_e}^2}\Delta\lambda_{T_e} \tag{5.40}$$

$$\Delta\mathrm{FWHM}_{G} = \sqrt{\frac{\mathrm{FWHM}_{RF}^2 \cdot \Delta\mathrm{FWHM}_{RF}^2}{\mathrm{FWHM}_{RF}^2 - \mathrm{FWHM}_{ThRF}^2}} \tag{5.41}$$

It should be noted that the extrapolated value for the Gaussian broadening by using this hypothetical model is about 20% higher than what would be obtained by a linear or exponencial fit to the function FWHM$_G$(E). Such a difference has a negligible impact on the FWHM of the response function, about 1%. Hence, no influence on the analysis of the μH data would be expected. However, despite the simplicity of the linear/exponential fit with its straightforward result, the present model offers in addition a fair physical explanation of the Gaussian broadening.

This constituted the last step on the characterization of the Z13 Si(111) crystal. All the gathered information will be used in the analysis of the $3p - 1s$ transition in μH.

Chapter 6

The μH($3p-1s$) transition: measurement and analysis

The energy shift by Doppler effect due to Coulomb deexcitation of the πH systems broadens the spectral lines of the $np-1s$ transitions measured in πH in addition to the strong interaction broadening Γ_{1s} of the ground state. It has therefore a direct impact on the accuracy of the extraction of Γ_{1s}.

At present, there is still some lack of knowledge in the understanding of the processes governing the deexcitation in exotic hydrogen. Mainly the cross sections of the Coulomb deexcitation are under debate. This might prevent a consistent prediction of the kinetic energy of the πH systems at the instant of the radiative decay. In fact, the use of the present predictions for πH led to contradictory results in the extraction of Γ_{1s} [114].

The μH system can be seen as a twin system of the πH, as the reduced masses are similar. The muon does not experience strong interaction and thus, a broadening of any measured line will be exclusively caused by Doppler effect due to Coulomb deexcitation. Therefore, the μH constitutes a natural testing ground in order to identify the effects of the Doppler broadening on the line shape of an emitted characteristic X-ray. An investigation of μH transitions will constrain the cascade parameters and lead to better understanding of the processes during the cascade deexcitation, which can be used afterwards for a more accurate extraction of Γ_{1s} in πH. Moreover, it can test the validity of the box model (section 3.5, page 41) as an alternative to describe the kinetic energy distribution at the time of a radiative decay.

The $3p-1s$ transition of the μH ensured a good compromise between count rate and dispersion with the relative yield being maximum around 10 bar (see figure 3.9). The $2p-1s$ transition has about 50% higher rate at 10 bar, however the lower energy (∼1.9 keV) would be a major drawback concerning photoelectric aborption in the target window. The $4p-1s$ transition has only half of the maximum relative yield, compared to the $3p-1s$ transition. Hence, the $3p-1s$ radiative transition was the selected transition to be measured.

In addition, due to the high resolution of the bent crystal Bragg spectrometer, the hyperfine splitting and population of the ground state levels in μH are identified. It will be shown that this measurement constitutes the first direct experimental confirmation of a statistical population of the ground state hyperfine levels in μH. Moreover, for the first time, various contributions from the Coulomb deexcitation are unambiguously observed from the line shape of a radiative transition between atomic levels of an exotic atom.

A description of the experimental setup and some important aspects of the experimental procedure will be addressed at the beginning of the chapter. Subsequently, the analysis will be presented and discussed in detail as well as its impact on the cascade development and πH analysis.

6.1 The μH experiment

6.1.1 Pion beam and muon production

The production of exotic atoms relies strongly on an exotic particle beam with high intensity and low kinetic energy in order to achieve a high stop and capture rates of the particles by the target atoms. The proton accelerator at the Paul Scherrer Institut (PSI) provides a pionic beam line with high intensity and suitable low energy.

A Cockcroft-Walton voltage multiplier [147] accelerates the protons out from an ion source up to 870 keV. The protons are then injected in a first cyclotron which provides high quality and intense beam of 72 MeV to be injected into a ring cyclotron [148]. The proton beam is extracted from the ring cyclotron with an energy of 590 MeV. The extraction efficiency is about 99.7% and very high currents are obtained [148]. During the μH experiment in 2004 the beam had a maximum current of 1800 μA but a maximum of 2000 μA was already acchieved in 2007 with some upgrades to the ring cyclotron.

The proton beam is guided inside a vacuum system by bending magnets and quadrupole lenses onto a carbon target with a length in beam direction of 40 mm, named **target E**. A secondary beam line, named π**E5**, collects π^- and guides them into the experimental zone at 10...11 meters from the production target E, with a typical transmission factor of about 70...80% [149]. The πE5 provides a low energy beam with a momentum ranging from 10 to 120 MeV/c which is selected by tuning the bending magnets and the quadrupoles accordingly. The momentum has an acceptance of about 10% and a resolution of 2%. At the focus, the beam is 15 mm wide and 20 mm high with a horizontal and vertical angular divergence of 450 mrad and 120 mrad, respectively. A high neutron background is present in the experimental area with a flux of about 150 neutrons·mA^{-1}·s^{-1}·cm^{-2} for a pion beam momentum of 120 MeV/c.

The beam is tuned to provide pions with a momentum of 112 MeV/c which are injected into the cyclotron trap at a rate of few 10^8 s^{-1} [149]. The pions are slowed down by interaction with several degraders and a scintillator along their trajectory which is bent by the perpendicular and strong magnetic field (about 2.2 Tesla in the central plane) generated by the 124 A current in the superconducting coils of the trap. This reduction in kinetic energy together with the action of the magnetic field induces a spiral trajectory and forces the pions to move towards the axis of the cyclotron trap where the hydrogen target cell is placed.

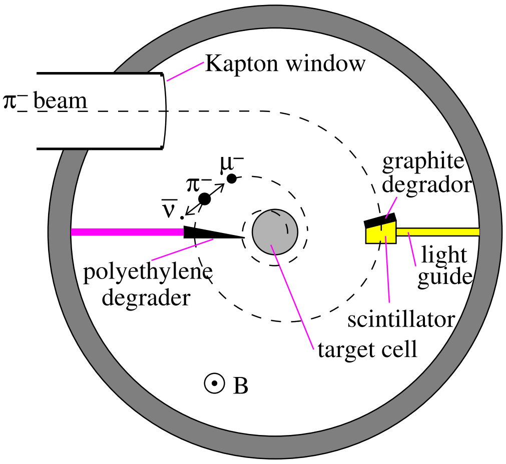

Figure 6.1: Schematic view of the deceleration process of the pions. The pionic beam is bent by the strong axial field. By crossing the degraders the pions loose momentum and consequently describe a spiral path towards the center. By adjusting the degraders a flux of low momentum muons can be obtained from the weak decay of the pions.

As pions decays to muons via weak interaction ($\pi^- \rightarrow \mu^- + \bar{\nu}$) with a very short lifetime ($\sim$ 26 ns), a muon flux can be produced inside the cyclotron trap by adjusting the degraders in order to extend the revolution time of the pions. Therefore, a flux of muons with low momentum is generated by the already slow pions close to the target cell. The muons will be driven in the same way as the pions to the center of the trap where they will stop and be captured by the target gas. A schematic view of the process is given in figure 6.1.

The magnetic field configuration and the deceleration scheme were optimized with tracking calculations [114]. About 1–3% of the incoming pions stops in hydrogen at 1 bar and room temperature. The pion stop rate scales linearly with the target density. The muon stop rate is calculated to be one order of magnitude smaller than the pion one.

The first degrader hit by the pions is made of graphite and its thickness can be adjusted in steps of 1 mm by piling elements with different thickness on top of each other. The graphite elements available ensured a maximum thickness of 10 mm. The graphite degrader is mounted on top of a plastic scintillator placed at 90 degrees from the top of the cyclotron trap. The scintillator is excited by the passage of the pions and the light pulses are led by a light guide to a photomultiplier placed outside of the cyclotron trap. The registered signals guarantee that the pion beam passed through the first degrader as well as they give a relative measurement of the number of pions entering the trap.

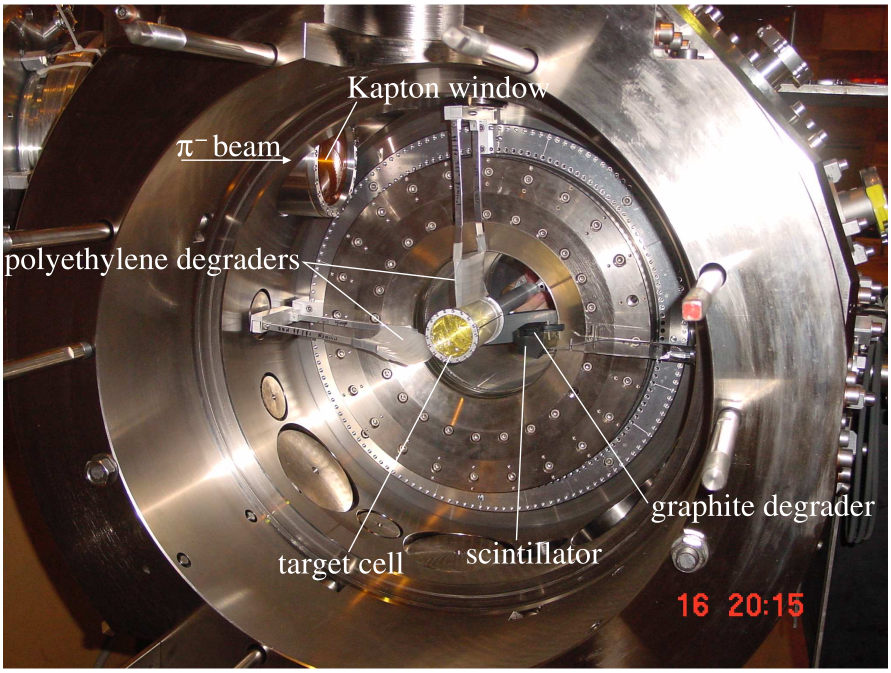

Figure 6.2: Picture of the chamber of the cyclotron trap with the diverse elements indicated. The deceleration scheme, given by the configuration of the degraders, is the one for the pionic hydrogen experiments.

A second degrader mounted in a aluminum frame was placed at a position of 270 degrees from the trap's top. The degrader was made of 105 μm thick polyethylene foils. The foils were "piled" with successive shorter lengths to ensure a wedge shape towards the center. Therefore, the pions with lower momentum and smaller orbit radius would cross less material. Four degraders were manufactured with approximately 120 mm width and 80 mm length and different maximum thicknesses: 5.6 mm, 4.2 mm, 2.8 mm and 1.4 mm, the last three having 75%, 50% and 25% of the thickness of the first one, respectively.

The polyethylene degrader with 5.6 mm at its thicker edge is named "nominal". This is the one which according to the tracking calculations maximizes the pion stop rate when placed at 270°, together with another polyethylene degrader at the position -5° and an extra graphite degrader. According to the calculations, to optimize the muon stop rate, the degrader with 50% of the nominal value placed at the 270° position together with extra an 3 mm graphite degrader should be used.

In figure 6.2, a picture of the cyclotron trap chamber is shown and the several degraders, sketched also in figure 6.1, are indicated. The extra degrader on top is the part of the deceleration scheme mentioned to be used in the pionic hydrogen experiments. It was removed for the muonic hydrogen measurements.

6.1.2 Target cell

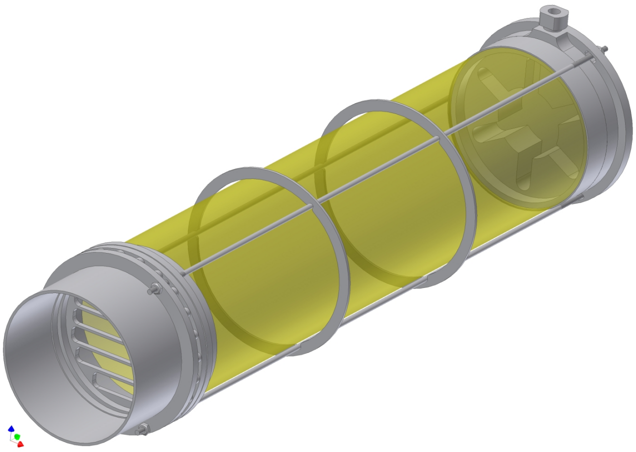

Figure 6.3: Three-dimensional view of the target cell used in the data acquisition. The gas inlet is visible at the back as well as the horizontal grating of the window frame at the front.

The target cell has a cylindrical shape with an inner length and inner diameter of about 250 an 60 mm, respectively. Aluminum frames stabilize the lateral Kapton wall of 50 μm thickness and the window made of 5 μm thick Mylar. The thin Mylar window minimizes the absorption of the 2.25 keV X-rays from the μH($3p-1s$) transition.

The window frame has a horizontal grating with seven horizontal slits, 6 mm high and separated by 1 mm. The three central ones are 48 mm long and the outer ones are 43 mm and 27 mm long. Although it reduces the exposed area, this is an essential feature to ensure that the thin Mylar window stands a pressure gradient up to 1.5 bar [150]. In figure 6.3 a three-dimensional view of the target cell is depicted.

The high hydrogen densities needed are obtained by cooling the target cell. The cooling was done through a cryostat externally mounted and the target cell was mounted on a copper cold finger connected to the cryostat. The mounting allowed the axial movement of the target cell without braking the vacuum. The target was cooled down to approximately 22 K and filled with about 1000 mbar of hydrogen which corresponds roughly to 10 bar at room temperature. More details about the cryogenic target can be found in [151].

6.1.3 General layout

The cyclotron trap is attached to the exit of the beam line in the πE5 area together with the Bragg spectrometer. A Kapton window separates the pion beam line from the cyclotron trap chamber. A massive concrete shielding provides a drastic background reduction. In figure 6.4 the layout of the setup at the πE5 experimental zone is shown together with the concrete shielding. The gap between the crystal and the detector was intentionally left open to allow the spectrometer movement. Once the spectrometer was correctly set, an additional wall of 100 cm was built around the vacuum tube by using small concrete bricks ($20\times10\times5$ cm) filling the gap and providing extra shielding. By piling small bricks an extra 30 cm concrete shielding was added in between the trap and the crystal. Moreover, where it was possible to fill the spaces between the massive blocks with the small bricks it was done.

The complete layout of the μH experiment is depicted in figures 6.5 and 6.6 with some elements indicated. More details about the concrete shielding are shown. The crystal was set 2620 mm away from the center of the cyclotron trap and 2552 mm from the linear table where the detector is mounted.

In order to solve the long term instability which had been seen in previous pionic hydrogen experiments [112] a bellow compensator was installed between the crystal's chamber and the detector's cryostat to release stresses possibly created when the cryo-

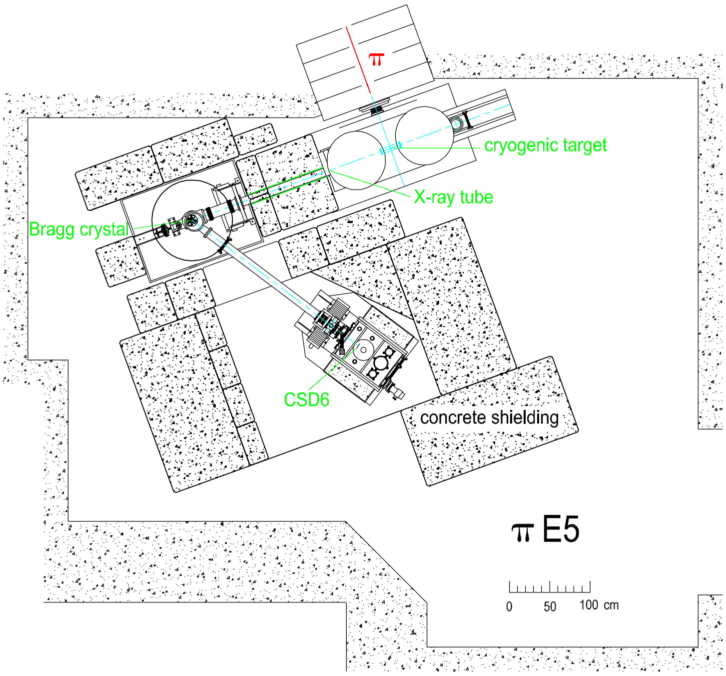

Figure 6.4: Layout of the μH setup at the πE5 experimental area. The massive concrete shielding is depicted and some elements are additionally indicated.

stat is moved. Moreover, the concrete blocks were placed on two layers of wood and hard plastic of about 3 cm thickness each. This helped to damp any vibrations of the concrete shielding and consequently increased the stability of the spectrometer.

The vacuum inside the system was ensured by three turbomolecular pumps placed at different positions: at the bottom of the cyclotron trap, at the crystal's chamber (both not depicted in figures 6.5 and 6.6) and at the detector's cryostat. During the data acquisition a vacuum better than 5×10^{-6} was achieved.

Two gate valves could isolate the three main parts: trap, crystal chamber and detector's cryostat. The one separating the trap from the spectrometer is not depicted in figure 6.5 and it was mounted in between the trap and the flange assembling the X-ray tube. The gate valve which isolated the detector's cryostat was a safety valve with a pneumatic actuator. It could automatically close in case of target explosion or a general vacuum break, minimizing the risk of damaging the CCD detectors. Nevertheless, manipulations of the target cell, such like filling, were always performed with the cyclotron trap isolated from the spectrometer to minimizes the damage of a possible explosion of the target cell.

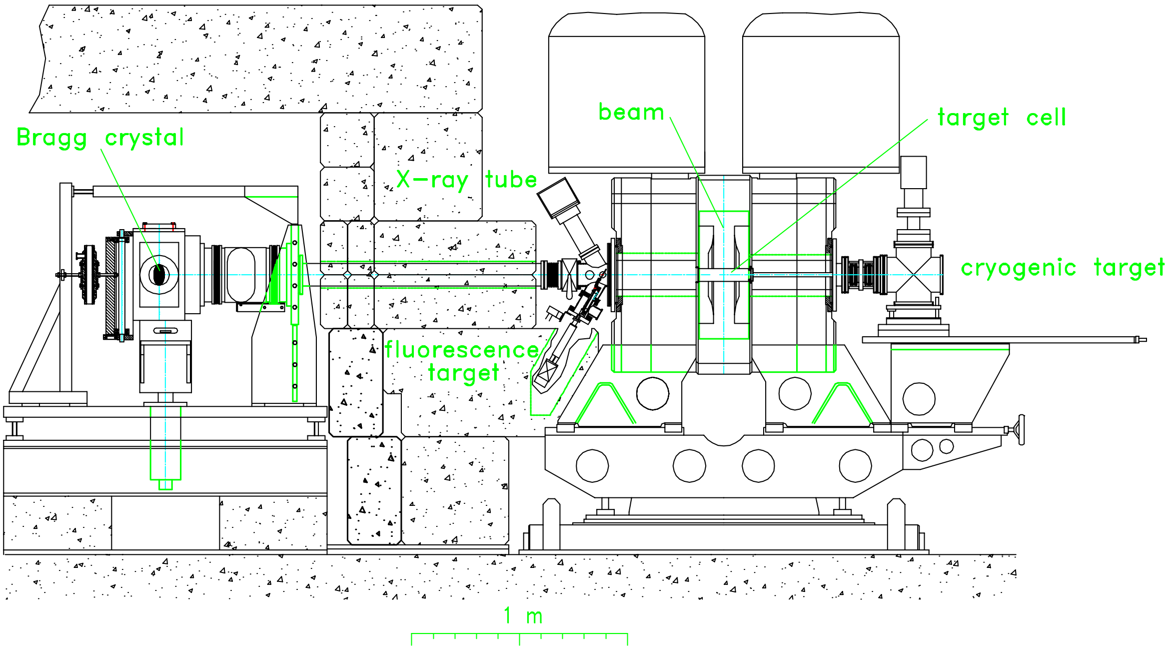

Figure 6.5: Technical drawing of the setup of the cyclotron trap and the crystal's chamber. The cryostat for the target cell can be seen flanged at the right of the cyclotron trap. A gate valve (not depicted) was placed between the cyclotron trap and the flange supporting the X-ray tube and the fluorescence target.

It is not feasible to use the radiative transitions in μH to align the spectrometer due to their very low count rate. Therefore, fluorescence X-rays with an overlapping Bragg angle and high intensity are desirable. The Kα_1 and Kα_2 fluorescence lines of selenium (Se) with 11222.52 eV and 11181.53 eV [152], respectively, are adequate candidates. Their energy is approximately 4.99 and 4.97 larger than the μH($3p-1s$) transition energy, respectively. Thus, in fifth order they have a similar Bragg angle.

A sample of metallic selenium powder with 28×25 mm was assembled on a support which could be moved by a step motor remotely controlled. The mounting was flanged with an orientation of 60 degrees to the vacuum tubes (see figure 6.5). An X-ray tube was used to excite Se and it was flanged to the tubes with an orientation of 120 degrees to the fluorescence target (see figure 6.5).

The Se-Kα lines were additionally used to monitor the stability of the spectrometer during the long term data acquisition. A nivelmeter was installed outside of the detector's cryostat to double check the system stability. The device was connected to a

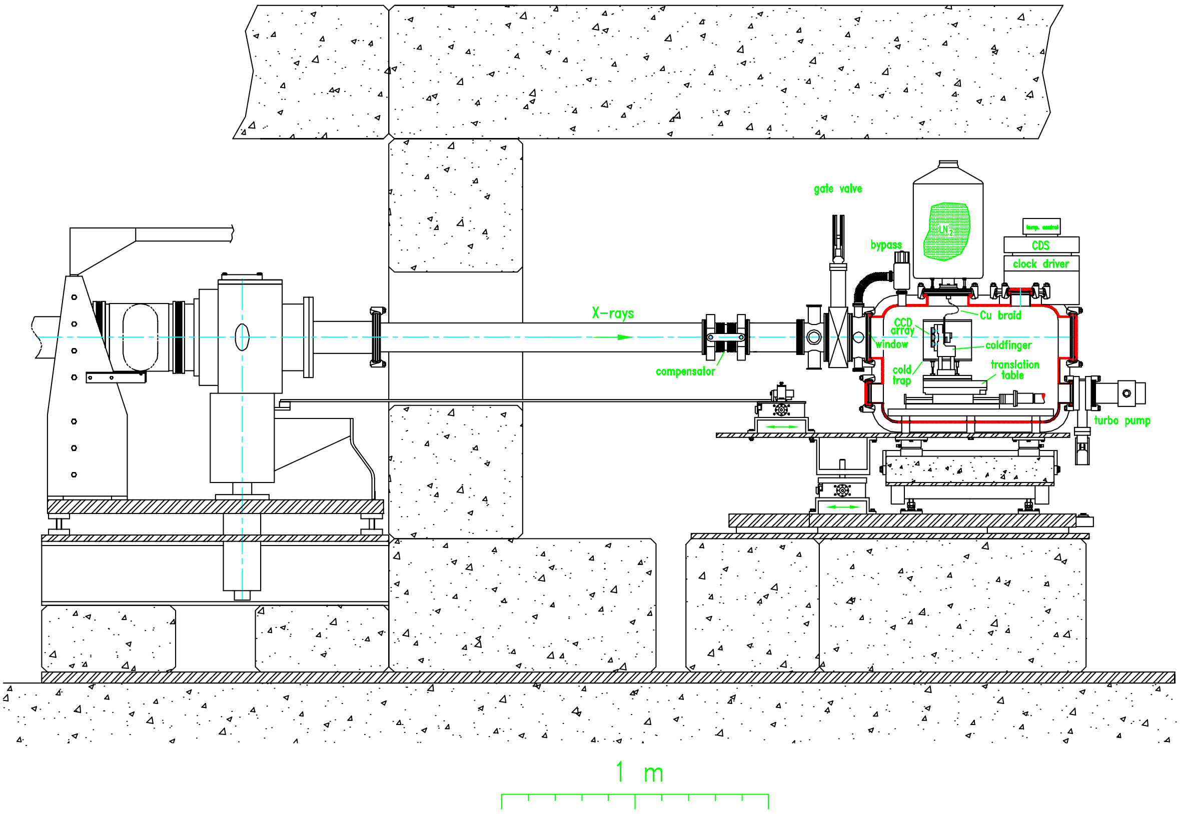

Figure 6.6: Technical drawing of the setup of crystal's chmaber and detector's cryostat. An ^{55}Fe source (not depicted) was installed at the flange drawn between the compensator and the gate valve in front of the detector's cryostat.

computer and through a dedicated software its coordinates could be registered. Once it had been set, its coordinates were registered every 15 minutes. Therefore, any change in the position of the cryostat could be tracked.

The ^{55}Fe source, which provides the energy calibration of the CCDs, was mounted on the flange between the compensator and the gate valve at the detector's cryostat. It could be shifted in front of the detector manually without braking the vacuum.

A 5 μm thick Mylar window was placed at the entrance of the detector's cryostat to provide additional protection to the CCDs. The Si(111) labeled Z13 was used. A circular aluminum aperture of 90 mm diameter was used to limit the active area of the crystal to almost the maximum. The detector was placed at the focal distance according to the best knowledge available at that time. The distance from the crystal to the CCDs was set to be 2622.61 mm. The table 6.1 resumes important geometrical quantities and some other important aspects of the experiment are collected in table 6.2.

Transition	E [eV]	m	θ_B [degrees]	Θ_{ARM} [degrees]	dispersion [pixel·eV^{-1}]	$R_c \sin\theta_B$ [mm]	Cry-Det [mm]
Se Kα_2	11181.53	5	62.1431	124.27	11.09	2636.98	2622.61
Se Kα_1	11222.52	5	61.7497	123.50	10.87	2627.35	2622.61
μH$(3p-1s)$	2249.46	1	61.5156	123.03	53.72	2621.86	2622.61

Table 6.1: Some important geometrical parameters of the μH setup corresponding to the energies of the Se-Kα calibration lines and the μH$(3p-1s)$ transition. The Bragg angles and dispersions were obtained considering the miscut of Z13 and taking the radius measured at *Zeiss*® (R_c = 2982.2 mm). The lattice spacing of Si(111) was from XOP [84] ($d = 6.2708322$ Å). The distance detector–crystal used during the experiment was set according to the best knowledge at the time.

H_2 target pressure:	$\approx$ 1020 mbar
H_2 target temperature:	$\approx$ 22 K
H_2 target equivalent pressure at 293 K:	$\approx$ 12.5 bar
ultimate pressure at the cyclotron trap:	$\approx 5\times10^{-7}$ mbar
ultimate pressure at the crystal's chamber:	$\approx 4\times10^{-6}$ mbar
ultimate pressure at the detector's cryostat:	$\approx 3\times10^{-7}$ mbar
distance from the crystal to the center of the cyclotron trap:	2620 mm
active area of the crystal	$\emptyset$ 90 mm
crystal's temperature:	$\approx$ 25°C
temperature of the CCDs:	≈ -100°C
current of the superconductor coils of the cyclotron trap:	124 A
beam current during the experiment:	< 1800 μA

Table 6.2: Some experimental conditions during the data acquisition. The vacuum pressures indicated correspond to the minimum values achieved during the run with each part isolated from the others.

6.1.4 Optimization of the muon stop rate

In order to maximize the muon stop ratio at the target cell, the settings of the last quadrupole elements at the πE5 beam line were optimized. Additionally, a study of the deceleration scheme inside the trap was performed. Both were possible by taking advantage of a compact pnCCD system with fast embedded read-out which was able to take 500 frames per second [153].

The pnCCD system is a XEDS (X-ray energy dispersive spectroscopy) detector with outstanding energy resolution, compared to other XEDS detectors. Moreover, it provides extremely good reduction of the beam background via cluster analysis. The system needs to be permanently cooled, which is done via a cold finger connected to a liquid nitrogen container. More details about the pnCCDs detector system can be found in references [153, 154].

The setup is depicted in figure 6.7. The pnCCD was placed 777 mm from the center of the cyclotron trap. The optimization of the beam injection was done with helium (easier to handle compared to hydrogen) at a pressure of 1.25 bar and room temperature.

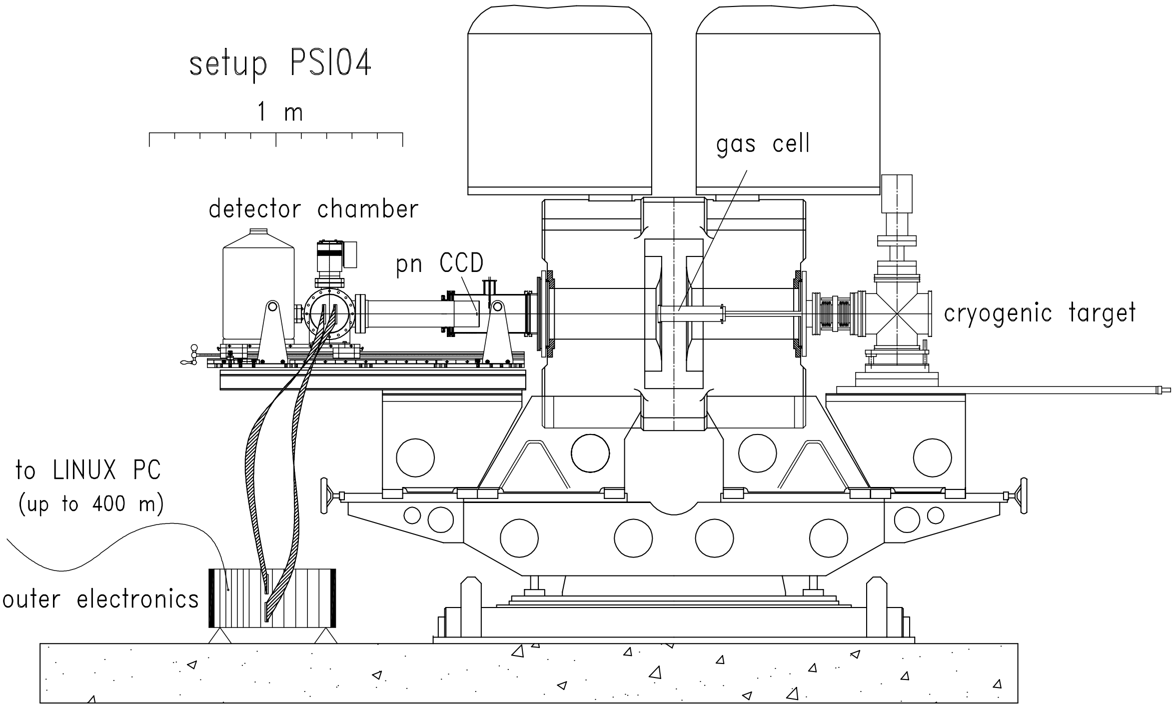

Figure 6.7: Setup to optimize the π injection for high muon stop rate. The detector system was flanged to the cyclotron trap with the pnCCD placed 777 mm from the center of the trap. The system is cooled by a cold finger connected to a liquid nitrogen reservoir placed behind the detector chamber.

In the first step of the optimization, the polyethylene degrader with 50% of the nomimal thickness was placed at the 270° position. No degrader was used at the -5° position, which would be the best case according to the tracking calculations. The thickness of the graphite degrader was changed in steps of 2 mm from 1 mm to 7 mm. The spectral line corresponding to the $2p-1s$ transition in μHe was evaluated by fitting a gaussian superimposed on a linear background. The area under the Gaussian is correlated to the line intensity. The intensities were normalized to the amount proton-beam charge collected in about 1 hour corresponding to approximately 2 million frames. In figure 6.8 an example of a helium spectrum taken with the pnCCD detector during the optimization is depicted. The fit to the Kα lines is shown as well.

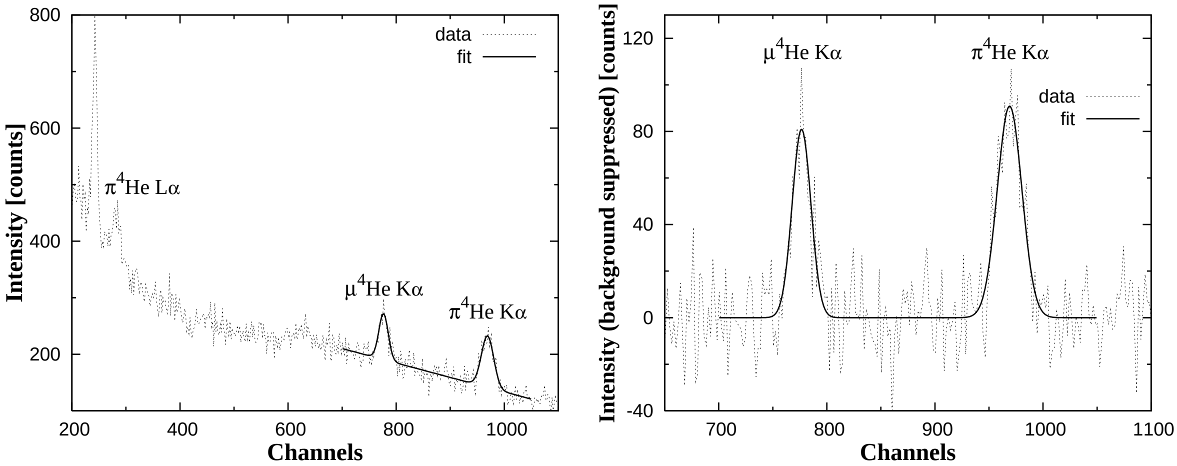

Figure 6.8: Example of a helium spectrum taken during the injection optimization with the main lines identified. The pressure at the target cell was 1.25 bar. A 2 mm thick graphite degrader was used. The polyethylene degrader with 75% of the nomimal thickness was placed at the 270° position. No degrader was placed at the -5° position. The Kα spectral lines were fitted by a Gaussian superimposed on a linear background which is good enough for the present purpose. The interval [700:1050] was used as region of interest. At the right, only the Kα transitions in μHe and πHe with the background subtracted are shown.

The results for the first step of the optimization are plotted in figure 6.9a. It is clear that the use of a degrader a bit thicker than 5 mm leads to a decrease of the stop rate of the muons. However, it is not possible to unequivocally conclude which thickness is better: 3 or 5 mm. The best muon stop rate is achieved within this thickness interval. Hence, 4 mm was used as best compromise in the following step.

A study of the polyethylene degrader was then performed. The results are shown in figure 6.9b. The optimum deceleration scheme was achieved with a polyethylene degrader of 75% of the nominal. By comparing to the result obtained with degrader with 50% of the nomimal thickness, an increase of more than 25% in the muon stop rate was verified.

Therefore, a new optimization by changing the thickness of the graphite degrader and using the polyethylene degrader with 75% of the nominal was performed. The results are shown in figure 6.9c. The thickness was varied in steps of 2 mm from 0 to 6 mm. The maximum stop rate of the muons was achieved in the interval from 2 to 4 mm. A significant reduction was verified outside this interval. The middle point was assumed to maximize the stop rate of the muons, hence 3 mm was taken as best value.

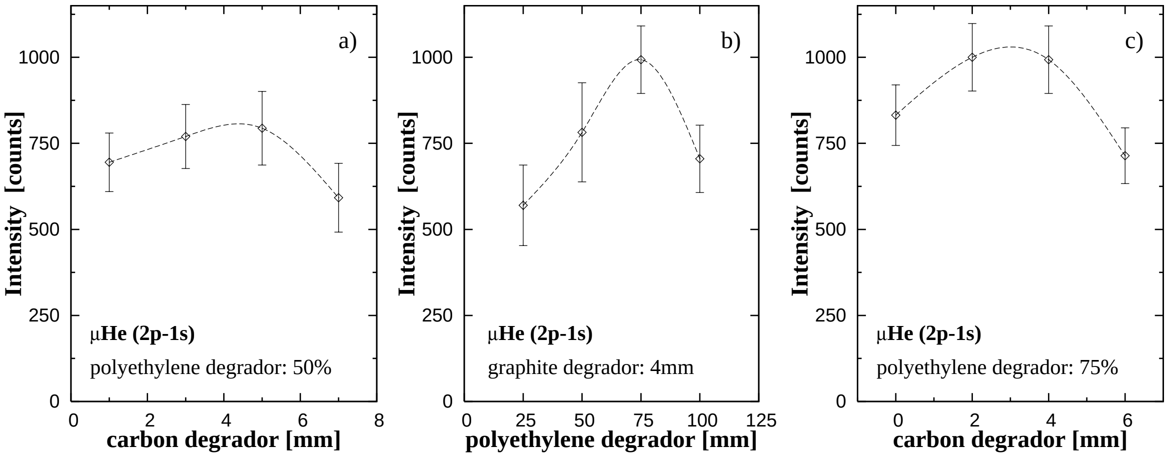

Figure 6.9: Results of the optimization of the deceleration scheme for high muon stop rate. The intensity of the μHe $(2p-1s)$ transition was evaluated by fitting a Gaussian superimposed on a flat background of first order. The results were normalized to the amount of charge collected in about 1 hour ($\approx$ 2 million frames). In a) the thickness of the graphite degrader was changed by using the polyethylene degrader of 50% of the nominal. In b) the thickness of the polyethylene degrader was changed by using the best graphite degrader found previously. In c) the thickness of the graphite degrader was evaluated by using the polyethylene degrader of 75% of the nominal.

A last test was done by using the optimum deceleration scheme found previously and introducing a polyethylene degrader at the -5° position. This degrader had a thickness of 1.5 mm at its thicker edge and 0.61 mm at its thinner edge. A reduction of about 20% in the muon stop rate was obtained. Accordingly, it was concluded that a graphite degrader 3 mm thick together with a polyethylene degrader 75% of the nominal and placed at the 270° position is the deceleration scheme which optimizes the pion injection for high muon stop rate.

6.1.5 Crystal alignment and target scan

A rough alignment by means of a laser, similar to the one described in section 5.1.3 (page 111), was initially performed.

A more refined alignment was done afterwards by using the Se-Kα lines. The tilt of the crystal was first adjusted by limiting the crystal active area to a height of 20 mm. The spectrometer was aligned so that the μH($3p-1s$) transition would be placed around channel 1000. Therefore, the Se-Kα_1 was set to be reflected around channel 740 as the lines should be about 255 pixels apart.

The energy range given by the 1000 pixels at the low energy side of the μH($3p-1s$) transition is about 20 eV. This was of particular interest to check the presence of satellite lines from the deexcitation of molecular resonance states at the $3p$ level to the ground state of the atomic muonic hydrogen:

$$pp\mu^*(3p) \rightarrow p\mu(1s) + p + \gamma \tag{6.1}$$

The binding energy of the molecular states would lead to a decrease of the energy of the $3p$ level and consequently to a radiative transition to the atomic ground state with reduced energy. Several of these possible transitions would fall in the 20 eV range below the atomic μH($3p-1s$) transition [155].

On the other hand, the 200 channels in the higher energy side would be enough to ensure a good coverage of the long tail of the μH($3p-1s$) spectral line as well as a good determination of the background level.

Se-Kα target scan

By keeping the Θ_{CRY} fixed, a target scan of the Se-Kα fluorescence transitions was performed. The X-ray tube was set to 40 kV and 20 mA. Four frames were taken at each Θ_{ARM} position. The intensity of the lines was evaluated by fitting a Lorentzian to the data which is sufficient for this purpose. The results, as well as an example of a fit, are depicted in figure 6.10. The 55° stated for the Θ_{ARM} is merely indicative and corresponds to the reading at the software used to control the spectrometer. As already stated before, only readings of the angular differences matter.

A Θ_{ARM} around $55°25'$ maximizes the intensity of the Se-Kα_1 transition. At this angle the Se-Kα_2 is almost suppressed. Hence, as Se-Kα_1 is closer to the μH($3p-1s$) transition, the spectrometer was set to $\Theta_{ARM} = 55°25'$.

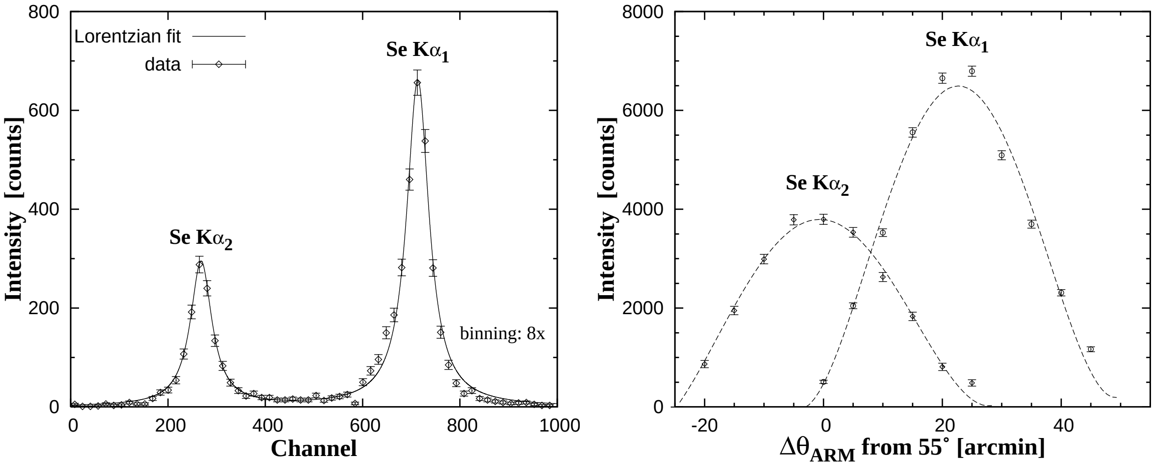

Figure 6.10: The results of the target scan with the Se-Kα are depicted at the right. $\Theta_{ARM} = 55°25'$ was found to maximize the intensity of the Se-Kα_1. At the left, an example of a fit to the Se-Kα lines by using two Lorentzians is shown. The spectrum has a binning factor of 8 in order to eliminate some statistical fluctuations. The fit is pretty fair and the procedure revealed to be sufficient for this purpose.

Afterwards, the electric potential of the X-ray tube was additionally optimized as function of the brightness of the selenium fluorescence Kα_1. An interval ranging from 30 kV up to 60 kV was studied. In order to have a constant power of 1 kW (the maximum power which could be delivered by the apparatus), the current was accordingly adjusted. An increase of more than 50% in the Se-Kα_1 intensity was registered when going from 30 kV to 40 kV followed by a saturation. Consequentely, the X-ray tube was set to 40 kV and 25 mA.

μH$(3p - 1s)$ target scan

With the spectrometer aligned, a target scan with the μH$(3p - 1s)$ X-rays was performed. Although it is assumed that the capture of the muons at the middle of the target cell is favored, this should not be taken for certain. Moreover, it could not be ensured that the optimum Θ_{ARM} for the Se-Kα_1 and μH$(3p - 1s)$ transitions coincide.

Several regions of the target were scanned and about 20 Cb of beam charge were collected at each position for Θ_{ARM}. The charge collected corresponds roughly to 3 hours of data acquisition at the maximum and constant beam current. The relation between the maximum opening of the target window (48 mm) and its distance to the crystal ($\approx$ 2495 mm) determines that $65'$ is the angular range for Θ_{ARM} which is possible to be studied.

Opposite to the selenium fluorescence lines, the very low statistics does not permit a line fitting. Hence, the number of events were estimated by doing the following procedure. Three regions of 100 channels each, one around the position where the μH($3p-1s$) transition was expected and the other two at each side of this region, were selected. The average between the number of events in the external regions was assumed to be the background per 100 pixels. Therefore, by subtracting this amount from the total number of events in the central region an estimate for the number of events in the μH($3p-1s$) spectral line was obtained. The results for the count rate of μH($3p-1s$) transitions as well as for the background are depicted in figure 6.11.

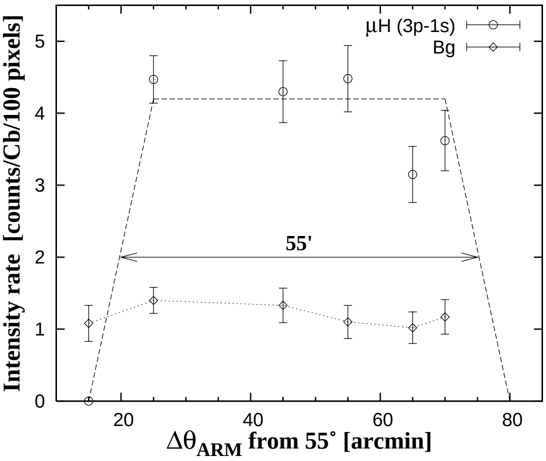

Figure 6.11: Results of the target scan for the count rate of the μH($3p-1s$) spectral line. The count rate of the background is shown as well for comparison. The trapezoid in dashed line is only to guide the eye along the angular range possible to be scanned.

A maximum of more than 4 events in the line per collected charge unit was achieved in a wide angular range. The background level was constant and about 1.1 event per Coulomb per 100 channels. The slightly decrease registered at one side of the target cannot be excluded to be merely due to statistics. Nevertheless, it was taken as a real drop in the count rate. Hence, based on the results the spectrometer was set to Θ_{ARM}=55°35′. Being far enough from the target limits, this position ensures a maximum count rate. A drop by about 50% on the Se-Kα_1 intensity is expected (see figure 6.10) which is irrelevant regarding its purpose to monitor the spectrometer stability.

Additionally, the crystal tilt was slightly readjusted by using the μH($3p-1s$) data. From this moment on the spectrometer remained fixed at these angular settings.

6.1.6 Mechanical stability of the spectrometer

In order to monitor the stability of the spectrometer, several Se-Kα_1 spectra were taken over the 4 weeks of data acquisition. The data was recorded during the long maintenance breaks when refilling the liquid helium of the reservoirs of the cyclotron trap. At least 60 frames of data were collected in each spectrum.

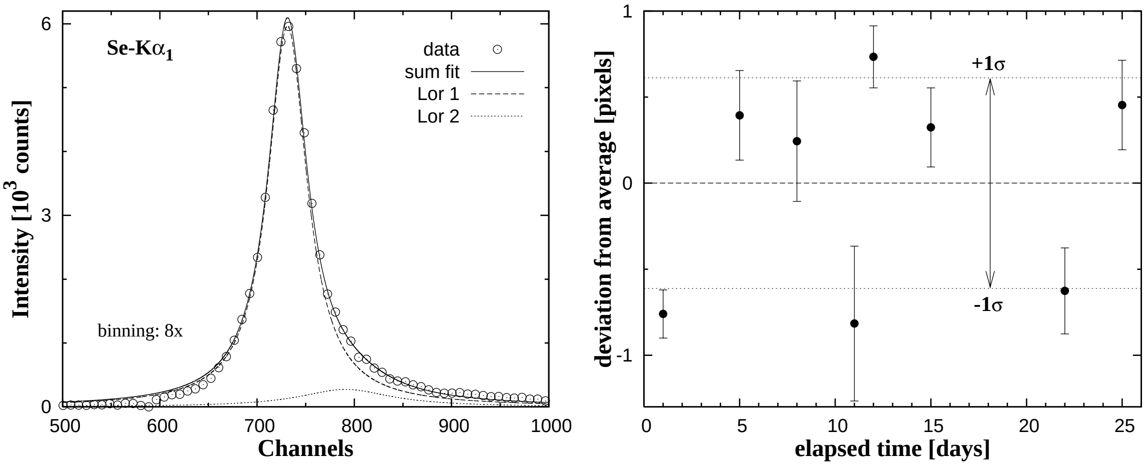

Figure 6.12: An example of the fit of the Se-Kα_1 line by means of two Lorentzians is depicted at the left. The error bars are smaller than the points used to plot the data. The spectrum has a binning factor of 8 times in order to not overload the figure. The variation, during the data acquisition, of the position of the main Lorentzian peak from the arithmetic mean is shown at the right. The dotted lines correspond to the standard deviation of the distribution. The elapsed time is counted from the target scan performed with the μH($3p-1s$) transition.

Several satellite lines are present in the Se-Kα_1 spectrum [156, 157]. However, a fair fit is already achieved by using two Lorentzians, as the example depicted in figure 6.12 shows. This approach is sufficient for the present purpose. The results for the variation of the position of the main peak from the average are also resumed in figure 6.12.

During the pre-analysis done at the time of data acquisition it was observed that a slightly different parameterization of the curvature correction could lead to a shift of about 2 pixels in the line position. Therefore, for the final analysis the same curvature parameterization, obtained with one of the spectra, was used to restore the line shape of all spectra.

The analysis of the Se-Kα_1 spectra demonstrated that the horizontal variation was less than 1.5 pixels, as shown in figure 6.12.

On the other hand, the data recorded by the nivelmeter confirmed the stability of the spectrometer. As shown in figure 6.13 [158], despite a continuous drift observed in the horizontal position of the spectrometer, a maximum variation of about 1.3 pixels was registered over all the μH$(3p-1s)$ data acquisition. The larger oscillations are well justified by the maintenance work (indicated in the figure), particularly the vertical spikes caused by the liquid nitrogen filling. No μH data was taken during these procedures.

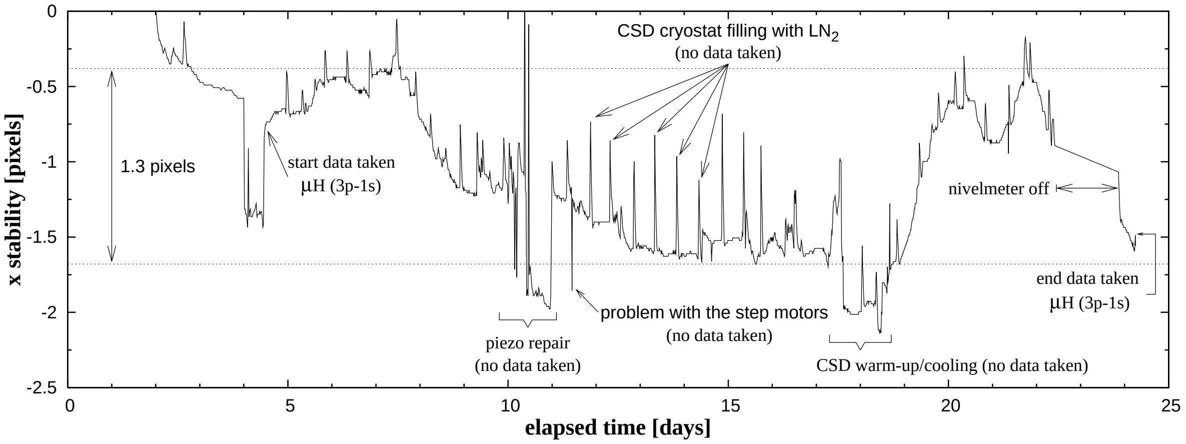

Figure 6.13: Variation of the horizontal position of the spectrometer based on the data of the nivelmeter which was installed outside the detector's cryostat [158]. The dotted lines represent the upper and lower limits of the region where the position varied during the data acquisition (from day #4 on). The main events which could induce abrupt oscillations are indicated.

Hence, the analysis of the variation of the horizontal position of the spectrometer by both methods revealed an unprecedent stability compared to previous runs. As example, during the run of 2001 a drift of about 10 pixels was observed in the positions of the spectral lines [112]. The small variation observed now, in the range of 1 pixel, can be neglected relative to the measured μH($3p-1s$) line width of approximately 27 pixels. Therefore, contrary to previous analysis [112], it is not required to perform a positional correction of the μH ($3p-1s$) data.

6.1.7 Evolution of the count rate

During the first days of data acquisition a significant drop in the count rate of the μH spectral line was noted. A decrease between 30% and 40% was registered after six days of measurement (see figure 6.14). As the decrease seemed to be more pronounced with the elapsed time, this could lead to a dramatic loss in the statistics of the experiment. Additionally, with the background remaining constant it would lead to a much poorer peak-to-background relation.

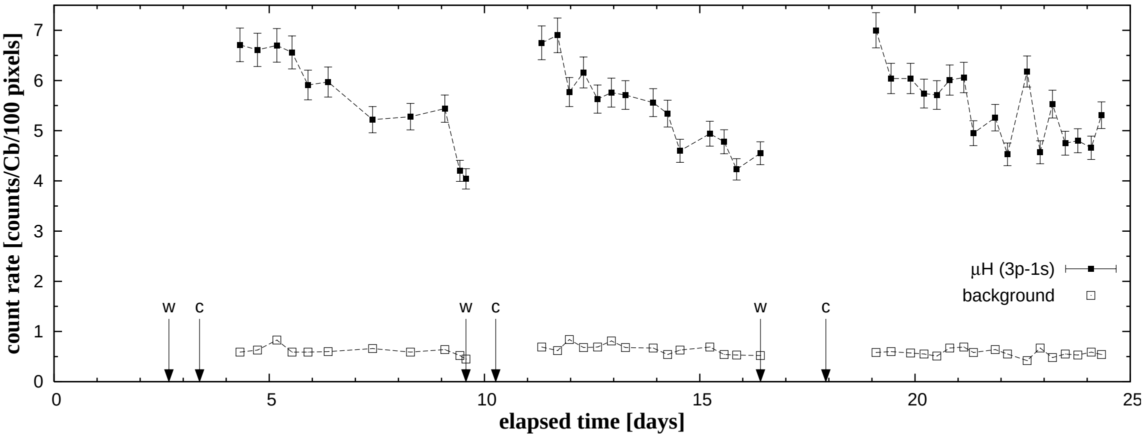

Figure 6.14: Evolution of the count rate of the μH($3p-1s$) spectral line. The count rate of the background is also depicted for comparison. The beginning of the warm-up and cool-down procedures are indicated by arrows with the label "w" and "c", respectively. The error bars of the count rate of the background are smaller than the size of the points chosen to plot the data.

The problem was related to the target cell which is the coldest element inside the cyclotron trap chamber. Its surface act like a cryogenic pump by collecting the moisture molecules which are still present in the vacuum. Consequently, the window can accumulate a thin ice layer which absorbs the μH($3p-1s$) X-rays. Therefore, it was decided to warm-up the target cell slightly above 0° to eliminate the possible ice layer on the window.

The figure 6.14 confirms that after the target cell has been warmed-up the count rate could be always restored. The procedure was repeated once a weak with very successful results. The warming-up and cooling-down of the target cell could take nearly 24 hours. However, it was possible to synchronize it with the weekly stop of the proton beam which always lasted more than the predicted 16 hours. Moreover, the mandatory filling of the reservoirs of the cyclotron trap with liquid helium once every three days and its synchronization with the weekly beam stop would force anyway a stop of 24 hours after the beam shutdown. Yet, no beam time was wasted due to the maintenance tasks as the synchronization was perfect.

In order to clarify the origin of the hypothetic ice layer, the development of the vacuum pressure during the warm-up process was registered as function of the temperature. A typical warm-up curve obtained during the procedure is depicted in figure 6.15.

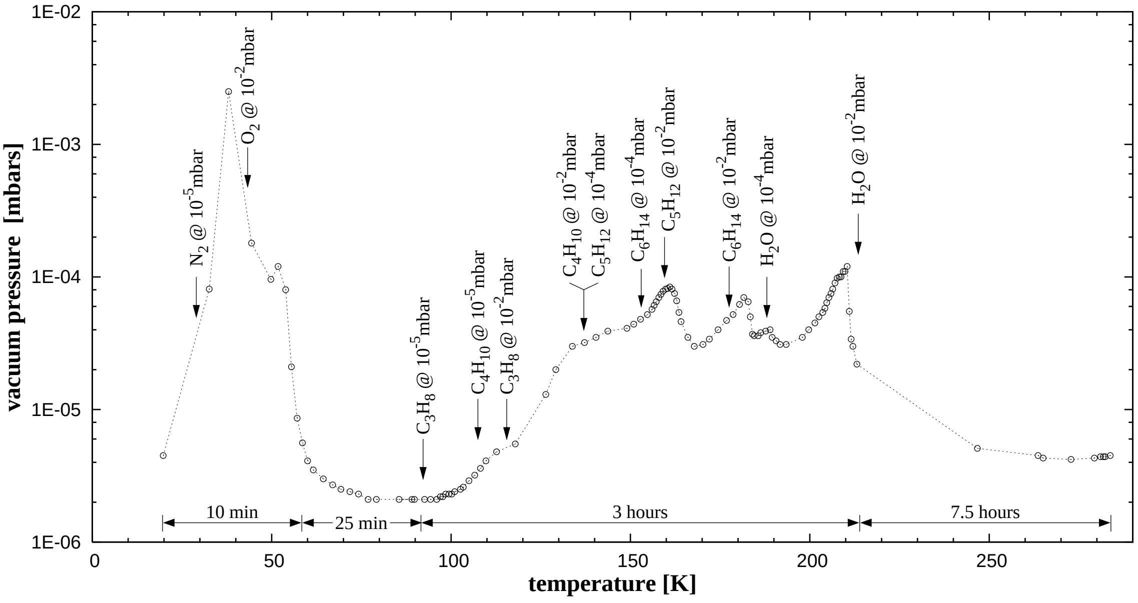

Figure 6.15: Example of a warm-up curve of the target cell obtained during the μH$(3p-1s)$ run. The sublimation points with the corresponding vapor pressures of the relevant compounds are indicated [159, 160]. The hydrocarbons mentioned are the ones with the simplest chain. The elapsed time of several temperature intervals is indicated for comparison.

The curve has several pressure peaks which can be explained by the sublimation of the compounds usually present in a vacuum system: air (mainly nitrogen and oxygen), hydrocarbons (C_nH_s, $n \geq 3$) and water, which would be frozen on the target surface. The sublimation points with the respective vapor pressure of the compounds of interest are indicated in the figure.

A more consistent and robust explanation of the curve would require further investigations but a fair interpretation can be given.

The warm-up process is done by turning off the compressor and by heating-up the target cell from its back through a resistor element of 6.2 W. The target cell was emptied to about 100 mbar and the heat transfer from its back part to the surface is done mainly by gas convection. The temperature is also measured at the back of the target cell and a gradient between the window and the back is admitted.

At the beginning of the process the window might be at few kelvin warmer than the measured 20 K and when the compressor is turned off the nitrogen starts immediately to sublimate leading to an increase of pressure. The first peak would thus correspond to nitrogen.At higher temperatures the oxygen can sublimate which generates a second little peak in the curve. This peak is shifted by about 6-10 K from where it would be expected. However, the temperature at the back of the target takes only 10 minutes to rise the first 40 K. Consequently, a shift on the gradient direction can be generated with the convection not being efficient enough to ensure an equilibrium between the surfaces and the back part of the target. Hence, the target walls would be at a slightly lower temperature than its back.

With the temperature increase, the pressure inside the target cell also increases and due to the limitation of the resistive element the warming-up becomes slower. Therefore, it is expected that the convection becomes more efficient and the temperature gradient fades. Basically, all nitrogen and oxygen is pumped away before the next compound can sublimate, which happens around 90 K with the sublimation of the first compound of the hydrocarbon series.

The sublimation of the hydrocarbon series would be responsible for the following pressure plateau. The temperatures which can prompt the sublimation of the hydrocarbon series up to C_6H_{14}, at the corresponding vacuum pressures, are indicated in figure 6.15 as well as the sublimation points at $\approx 10^{-2}$ mbar. With the temperature rising, the sublimation rate of hydrocarbons is enhanced: more compounds can sublimate; the difference between the vacuum pressure and the corresponding vapor pressures for compounds which already initiate the sublimation is larger. The peaks were observed at the temperature corresponding to a vapor pressure $\approx 10^{-2}$ mbar, two order of magnitude higher than the vacuum pressure ($\approx 10^{-4}$ mbar). They can be explained by a large increase in the sublimation rate of the respective hydrocarbon leading to its total depletion from the target surface. In figure 6.15 only the hydrocarbons with a simple chain are indicated.

According to the vacuum pressure, the water would start to sublimate around 185 K leading to the pressure peak observed around 210 K. The slow pressure drop registered afterwards simply shows the difficulty to remove the water from a vacuum system.

The sublimation points with the corresponding vapor pressures were taken from *AVS reference guide* [159] for nitrogen and oxygen and calculated for the hydrocarbons and water based on Antoine's equation:

$$\log_{10}(\mathcal{P}) = A - \frac{B}{\mathcal{T} - C} \tag{6.2}$$

where $\mathcal{P}$ is the vapor pressure at a certain temperature $\mathcal{T}$ and A, B, C are experimental coefficients determined for a certain temperature range. The respective coefficients were taken from *NIST* [160] by chosing the most appropriate temperature range available.

6.1.8 The experimental routine and the data collected

The manpower was distributed according to the personal availability during the 20 days and by three daily shifts. The experiment was run 24/24 hours.

Individual files with 60 frames were recorded, which corresponds to approximately 65 minutes of acquisition time. Several experimental parameters were constantly monitored in order to ensure a steadily running setup. Two daily breaks of about 20 minutes were done to refill the detector cryostat and the trap reservoirs with liquid nitrogen.

At Wednesdays no proton beam was provided due to maintenance work and beam development. Hence, this time window was used to refill the reservoirs of the cyclotron trap with liquid helium and warm-up the target cell. The procedures caused a total stop of about 1.5 days. An extra break of about 6 hours was done every Sunday for the helium refilling. As already mentioned, the long breaks were used to obtain Selenium fluorescence spectra. This weekly schedule provided a very good synchronization between the forced breaks which minimized the beam time losses.

Unfortunately, during the acquisition time several unpredictable stops of the beam occurred due to multiple problems related with the beam line: vacuum problems and component failures. This resulted in the loss of about 20% of the total amount of statistics possible to be collected. Therefore, by taking into account all the forced stops and beam problems, only about 11 days of beam time were effectively used to obtain the data.

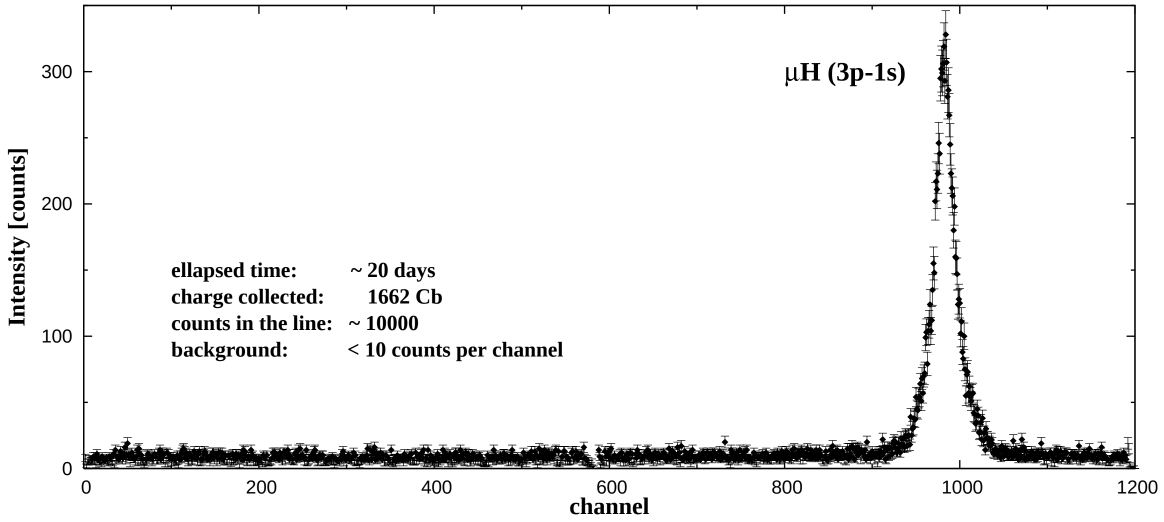

Figure 6.16: Overall spectrum of the μH($3p-1s$) transition with all data taken into account. A cluster size up to 2 was used.

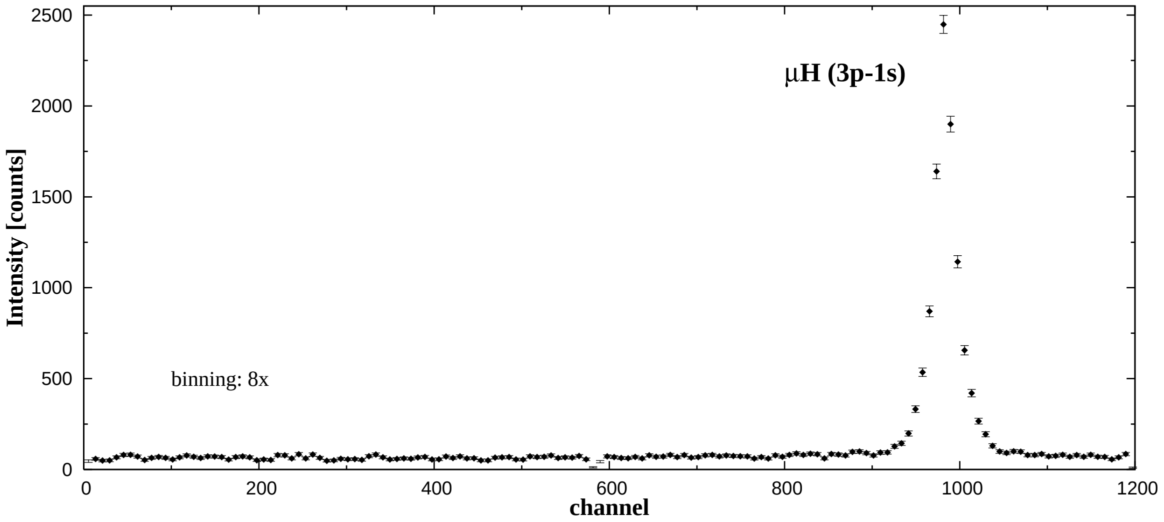

Figure 6.17: Binned spectrum of the μH($3p-1s$) transition. A binning factor of 8 was used. This was also done to identify possible low energy satellites. The statistical fluctuations become smoother which contributes to emphasize the flatness of the background over the whole detector.

In figure 6.16 the μH($3p-1s$) spectrum is shown after curvature correction and suitable energy cuts. It corresponds to the total amount of data collected. By applying a binning factor of 8, the statistical fluctuations become smoother which gives a better idea of the background level (see figure 6.17).

A major achievement was the very low background level, hence a good peak-to-background ratio (about 35). One main reason was the massive concrete shielding very well designed [114]. The other relies on the cluster analysis, which by using a cluster size of 1 and 2 eliminates most of the background hits. Moreover, a good background determination was expected due to its flatness over all the length of the detector.

6.2 Analysis

The analysis of the μH($3p-1s$) transition aims to extract the hyperfine splitting of the μH ground state and the population ratio of the triplet-to-singlet by approaching the kinetic energy distribution at the time of the radiative decay with so called "boxes" (see section 3.5). Therefore, the agreement between the extracted values and the theoretical predictions will serve as test to the validity of the box model as an alternative to the real distribution.

Based on the geometrical constraints of the setup and on the best knowledge about Si(111) Z13 crystal (curvature radius, miscut, Gaussian broadening – discussed in the previous chapter) the response function of the spectrometer at the energy of the μH($3p-1s$) transition was obtained via XTRACK. The superimposition of the convolution of the response function with the kinetic energy boxes on a flat background composes the fit function of each multiplet.

The convolution is performed by a dedicated routine named FOLD4MINUIT. The routine takes the response function as well as the number of boxes and their limits as inputs and computes the convolution of each box with the response function. Hence, the number of boxes and their respective limits are adjustable by "hand".

The background level, the positions of the multiplets, the population ratio, a scaling factor and the relative weights of each kinetic energy component corresponding to the different boxes are free parameters. The sum of the relative weights should be 1. Hence, the total number of free parameters during a fit routine is: $(5+[j-1])$, where j is the number of energy boxes used. The fit region was limited from channel 700 to channel 1180 which was sufficient to obtain a very good determination of the background.

The complexity of the fit led to some convergence difficulties for a number of parameters higher than 5. Apart from the minimization problems of the χ^2 (mentioned in section 5.3.2), the fit revealed a very high dependence of the convergence on the initial values of the positions of the multiplets. Therefore, for each new fit trial an exhaustive scanning of the initialization of the multiplet positions was done. In order to check the consistency of each result, several different initializations of the other free parameters were additionally tried.

Immediately after the first fit trials, the presence of a low energy component (with a few eV range) in the kinetic energy distribution turned out to be of most importance; a relative weight as high as 50...60% was mandatory. Whatever box arrangement was input, without this low energy box the fit results were disastrous. During a pre-analysis, an indication that the fit was not sensitive to the width of the boxes was obtained. Moreover, a relatively small number of boxes centered around the kinetic energies corresponding to preceding Coulomb deexcitations was sufficient to achieve a good agreement with the data.

Based on this information, the procedure was divided in two steps. In the first step, a systematic study of the number of boxes and their limits was performed with all the parameters $(5 + [j - 1])$ left free for the fit routine. In the second step, the fit function was frozen and the positions of the multiplets and the population ratio were adjusted by hand and kept fixed during the fit routine. This overcame the problems with the convergence of the χ^2 minimization and led to a more robust and better supported procedure. The results will be addressed in the next two sections.

6.2.1 Study of the fit function

Upper limit of the low energy box

The low energy box straddles kinetic energies from 0 up to a few eV. It corresponds to μH atoms which arrive at $n = 3$ with their kinetic energy gained only at the upper levels of the cascade $(n > 10)$ by Coulomb deexcitation, and/or to μH systems which lost their larger kinetic energies through elastic collisions.

The upper limit of the low energy box was evaluated based on the χ^2 distribution and on the result for the triplet-to-singlet population ratio. Two additional energy boxes 4 eV wide and centered at 58.2 eV and 26.9 eV were used. These energies correspond to the kinetic energy gains from a $n = 4 \rightarrow 3$ and $n = 5 \rightarrow 4$ Coulomb deexcitation, respectively. The results are depicted in figure 6.18.

The results clearly show that a very good agreement is obtained by using the 3 box arrangement mentioned. Even a very narrow low energy box (0.2 eV) leads to a very good fit ($\chi^2 = 451.526$, $\chi^2_r = 0.953$). Nevertheless, the quality of the fit improves to $\chi^2 = 448.976$ by expanding the box limit till 1.8 eV. The difference between these two χ^2-values corresponds to 1.6σ. For wider boxes the χ^2 does not suffer a significant degradation, however, the fit delivers unphysical values for the population ratio. Therefore, 1.8 eV was chosen as the higher limit of the low energy box and kept fixed in the following studies.

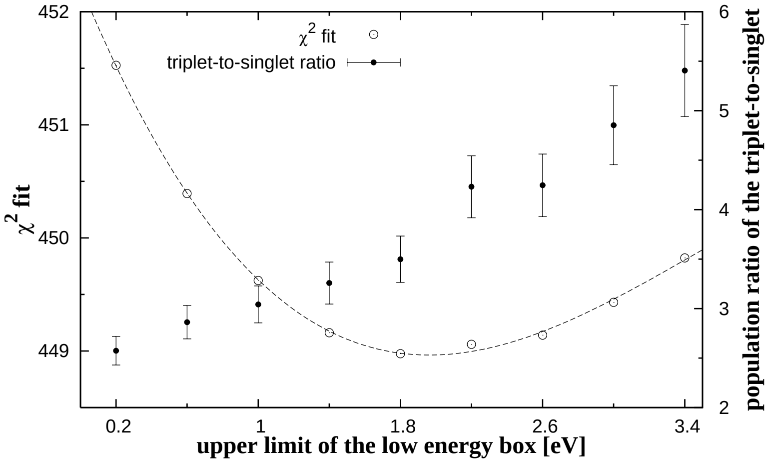

Figure 6.18: Fit quality as a function of the upper limit of the low energy box. Two additional energy boxes centered at 58.2 eV and 26.9 eV and 4 eV wide were used. They correspond to the kinetic energy gain from a $n = 4 \rightarrow 3$ and $n = 5 \rightarrow 4$ Coulomb deexcitation, respectively. By considering the 474 degrees of freedom of the fit, the minimum χ^2 (448.976) corresponds a reduced χ^2 of 0.947. The errors of the triplet-to-singlet ratio were taken from MINUIT. The dashed line is only to guide the eye.

Medium and higher kinetic energy boxes

Coulomb deexcitations with $\Delta n = 1, 2$ were considered to study the position of a second and third energy box. Hence, very narrow boxes, with only 1 eV, centered at the corresponding kinetic energy gains were used to find the best candidates for the second and third kinetic energy boxes. The low kinetic energy box from 0 to 1.8 eV remained fixed.

A first series of fits by using only two kinetic energy boxes was initially done and the best candidates to a second box identified. Subsequently, a second series with three kinetic energy boxes was performed with each best candidate for a second box being frozen. The results are depicted in figure 6.19.

The figure shows that the χ^2 of the fit improves significantly when using a second kinetic energy box placed between 20 and 60 eV. The minimum χ^2 (452.410) is achieved with a kinetic energy box placed around 40 eV and indicates already a very good agreement between the fit function and the spectral line. Thus, by using only two kinetic energy boxes to build up the fit function, the best positions to place the second box are 26.9, 41.6 and 58.2 eV which correspond to the kinetic energy gain via a $n = 5 \rightarrow 4$, $n = 6 \rightarrow 4$ and $n = 4 \rightarrow 3$ Coulomb deexcitation, respectively.

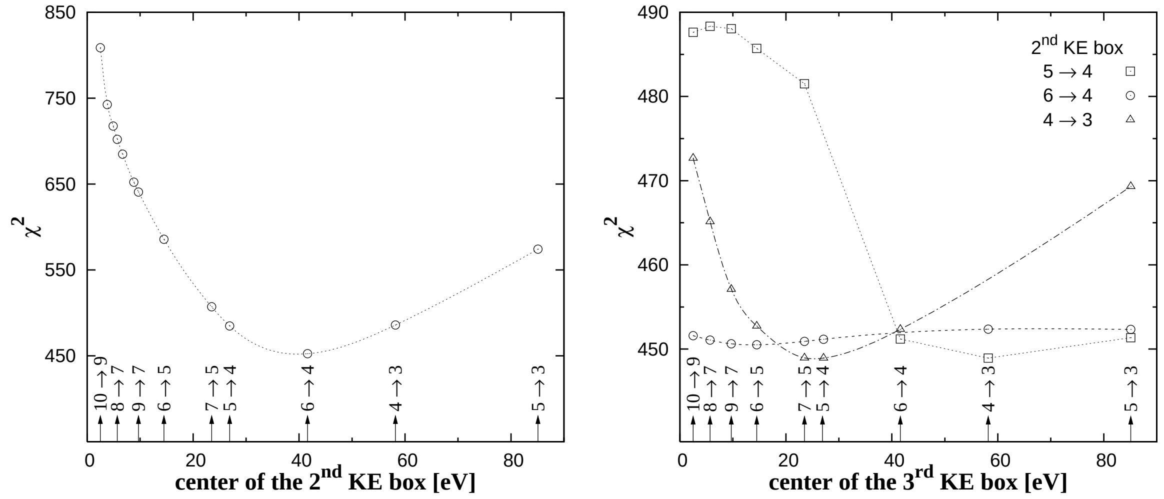

Figure 6.19: Fit quality as a function of the position of the 2^{nd} and 3^{rd} kinetic energy boxes. At the left only two boxes were used. At the right the best candidates for the 2^{nd} were frozen and the 3^{rd} box changed. The boxes were admitted to be only 1 eV wide. The kinetic energy gains from the respective Coulomb deexcitation are indicated. The best χ^2 (448.933) was achieved by considering the $n = 5 \rightarrow 4$ and $n = 4 \rightarrow 3$ Coulomb transitions to place the 2^{nd} and 3^{rd} kinetic energy boxes. Taking into account the 474 degrees of freedom it corresponds to $\chi^2_r = 0.947$. The dashed and dotted lines are just to guide the eye.

Figure 6.19 demonstrates also that the introduction of a third kinetic energy box improves the fit quality. However, this is not as clear when using the 41.6 eV to center the second box. In this case the fit does not show much sensitivity to the position of a third box, with the minimum χ^2 being ≈ 450.5 and varying less than 1.4σ.

On the other hand, when using the other two boxes a clearer improvement was achieved and the fit revealed to be quite sensitive to the position of the third box. The minimum χ^2 is 448.933 in both cases and corresponds to have a second and third kinetic energy boxes centered at 26.9 and 58.2 eV. The improvement, compared to the series based on the $n = 6 \rightarrow 4$ Coulomb transition for the second box, is only about 1.25σ. However, the fit is unequivocally better and the Coulomb transitions with $\Delta n > 1$ are less probable to occur. Therefore, 26.9 and 58.2 eV were chosen to place the two higher kinetic energy boxes which correspond to the kinetic energy gains via a $n = 5 \rightarrow 4$ and $n = 4 \rightarrow 3$ Coulomb transition, respectively.

Fourth kinetic energy box

A further investigation was performed to find out if the introduction of a fourth kinetic energy box would improve the fit quality. The results are depicted in figure 6.20.

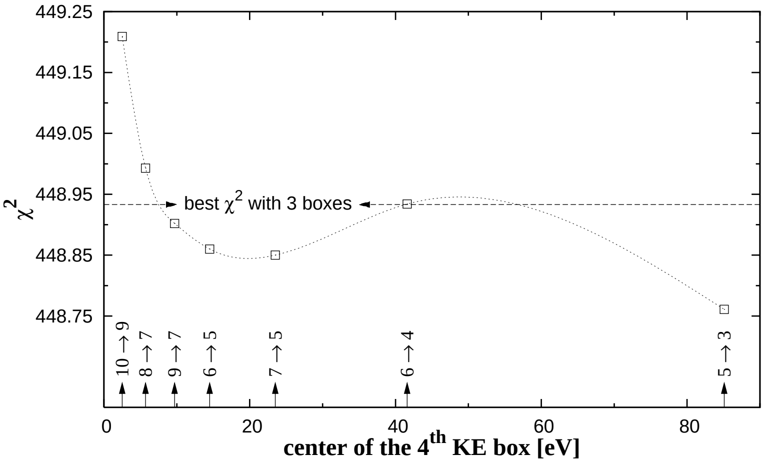

Figure 6.20: Fit quality as a function of the position of the 4th kinetic energy box. Similarly to the 2nd and 3rd boxes, the fourth box was tested with a width of 1 eV. The positions and limits of the remaining 3 boxes were kept fixed at the values found previously. The kinetic energy gains from the respective Coulomb deexcitation are indicated. The best χ^2 (448.761) was achieved by considering the $n = 5 \rightarrow 3$ Coulomb transition to place the 4th kinetic energy box. The dotted line is just to guide the eye. The best χ^2 found by using 3 boxes is indicated by the horizontal dashed line.

Indeed, the quality of the fit can be improved, as the figure shows. By assuming a fourth kinetic energy box centered at 85.1 eV the χ^2 is reduced to its minimum value.

However, the improvement is less than 0.2 χ^2 units which is negligible. Moreover, the introduction of a fourth box enhances significantly the problems related to the χ^2 minimization and convergence. Therefore, a fourth kinetic energy box was not considered.

Limits of the medium and high kinetic energy boxes

Afterwards, a systematic study on the influence of the range of the boxes on the fit quality was performed. The low kinetic energy box was set from 0 to 1.8 eV and kept fixed. The other two boxes were assumed to be centered at the kinetic energy gain from a $n = 5 \to 4$ and $n = 4 \to 3$ Coulomb transition. Their limits were set to the nominal ranges [25 : 29] eV and [56 : 60] eV, respectively. Each of these limits was then varied with the others frozen and the resultant fit function used to fit the μH line. The results are plotted in figure 6.21.

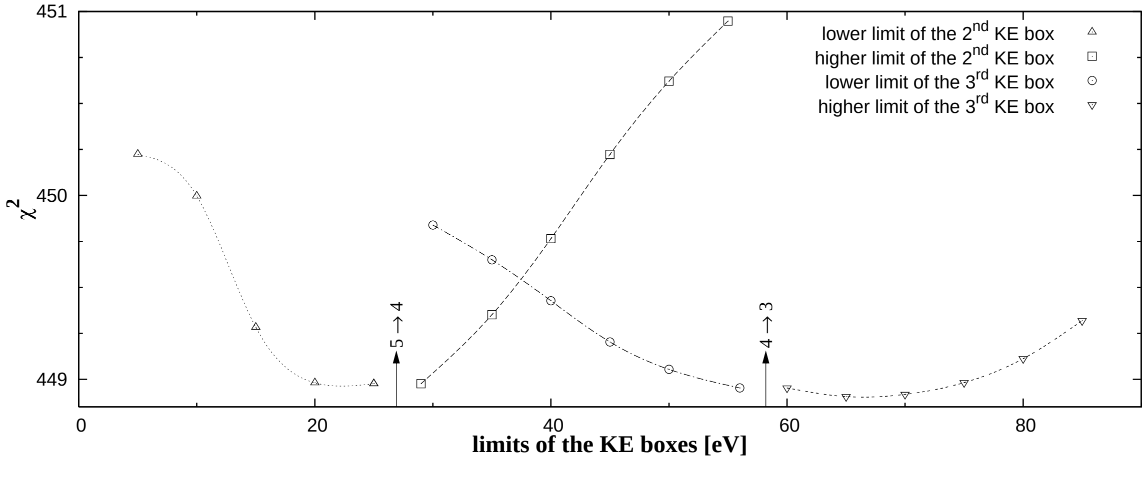

Figure 6.21: The change in the χ^2 is plotted as function of the limits of the boxes of medium and high kinetic energy. A 3-box approximation of the kinetic energy distribution at the time of the μH$(3p - 1s)$ radiative transition was assumed. The low energy box was fixed at [0 : 1.8] eV. The others were centered at the kinetic energy gains from a $n = 5 \to 4$ and $n = 4 \to 3$ Coulomb transition with a width of 4 eV. Each series corresponds to the change of one of the limits of one box with all the other box parameters being frozen. The dashed lines are just to guide the eye.

The low sensitivity of the fit to the limits of the medium and high kinetic energy boxes is evident. In a general way, the χ^2 does not vary more than 1.4σ. The changes are even smaller than 1σ when considering only the limits of the high energy box. Nevertheless, the figure points to a better fit quality when using smaller widths for the boxes.

Several fits were additionally done by expanding the ranges of the boxes in both directions, and changes in both boxes at the same time were even tried. The results were similar. No significant change in the fit quality was seen.

Conclusions

The systematic study of the fit function revealed that three boxes are essential but also sufficient to model the kinetic energy distribution and yield a good fit of the μH($3p-1s$) line shape: a low energy component $T < 2$ eV and two higher kinetic energy components corresponding to the Coulomb transitions $n = 5 \rightarrow 4$ ($T = 26.9$ eV) and $n = 4 \rightarrow 3$ ($T = 58.2$ eV). Moreover, the χ^2 analysis showed that the fit is not sensitive to the limits of the boxes corresponding to the higher kinetic energy components.

Furthermore, during all the analysis described the background turned out to be well determined by the fit routine. Apart from the fit sequence with only two kinetic energy boxes, only minor changes with less than 0.5% were seen among all the fits performed.

Within the three boxes approach, the best χ^2 was found to be 448.933 which corresponds to a χ^2_r of 0.947 ($n_{df} = 474$) when using kinetic energy boxes with intervals [0 : 1.8], [26.4 : 27.4] and [57.7 : 58.7] eV. The resultant relative weights for these boxes were 61 ± 2%, 25 ± 3% and 14 ± 4%, respectively. The hyperfine splitting of the μH ground state was found to be 211 ± 6 meV with a triplet-to-singlet population of 3.66 ± 0.25. The uncertanties are statistical errors taken from the fit routine. The numerical results are just preliminary. The final ones will be achieved with the more robust study described in the next section.

6.2.2 Study of the correlation between the triplet-to-singlet population and the hyperfine splitting

A second systematic study was subsequently performed by using the best kinetic energy boxes found previously. The hyperfine splitting, the population ratio and the position of the triplet peak were changed manually in small steps and one at each time. Hence, the fit routine had to handle only four free parameters: background, scale factor and two parameters for the relative weights of the energy boxes. With four free parameters no problems related to convergence and χ^2 minimization were registered.

The hyperfine spitting of the ground state of the μH is theoretically predicted to be about 183 meV [161]. The estimated dispersion of the spectrometer at the energy of the μH$(3p - 1s)$ transition is approximately 18.6 meV/pixel. Therefore, a splitting of about 10 channels is expected between the triplet and singlet positions.

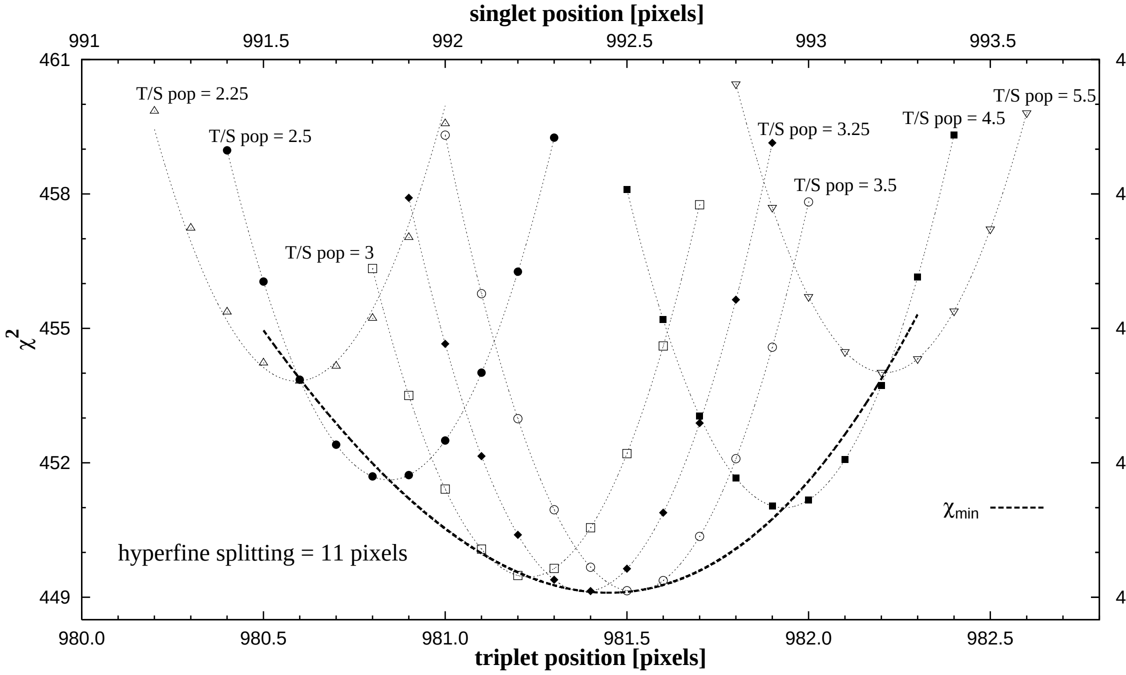

Figure 6.22: χ^2 distributions obtained with the hyperfine splitting fixed to 11 pixels ($\approx$ 205 meV). The different distributions were obtained by keeping the population ratio to the values indicated and changing the triplet position in steps of 0.1 pixels. The χ^2 curves show a quadratic behavior with their minima placed on a slightly asymmetric curve. The dotted lines are quadratic fits to the series. The bold dashed line is a fit to the minima of a third order polynomial. All the fits showed a very good quality. The distributions obtained with a population ratio of 2.75, 3.75, 4, 4.25 and 5 were not depicted to not overload the figure.

The hyperfine splitting was changed around 10 pixels in steps of 0.5 pixels. On the other hand, the population ratio was changed in steps of 0.25 around 3 (its statistical value). Therefore, by changing the triplet position a χ^2 distribution curve could be obtained for each pair (splitting;population) tried. An example of a typical series of distributions of χ^2 is given in figure 6.22 for a hyperfine splitting of 11 pixels.

Figure 6.22 shows that for each (splitting;population) pair the χ^2 is symmetrically distributed around a minimum which can be determined by fitting a quadratic function. Moreover, the different χ^2 curves are distributed with their minima placed over a slightly asymmetric curve. A very good approximation of this curve is guaranteed by a third order polynomial.

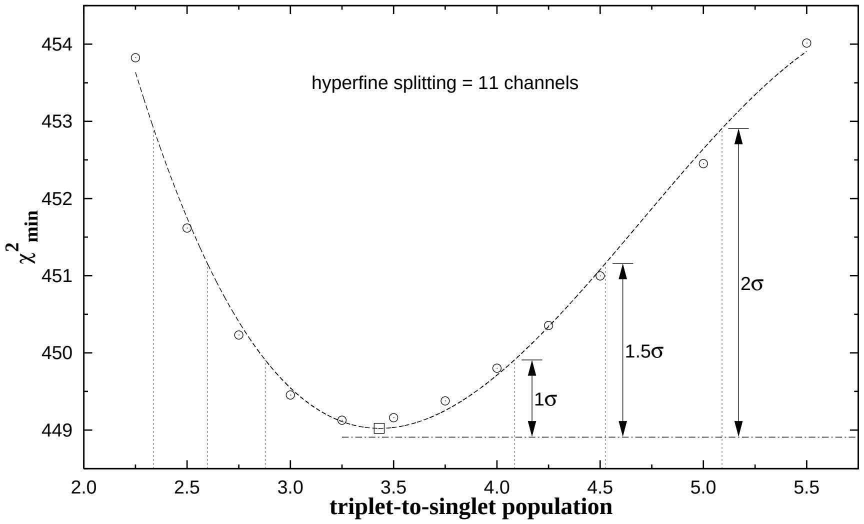

Figure 6.23: Distribution of the best χ^2 as function of the population ratio with the hyperfine splitting fixed to 11 pixels ($\approx$ 205 meV). The dashed line is a fit of a third order polynomial to the points. The minimum is indicated in the curve by an open square. The dashed-doted line represents the absolute best χ^2 found and corresponds to the final result for the hyperfine splitting and triplet-to-singlet population. The 1, 1.5 and 2σ limits, counting from this value, are indicated in the curve together with the corresponding population ratios (dotted vertical lines) used to generate figure 6.25.

In order to find the best fit with the different (splitting;population) pairs, for each fixed value for the hyperfine splitting, the χ^2 minima (found previously) are correlated with the triplet-to-singlet populations. The resultant distribution for a hyperfine splitting of 11 pixels is depicted in the figure 6.23. Similar distributions were obtained with other values considered for the hyperfine splitting. Once more, a third order polynomial provides a very good fit to the points and the absolute miminum of the series is determined (see figure). Thus, the triplet-to-singlet population is pinned down which together with a hyperfine splitting of 11 pixels provides the best fit. The same procedure was applied to the other values for the hyperfine splitting.

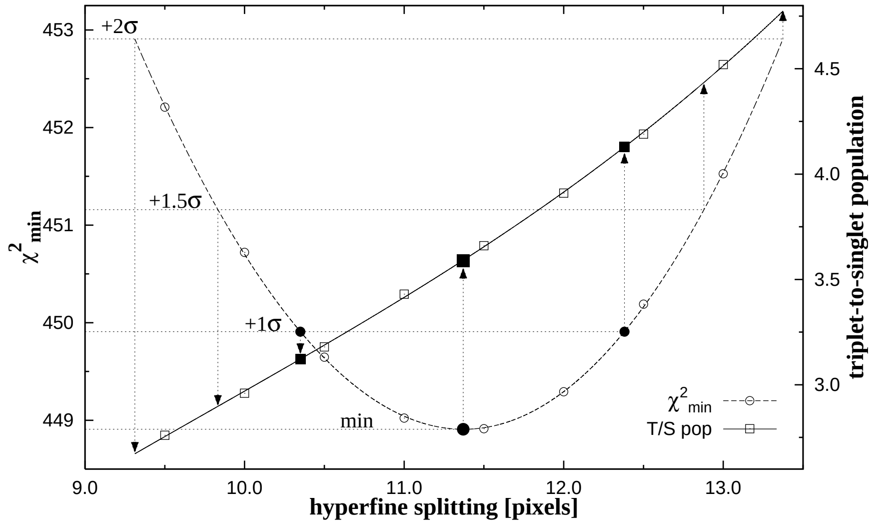

Figure 6.24: The correlation curve between the hyperfine splitting and the population ratio which delivers the best χ^2 is described by the solid line with the related χ^2 minima described by the dashed line. Both lines are fits of a third order polynomial to the values found by the procedure exemplified in figure 6.23 and plotted with open symbols. The χ^2 which corresponds to the best fit and the respective population ratio are indicated by the larger filled circle and square, respectively. The 1σ limits are indicated in the χ^2_{min} by small filled circles with the correspondent population ratio indicated by small filled squares. The values are used to estimate the errors. Additionally, the 1.5 and 2σ limits are indicated as well.

Consequently, the correlation between the hyperfine splitting, the triplet-to-singlet population and the best fit possible to achieve is determined. The result is presented in figure 6.24 by plotting the best χ^2 achieved with each value for the hyperfine splitting and the correspondent population ratio. The final result is determined by finding the hyperfine splitting which minimizes χ^2_{min} and by calculating the correspondent population ratio on the respective curve. In both cases, a third order polynomial serves well the purpose. The error is found by verifying which values for the hyperfine splitting and population ratio lead to a χ^2 higher than the minimum by one unit, i.e. one standard deviation away.

Thus, the hyperfine splitting is found to be 11.37 ± 1.03 channels, i.e 211 ± 19 meV, and the triplet-to-singlet population 3.59 ± 0.51. It corresponds to a $\chi^2=448.903$ and a $\chi_r^2=0.941$ ($n_{df}=477$). The relative weight of the low energy box which corresponds to this χ^2 is 61 ± 1%. It was determined by taking into account the results from the fit routine corresponding to the different χ^2_{min} and by performing a similar procedure.

The information about the results for the hyperfine splitting and population ratio which correspond to different σ limits can be collected in order to have a more general view. This is done in figure 6.25. The figure shows the limits of the different σ for the fitting of the ground state hyperfine splitting and population. Hence, it resumes the correlation between these parameters.

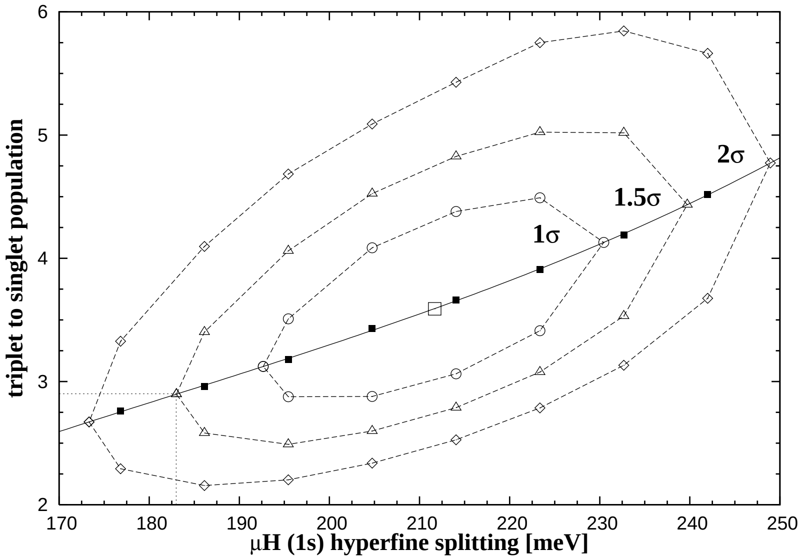

Figure 6.25: Contour of the σ limits (dashed lines) obtained by fixing the (hyperfine,population) pairs when fitting the μH($3p-1s$) transition line. The filled squares are the triplet-to-singlet populations which lead to the best fits. The solid line is a fit to these points of a third order polynomial. The (hyperfine,population) for which the best χ^2 is found is depicted by an open square. By fixing the hyperfine splitting of the μH ground state to its theoretical value (vertical dotted line) the best fit is achieved for a population ratio of 2.9 (horizontal dotted line). This is very close to its statistical value and only about 1.5σ away from the best fit result.

The most striking and revelant conclusion revealed in figure 6.25 is that by fixing the hyperfine spitting to the theoretical value of 183 meV [161], the best fit is obtained for a triplet-to-singlet population of 2.9:1 which is very close to the statistical value. Furthermore, this result is approximately 1.5σ away from the best fit.

6.3 Final results and remarks

The line shape of the μH($3p-1s$) transition could not be reproduced by taken the predictions of the ESCM for the kinetic energy distribution directly as an input for the fitting. Such a fit yielded a poor reduced χ^2 of $\chi^2 = 1.353$ only and it is clear that the lower kinetic energies are underrepresented [114] as can be seen in figure 6.26.

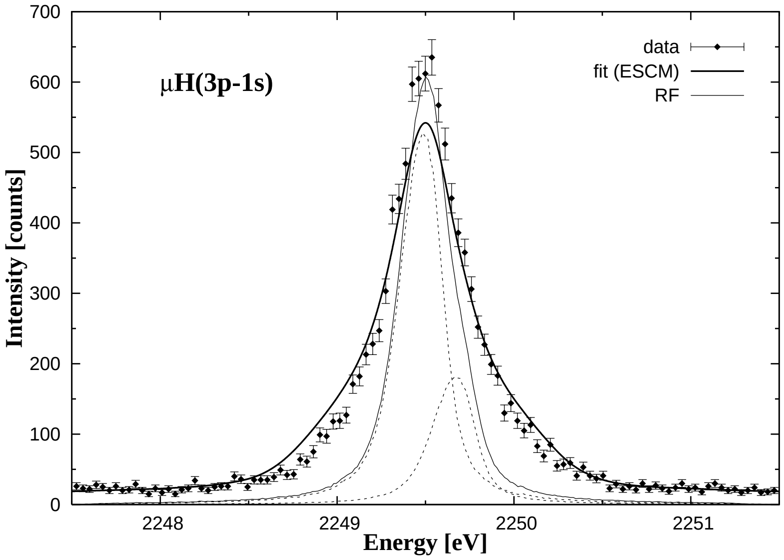

Figure 6.26: Line shape of the μH($3p-1s$) transition as measured with the Si(111) Z13 crystal. The data is depicted by filled circles with the respective statistical error bars. The spectrum was binned by a factor of 2. The bold solid line is the best fit to the data by using the ESCM predictions for the kinetic energy distribution at the time of the μH($3p-1s$) radiative transition. The sum of the response functions of the spectrometer at the energies of the each multiplet (in dashed lines) is the light solid line. Obviously the data is not reproduced.

Consequently, further analysis showed that the kinetic energy distribution at the time of the radiative transitions can be modeled by rectangular boxes with good results. Three boxes were sufficient to yield a good fit of the μH($3p-1s$) transition line (see figure 6.27). A low energy component with energies below 2 eV and relative weight higher than 50% turned out to be crucial to describe the line shape. The final value for its weight was estimated to be 61±1%. This high value contradicts the published result of the ESCM calculations [32, 33, 38]. For $T \leq 2$ eV, a contribution of about 30% on the total distribution at the time of the μH$(3p-1s)$ radiative transition is predicted, with consequently enhanced high energy contributions. Thus, it indicates that the kinematics of the lower part of the cascade is not yet fully understood. Moreover, further evidences came from the πH analysis where the kinetic energy distributions provided by the ESCM calculations failed to consistently describe the line shape of all measured πH$(np-1s)$ transitions [114].

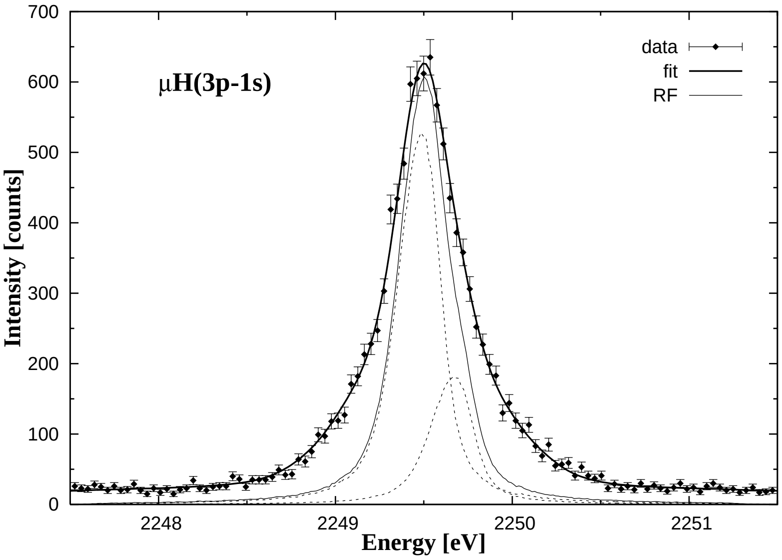

Figure 6.27: Best fit of the μH$(3p-1s)$ transition. The data is depicted by filled circles with the respective statistical error bars. The spectrum was binned by a factor of 2. The bold solid line is the fit to the data. The sum of the response functions of the spectrometer at the energies of the each multiplet (in dashed lines) is the light solid line. The effect of the high energetic Coulomb transitions ($n = 5 \rightarrow 4$,$n = 4 \rightarrow 3$) is evidenced by the long tales of the line.

Based on the large contribution of low kinetic energies it can be inferred that the cross sections for elastic collisions are substantially different from the ones used in the ESCM code. Additionally, the possibly stronger effects from Coulomb deexcitations in the outer levels ($n > 10$, $T < 2$) might have been neglected so far by starting the cascade calculations at $n = 8$.

In summary, the line shape of the μH($3p - 1s$) transition has been measured for the first time with a high resolution Bragg spectrometer. By comparing the line shape with the response function, previously determined, the measurement granted the direct observation of the influence of the Coulomb deexcitations.

Within the box approximation for the kinetic energy distribution, the best fit of the μH($3p - 1s$) transition line yielded a hyperfine splitting of the ground state of 211 ± 19 meV and a triplet-to-singlet population of 3.59 ± 0.51. This reproduces within 1.5σ the theoretical hyperfine splitting of the μH ground state, as calculated from QED, and confirms as well the statistical population distribution of the triplet-to-singlet. Figure 6.27 shows the best fit achieved. The response function of the spectrometer is depicted for comparison. The fit has a $\chi^2 = 448.9$ which corresponds to a $\chi^2_r = 0.941$. Though the χ^2_r is slightly lower than 1, the discrepancy can be assumed to be purely statistical. The lower limit in the χ^2 distribution for $n_{df} = 477$ which corresponds to the $\pm 1\sigma$ region is $\chi^2 = 446.3$ [162]. Thus, $\chi^2 = 448.9$ is inside the $\pm 1\sigma$ region.

The quite good agreement with the theoretical prediction for the hyperfine splitting and population of the ground state of the μH validate the box model as a reasonable approximation to the kinetic energy distribution.

Furthermore, an investigation was done whether the line shape could be affected by molecular formation with subsequent radiative deexcitation [53, 163]:

$$(\mu p)_{nl} + \mathrm{H}_2 \rightarrow [(\mu pp)_s pee]^* \rightarrow [(\mu pp)_{s'} pee]^* + \gamma$$

being s and s' the set of rotational and vibrational quantum numbers describing the molecular states and γ the emitted photon. A line broadening or even satellites at the low energy side are expected in case of a significant contribution of these radiative decays. In fact, a branching ratio for the radiative decay of the μpp system at a few percent level was predicted [155, 164]. However, in this experiment, no evidence was found at the 1% level for any additional broadening besides the Coulomb deexcitation. Moreover, the low energy side of the spectrum revealed to be clean of satellites as the flat background evidences. The result is corroborated by the absence of any density dependence of the πH(3p-1s) transition energy [116].

Chapter 7

Conclusion and outlook

The present investigations have unequivocally demonstrated that the kinetic energy distribution at the time of a radiative decay in μH can be approximated by several boxes with successful results.

By using this “model free” method the hyperfine structure of the ground state of the μH system could be resolved for the first time by measuring X-rays of the $3p-1s$ transition with a high resolution crystal spectrometer. The Doppler broadening of the spectral line was well established and could be correlated with different Coulomb deexcitation steps preceding the measured radiative transition. Furthermore, the assumption that the hyperfine states of the ground state of the μH are statistically populated was directly confirmed. The analysis has delivered a hyperfine splitting of 211 ± 19 meV which is 1.5σ away from the theoretical value of 183 eV [161] and a triplet-to-singlet population of 3.59 ± 0.51.

Furthermore, the study of the correlation between the population ratio and the hyperfine splitting has shown the consistency of the method. By fixing one of these quantities to its theoretical value, the other one was obtained very close the its theoretical prediction. The discrepancy was less than 3.5% in the case of the population ratio and less than 1.5% in the case of the hyperfine splitting.

On the other hand, the line shape of the μH$(3p-1s)$ transition could not be fairly reproduced by using the ESCM predictions for the kinetic energy distribution at the moment of the $3p-1s$ radiative transition. Hence, it is clear that the present status of the advanced cascade model (ESCM) still needs some fine tunings and can not be used in the analysis of the Γ_{1s} of the πH ground state. In alternative, the box approximation turned out to overcome the lack of knowledge in the ESCM and it was already extended to the ongoing analysis of the width Γ_{1s} of the πH ground state.

The results presented here have triggered further efforts to improve the ESCM. The cross sections involved in the exotic hydrogen deexcitation have been reconsidered and calculated in a fully quantum mechanical close coupling approach [61, 62, 63]. The cross sections for elastic scattering, Stark transitions and Coulomb deexcitation have been now calculated in an unified manner.

In fact, by including the new cross sections in the ESCM [60] an increase of the relative weight of the low energy component ($T \leq 2$ eV) to about 55% for μH at the time of the $3p-1s$ radiative transition was obtained. This is close to the $61 \pm 1\%$ predicted by the "model free" approach and agrees with the constraint given by it (about 50% to 60%). A fit to the measured μH$(3p-1s)$ line shape by using the new kinetic energy distribution yields perfect agreement with the data even by leaving the hyperfine splitting and population ratio as free parameters (χ^2_r=0.984) [114]. The hyperfine splitting is found to be 201 ± 11 meV and the triplet-to-singlet population ratio 2.98 ± 0.21.

Furthermore, a subsequent trial to provide new kinetic energy distributions for the measured πH transitions has recently been made [165]. However, the results for Γ_{1s} of the πH ground state are still dubious [114]. Further developments are needed. Meanwhile, the "model free" approach remains as the only reliable possibility to be used in the πH data analysis.

The μH analysis has also shown that no additional contribution to the line broadening exists on the 1% level besides the one caused by Coulomb deexcitation. Radiative decays from μpp molecular systems with a branching ratio of the order of a few percent and the corresponding low energy satellites were expected [53, 164]. Clearly, no evidence of such lines was seen, which agrees with the absence of any density dependence of the measured πH transition energy [116].

As a second aspect, the characterization of the Si(111) crystal was successfully accomplished. Contributions to about 5% of the FWHM of the response function were identified to be related to the imperfect nature of the crystal. Moreover, the determination of the response function at different energies revealed an astonishing sensibility to experimental conditions. This fact stimulated new investigations on geometrical properties of the crystal which have been neglected so far, namely the asymmetric cut angle and the curvature radius. Consequently, a practical method to characterize the asymetric cut angles in already mounted spherical bent crystals has been developed. Nevertheless, some features seen in the analysis still lack a more consistent explanation and future investigations are planned.

Appendix A

List of symbols

α	miscut angle
α_f	fine structure constant
$\beta(\text{E1})$	probability of the electron conversion in electrodipole transitions (E1)
$\Gamma_{St,Col,Au,\gamma}$	Stark mixing, Coulomb deexcitation, Auger emission and radiative rate
Γ_{1s}	Strong interaction broadening of the ground state in πH
$\Delta\theta_a$	maximum Johann broadening due to the crystal height
$\Delta\theta_b$	maximum Johann broadening due to the crystal width
$\Delta\theta_d$	maximum Johann broadening due to variations in the lattice parameter d
$\Delta\theta_J$	maximum Johann broadening
$\Delta\theta_z$	maximum Johann broadening due to the source height
Δ^{hs}	hyperfine splitting
ζ	relative deviation of the scattering vector
ε	efficiency
ε_{1s}	strong interaction shift of the ground state of the pionic hydrogen
ζ_0	displacement of the Bragg reflection
ζ_D^{FWHM}	FWHM of the Darwin curve
η	related with ζ so that the total reflection region is limited by $-1 < \eta < 1$
θ_B	Bragg angle
λ	wavelength
λ_D	absorption depth in a Bragg scattering due to photoelectric effect
λ_P	mean free path of a photon in a material considering photoelectric effect
λ_T	total penetration depth including extinction and absorption
Λ	extinction depth
μ_a	linear attenuation coefficient
μ_N	nuclear magneton

μ_p	magnetic moment
μ_{xp}	reduced mass of the x^-p bound system
ρ	density
ρ_e	electron density
ρ_L	Larmor radius
σ	standard deviation
σ_j	half of the crystal opening angle
σ_{St}	cross section of the Stark mixing
τ_{St}	collision time of the Stark mixing
$\upsilon_{ee,ie,ii}$	frequency of the collisions electron-electron, electron-ion or ion-ion
Υ	small deviation from $m\pi$ on the wave phase in Bragg scattering
ϕ	wave phase
Φ	rotation of the crystal in the setup of the miscut determination
Φ_0	miscut orientation with respect to a reference mark on the glass lens rim
φ	orientation of the miscut
Ψ_r	measured angle of the Bragg reflection in the presence of a miscut
ω	angular frequency
Ω	solid angle
a	vertical crystal extension
a_0	Bohr radius $\approx 5.291772108(18) \times 10^{-11}$ m
A	mass number
$\vec{A}$	magnetic vector potential
b	horizontal crystal extension
$\vec{B}$	magnetic field
c	light velocity in vacuum
$C_{JohannCyl}$	Johann average shift caused by a cylindrical crystal
$C_{JohannSph}$	Johann average shift caused by a spherical crystal
d	spacing between the planes in the crystal lattice
e	unitary charge
E	energy
E_{1s}	binding energy of the atomic ground state as predicted by QED
$\vec{E}$	electric field
F_B	magnetic force
F	unit cell structure factor
$\mathbf{F}$	total momentum operator of the proton-lepton magnetic interaction
$\mathcal{F}$	focal distance

g_0	phase shift in a scattered process in forward direction
g_p	g-factor of the proton
g	magnitude of the reflectivity of a thin layer of electrons
G	vector in the reciprocal space
h	Planck constant
$\hbar$	Dirac constant ($h/2\pi$)
J	action integral
$\mathbf{J}$	spin-orbit coupling operator
k	wavenumber
$\mathcal{K}$	constant of the ineffective layer model
l	angular momentum quantum number
$\mathbf{L}$	angular momentum operator
$\mathcal{L}$	length of the ineffective layer
m	diffraction order (integer)
m_e	electron mass
m_H	hydrogen mass
m_p	proton mass
m_{xp}	exotic hydrogen mass
n	principal quantum number
n_{df}	number of degrees of freedom
N	number of slits/layers in a diffraction grating
p	momentum
P	Panofsky ratio
$\mathcal{P}$	pressure
q	charge
Q	scattering vector
Q_0	π^0 momentum in the CMS
$R_{n_i \to n_f}$	dipole matrix element
R_c	crystal bending radius
r_0	Classical electron radius ($\approx 2.82 \times 10^{-5}$Å)
$\|r_N\left(\zeta\right)\|^2$	total intensity of the reflectivity using the kinematical approach
$r(a)$	amplitude reflectivity in dynamical approach
r_b	Bohr radius
$R(a)$	total intensity of the reflectivity in dynamical approach
$\mathbf{S}$	spin operator
t	time

T	kinetic energy
$\mathcal{T}$	temperature
T_r	transmission
v	velocity
v_c	volume of the unit cell
w_D^{FWHM}	angular FWHM of the Darwin curve
w_D^{total}	angular width of the total reflection region of the Darwin curve
Y	real distance between the detector and the crystal in the spectrometer
$Y^{n_i f_i \to n_f l_f}$	radiative yield
z	height of the source in a Bent crystal Bragg spectrometer
Z	atomic number

Appendix B

Acronyms and Abbreviations

BPM	**B**ad **P**ixel **M**ap
CCD	**C**harge **C**oupled **D**evice
ChPT	**Ch**iral **P**erturbation **T**heory
CMC	**C**lassical **M**onte-**C**arlo
CMS	**C**enter of **M**ass **S**ystem
CSDCLUSTER	Program to treat the CDD raw data
ECR	**E**lectron **C**yclotron **R**esonance
ECRIS	**E**lectron **C**yclotron **R**esonance **I**on **S**ource
ECRIT	**E**lectron **C**yclotron **R**esonance **I**on **T**rap
ESCM	**E**xtended **S**tandard **C**ascade **M**odel
FWHM	**F**ull **W**idth at **H**alf **M**aximum
HBChPT	**H**eavy **B**aryon **Ch**iral **P**erturbation **T**heory
HF	**H**igh **F**requency
LHD	**L**iquid **H**ydrogen **D**ensity (4.25×10^{22} atoms$\cdot$cm^{-3})
PSI	**P**aul **S**cherrer **I**nstitut - Villigen, Switzerland
QCD	**Q**uantum **C**hromo**D**ynamics
QE	**Q**uantum **E**fficiency
QED	**Q**uantum **E**lectro**D**ynamics
RF	**R**esponse **F**unction
SCM	**S**tandard **C**ascade **M**odel
ThRF	**Th**eoretical **R**esponse **F**unction
TOF	**T**ime **O**f **F**light
UHV	**U**ltra **H**igh **V**acuum
XOP	Software which provides the response function for a flat perfect crystal [84]
XEDS	**X**–Ray **E**nergy **D**ispersive **S**pectroscopy

XRD	**X**–**R**ay **D**iffraction
XTRACK	Simulation tracking routine of the PSI spectrometer

Appendix C

Accurate miscut angle determination

REVIEW OF SCIENTIFIC INSTRUMENTS **79**, 033102 (2008)

Accurate miscut angle determination for spherically bent Bragg crystals

D. S. Covita,[1,a)] M. Ay,[2] S. Schlesser,[4] D. Gotta,[3] L. M. Simons,[5,b)] E.-O. Le Bigot,[4] and J. M. F. dos Santos[1]
[1]*Departamento de Física, Universidade de Coimbra, 3004-516 Coimbra, Portugal*
[2]*Laboratory for Neutron Scattering, ETHZ and Paul Scherrer Institut, CH-5232 Villigen PSI, Switzerland*
[3]*Institut für Kernphysik, Forschungszentrum Jülich, D-52425 Jülich, Germany*
[4]*Laboratoire Kastler Brossel, UPMC-Paris 6, ENS, CNRS; Case 74, 4 place Jussieu, 75005 Paris, France*
[5]*Laboratory for Particle Physics (LTP), Paul Scherrer Institut, CH-5232 Villigen PSI, Switzerland*

(Received 11 January 2008; accepted 30 January 2008; published online 5 March 2008)

Spherically bent crystals are used as analyzers in high-resolution spectroscopy, in particular, in low count-rate applications such as exotic-atom research. The focal conditions are determined not only by the bending radius and the Bragg angle but also by the crystal cut angle between its surface and the reflecting crystal planes, along with their orientation with respect to the direction of dispersion. We describe a simple but precise method for measuring the cut angle and its orientation for mounted spherically bent crystals, by combining x-ray diffraction and laser optical alignment, which can be easily performed with standard x-ray laboratory equipment. © *2008 American Institute of Physics.* [DOI: 10.1063/1.2884149]

I. INTRODUCTION

Large area spherically bent Bragg crystals are used in the x-ray spectroscopy of exotic atoms in the few keV range.[1–3] Owing to their focusing properties, they reduce measuring times by an order of magnitude compared to plane crystal arrangements. In this (Johann-type) setup,[4] defocusing due to the imaging properties can be well controlled by choosing appropriate dimensions for x-ray source, crystal, and its radius of curvature, in combination with a large area position-sensitive detector.[5]

A general problem is that the precise knowledge of the orientation of the lattice planes of the slabs, cut from a crystal bulk and subsequently polished, may be lost. Deviations are due not only to an imperfect determination of the orientation of the bulk material but especially from alignment problems of the sawing machine. Spherically bent crystals are made by forcing thin slabs into a spherical shape; therefore the crystal cut angle (miscut) can be assumed to be constant over the whole crystal surface. In our case, the plates follow the curvature of a high-quality polished spherical glass lens kept in place by molecular forces (Fig. 1). The meridional orientation may also change during the contacting process. In fact, x-ray diffraction diagnostics are usually not available during the industrial fabrication procedure which is necessary for achieving highest polishing quality. Hence, after mounting the crystal, determining the miscut and its orientation is essential.

A miscut is characterized by an angle α between the crystal surface and the reflecting planes. As is seen from Guinier's focusing condition for cylindrically bent crystals,[6] the crystal cut angle contributes to the focal positions, i.e., in the distances between crystal (C), detector (D), and source (S) (Fig. 2),

$$\overline{\mathrm{CD}} = R_c \sin(\Theta_B + \alpha), \tag{1}$$

$$\overline{\mathrm{SC}} = R_c \sin(\Theta_B - \alpha). \tag{2}$$

For $\alpha=0$, the Guinier condition reduces to the usual (meridional) focusing condition for the symmetric Bragg case, $\overline{\mathrm{CD}}=R_c \sin\Theta_B$, where Θ_B is the Bragg angle according to Bragg's law and R_c the crystal's bending radius. Similarly, the knowledge of α is equally important when using asymmetric Bragg reflections. For the sign of α, we follow Guinier's convention, where a positive angle corresponds to a larger crystal-detector distance.

Equations (1) and (2) are only valid for a particular orientation of the crystallographic planes, i.e., when the directions of dispersion and the meridional plane are perpendicular; it also neglects bending itself.[7] An arbitrary orientation of the miscut plane is equivalent to a rotation of the meridional plane by an angle φ around the diameter R_c of Fig. 2. The effective miscut α' can then be obtained as the projection $\alpha\cos\varphi$. Rewriting Eq. (1) as $\overline{\mathrm{CD}}=R_c \sin\Theta_B \cos\alpha' + R_c \cos\Theta_B \sin\alpha'$ and assuming a small miscut ($\alpha\approx 0$), one obtains for any orientation φ the focusing condition

$$\overline{\mathrm{CD}} = R_c \sin\Theta_B + R_c \cos\Theta_B \sin(\alpha\cos\varphi). \tag{3}$$

As expected, an orientation according to $\varphi=90°$ or $270°$ does not change the focal length: rays in the plane of Fig. 2 are simply reflected above or below the symmetry plane, which can be corrected by tilting the crystal but leads to a top-bottom asymmetry of the reflection.

The following example reveals the importance of a precise determination of both the miscut and its orientation: for a Si(111) crystal and x-rays of the $3p$-$1s$ transition in pionic hydrogen (2.89 keV) the Bragg angle is $\Theta_B=43.2°$.[3] A mis-

---

[a)] Author to whom correspondence should be addressed. Electronic mail: daniel.covita@psi.ch. Also at LTP, PSI, CH-5232 Villigen, Switzerland.

[b)] Present address: Departamento de Física da Universidade de Coimbra, 3004-516 Coimbra, Portugal.

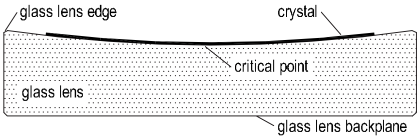

FIG. 1. Cross section of the crystal mounting on a concave glass lens of 3 m curvature, 12 cm diameter, and 3 cm thickness. The thickness of the crystal slabs is about 0.2–0.3 mm (curvature and crystal thickness not to scale).

cut as small as 0.1° results in a change of the focal length of about 4 mm or 0.2% for R_c=2.98 m. If such a miscut is ignored and the detector is positioned at the supposed focal position, the displacement of the focus broadens the line by about 10 s of arc (for a horizontal crystal aperture of 60 mm); this is to be compared to the intrinsic resolution of the silicon crystal of about 26 s of arc.[8]

II. X-RAY DIFFRACTION BASED TECHNIQUES

Techniques for determining the orientation of lattice planes within crystal blocks by diffraction methods are well established,[9] in particular, for measuring the orientation of epitaxial layers and implantation profiles.[10–14] The methods are based on angle differences and/or rocking curve width measurements, among others, with strongly asymmetric reflection setups. When adapted to flat specimen[14] or a special form of the crystal material,[13] they are not easily applicable to the spherically bent crystal setup.

The only alignment required for the method described in this paper is an adjustment of the x-ray spectrometer to the *critical point* (Fig. 1) where the bent surface is parallel to the reference plane defined by the spectrometer sample holder being perpendicular to the rotation axis (Fig. 3). The critical point is always the lowest point and, so, no further tilt adjustment is needed.

III. CRYSTAL ALIGNMENT

In practice, the lowest point does not coincide with the geometrical center of the crystal mounting. Therefore, at first the center offset of the critical point is found by means of a laser beam reflected from the crystal surface onto a screen. When rotating the crystal-lens mounting, the position of the reflected light remains unchanged if the critical point is on the axis of rotation, as is required by this method (Fig. 3). Otherwise, the reflected spot describes an ellipse. The closer the crystal sphere center to the rotation axis, the smaller the ellipse axes; the ellipse eventually collapses into a spot. During this procedure, the laser and the rotation axes are kept fixed and the sample holder, together with the crystal mounting clamped on it, is moved along the y and z coordinate in order to position the critical point onto the rotation axis (Fig. 3). The accuracy of this procedure depends on the surface to screen distance. In addition, the laser spot diameter can limit the accuracy. Placing the laser's aperture at a distance R_c the crystal acts as a concave mirror, and the crystal will focus the reflected beam also at that distance.

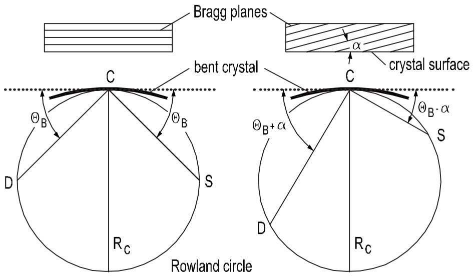

FIG. 2. Bragg reflection and focusing condition without and with miscut α for a bent crystal setup in the symmetry plane. The left drawing corresponds to the symmetric Bragg case, the right one to the asymmetric one for a miscut orientation $\varphi=0°$ (adapted from Ref. 6).

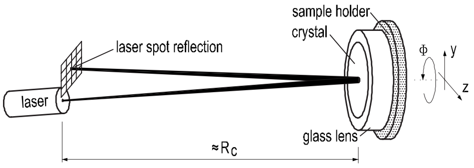

FIG. 3. Schematic of the method used for positioning the critical point (Fig. 1) onto the holder rotation axis.

In the absence of any miscut (α=0), an x-ray beam hitting the crystal surface at the critical point is always Bragg reflected under the angle $\Omega_0=\Theta_B$, whatever the holder rotation angle. For nonzero values of α, the reflection angle Ω with respect to the reference plane varies periodically around Ω_0 according to

$$\Omega=\Omega_0+\alpha\cos(\Phi-\Phi_0), \tag{4}$$

where $\varphi=\Phi-\Phi_0$ is the actual orientation. The angle Φ is measured relative to an arbitrary reference mark placed on the rim of the glass lens; the phase Φ_0 represents the direction of the miscut with respect to the reference mark. Miscut angle and orientation (α,Φ_0) are then obtained through a fit of the $\Omega(\Phi)$ curve (Fig. 4). During the x-ray sample spectrometer alignment, it was necessary to redefine the *zero* of the angle encoder. This explains the small offset on the $\Omega(\Phi)$ curves, which are not vertically centered at the corresponding Bragg angle Θ_B. However, this has no impact on the extracted values of α and Φ_0, as can be seen in Eq. (4).

IV. MEASUREMENT

The measurements were performed with a SEIFERT® XRD 3003 PTS high-resolution x-ray diffraction spectrometer, which provides a collimated and monochromatic beam of Cu $K\alpha$ x-rays (8.041 keV). A sample spectrometer x-ray alignment was first performed. The optical alignment described above was done with a general-purpose gas laser (660 nm). The light spots were, respectively, about 6 and 0.5 mm on the crystal surface and on the screen catching the reflected laser beam. The x-ray beam was collimated to 1 cm in height and 1 mm in width, about 20 cm away from the sample. The collimator width at the detector side was 0.5 mm and its distance was also 20 cm.

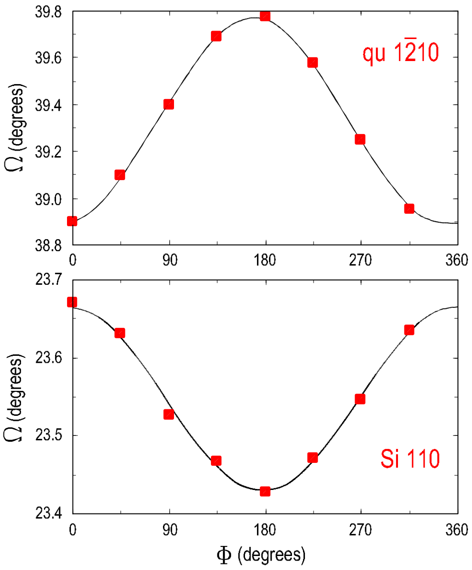

FIG. 4. (Color online) Variation of the reflection angle Ω for second order Bragg diffraction of the Cu $K\alpha$ x-rays for a quartz (1$\bar{2}$10) crystal [corresponding to Θ_B=39.41° (Ref. 8)] and a Si (110) crystal [Θ_B=23.67° (Ref. 8)]. The experimental errors for Ω are smaller than the dots depicting the data points. The solid line is a fit according to Eq. (4).

A set of 13 spherically bent crystals was characterized. As an example of a relatively large and of a relatively small miscut, the results for a quartz (1$\bar{2}$10) and a silicon (110) crystal are shown (Fig. 4). The fit to the predicted cosine behavior [Eq. (4)] is almost perfect. The angles α and Φ_0 obtained for the quartz crystal are 0.442° ± 0.005° and 169.0° ± 0.7° and for silicon 0.119° ± 0.004° and −3.0° ± 2.0°, respectively.

V. DISCUSSION

In addition to the fit error, experimental uncertainties must be considered. The hitting position of the collimated x-ray beam may deviate from the critical point by the step width of the y-z movement, which was about 0.5 mm. This results in ellipses with an axis up to 4 mm corresponding to an uncertainty of 0.019° on the cut angle for crystals with 3 m bending radius. As the laser spot is less than 1 mm, the step width dominates the error of α in this setup. As mentioned, the orientation angle Φ_0 of the miscut is measured relative to a reference mark on the glass lens. The accuracy $\Delta\Phi_0$ for the mounting of the glass lens on our sample holder is better than 2°.

Of great advantage is the fact that the results are obtained by fitting a simple cosine function, which makes a specific adjustment of the meridional plane unnecessary. Obviously, the accuracy of the method scales linearly with the dimensions of the laser setup. The accuracy can easily be increased by adding data points to such curves—being advantageous for very small cut angles—as far as mechanical limitations appear. Furthermore, almost no restrictions for the Bragg angle arise because any diffraction angle accessible by the diffraction spectrometer can be used. Noteworthy is that the method can also be applied to the measurement of the miscut at any point of the crystal surface, by using a holder capable of tilting the crystal mounting.

VI. SUMMARY

We describe a simple and precise method for determining or checking the miscut and its orientation of spherically bent crystal mountings, which have been used in ultimate resolution x-ray spectroscopy of exotic atoms. The method uses a commercially available x-ray diffraction spectrometer and a general-purpose laser. For bending radii of 3 m, in the worst case an accuracy of 0.02° was achieved for the cut angle, which is easily enhanced to a few millidegrees when using a better y-z table.

ACKNOWLEDGMENTS

The authors thank the Laboratory for Developments and Methods at PSI and, in particular, Dr. H. Grimmer, who made possible the use of the SEIFERT® spectrometer and gave his advice for operating the machine. We are grateful to A. Schmidheiny from the PSI HF group for providing the mechanical support. The Bragg crystals were manufactured by Carl Zeiss AG, Oberkochen, Germany. D.S.C. has a Ph.D. scholarship granted by FCT (Lisbon) through the POCI 2010 program.

[1] D. Gotta, Prog. Part. Nucl. Phys. **52**, 133 (2004).
[2] D. F. Anagnostopoulos, S. Biri, D. Gotta, A. Gruber, P. Indelicato, B. Leoni, H. Fuhrmann, L. M. Simons, L. Stingelin, A. Wasser, and J. Zmeskal, Nucl. Instrum. Methods Phys. Res. A **545**, 217 (2005).
[3] D. Gotta, F. Amaro, D. F. Anagnostopoulos, S. Biri, D. S. Covita, H. Gorke, A. Gruber, M. Hennebach, A. Hirtl, T. Ishiwatari, P. Indelicato, Th. Jensen, E.-O. Le Bigot, J. Marton, M. Nekipelov, J. M. F. dos Santos, S. Schlesser, Ph. Schmid, L. M. Simons, Th. Strauch, M. Trassinelli, J. F. C. A. Veloso, and J. Zmeskal, Lect. Notes Phys. **745**, 165 (2008).
[4] H. H. Johann, Z. Phys. **69**, 185 (1931).
[5] J. Eggs and K. Ulmer, Z. Angew. Phys. **5**, 118 (1965).
[6] A. Guinier, Comptes rendus hebdomadaires des séances de l'l Académie des Sciences **223**, 31 (1946).
[7] M. Sanchez del Rio and F. Cerrina, Rev. Sci. Instrum. **63**, 936 (1992).
[8] M. Sanchez del Rio and R. J. Dejus, AIP Conf. Proc. **705**, 784 (2004).
[9] G. Filscher, F. Adolph, and L. Adler, Krist. Tech. **9**, 437 (1974).
[10] S. E. G. Slusky and A. T. Macrander, Appl. Phys. Lett. **53**, 2042 (1988).
[11] B. K. Tanner, S. J. Miles, G. G. Peterson, and R. N. Sacks, Mater. Lett. **7**, 239 (1988).
[12] Y. Chen, M. F. Morris, B. Obradovic, D. Li, Al. F. Tasch, and J. S. Swinnea, IEEE Trans. Semicond. Manuf. **13**, 243 (2000).
[13] M. Gailhanou, Appl. Phys. Lett. **63**, 458 (1993).
[14] L. D. Doucette, M. Pereira da Cunha, and R. J. Lad, Rev. Sci. Instrum. **76**, 036106 (2005).

Appendix D

Line shape of the μH$(3p-1s)$ transition

Line shape of the μH$(3p-1s)$ transition

D. S. Covita,[1, 2] D. F. Anagnostopoulos,[3] H. Gorke,[4] D. Gotta,[5] A. Gruber,[6] A. Hirtl,[6]
T. Ishiwatari,[6] P. Indelicato,[7] E.-O. Le Bigot,[7] M. Nekipelov,[5] J. M. F. dos Santos,[1]
Ph. Schmid,[6] L. M. Simons,[2, *] M. Trassinelli,[7, †] J. F. C. A. Veloso,[8] and J. Zmeskal[6]

[1]*Dept. of Physics, Coimbra University, P-3000 Coimbra, Portugal*
[2]*Paul Scherrer Institut (PSI), CH 5232-Villigen, Switzerland*
[3]*Dept. of Material Science and Engineering, University of Ioannina, Ioannina, GR-45110, Greece*
[4]*Zentralabteilung für Elektronik, Forschungszentrum Jülich, D-52425 Jülich, Germany*
[5]*Institut für Kernphysik, Forschungszentrum Jülich, D-52425 Jülich, Germany*
[6]*Stefan Meyer Institut, Austrian Academy of Sciences, A-1090 Vienna, Austria*
[7]*Laboratoire Kastler Brossel, UPMC-Paris 6, ENS,*
CNRS; Case 74, 4 place Jussieu, 75005 Paris, France
[8]*Dept. of Physics, Aveiro University, 3810-193 Aveiro, Portugal*

(Dated: July 14, 2008)

The hyperfine structure of the ground state of the muonic hydrogen atom could be resolved for the first time by measuring X-rays of the $(3p-1s)$ transition with a high-resolution crystal spectrometer. A Doppler effect broadening of the X-ray line was established which could be attributed to different Coulomb de-excitation steps preceding the measured transition. The assumption of a statistical population of the hyperfine levels of the muonic hydrogen ground state was directly confirmed by experiment and measured values for the hyperfine splitting can be reported. The results allow a decisive test of advanced cascade model calculations and establish a method to extract fundamental strong interaction parameters from pionic hydrogen experiments.

PACS numbers: 36.10.-k

A series of experiments has been conducted at PSI to extract the isospin separated pion-nucleon scattering lengths from the observation of X-ray transitions feeding the ground state of pionic hydrogen [1–3]. The experimental difficulties especially in the extraction of the isovector scattering length, equivalent to the determination of the strong interaction broadening of the ground state, are considerable. With transition energies of the order of 2-3 keV and values for the strong-interaction shift and width being of the order of 7 eV and 1 eV, respectively, the use of a high resolution Bragg X-ray spectrometer was mandatory to reach the envisaged precision on the percent level. The extraction of the strong-interaction broadening requires an unfolding of a Lorentzian line shape from the measured line shape which consists out of a convolution of the Lorentzian with a resolution function and several contributions of Doppler broadenings from different velocity states of the exotic atom.

Such velocity states can develop in exotic hydrogen atoms. These systems are electrically neutral and may dive deeply into the electron cloud of a neighbouring hydrogen molecule. These close encounters lead to violent processes strongly influencing the de-excitation (cascade) of exotic hydrogen atoms.

The most important of these processes are the so-called Coulomb transitions [4–6]. In these radiationless collision-induced de-excitations, the released energy is shared between the exotic atom and a normal hydrogen atom as recoil partner. During the cascade, acceleration by Coulomb transitions and deceleration by elastic and inelastic collisions compete which results in a complex and level dependent kinetic energy distribution.

Historically, the first evidence for high velocity states was found in the charge exchange reaction $\pi^-p \rightarrow \pi^o n$ with stopped pions from the Doppler broadening of the time-of-flight (TOF) of the mono-energetic neutrons [7]. Later on, detailed studies confirmed that Coulomb de-excitation affects substantially the kinetic energy of πH [8] and μH atoms [9] even at lowest densities. From the neutron TOF spectra, several components were identified and are attributed to specific Coulomb transitions. Hints for the influence of the Doppler broadening in X-ray transitions were identified in first experiments measuring the strong-interaction width of the πH ground state [2, 3]. A correction for the cascade-induced broadening is therefore indispensible for a proper extraction of the hadronic contribution to the X-ray line width. Unfortunately the high precision information from the reaction $\pi^-p \rightarrow \pi^o n$ cannot be directly transfered to X-ray studies. Charge exchange occurs from ns states, mainly with principal quantum numbers $n = 3-5$ of the π^-p system, whereas the initial states for K X-ray emission are np levels. The preceding cascade steps for the two processes are very different. Consequently, the Doppler contributions to the X-ray line shape may deviate significantly from the ones derived from neutron TOF experiments.

As the intensities of the X-ray transitions are strongly dependent on pressure there was a first approach to extract information about the cross sections of the Coulomb de-excitation from intensity studies. Different processes like Stark and Auger effect, however, are overwhelming in their importance for the intensity of the X-rays compared to Coulomb de-excitation. In consequence the kinetic energy of the exotic hydrogen atom was used in earlier cascade codes (the so-called Standard Cascade Model: SCM) as one constant fitting parameter with values around $T_{kin} = 1$ eV explaining the measured intensities with sufficient accuracy [10].

Based on the SCM an extended standard cascade model (ESCM) was developed which provides a new approach to calculate the Doppler contributions to neutron TOF and exotic hydrogen X-ray spectra [11]. Taking into account the competing processes in each de-excitation step, a kinetic energy distribution at the time of X-ray emission is obtained. An example of a kinetic energy distribution obtained with the ESCM for muonic hydrogen reaching the $3p$ state is shown in Figure 1. Monoenergetic lines corresponding to specific Coulomb transitions $n \to n'$ are smeared out because of the numerous elastic collisions after the Coulomb transition and before X-ray emission. The validity of the ESCM calculations cannot be tested directly in pionic hydrogen as the strong-interaction broadening completely masks the fine details of different Doppler effect contributions.

Muonic hydrogen as a purely electromagnetic twin system to pionic hydrogen offers itself as an ideal candidate for the direct observation of the Coulomb de-excitation in X-ray transitions. Ideally, it could be used as a test of the validity of the ESCM by reproducing the line shape of muonic hydrogen X-ray transitions in a fitting routine with the predictions of the ESCM as input. In case of success the measuresd line shape would be obtained without additional free parameters and the calculated values for the ground state hyperfine splitting, and more important, for the relative intensity of the transitions feeding the triplet and singlet components should result.

The understanding of the de-excitation cascade in exotic hydrogen is needed in other experimental studies as well, e. g., (i) for the precision determination of the proton charge radius from the muonic hydrogen $2s - 2p$ Lamb shift [9, 12] or (ii) in the measurement of the induced pseudoscalar coupling in muon capture by the proton [13–15].

The experiment was performed at the πE5 channel of the proton accelerator of the Paul Scherrer Institut (PSI), Switzerland, which provides a low-energy pion beam with intensities of up to a few 10^8/s. Pions of 112 MeV/c were injected into the cyclotron trap II and decelerated by a set of degraders optimized to the muon stop rate. Muonic hydrogen is formed by slow muons originating from the decay of almost stopped pions close to or in a cylindrical cryogenic target cell of 22 cm length and 5 cm in diameter in the center of the trap. The cell was filled with hydrogen gas cooled down to 22K at 1 bar absolute pressure, which corresponds to a density equivalent to 12 bar at room temperature. X-radiation could exit the target cell axially through a 5 μm thick mylar® window.

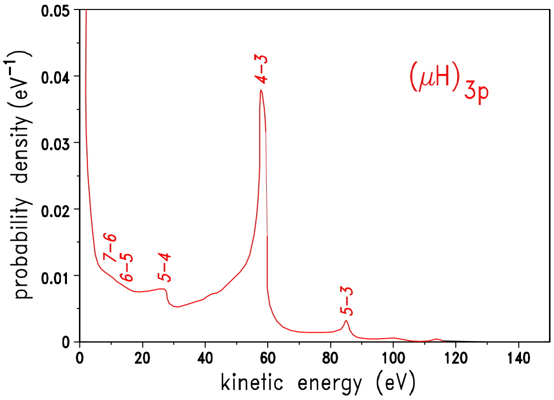

FIG. 1: Kinetic energy distribution of μH atoms at the instant of the $(3p-1s)$ transition as predicted from the ECSM [11] for a hydrogen density equivalent to 10 bar ($\approx 1.3 \cdot 10^{-2}$ LHD). Numbers indicate the corresponding Coulomb transitions $n \to n'$. The cascade calculation uses an initial kinetic energy of 0.5 eV in the laboratory frame.

X-rays from the μH$(3p-1s)$ transition were measured with a Johann-type Bragg spectrometer equipped with a spherically bent crystal Si(111) having a radius of curvature of 2982.2±0.3 mm and a free diameter of 90 mm [16]. Such a spectrometer is able to measure simultaneously an energy interval according to the width of the X-ray source when using a correspondingly extended X-ray detector, in this case a 3×2 array of charge-coupled devices [17]. The total extensions of the detector were 72 mm in height and 48 mm in width. The device's pixel size of 40 μm provides the two dimensional position resolution necessary to measure precisely the line shape. Because the charge originating from the conversion of a low-energy X-ray is collected under one or two pixels only, the ability to detect the hit pattern combined with the good energy resolution of semiconductor devices of about 200 eV leads to a significant background reduction. In addition, a massive concrete shielding suppresses background from beam induced reactions. In total almost 10000 events were collected for the μH$(3p-1s)$ line (Fig. 2). The theoretical values for the spin-averaged μH$(3p-1s)$ transition energy and the ground-state hyperfine splitting are calculated to be 2249.461 ± 0.001 eV [18] and 182.7 ± 0.1 meV [19]. The precise determination of the crystal response function and the experimental setup are described in detail elsewhere [20–22]. Identical response functions are assumed for the two hyperfine components.

As a first trial the kinetic energy distribution given by the ESCM was taken directly as an input for the fitting of the line shape. The comparison of such an "ESCM fit" to the measured line shape is shown in Figure 2 yielding a poor reduced χ^2 of $\chi^2_r = 1.353$ only. Obviously, the ESCM result does not reproduce the data. Especially

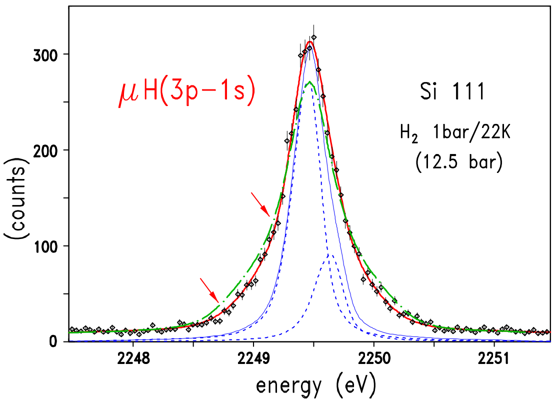

FIG. 2: Line shape of the μH$(3p-1s)$ transition as measured with a Si (111) crystal in first order. The narrow solid line represents the line shape expected in absence of any Doppler broadening being the sum of the two hyperfine components (dashed lines) and is normalised to the peak height after background subtraction. The prediction for the line shape from the ESCM is shown (dashed-dotted line) together with the "best fit"(solid line following the data) in the "model free" approach (see text). Evidence for the onset of the two high-energetic Coulomb components $(5-4)$ and $(4-3)$ are visible in the tails at about 40% and 10% of the peak height (arrows). A very good line shape discription – being indistiguishable by eye from the "best fit" – was found when using for the ESCM calculation the recently recalculated cross sections. One energy bin corresponds to 2 CCD pixels or 37.2 meV.

lower kinetic energies are underepresented.

Consequently, as a further approach a "model free" method was applied, which has already been used in the case of the neutron TOF spectra [8]. The Doppler contributions from Coulomb de-excitation to the μH$(3p-1s)$ line shape were determined by approximating the kinetic energy distribution by several rectangular boxes, the number of which is assessed by the transitions in the preceding cascade.

Several sets of kinetic energy boxes, also varying their number, were investigated including besides $\Delta n = 1$ also $\Delta n = 2$ Coulomb transitions. Hyperfine splitting, i. e., both line positions, relative population, (flat) background, and the relative weight of the boxes were free parameters in the fit. The sum of the relative weights of the boxes was always normalized to one.

It is a major result of the present study, that three boxes are essential but also sufficient to model a kinetic energy distribution yielding a good fit to the μH$(3p-1s)$ line shape: a low-energy component below $T_{kin} = 2$ eV and two at higher energies corresponding to the Coulomb transitions $n = 5 \rightarrow 4$ ($T_{kin} = 26.9$ eV) and $n = 4 \rightarrow 3$ ($T_{kin} = 58.2$ eV). A χ^2 analysis shows that in all cases a relative weight of about 60% of the low-energy component is mandatory. Furthermore, the fit is sensitive to the relative weight but not to the limits of the boxes. Changing their bounderies affects the relative weights by less than 1.4 standard deviations. Therefore, the kinetic energy distribution could be condensed to three narrow intervals.

Within the three box approach, the best χ^2 is found to be 448.9 which corresponds to a reduced χ^2_r of 0.947 ($n_{df} = 474$ degrees of freedom) with the kinetic energy intervals [0-1.8], [26.4-27.4] and [57.7-58.7] eV with relative weights of (61±2)%, (25±3)%, and (14±4)%. For the hyperfine splitting of the μH ground state 211 ± 6 meV was obtained with a triplet to singlet population of 3.66±0.25. Uncertainties represent statistical errors only.

Secondly, a correlation study of hyperfine splitting and relative population was performed keeping these parameters but one fixed and changed in small steps. The results found in the previous analysis were used as boundaries for the three kinetic energy intervals. Their weights, the total intensity and the background were taken as free parameters. The result is resumed in Figure 3. The best χ^2 is obtained for a hyperfine splitting of 211 ± 19 meV and a triplet to singlet population of 3.59 ± 0.51 ($\chi^2 = 448.9$ or $\chi^2_r = 0.941$ with $n_{df} = 477$). The errors correspond to the 1σ region. Again, a large relative weight of 61 ± 1% was found for the low-energy component.

When fixing the hyperfine splitting to the theoretical value of 182.7 meV, the best fit is obtained for a relative triplet to singlet population of 2.9 : 1, very close to the statistical value and less than $1.5\,\sigma$ away from the best χ^2(Fig. 3). In Figure 2, this "best fit" in the "model free" approach to the μH$(3p-1s)$ line shape is shown.

An additional process which may affect the line shape is due to molecular formation with subsequent radiative de-excitation: $(\mu p)_{nl} + H_2 \rightarrow [(\mu pp)_s p]ee \rightarrow [(\mu pp)_{s'} pee] + \gamma$ [23, 24], where s or s' represent the set of rotational and vibrational quantum numbers describing

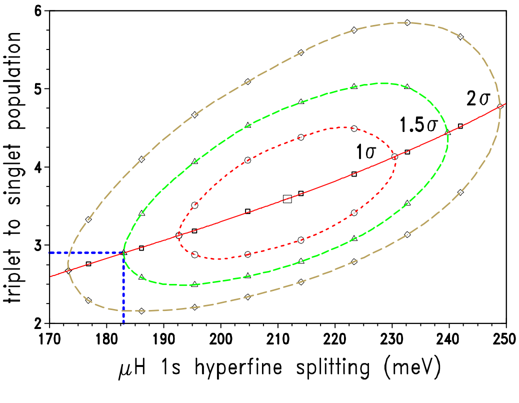

FIG. 3: χ^2 contour for the correlation of the ground state hyperfine splitting and relative population in the "model free" approach.

the molecular states. If radiative decay contributes significantly, a line broadening or even satellites at the low-energy side are expected. In the case of μpp, a branching ratio for radiative decay at the few per cent level was predicted [25, 26]. However, in this experiment, no evidence was found at the 1% level for any broadening except from Coulomb de-excitation. The result is corroborated from the absense of any density dependence of the πH($3p-1s$) transition energy [3].

As already seen in the direct ESCM fit of the data the low weight of the low-energy component is in contradiction to the measurement. The ESCM calculations predict values of about 30% for the low-energy component $T_{kin} \leq 2\,\mathrm{eV}$, a factor of two too low compared to the "model free" fit [11].

It is evident from the large contribution of low kinetic energies, that a correct treatment of the cross sections responsable for the development of the low energies coming from an interplay of Coulomb de-excitation and elastic collisions is still lacking in the ESCM code. In addition, the cascade calculation starting at $n = 8$, possibly neglects stronger effects from Coulomb de-excitation in the outer shells ($n > 11$), where the ESCM uses a classical trajectory Monte-Carlo approach [11].

The results from the present experiment led to a reconsideration of cross sections involved in exotic-hydrogen de-excitation. In a fully quantum-mechanical close-coupling approach, elastic scattering, Stark transitions and Coulomb de-excitation now have been calculated by a unified manner [5, 6].

Including these cross-section results in the ESCM model [27], the relative weight of the low energies ($T_{kin} \leq 2\,\mathrm{eV}$) increased to about 55% for μH, which is close to the constraint found in the "model free" approach. A fit to the measured μH($3p-1s$) line shape by using the new kinetic energy distribution yields much better agreement with the data even leaving hyperfine splitting and triplet to singlet intensity ratio as free parameters (Fig. 2). The striking agreement is indicated by $\chi^2_r = 0.984$. Values of $201 \pm 11\,\mathrm{meV}$ and 2.98 ± 0.21 were obtained for the hyperfine splitting and the triplet to singlet intensity ratio.

To summarize, the line shape of the μH($3p-1s$) transition was measured for the first time with a high resolution Bragg spectrometer. The influence of Coulomb de-excitation was directly seen from a line broadening compared to the spectrometer response function. By using a "model free" fitting approach various Doppler contributions are identified, which are attributed to preceding Coulomb transitions. A large fraction of the μH systems are found to be degraded by collisions to kinetic energies below 2 eV. The measurement yields the μH ground state hyperfine splitting as calculated from QED and, also for the first time, confirms experimentally the statistical population of the triplet and singlet ground states. The measurement triggered a new calculation of cross sections influencing the de-excitation processes which reproduces the muonic data and serves as a basis for a further evaluation of the determination of the isovector scattering amplitude from pionic hydrogen data with increased precision.

We gratefully acknowledge the excellent technical support by B. Leoni, N. Dolfus, and K.-P. Wieder. The Bragg crystal was manufactured by Carl Zeiss AG, Oberkochen, Germany. D. S. Covita has a Ph. D. scholarship granted by FCT (Lisbon) through the POCI 2010 program. This work is part of the PhD thesis of one of us (D. S.Ċ., University of Coimbra, 2008).

---

[*] present address: Dept. of Physics, Coimbra University, P-3000 Coimbra, Portugal

[†] present address: Institut des NanoSciences de Paris, 140 rue de Lourmel, 75015 Paris, France

[1] PSI proposal R-98-01, `www.fz-juelich.de\ikp\exotic-atoms`.

[2] H.-Ch. Schröder et al., Eur. Phys. J C **21**, 473 (2001).

[3] D. Gotta et al., Lect. Notes Phys. **745**, 165 (2008).

[4] L. Bracci and G. Fiorentini, Nuovo Cim. A , 43, 9 (1978).

[5] G. Ya. Korenman, V. N. Pomerantsev, and V. P. Popov, JETP. Lett. **81**, 543 (2005).

[6] V. N. Pomerantsev and V. P. Popov, JETP. Lett. **83**, 331 (2006); Phys. Rev. A **73**, 040501(R) (2006).

[7] J. B. Czirr et al., Phys. Rev. **130**, 341 (1963).

[8] A. Badertscher et al., Europhys. Lett. **54**, 313 (2001), and references therein.

[9] R. Pohl et al., Hyperfine Interact. **138**, 71 (2001).

[10] E. Borie and M. Leon, Phys. Rev. A **21**, 1460 (1980).

[11] T. S. Jensen and V. E. Markushin, Eur. Phys. J. D **19**, 165 (2002); Eur. Phys. J. D **21**, 261 (2002); Eur. Phys. J. D **21**, 271 (2002).

[12] D. Taqqu et al., Hyperfine Interact. **119**, 311 (1999).

[13] D. F. Measday, Phys. Rep. **354**, 243 (2001).

[14] T. Gorringe and H. W. Fearing, Rev. Mod. Phys. **76**, 31 (2004).

[15] V. A. Andreev et al., Phys. Rev. Lett. **99**, 032002 (2007).

[16] D. Gotta, Prog. Part. Nucl. Phys. **52**, 133 (2004).

[17] N. Nelms et al., Nucl. Instr. Meth. A **484**, 419 (2002).

[18] P. Indelicato, priv. comm.

[19] A. P. Martynenko and R. N. Faustov, JETP **98**, 39 (2004).

[20] D. F. Anagnostopulos et al., Nucl. Instr. Meth. A **545**, 217 (2005).

[21] M. Trassinelli et al., J. Phys., Conf. Ser. **58**, 129 (2007).

[22] D. S. Covita, thesis, Univ. of Coimbra (2008), unpublished.

[23] D. Taqqu, *Muon Catalyzed Fusion*, AIP Conference Proceedings **181**, 217 (1989).

[24] S. Jonsell, J. Wallenius, P. Froelich, Phys. Rev. A **59**, 3440 (1999).

[25] E. Lindroth, J. Wallenius, S. Jonsell, Phys. Rev. A **68**, 032502 (2003).

[26] S. Kilic, J.-P. Karr, L. Hilico, Phys. Rev. A **70**, 042506 (2004).

[27] T. S. Jensen, V. N. Pomerantsev, and V. P. Popov, arXiv:0712.3010v1 [nucl-th] (2007).

Bibliography

[1] **David Griffiths**,
"Introduction to Elementary Particles"
Wiley-VCH, Mörlenbach, Germany (2004);

[2] **W.N. Cottingham and D.A. Greenwood**,
"An Introduction to the Standard Model of Particle Physics"
Cambridge University Press, Cambridge, UK (2003);

[3] **W. Greiner, S. Schramm and E. Stein**,
"Quantum Chromodynamics"
Springer, **3rd edition**, Berlin, Germany (2007);

[4] **A.W. Thomas and W. Weise**,
"The structure of the Nucleon"
Wiley-VCH, **1st edition**, Berlin, Germany (2001);

[5] **S. Scherer and M.R. Schindler**,
"A Chiral Perturbation Theory Primer "
arXiv:hep-ph/0505265 (2005);

[6] **A. Zee**,
"Quantum field theory in a nutshell"
Princeton University Press, **1st edition**, Princeton, USA (2003);

[7] **M. Srednicki**,
"Quantum Field Theory"
Cambridge University Press, Cambridge, UK (2007);

[8] **J. Gasser, V. E. Lyubovitskij, A. Rusetsky, and A. Gall**,
"Decays of the $\pi^+\pi^-$ atom"
Phys. Rev. D **64**, 016008 (2001);

[9] **G. Colangelo, J. Gasser and H. Leutwyler**,
"$\pi\pi$ scattering"
Nucl. Phys. B **603**, 125-179 (2001);

[10] **G. Ecker**,
"Chiral perturbation theory"
Prog. Part. Nucl. Phys. **35**, 1-80 (1995);

[11] **B. Adeva et al.**,
"CERN experiment PS212(DIRAC), Proposal CERN/SPSLC 95-1", CERN (1995);

[12] **G. Beer, A. M. Bragadireanu, M. Cargnelli, C. Curceanu-Petrascu, J.-P. Egger, H. Fuhrmann, C. Guaraldo, M. Iliescu, T. Ishiwatari, K. Itahashi, M. Iwasaki, P. Kienle, T. Koike, B. Lauss, V. Lucherini, L. Ludhova, J. Marton, F. Mulhauser, T. Ponta, L. A. Schaller, R. Seki, D. L. Sirghi, F. Sirghi, and J. Zmeskal**,
“ Measurement of the Kaonic Hydrogen X-Ray Spectrum”
Phys. Rev. Lett **94**, 212302 (2005);

[13] *http://www.Inf.infn.it/esperimenti/siddharta/*;

[14] “Proceedings of HADATOM02, CERN, Geneva, October 14-15 (2002)”
arXiv:hep-ph/0301266 (2003);

[15] **T. Ericson and Wolfram Weise**,
“Pions and Nuclei”
Clarendon Press, (1988);

[16] **J.R. Taylor**,
“Introduction to the Quantum Theory of Scattering”
Dover Publications, (2006);

[17] **B.H. Brandsen and R.G. Moorhouse**,
“The Pion–Nucleon System”
Princeton University Press, (1967);

[18] **G. Rasche and W. S. Woolcock**,
“Connection between low-energy scattering parameters and energy shifts for pionic hydrogen”
Nucl. Phys. A **381**, 405-418 (1982);

[19] **D. Sigg, A. Badertscher, P.F.A. Goudsmit, H.J. Leisi and G.C. Oades**,
“Electromagnetic corrections to the s wave scattering lengths ion pion hydrogen”
Nucl. Phys. A **609**, 310-325 (1982);

[20] **J. Gasser, M.A. Ivanov, E. Lipartia, M. Mojžiš adn A. Rusetsky**,
“Ground-state energy of pionic hydrogen to one loop”
Eur. Phys. J. C **26**, 13-34 (2002);

[21] **A.N. Ivanov, M. Faber, A. Hirtl, J. Marton and N.I. Troitskaya**,
“Energy level displacement of the excited nl state of pionic hydrogen”
Eur. Phys. J. A **19**, 413-422 (2004);

[22] **P.J. Mohr and B.N. Taylor**,
“CODATA recommended values of the fundamental physical constants: 2002”
Rev. Mod. Phys **77**, 1-107 (2005);

[23] **C.C. -Tannoudji**,
“Quantum Mechanics, volume two”
Wiley-VCH, Paris, France (2003);

[24] **V.E. Lyubovitskij and A. Rusetsky**,
“$\pi^- p$ atom in ChPT: Strong energy-level shift”
Phys. Lett B **495**, 9-18 (2000);

[25] **P. Zemp**,
“Pionic Hydrogen in QCD+QED: Decay width at NNLO — PhD thesis”
Institut für theoretishe Physik, Universität Bern, Bern (2004);

[26] **J. Gasser, V.E. Lyubovitskij and A. Rusetsky**,
"Hadronic atoms in QCD+QED"
Phys. Reports **456**, 167-251 (2008);

[27] **M. Leon and H.A. Bethe**,
"Negative meson absorption in liquid hydrogen"
Phys. Rev. **127**, 636-647 (1962);

[28] **L. Bracci and G. Fiorentini**,
"Coulomb de-excitation of mesic hydrogen"
Nuovo Cimento **43A**, 9 (1978);

[29] **E. Borie and M. Leon**,
"X–ray yields in protonium and mesic atoms"
Phys. Rev. A **21**, 1460-1468 (1980);

[30] **V.E. Markushin**,
"Light μ^- atoms in liquid and gaseous hydrogen and deuterium"
Sov. Phys. JETP **53**, 16 (1981);

[31] **G. Reifenröther and E. Klempt**,
"Antiprotonic hydrogen: From atomic capture to annihilation"
Nucl. Phys. A **503**, 885-898 (1989);

[32] **T.S. Jensen and V.E. Markushin**,
"Collisional deexcitation of exotic hydrogen atoms in highly excited states, I. Cross–sections"
Eur. Phys. J. D **21**, 261-270 (2002);

[33] **T.S. Jensen and V.E. Markushin**,
"Collisional deexcitation of exotic hydrogen atoms in highly excited states, II. Cascade calculations"
Eur. Phys. J. D **21**, 271-283 (2002);

[34] **J.S. Cohen**,
"Formation of exotic hydrogen atoms"
Electromagnetic Cascade and Chemistry of Exotic Atoms , edited by L.M. Simons et al. , Plenum Press, 1-22 (1990);

[35] **J.S. Cohen**,
"Isotope effects on antiproton and muon capture by hydrogen and deuterium atoms and molecules"
Phys. Rev. A **59**, 1160-1169 (1999);

[36] **K. Kirch, D. Abbott, B. Bach, P. Hauser, P. Indelicato, F. Kottmann, J. Missimer, P. Patte, R.T. Siegel, L.M. Simons and V. Viel**,
"Muonic cascades in isolated low–Z atoms and molecules"
Phys. Rev. A **59**, 3375-3385 (1999);

[37] **H.A. Bethe and E.E. Salpeter**,
"Handbuch der Physik, Band XXXV"
Springer, Berlin, Germany (1957);

[38] **T.S. Jensen and V.E. Markushin**,
"Scattering of light exotic atoms in excited states"
Eur. Phys. J. D **19**, 165-181 (2002);

[39] **V.E. Markushin**,
"Cascade in muonic and pionic atoms with Z = 1"
Hyperf. Interact. **119**, 11-21 (1999);

[40] **A.P. Bukhvostov and N.P. Popov**,
"Depolarisation of negative muons in hydrogen"
Sov. Phys. JETP **55**, 12 (1982);

[41] **J.B. Czirr**,
"Determination of π–Meson by Neutron Time of Flight"
Phys. Rev. **130**, 341-350 (1963);

[42] **J.E Crawford, M. Daum, R. Forsch, B. Jost, P.-R. Kettle, R.M. Marshall, B.K. Wright and K.O.H. Ziock**,
"Precision measurement of the mass difference $m_{\pi^-} - m_{\pi^0}$"
Phys. Lett. B **213**, 391-394 (1988);

[43] **J.E Crawford, M. Daum, R. Forsch, B. Jost, P.-R. Kettle, R.M. Marshall, B.K. Wright and K.O.H. Ziock**,
"Precision measurement of the pion mass difference $m_{\pi^-} - m_{\pi^0}$"
Phys. Rev. D **43**, 46-58 (1991);

[44] **A. Badertscher, M. Daum, R. Frosch, P.F.A. Goudsmit, W. Hajdas, M. Janousch, P.-R. Kettle, V. Markushin, J. Schottmüller and Z.G. Zhao** ,
"Experimental determination of the kinetic energy distribution of $\pi^- p$ atoms in liquid hydrogen"
Phys. Lett. B **292**, 278-282 (1997);

[45] **J. Schottmüller, A. Badertscher, M. Daum, P.F.A. Goudsmit, M. Janousch, P.-R. Kettle, J. Koglin, V.E. Markushin and Z.G. Zhao**,
"Kinetic energy of $\pi^- - p$-atoms in liquid and gaseous hydrogen"
Hyperf. Interact. **119**, 95-102 (1999);

[46] **T.S. Jensen and V.E. Markushin**,
"Atomic Cascade and Precision Physics with Light Muonic and Hadronic Atoms"
Proceedings of Precision Physics of Simple Atomic Systems PSAS'02, Lecture Notes in Physics, edited by S.G. Karshenboim et V.B. Smirnov , Springer **627**, 37-57, Berlim (2003);

[47] **T.B. Day, G.A. Snow and J. Sucher**,
"Supression of P–state capture in (K^-,p) atoms"
Phys. Rev. Lett **3**, 61-64 (1959);

[48] **T.B. Day, G.A. Snow and J. Sucher**,
"High–Orbital S–State Capture of π^- Mesons by Protons"
Phys. Rev. **118**, 864-866 (1960);

[49] **V.E. Markushin**,
"Cascade processes in exotic atoms with Z = 1"
Electromagnetic Cascade and Chemistry of Exotic Atoms , edited by L.M. Simons et al. , Plenum Press, 73-96 (1990);

[50] **H.A. Bethe and E.E. Salpeter**,
"Quantum mechanics of one– and two–electron atoms"
Plenum Publishing Corporation, **Paperback 1st edition**, New York, USA (1977);

[51] **T.S. Jensen**,
"Kinetic energy distribution in pionic hydrogen"
Eur. Phys. J. D **31**, 11-19 (2004);

[52] **J. Wallenius and P. Froelich**,
"Formation of metastable $dt\mu$ molecules in $t\mu(2s)$-D_2 collisions"
Phys. Lett. A **54**, 1171-1182 (1996);

[53] **S. Jonsell, J. Wallenius and P. Froelich**,
"Influence of $pp\pi$ ions on pion absorption in H_2"
Phys. Lett. A **59**, 3440-3453 (1999);

[54] **A.S. Wightmann**,
"Moderation of Negative Mesons in Hydrogen I: Moderation from High Energies to Capture by H_2 Molecule"
Phys. Rev. **77**, 521-528 (1960);

[55] **V.E. Markushin**,
"Atomic cascade in muonic hydrogen and the problem of kinetic–energy distribution in the ground state"
Phys. Lett. A **50**, 1137-1143 (1994);

[56] **T.S. Jensen**,
"Atomic Cascade in Light Exotic Atoms — PhD thesis"
Mathematisch–Naturwissenschatlichen Fakultät der Universität Zürich, Zürich (2002);

[57] **T.S. Jensen and V.E. Markushin**,
"Collisional Quenching of the $2S$ State of Muonic Hydrogen"
PSI-PR-99-32(1999), nucl-th/0001009;

[58] "Proceedings of the International Symposium on Exotic Atoms, Molecules, and Muon Catalyzed Fusion (EXAT98)"
Hyperf. Interact. **118/119** (1999);

[59] **M.P. Faifman and L.I. Men'shikov**,
"Cascade Processes in Muonic Hydrogen Atoms"
Hyperf. Interact. **138**, 61-70 (2001);

[60] **T.S. Jensen, V.N. Pomerantsev and V.P. Popov**,
"Atomic Cascade in Muonic and Hadronic Hydrogen"
arXiv:0712.3010v1 [nucl-th] (2007);

[61] **G.Ya. Korenman, V.N. Pomerantsev and V.P. Popov**,
"Coulomb Deexcitation of Muonic Hydrogen within the Quantum Close-Coupling Method"
JETP Lett **81**, 543-547 (2005);

[62] **V.N. Pomerantsev and V.P. Popov**,
"Angular Distributions of Scattered Excited Muonic Hydrogen Atoms"
JETP Lett **83**, 273-278 (2006);

[63] **V.N. Pomerantsev and V.P. Popov**,
"Coulomb deexcitation of pionic hydrogen within the close-coupling method"
Phys. Rev. A **73**, 040501 (2006);

[64] **V.E. Markushin**,
Soviet J. Nuclear Phys. **40**, 612 (1984);

[65] **H. Anderhub, H.P. von Arb, J. Böcklin, F. Dittus, R. Ferreira Marques, H. Hoper, F. Kottmann, D. Taqqu and J. Unternährer**,
"Measurement of the *K* X–ray intensity ratios in muonic hydrogen at low gas densities"
Phys. Lett. B **143**, 65-68 (1984);

[66] **M. Bregant, D. Chatellard, J.-P. Egger, P. Hauser, E. Jeannet, K. Kirch, F. Kottmann, E. Milotti, C. Petitjean, L.M. Simons, D. Taqqu and E. Zavattini**,
"Measurement of the *K* X–ray intensity ratios in muonic hydrogen at low gas densities"
Phys. Lett. A **241**, 344-350 (1998);

[67] **B. Lauss, P. Ackerbauer, W.H. Breunlich, B. Gartner, M. Jeitler, P. Kammel, J. Marton, W. Prymas, J. Zmeskal, D. Chatellard, J.-P. Egger, E. Jeannet, D. Daniel, F.J. Hartmann, A. Kosak and C. Petitjean**,
"X–ray Emission during the Muonic Cascade in Hydrogen"
Phys. Rev. Lett. **80**, 3041-3044 (1998);

[68] **D.J. Abbott, G.F. Chen, P. Guss, A.D. Hancock, J.B. Kraiman, R.T. Siegel, W.F. Vulcan, D.W. Viel, R.E. Welsh, C. Petijean, A. Zehnder, W.H. Breunlich, M. Cargnelli, P. Kammel, A. Scrinzi, J. Marton, J. Zmeskal, J.J. Reidy, H.L. Woolverton, F.J. Hartmann, A. Adamczak, V.E. Markushin and V.S. Melezhik**,
"Diffusion of muonic deuterium and hydrogen atoms"
Phys. Lett. A **55**, 214-229 (1997);

[69] **F. Kottmann, H. Daniel, F.J. Hartmann, P. Hauser, C. Maierl, V.E. Markushin, M. Mhlbauer, C. Petitjean, R. Pohl, W. Schott and D. Taqqu** ,
"Kinetic energies of exotic H atoms at formation and cascade"
Hyperf. Interact. **119**, 3-10 (1999);

[70] **R. Pohl**,
"Investigation of the long–lived metastable 2S state in muonic hydrogen — PhD thesis"
Eidgenössische Technische Hochschule Zürich, Zürich (2001);

[71] **R. Pohl, H. Daniel, F.J. Hartmann, P. Hauser, Y.W. Liu, F. Kottmann, C. Maierl, V.E. Markushin, M. Mhlbauer, C. Petitjean, W. Schott and D. Taqqu**
"Observation of the Molecular Quenching of μp(2S) Atoms"
Hyperf. Interact. **138**, 35-40 (2001);

[72] **R. Pohl** *Private communication*;

[73] **R. Frosch** "Kinetic energy of $\pi^- p$ atoms in liquid hydrogen" *Technical report* **TM 37-21**, Paul Scherrer Institut;

[74] **A.J. Rusi, E.L. Hassani, W. Beer, M. Bogdan, D. Bovet, E. Bovet, J.P. Egger, G. Fiorucci, J.L. Vuilleumier, K. Gabathuler and L.M. Simons**,
"Determination of X-ray yields in pionic hydrogen as function of gas pressure"
Electromagnetic Cascade and Chemistry of Exotic Atoms , edited by L.M. Simons et al. , Plenum Press, 105-109 (1990);

[75] **E.L. Koller and A.M. Sachs**,
"Panofsky Ratio for Negative Pions Absorbed in Hydrogen"
Phys. Rev. **116**, 760-768 (1959);

[76] **J. Spuller, D. Berghofer, M. D. Hasinoff, R. Macdonald, D. F. Measday, M. Salomon, T. Suzuki, J. -M. Poutissou, R. Poutissou and J. K. P. Lee**,
"A remeasurement of the Panofsky ratio"
Phys. Lett. B **67**, 479-482 (1977);

[77] **D. Gotta**,
"Precision spectroscopy of light exotic atoms"
Prog. Part. Nucl. Phys. **52**, 133-195 (2004);

[78] **W. Fridrich, P. Knipping and M.v.Laue**,
Sitzungsberichte Bayer. Akad. Wiss. **303** (1912); *Ann. Phys.* **41**, 971 (1913)

[79] **W.L. Bragg**,
"The diffraction of short electromagnetic waves by a crystal"
Proc. Cambridge Philos. Soc. **17, I**, 43-57 (1913);

[80] **B.E. Warren**,
"X-Ray Diffraction"
Dover Publications Inc, **1st edition**, New York, US (1990);

[81] **J.Als-Nielsen and Des McMorrow**,
"Elements of Modern X-Ray Physics"
John Wiley & Sons Ltd, **1st edition**, West Sussex, England (2001);

[82] **C.G. Darwin**,
"The theory of X-ray reflection"
Phil. Mag. **27**, 315-333 (1914);

[83] **C.G. Darwin**,
"The theory of X-ray reflection, Part II"
Phil. Mag. **27**, 675-690 (1914);

[84] **M. Sanchez del Rio and R.J. Dejus**,
"XOP 2.1: A new version of the X-ray optics software toolkit"
AIP Conf. Proc **705**, 784-787 (2004);

[85] **P.P. Ewald**,
"Zur Begründung der Kristalloptik. Teil I-III "
Ann. Phys. (Leipzig) **49**, 1-38, 117-143 (1916);

[86] **P.P. Ewald**,
Ann. Phys. (Leipzig) **54**, 519-597 (1917);

[87] **M.v. Laue**,
Ergeb. Exakten Naturwiss **10**, 133-158 (1931);

[88] **T. Kryshtab, J. Palacios Gmez, M. Mazin and G. Gmez Gasga**,
"Phenomenon of extinction in textured materials analysis as a source of both physical error and information on microstructure characteristics"
Acta Materialia **52**, 3027-3034 (2004);

[89] **E. Rossmanith**,
"The Resolution Function of Single-Crystal Diffractometers at a Synchrotron-Radiation Source: the influence of Absorption and Extinction on the FWHM"
Acta Cryst. A **49**, 80-91 (1993);

[90] **C.T. Chantler and R.D. Deslattes**,
"Systematic corrections in Bragg x-ray diffraction of flat and curved crystals"
Rev. Sci. Instrum. **66(11)**, 5123-5147 (1995);

[91] **A. Burek**,
"Crystals for Astronomical X-ray Spectroscopy"
Space Science Instrumentation **2**, 53-104 (1976);

[92] **E. Wagner**,
Phys. ZS **17** , 407 (1916);

[93] **J.W. DuMond and H.A. Kirkpatrick**,
Rev. Sci. Instrum. **1** , 88 (1930);

[94] **H.H. Johann**,
"Die Erzeugung lichtstarker Röntgenspektren mit Hilfe von Konkavkristallen"
Zeitschrift für Physik **69**, 185 (1931);

[95] **J. Eggs and K. Ulmer**,
"Röntgenspektroskopie mit sphärisch gekrümmten Kristallen"
Zeitschrift für angewandte Physik **20** Band, Hefte 2, 118-128 (1965);

[96] **G. Zschornack, G. Müller and G. Musiol**,
"Geometrical aberrations in curved Bragg crystal spectrometers"
Nuclear Instrum. Meth. **200**, 481-489 (1982);

[97] **T. Johansson**,
Z. Phys. **82**, 507-515 (1933);

[98] **L.V. Azároff**,
"Elements of X-ray crystallography";

[99] **F. Cembali, R. Fabbri, M. Servidori, A. Zani, G. Basile, G. Cavagnero, A. Bergamin and G. Zosi**,
"Precise X-ray relative measurement of lattice parameters of silicon wafers by multiple-Crystal Bragg-case diffractometry. Computer simulation of the experiment."
J. Appl. Cryst. **25**, 424-431 (1992);

[100] **V. Mocella, W.-K. Lee, G. Tajiri, D. Mills, C. Ferrero and Y. Epelboin**,
"A new approach to the solution of the Takagi–Taupin equations for X-ray optics: application to a thermally deformed crystal monochromator"
J. Appl. Cryst. **36**, 129-136 (2003);

[101] **G. Hölzer, O. Wehrhan and E. Föster**,
"Charactezization on flat and bent crystals for X-ray spectroscopy and imaging"
Crystal Research and Technology **33**, 555-567 (1998);

[102] **D.F. Anagnostopoulos, S. Biri, D. Gotta, A. Gruber, P. Indelicato, B. Leoni, H. Fuhrmann, L.M. Simons, L. Stingelin, A. Wasser and J. Zmeskal**,
"On the characterisation of a Bragg spectrometer with X-rays from an ECR source"
Nuclear Instrum. Meth. A **545**, 217-224 (2005);

[103] **A.D. Short, A. Keay and M.J.L Turner**,
"Performance of the XMM EPIC MOS CCD detectors"
SPIE proceedings **3445**, 13-27 (1998);

[104] **N. Nelms, D.F. Anagnostopoulos, O. Ayranov, G. Borchert, J.-P. Egger, D. Gotta, M. Hennebach, P. Indelicato, B. Leoni, Y.W. Liu, B. Manil, L.M. Simons and A. Wells** ,
"A large area CCD X-ray detector for exotic atom spectroscopy"
Nuclear Instrum. Meth. A **484**, 419-431 (2002);

[105] **P. Indelicato, E.-O Le Bigot, M. Trassinelli, D. Gotta, M. Hennebach, N. Nelms, C. David and L.M. Simons**,
"Characterization of a charge-coupled device array for Bragg spectroscopy"
Rev. Sci. Instrum. **77**, (2006);

[106] **N. Sadeghi, T. Nakano, D.J. Trevor and R.A. Gottscho** ,
"Ion transport in an electron cyclotron resonance plasma"
J. Appl. Phys. **70**, 2552 (1991);

[107] **C. Bernard**,
"PhD thesis" *Université J. Fourrier*, Lyon (1996);

[108] "PSI Proposal R-98-01", *http://www.fz-juelich.de/ikp/exotic-atoms/papers/pip_prop.pdf*;

[109] **D.R. Plante, W.R. Johnson and J. Sapirstein**,
"Relativistic all-order many-body calculations of the n=1 and n=2 states of the helium–like ion"
Phys. Rev A **49**, 3519-3530 (1994);

[110] **P. Indelicato** *Private communication*;

[111] *http://encyclopedia.airliquide.com/encyclopedia.asp*;

[112] **M. Hennebach** ,
"Precision measurement of ground state transitions in pionic hydrogen — PhD thesis" *Mathematisch–Naturwissenschatlichen Fakultät der Universität zu Köln*, Forschungszentrum Jülich (2003);

[113] **W.H. Press, B.P. Flannery, S.A. Teukossky and W.T. Vetterling**
"Numerical Recipes, The Art of Scientific Computing "
Cambridge University Press, **1st edition**, Cambridge, England (1986);

[114] **L.M. Simons** *Private communication*;

[115] **D. Gotta** *Private communication*;

[116] **D. Gotta, F. Amaro, D. F. Anagnostopoulos, S. Biri, D.S. Covita, H. Gorke, A. Gruber, M. Hennebach, A. Hirtl, T. Ishiwatari, P. Indelicato, Th. Jensen, E.-O. Le Bigot, J. Marton, M. Nekipelov, J.M.F. dos Santos, S. Schlesser, Ph. Schmid, L.M. Simons, Th. Strauch, M. Trassinelli, J.F.C.A. Veloso and J. Zmeskal**,
"Pionic Hydrogen"
Lect. Notes Phys. **745**, 165-186 (2008);

[117] **D. F. Anagnostopoulos, D. Gotta, P. Indelicato, L.M. Simons**,
"Low-Energy X-Ray Standards from Hydrogenlike Pionic Atoms"
Phys. Rev. Lett. **91**, 240801 (2003);

[118] **Geller et al.**,
Proc. 2nd Int. Conf. Ion Sources, Vienna, 632(1971);

[119] **R. Geller**,
"Electron Cyclotron Resonance Ion Sources and ECR Plasmas"
IOP Publishing, **1st edition**, Bristol, England (1996);

[120] **B. Wolf**,
"Hanbook of Ion Sources"
CRC Press, **1st edition**, New York, USA (1995);

[121] **J. Pivarč, J. Pivarč (Jr.) and M.N. El-Shazly**
"Some remarks to construction of ECR ion source hexapoles"
Proceedings of the 1999 Particle Accelerator Conference, New York, USA (1999);

[122] **M. Trassinelli**,
"Quantum Electrodynamics Test and X-rays Standards using Pionic Atoms and Highly Charged Ions — PhD thesis"
Université Paris VI, Paris (2005)

[123] **Z.Q. Xie**,
"Production of highly charged ion beams from electron cyclotron resonance ion sources"
Rev. Sci. Instrum. **69**, 625-630 (1998);

[124] **S. Biri, L.M. Simons and D. Hitz**,
"Electron cyclotron resonance ion trap: A hybrid magnetic system with very high mirror ratio for highly charged ion production and trapping"
Rev. Sci. Instrum. **71**, 1116-1118 (2000);

[125] **S. Biri, A. Valek, T. Suta, E. Takacs, C. Szabo, L.T. Hudson, B. Radics, J. Imrek, B. Juhasz and J. Palinkas**,
"Imaging of ECR Plasma with a Pinhole X-ray Camera"
Rev. Sci. Instrum. **75**, 1420-1422 (2004);

[126] **M. Stampanoni, G. Borchert and R. Abela**,
"Towards nanotomography with asymmetrically cut crystals"
Nuclear Instrum. Meth. A **551**, 119-124 (2005);

[127] **M. Sanchez del Rio and F. Cerrina**,
"Aymmetrically cut crystals for synchrotron radiation monochromators"
Rev. Sci. Instrum. **63**, 936-940 (1992);

[128] **A. Guinier**,
"RAYONS-X. Sur les monochromateurs à cristal courbé"
Comptes rendus hebdomadaires des séances de L' Académie des Sciences **223**, 31-32 (1946);

[129] **D.S. Covita, M. Ay, S. Schlesser, D. Gotta, L.M. Simons, E.-O. Le Bigot and J.M.F. dos Santos**,
"Accurate miscut angle determination for spherically bent Bragg crystals"
Rev. Sci. Instrum. **79**, 033102 (2008);

[130] **G. Filsher, F. Adolph and L. Adler**,
"Ein Gerätesystem zur röntgenographischen Orientierung von Einkristallen"
Kris. Tech. **9**, 437-442 (1974);

[131] **S.E.G. Slusky and A.T. Macrander**,
"Measurement of the miscut angle of crystal surfaces vicinal to major crystal planes by x-ray diffractometry at glancing incidence"
Appl. Phys. Lett. **53**, 2042-2043 (1988);

[132] **B.K. Tanner, S.J. Miles, G.G. Peterson and R.N. Sacks**,
"Measurement of aluminium concentration in GaAlAs epitaxial layers by double-axis X-ray diffraction"
Mater. Lett. **7**, 239-241 (1988);

[133] **Y. Chen, M.F. Morris, B. Obradovic, D. Li, Al.F. Tash and J.S. Swinnea**,
"The impact of crystal cut error on the measured impurity profiles resulting from ion implantation"
IEEE Trans. Semicond. Manuf. **13**, 243-248 (2000);

[134] **L.D. Doucette, M. Pereira da Cunha and R.J. Lad**,
"Precise orientation of single crystals by a simple x-ray diffraction rocking curve method"
Rev. Sci. Instrum. **76**, 036106 (2005);

[135] **M. Gailhanou**,
"Accurate monocrystal miscut angle determination by x-ray diffraction on a wedge"
Appl. Phys. Lett. **63**, 458-460 (1993);

[136] **M. Born**,
"The mechanics of the Atom"
Bell, London, England (1927);

[137] **J.D. Jackson**,
"Classical Electrodynamics"
John Wiley & Sons, **2nd edition**, USA (1975);

[138] **A.G. Drentje, A. Girard, D. Hitz and G. Melin**,
"Role of low charge state ions in electron cyclotron resonance ion source plasmas"
Rev. Sci. Instrum. **71**, 623-626 (2000);

[139] *http://www.dreebit.com/en/highly_charged_ions/data/*;

[140] **M.C. Martins, A.M. Costa, J.P. Santos, P. Indelicato and F. Parente**,
"Interpretation of x-ray spectra emitted by Ar ions in an electron-cyclotron resonance ion source"
J. Phys. B: At. Mol. Opt. Phys. **34**, 533-543 (2001);

[141] **A.M. Costa, M.C. Martins, F. Parente, J.P. Santos and P. Indelicato**,
"Dirac–Fock transition energies and radiative radiationless transition probabilities for Ar^{+9} to Ar^{+16} ion levels with K-shell holes"
At. Data Nucl. Data Tables **79**, 223-239 (2001);

[142] **V.E. Markushin** *Private communication*;

[143] **CERN program library** *http://seal.web.cern.ch/seal/work-packages/mathlibs/minuit/*;

[144] **A. Hirtl**,
"Determination of the strong interaction ground state width in pionic hydrogen — PhD thesis"
Technische Universität Wien Wien (2008);

[145] **D.S. Covita** *Private communication*;

[146] **S. Schlesser** *Private communication*;

[147] **J.D. Cockcroft and E.T.S. Walton** ,
" Experiments with High Velocity Positive Ions. II. The Disintegration of Elements by High Velocity Protons"
Proc. R. Soc. London A **137**, 229-242 (1932);

[148] *http://abe.web.psi.ch/facilities/facilities.php*;

[149] *http://aea.web.psi.ch/beam2lines/beam_pie5.html*;

[150] **A. Hirtl** *Private communication*;

[151] **A. Gruber**,
"Coulomb-Explosion in pionischem Kohlenstoff — Diploma thesis"
Institut für Mittelenergiephysik (present: Stefan-Meyer-Institute of subatomic physics) Vienna (2003);

[152] **R.D. Deslattes, E.G. Kessler Jr., P. Indelicato, L. de Billy, E. Lindroth and J. Anton**,
"X-ray transition energies: new approach to a comprehensive evaluation"
Rev. Mod. Phys. **75**, 35-99 (2003);

[153] **H. Gorke, W. Erven, D. Gotta, R. Hartmann, L. Strüder and L. Simons**,
"A compact setup of fast pnCCDs for exotic atom measurement"
AIP Conf. Proc. **793**, 341-346 (2005);

[154] **A. Ackens, U. Clemens, H. Gorke, P. Holl, J. Kemmer, H. Loevenich, D. Maeckelburg, M. Ramm, L. Strüder, C. Von Zanthier and K. Zwoll**,
"A compact and flexible CCD readout-system"
IEEE Trans. Nucl. Sci. **46**, 1995-1997 (1995);

[155] **S. Kilic, J-F. Karr and L. Hilico** ,
"Coulombic and radiative decay rates of the resonances of the exotic molecular ions $pp\mu$, $pp\pi$, $dd\mu$, $dd\pi$ and $dt\mu$"
Phys. Rev. A **70**, 042506 (2004);

[156] **L. G. Parratt**,
"Kα Satellite Lines"
Phys. Rev. **50**, 1-15 (1936);

[157] **M. Deutsch, G. Hölzer, J. Härtwig, J. Wolf, M. Fritsch and E. Förster**,
"Kα and Kβ x-ray emission spectra of copper"
Phys. Rev. A **51**, 283-296 (1995);

[158] **T. Strauch** *Private communication*;

[159] *http://www.aip.org/avsguide/refguide/vapor.html*;

[160] *http://webbook.nist.gov/chemistry/form-ser.html*;

[161] **A.P. Martynenko and R.N. Faustov**,
"Hyperfine Ground-State Structure of the Muonic Hydrogen"
JETP **98**, 39-52 (2004);

[162] *http://www.stat.sc.edu/~west/applets/chisqdemo.html* ;

[163] **D. Taqqu**,
“ Molecular effects in muonic hydrogen cascade”
Muon Catalyzed Fusion, AIP Conference Proceedings **181**, 217 (1989);

[164] **E. Lindroth, J. Wallenius and S. Jonsell** ,
“Decay rates of excited muonic molecular ions”
Phys. Rev. A **68**, 032502 (2003);

[165] **V.P. Popov and V.N. Pomerantsev** *Private communication*;